UNIVERSITÀ DI PARMA

UNIVERSITA' DEGLI STUDI DI PARMA

DOTTORATO DI RICERCA IN

"Scienze Chimiche"

CICLO XXXIV

Porous materials for catalytic applications: from Coordination Polymers to Metal Organic Frameworks

Coordinatore:

Chiar.ma Prof. Alessia Bacchi

Tutore:

Chiar.mo Prof. Luciano Marchiò

Dottorando: Giulia Bonfant

Anni Accademici 2018/2019 – 2020/2021

Preface

Porous solids are materials having structural voids (channels or confined cavities). These materials have always attracted a considerable interest in chemistry. Nowadays many porous materials can be made in the laboratory and they can even be produced on a large industrial scale and used as catalyst, adsorbent, and for small molecule separation. As far as catalysis is concerned, one of the main goals of the present-day research is the design of hetereogeneous systems that could work in mild conditions, and which could be synthetized in a simple and economical way. This research work had the aim to investigate porous materials for electrocatalytic applications. The study initially focused on the investigation of bis(3,5-dimethylpyrazolyl)methane silver complexes to generate molecular architectures based on weak interactions as halogen bond (Chapter 2). These crystalline complexes have large channels filled with crystallization solvent, but they do not possess permanent porosity after the removal of the solvent. Due to their metastable nature, we moved our interest towards more robust materials, which could sustain harsher conditions usually found in catalytic processes. For this reason, we focused on a class of amorphous porous materials namely, porous organic polymers (POPs) containing phosphine oxide groups, which was able to bind transition metals centres such as cobalt, iron, nichel or molybdenum (Chapter 3). The composition, the thermal and adsorption properties of these materials were determined. POPs functionalized with different metal ions were studied (a proof-of-concept) for the electrocatalytic activity towards the hydrogen evolution reaction (HER). The major drawbacks are related to their amorphous nature and consequently the challenge to control their pore size and in some cases the functionalization with metal centers was not successful. For these reasons, we moved our attention on crystalline systems such as metal organic frameworks (MOFs), incorporating metal binding systems on the linker. We designed sulphur and phosphorus based carboxilate ligands for the construction of MOFs having zirconium clusters as nodes. These family of MOFs (Chapter 4) are extremely robust and easily to functionalize. We characterized the chemical, thermal and adsorption properties of the obtained materials, and we studied the possibility to incorporating transition metals in the MOFs cavities.

Contents

Chapter 1

1. INTRODUCTION

1.1 Functional Porous Materials

1.1.1 Chemistry beyond the molecule

In the past century chemists has focused their works on molecular chemistry, by which we can combine atoms to obtain molecules. Synthetic chemists are now capable to build specific molecules with functional groups that mimic nature architectures, not only in their composition, but also in their three-dimensional arrangements. With the advancement of crystallography from the past century to the present day, we can now identify how these molecules can interact with each other to generate supramolecular architectures. One of the most important questions for material scientists, is how to arrange atoms and molecules in a predetermined and well-ordered way, to design complex and ordered systems. This approach, namely *bottom-up* approach is used by nature to build complex systems by which materials themselves are assembled in a controlled manner from their components, with a a fine tuning of their structure and properties. Beautiful examples of the application of these principles can be found inthe living systems, which can build supramolecules (proteins, DNA, RNAs) in mild conditions with extreme precision and with a specific function.

1.1.2 Pore chemistry

Another major aspect of materials science is the design of porous functional materials, having tailor-made functionalities, that can host a a specific catalytic transformation. The functional properties of these materials are strongly dependent by the high accessible surface area, permanent porosity, and size and shape of the pores. Porous solids are characterized by discontinuous matter distribution that can have amorphous or crystalline structure. Their cavities can act as a host for other molecules to obtain a host-guest system with various applications. Pore architectures (size, shape, connectivity) and pore distribution, in combination with the chemical features of the components, determine the properties of such materials and the possibility to exploit these systems for many applications: gas storage and separation, drug transport, heterogeneous catalysis, water storage, environmental remediation and chemical sensing.[1–7] Zeolites, metal-organic frameworks (MOFs), and covalent organic frameworks (COFs) are, crystalline materials with regular porosity, and they are characterized by a significant chemical diversity; throuought the years they have been as materials with high adsorption capacities as well as for catalytic applications.[8]

The concept of "*porous material*" and "*zeolite*" was firstly introduced in 1756 with the discovery made by Fredrik Cronstedt of a curious property of the mineral stilbite. The Swedish scientist, found out that the mineral, heated at elevated temperature, produced high amount of steam from the water previously adsorbed into its cavities. Based on this, he called the material *zeolite*, from the *Greek zéo-lithos*, which means boiling stone.[9] Nearly 100 years later, the study of natural porous materials continues with the discovery by Sir Humphrey Davy of another class of inclusion compounds "in which the guest molecule is in a cage formed by the host molecule or by a lattice of host molecules".[10] The name "*clathrate*" (meaning 'with bars, latticed') was choose by H. M. Powell only in 1947, after the advent of crystallography and the determination of the the crystal structure of Hofmann's nickel clathrate with benzene as guest.[11–13] At the beginning of the 20th century Y. Shibata coined the term "coordination polymers" as a class of material formed by repetitive coordination entities, usually metal ions linked via coordination bonds with organic ligands[14], as Werner cobalt complexes or prussian blue. These coordination frameworks have small

openings, generally filled with solvents or ions, but their discrete molecular structures did not allow permanent porosity.

In the 1964 a review was published by the american chemist J.C. Bailar to compare inorganic coordination polymers to organic polymers.[15] Later, F. Hoskins and R. Robson introduced the node and linker approach for the design of coordination networks (CNs), and the number of studies of porous materials increased and lead to the discovery of new classes of compounds such as porous coordination networks[16–19] (PCNs, Fujita 1994) and metal organic frameworks[20,21] (MOFs, I. D. Williams and O. M. Yaghi 1999). MOFs exhibits permanent porosity as evidenced by their gas adsorption isotherms (Type I), mainly as a result of their rigid multi-nuclear metal-carboxylate secondary building units and strong ligand-metal bonds.

With the introduction of the reticular chemistry[22]concept, by Yaghi and M. O'Keeffe in 2003, porous 3D architectures can now be prepared by modelling metal nodes and organic linkers. Since then, a great number of new crystalline structures with permanent porosity and high surface area was reported. In 2005, another class of crystalline solids, namely covalent organic frameworks[23] (COFs) was synthetized from purely organic molecules linked by covalent bonds. In addition, in 2006 a new subclass of MOFs, with permanent porosity are discovered: zeolitic imidazolate frameworks[24] (ZIFs) formed from carboxylate functionalized imidazoles or pyrimidine units and tetrahedral single transition metal nodes, topologically isomorphous to natural zeolites. In the same years new classes of amorphous solids was discovered as hypercrosslinked polymers[25] (HCPs) from Ullmann and Buchwald coupling reaction; porous aromatic frameworks (PAFs) via Yamamoto reaction; porous organic polymers (POPs) via Friedel–Crafts alkylation; conjugated microporous polymers[26] (CMPs, 2007) via Sonogashira–Hagihara coupling and polymers with intrinsic microporosity[27,28] (PIMs).

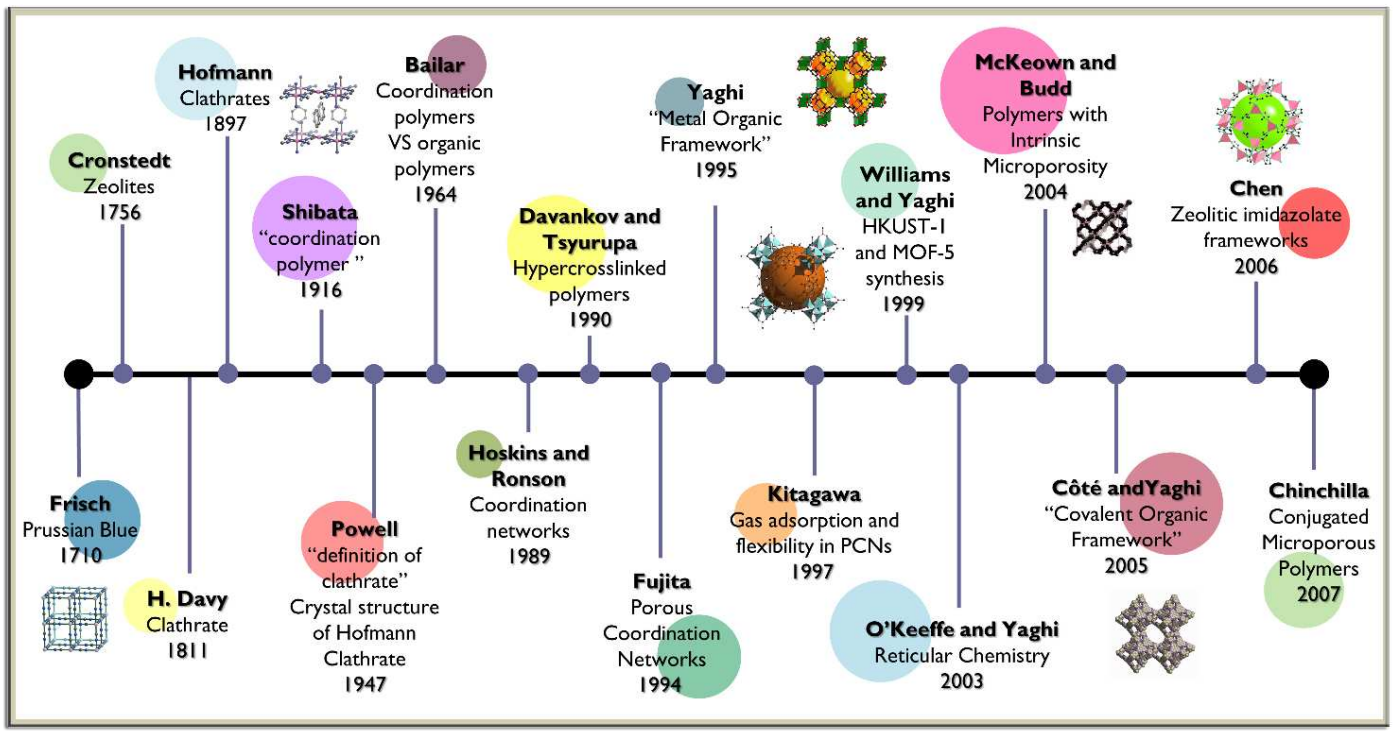

Figure 1. Timeline of porous material key researches in the last three centuries.[29]

1.1.3 Classification of porous materials

The classification of porous materials is usually based on two parameters: the pore size and the nature of the building blocks. Depending on the former, the International Union of Pure and Applied Chemistry (IUPAC) has classified porous materials into three categories:[30]

I. Microporous (pore sizes < 2 nm);

II. Mesoporous (pore sizes between 2–50 nm);

III. Macroporous materials (pore sizes between 51–100 nm);

These categories, which were suggested by the analysis of nitrogen adsorption isotherms are to some extent arbitrary. Nevertheless, they are still useful and broadly accepted today. On the other hand, by using a classification based on the building blocks and chemical composition, three other main categories can be identified:[31]

I. Inorganic (i.e. porous carbon derivatives, porous metal oxides, zeolites);

II. Organic–inorganic hybrid (i.e. Metal–Organic Frameworks (MOFs);

III. Organic porous materials (i.e. porous organic framworks (POFs)).

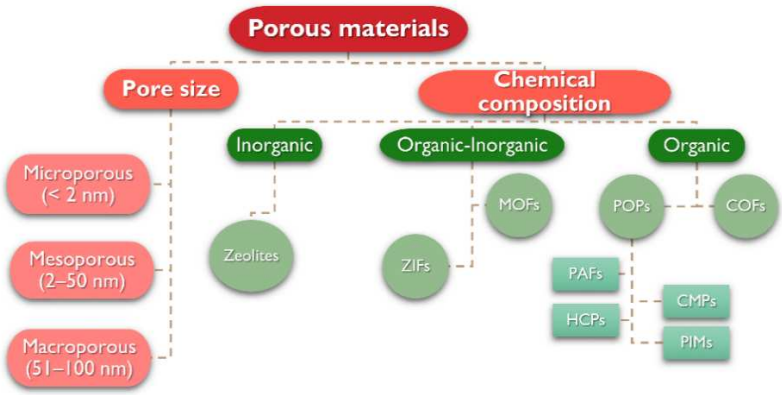

Figure 2. Schematic classification on porous materials.

In the following section we are going to present the main families of porous materials with their peculiar characteristics:[32]

a) Zeolites. Zeolites are crystalline aluminosilicates with a usually microporous cavities (0.3-1.5 nm) built by corner-sharing $[SiO_4]_4$ and $[AlO_4]_5$ tetrahedra; usually with a Si/Al ratio greater than one. The general formula of a zeolite is tipically $M_{x/n}[(AlO_2)_x(SiO_2)_y]\cdot m\ H_2O$. The electroneutrality is balanced with small exchangeable cations such as Na^+ or H^+, in their cavities. Since their discovery, two hundred thirty-two types of zeolite frameworks have been officially recognized by the Structure Commission of the International Zeolite Association (IZA-SC) and today represent the most used porous materials in industry, with an annual production of 5.5 million tonnes. This class of materials are largely used in the petroleum industry as heterogeneos catalyst, as water softeners in detergents production and as purification agents (molecular sieves).[8] Zeolites are synthetized by hydrothermal synthesis at high temperature and pressures with templates, mainly surfactants, to obtain the right pore structures. Other atoms with tetrahedral coordination such as Ge, B, and Ti can also be introduced into the framework to tune the dimension of the pore size. For instance, introducing titanium gives a mesoporous structure to the system against a minor hydrothermal stability. Typical examples of these titanosilicates are Ti-MCM-415 and Ti-SBA-156 materials.[33,34]

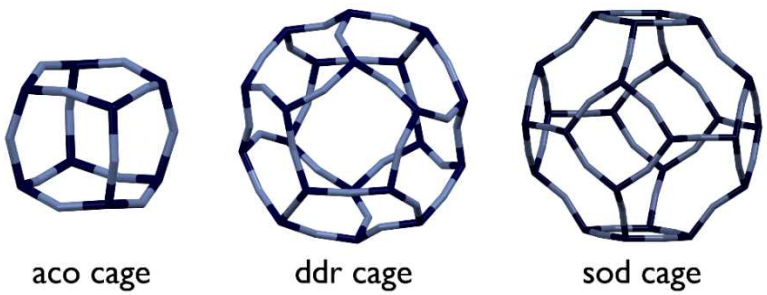

Figure 3. Some examples of secondary building units (SBUs) found in zeolite. Sod cage is the characteristic repetitive unit of sodalite zeolite. T-atoms [blue] represent Si and Al atoms in aluminosilicates; Oxygen atoms [light blue].

b) **Nanocarbons.** Nanocarbons belong to a carbon-based family of porous materials, with graphite-like structure in which at least one dimension is less than 100 nm. This family have sp^2 carbons and include carbon nanotubes (CNTs), fullerenes, graphene nanoribbons.[35,36] In particular, carbon nanotubes are allotropic form of carbon with cylindrical shape. CNTs can be single or multiple walled and for single walled carbon nanotubes (SWNTs) the pore diameter is about 1 nm.[37] On the contrary multiple-walled CNTs are made from concentrically cylindrical nanosheet of graphite, they have higher stability than single NTs and different properties because of different synthetic conditions (chemical vapor deposition, laser ablation and discharge). Porous carbons have high physicochemical stability that make them suitable for industrial applications. Nevertheless, it is difficult to tune the pore surface chemistry during synthesis and also with post-synthetic modifications it is challenging to have full control.[38]

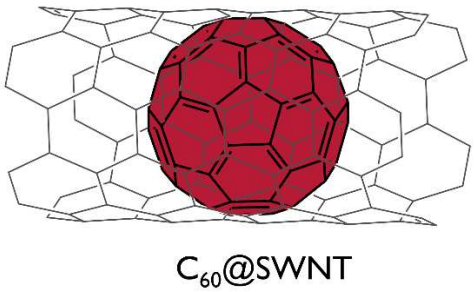

Figure 4. Schematic rapresentation of single-walled CNTs with fullerene C_{60} in the porous channel.

c) **Porous Organic Frameworks (POFs).** Another class of porous materials that has gained a significant importance in the last years, due to their simple synthesis and characterization, is that of porous organic frameworks (POFs). POFs are built by polymerization of rigid monomers and the characteristics of the pores is a result of the topology of the monomers used. A lot of family of POFs have been synthetized. They can amorphous such as porous aromatic frameworks (PAFs), conjugated microporous polymers (CMPs), polymers with intrinsic microporosity (PIMs), hyper-cross-linked polymers (HCPs) and porous

organic polymers (POPs) or crystalline as covalent organic frameworks (COFs). Amorphous POFs will be illustrated in Chapter 3.

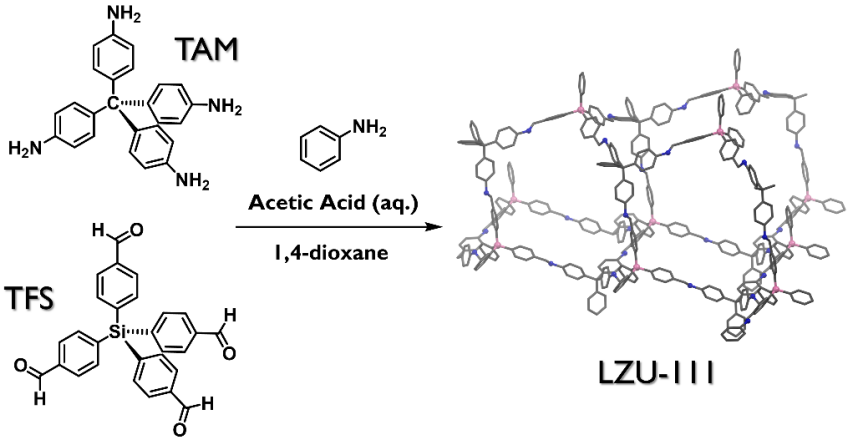

Figure 5. Example of 3D-COF synthesis by imine condensation between tetrakis(4-aminophenyl)methane (TAM) and silane-based tetraaldehyde (TFS) yielding LZU-111 as single-crystal with diamond-like structure. Carbon [grey], nitrogen [blue], silicon [purple], hydrogens are omitted for clarity.

Crystalline COFs were synthetized in 2005 for the first time by Yaghi and co-workers[23] and are made from organic ligands covalently bonded together. These porous systems present low density, large surface area that can rise up to 3600 m^2/g (COF-102), tunable pore size and chemical stability.[39]

Since their discovery, several reactions were used to build COFs architecture: imine condensation,[40] condensation of boronic acids in boronate ester or boronate anhydride,[41] nitrile cyclotrimerization and hydrazone synthesis.[42] Different functional groups have been successfully introduced into frameworks, yielding urea, borazine,[43] phenazine,[44] polyamide[45] and triazine[46] COFs. For their unique properties these frameworks have been investigated in several applicative fields, such as catalysis, photoelectronics and gas storage. Especially, hydrogen, methane and ammonia storage properties have been studied. As for other porous materials, 3D-COFs, having higher surface areas, possess higher gas uptake capacities with respect to 2D-COFs. For example, 3D COF-102 has hydrogen uptake of 7.24 wt% at saturation (77 K, 35 bar), which is similar to that found for amorphous PAF-1 (7.0 wt%).[47]

d) Metal-organic frameworks (MOFs). Metal organic frameworks is another class of hybrid porous materials. In contrast to the purely inorganic materials such as zeolites and mesoporous silica, MOFs are constructed from inorganic nodes (metal ions or clusters) coordinated with organic linkers to form 3D coordination networks with crystalline periodicity. One of the most notable functional features that characterize MOFs is the permanent porosity and high surface area (up to 7800

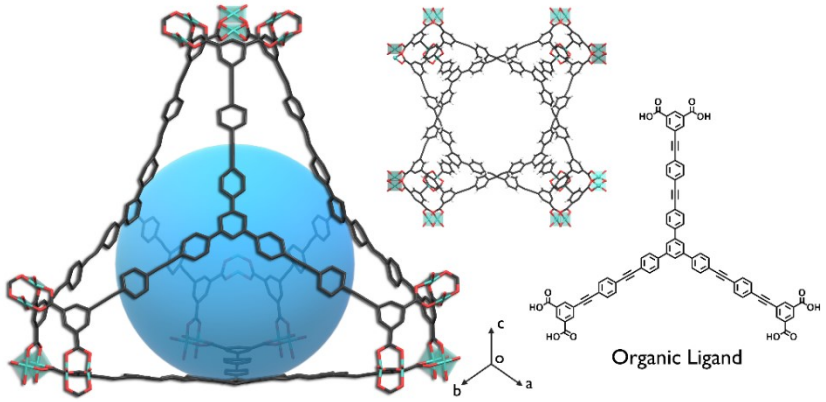

Figure 6. Single crystal features of NU-110 MOF. Different cages of NU-110 and the organic ligand used to build the framework. Carbon [grey], oxygen [red], copper [light blue]. Hydrogens are omitted for clarity.[49]

These features make MOFs suitable to be applied in various fields, the most popular applications are gas adsorption and storage (H_2, CO_2, CH_4). The capture and separation of small molecules (O_2, N_2, H_2S, NH_3, CO, NO_x)[50,51] are also relevant in the industrial fields, due to the possibility of the functionalization of the pore walls of the frameworks.[52] MOFs can be also used as host system to encapsulate small molecules such as bio-active molecules, or active pharmaceutical ingredients (APIs) for drug delivery and drug release applications. In particular, APIs are entrapped inside MOFs cavities by means of weak interactions between the chemical functionality on the pore wall and the drug. In this case, the MOFs had to be biocompatible, thus limit the use of only some type of metals such as Zn, Zr, Fe, or Mg, and a linker with low toxicity.[53] There also some examples of entrapment of macromolecules therapeutics inside MOFs such as proteins and nucleic acids, to protect them from degradation in biological systems.[54] The well-defined porous structure of MOFs displays

advantages over conventional carriers (polymers, quantum dots, nanoparticles, liposomes) reducing the problems related to instability in biological systems, toxicity and drug loading.[55]

The permanent porosity of MOFs has also led to the preparation of MOF composites in which the MOF cavities are filled with a variety of components such as metal nanoparticles, silica particles, metal oxides and carbon nanotubes. MOFs are also used as chemical sensors, optoelectronic devices and heterogeneous catalyst. The last application, among MOFs structure and properties will be discussed in detail in Chapter 4.

1.2 Adsorption properties of porous materials

Understanding the adsorption properties of porous materials is the key to the characterization and application of these materials for heterogeneous catalysis, adsorption and all the processes involving solid surface. Therefore, we can obtain plenty of information (pore size distributions and surface area) of porous materials from their adsorption isotherms. These data are fundamentals to predict the macroscopic properties of the porous material and their functional behaviour.

For this reason, it is mandatory when we discuss about porous materials to give some basic definitions concerning the adsorption process. *Adsorption* is a surface phenomenon and is defined by IUPAC as the process of enrichment of molecules, atoms or ions in the proximity of a surface.[30] Considering a gas/solid system, adsorption takes place in the vicinity of the solid surface and outside the solid structure. The term "*adsorption*" is not to be confused with "*absorption*" process in which the adsoptive molecules enter in the bulk structure of the porous materials (*adsorbent*). Sometimes it is impossible to distinguish between the two processes therefore the general term "*sorption*" is used.

The *adsorbate* is the material adsorbed on the surface and the *adsorbent* is the porous surface on whitch the adsorbate is adsorbed. Before soption process or after, the adsorbate in the fluid phase is called *adsorptive.*

Depending on the strength of the interaction between the adsorbent and the adsorbate, two type of adsorption can occurd: chemical (chemisorption) or physical (physisorption). *Physisorption* take place whenever an adsorbable gas encounters the surface of the adsorbent. The mechanism is not specific; thus the molecules of adsorbate are not restrained to specific site on the solid. The intermolecular forces involved are of the same kind of those that characterize the deviation from the ideal behaviour of gases and those involved in the vapour condensation (Van der Waals attraction).

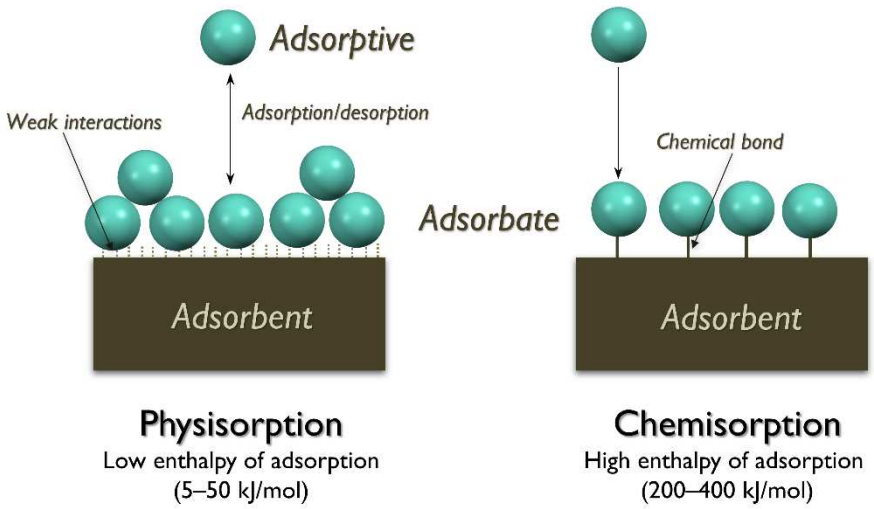

Figure 7. Physical (left) and chemical (right) adsorption process.

This process is achieved rapidly because no activation energy is required, therefore is characterized by low entalpies of adsorption (5-50 kJ/mol). Physisorption is a fully reversible process. On the contrary, *chemisorption*, is not reversible due to the formation of chemical bonds between the adsorbate and the adsorbent. This type of sorption is characterized by large interaction energies, which lead to high heats of adsorption (200-400 kJ/mol) often comparable with value of chemical bonds. The chemisorption is usually highly specific and characterized by monolayer of chemically bond adsorbate. Reactive gases adsorbed on a surface (ex. H_2 on Pt(0)/Pd(0)) are example of chemisorption.

The physorption process depend on the pore shape and pore dimension. Usually, in the case of microporous materials the *micropore filling* with the gas molecules is the first process that takes place. When mesopores and macropores are involved instead, there are multi-stage physoroption processes. The first process is the covering of the pore walls with a monolayer of adsorbate (*monolayer condensation*). As the pressure increases, multilayer adsorption occurs. The adsorption space accomodates more than one layer of gas molecules. In the end, the residual space left in the pore volume is filled with adsorptive molecules until saturation *(pore or capillary condensation)*. In this process a gas condenses to a liquid-like phase in a pore at a pressure p less than the saturation pressure p^0 of the liquid (bulk). Pore condensation is often characterized by hysteresis on the adsorption-desorption isotherm.

1.2.1 Adsorption isotherms

The adsorption ability of a porous structure towards gas molecules can be confirmed with the investigation of its physisorption properties through graphs known as adsorption isotherms. Adsorption isotherms illustrate the relation between the amounts of molecules adsorbed on the surface of adsorbent and equilibrium pressure of the gas, at constant temperature. Usually, when the adsorption temperature is below the critical point of the adsorptive, relative pressure (p/p^0) is plotted against the amount adsorbed, where p is the equilibrium pressure and p^0 the saturation pressure of the gas.

The shape of the sorption isotherm is the fingerprint of the material texure. Nowadays, specific adsorption isotherms are associated to peculiar pore structures. According to IUPAC adsorption/desorption isotherms are classified into six groups as shown in **Figure 8**.

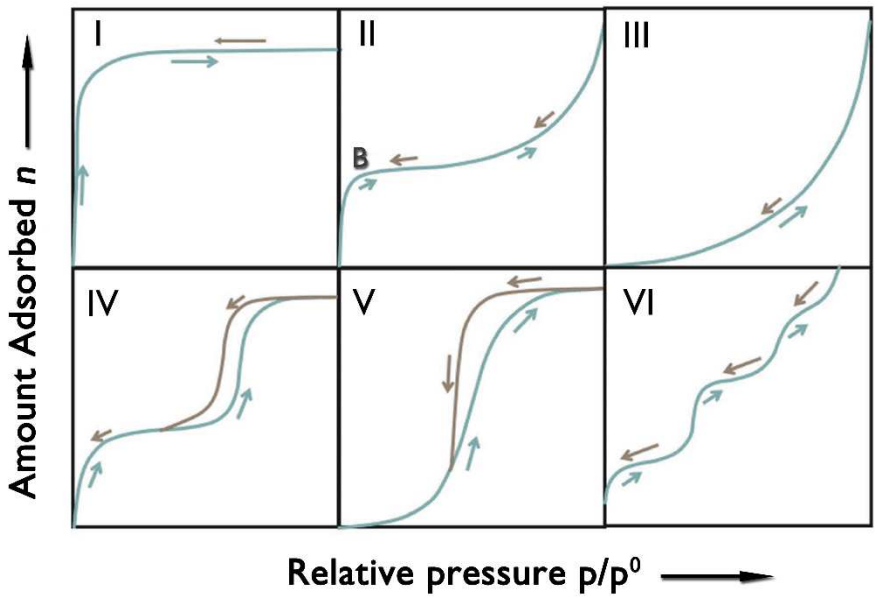

Figure 8. IUPAC main adsorption isotherm types. Adsorption branch [blue] desorption branch [grey].

Reversible **type I isotherms** are characterized by an initial steep rise at very low p/p^0 and a horizontal plateau in which the amount adsorbed tend to the limiting value. The curve pattern can be described by the Langmuir equation. This situation is typical for microporous systems with a quite small external surfac (e.g. zeolites, activated carbons).

Reversible **type II isotherm**, also called the Freundlich isotherm, describes adsorption on non-porous and macroporous systems or systems with different kinds of adsorption sites. Point B usually indicates the relative pressure at which the monolayer coverage is complete, and the multilayer adsorption begins. A more continuous curvature (a less distinctive Point B) corresponds to a significant overlap of monolayer coverage with a multilayer adsorption.

Type III isotherms are characterized by the absence of point B because there is no monolayer adsorpion. In this case the adsorbate–adsorbate interaction is huge if compared to adsorbate-sorbent interaction; this means that the monolayer interactions are weak and the adsobate are present only around the most favourable sites.

Type IV isotherm describes mesoporous materials behaviour. This pattern is the same of type II isotherm: the initial part is relative to mono-multilayers sorption on mesopore walls and in the second part the behaviour is dominated by the interaction between the molecules and the condensed state (pore condensation). Final saturation plateau is a typical feature of Type IV isotherms. Furthermore, hysteresis is usually present evidenced by a non-overlap between the desorption and adsorption branches.

At low pressure **Type V isotherm** is like type III one, due to the weak adsorbent-adsorbate interactions. At higher value of p/p^0, molecular clustering is followed by pore filling. This sigmoid isotherm is not common and reveals the presence of cooperation effects as further bonds with the surface are facilitated by the presence of other already adsorbed molecules.

Reversible **Type VI isotherm** shows a stepwise progression because it represents the formation of a multi-layered adsorption on a uniform non-porous surface. The height of the single step shows the capacity of each adsorbed monolayer.

1.2.2 Adsorption hysteresis

Physisorption characterized by capillary condensation in mesopore, can be recognized from the shape of the isotherm, mainly due to the presence of hystereris loops as shown in **Figure 9**.

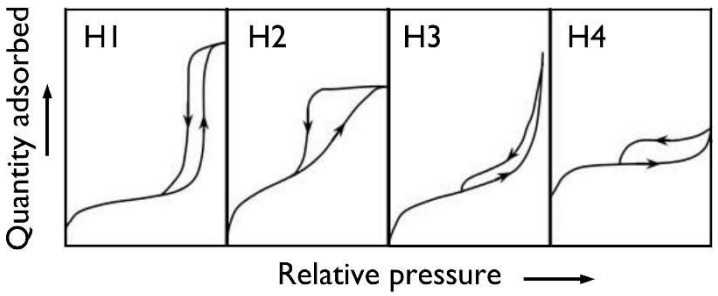

Figure 9. Types of hysteresis.

Type H1 loop is found in porous materials with a well-defined cylindrical pore channels or uniform and compact spherical pores. Type H2 is characteristic of disordered materials with a large distribution of pore size and shape. Type H3 is observed with slit-shape pores of plate-like aggregates (e.g. some clays). Type H4 hysteresis is often associated with narrow slit-like pores and is typical of microporosity for Type I isotherms.

Hysteresis can also be observed at low pressure. These loops may be associated with the *swelling of a non-rigid porous* structure or with irreversible adsorption of molecules in the pores due to some chemical interaction with the adsorbent.

1.2.3 The Langmuir model

The Langmuir isotherms describes the sorption of one monolayer of molecules on the surface of the adsorbent.[30,32] This model is based on three assumptions:

1. Only one monolayer is formed.

2. The surface is uniform; thus all the adsorption sites are equivalent.

3. The tendency of a molecule to be adsorbed does not depend on the occupation rate of the near sites, because the molecules do not interact with each other.

The dynamic equilibrium is:

$$A\ (g) + M\ (surface) \underset{k_d}{\overset{k_a}{\rightleftharpoons}} AM\ (surface)$$

Where *A* are the adsorbate, *M* is the adsorbent and k_a, k_d are the kinetic constants for the adsorption and for the desorption, respectively.

The fractional occupancy, or coverage rate θ, is the fraction of surface occupied by the adsorbate A and (1- θ) is the surface unoccupied by A. θ value is proportional to the partial pressure of adsorbate *p* and to the number of empty sites *N*(1- θ), where *N* is the total number of sites:

$$\left(\frac{d\theta}{dt}\right)_{ads} = k_a p N(1-\theta)$$

In the case of desorption, we can assume that:

$$\left(\frac{d\theta}{dt}\right)_{des} = -k_d N\theta$$

Where *N*θ represents the desorbed guest molecules. At the equilibrium, the rates of adsorption and desorption process are the same. In other words:

$$\left(\frac{d\theta}{dt}\right)_{ads} = \left(\frac{d\theta}{dt}\right)_{des}$$

$$k_a p N(1-\theta) = -k_d N\theta$$

Introducing the constant K as $K = k_a/k_d$, we can obtain the **Langmuir equation**that describes Type 1 isotherms:

$$\theta = \frac{Kp}{1+Kp}$$

Eq. 1

This means that at low pressure where p and K are very small, the Eq. 1 can be simplified to:

$$\theta = Kp$$

In this region, there is a linear relationship between the pressure and the fractional occupancy of the adsorbate, giving the characteristic sharp increase of Langmuir isotherm (Figure 8). When the pressure increase, the gas molecules are forced to cover every site available, so the Langmuir plots tends to 1.

1.2.4 The BET isotherm

In reals systems, the first sites to be covered on the surface are the more energetic ones, but with the increase of pressure increases the probability that new molecules will pile on the molecules already present on the surface, creating multilayers. This means that multilayers adsorption starts prior to the completion of the single monolayer.

In 1938 S. Brunauer, P. Emmett, and E. Teller[56] extended the Langmuir theory to the real systems, assuming that molecules adsorbed became the substrate for other layers of adsorbed molecules, so the isotherm, in this case, present a plateau followed by a further increase of pressure (Type IV, Figure 8).

We can describe the adsorption process with BET model as:

$$\frac{v}{v_{mono}} = \frac{cz}{(1-z)(1-(z-cz))}$$

Where:

- v is total volume adsorbed
- v_{mono} is volume of adsorbed monolayer
- z is the ratio between the equilibrium pressure $\mathbf{p}$ and the saturation pressure of adsorbate $\mathbf{p^0}$.
- c is the BET constant defined as $c = e^{(\Delta H_{des} - \Delta H_{vap})/RT}$

When *c* is high, as in the case of inert gasses, the BET equation can be reduced to:

$$\frac{v}{v_{mono}} = \frac{1}{1 - (\frac{p}{p^0})}$$

1.2.5 Determination of the specific surface area

The BET model is used to estimate the surface area of porous solids, though the determination of the monolayer capacity n_m and the monolayer gas volume v_{mono}.

The specific monolayer capacity n_m is defined as the amount of adsorbate to cover the surface with one layer of molecules, so, we can define the **total surface area** A_s of the adsorbent as:

$$A_S = n_m N_A \sigma_m$$

And the **specific surface area** a_{BET} as:

$$a_{BET} = \frac{A_S}{m} \quad [m^2/g]$$

Where N_A is the Avogadro number, σ is the *molecular cross-sectional area* or the area occupied by a molecule on the monolayer and *m* is the mass of the sample.

Due to its availability, liquid nitrogen (at 77 K) was traditionally the adsorptive gas generally used to obtain the *specific surface area* (BET), with $\sigma(N_2)$ assumed to be 0.162 nm^2.

To derive the monolayer capacity from the adsorption isotherm we can linearized the relationship between the $[(p/p^0)/\mathbf{n}(1-p/p^0)]$ and p/p^0 as:

$$\frac{p/p^0}{\boldsymbol{n}(1 - p/p^0)} = \frac{1}{n_m c} + \frac{c - 1}{n_m c}(p/p^0)$$

With ***n*** is the specific amount adsorbed at a specific value of relative pressure.

The graphical representation is called the BET plot as shown in Figure 10. The range of linearity of the BET plot is usually between 0.05–0.30 values of p/p^0 for Type II and Type IV isotherms.

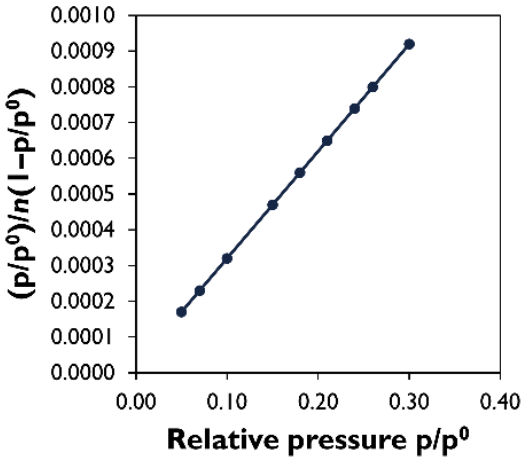

Figure 10. Example of "BET plot".

Chapter 2

2. Supramolecular assemblies in silver complexes

Silver(I) is an attractive metal center for the synthesis of coordination networks, and it has been extensively used to have access to a wide range of materials with multiple applications, spanning from antibacterial activity[57,58] to luminescence[59]. Due to the lack of crystal field effect, silver can adopt different coordination geometries, and this peculiar feature allow to obtain a wide collection of different architectures, simply changing the properties of the bridging ligand. This intrinsic structure diversity has been largely used with bispyrazole[60,61] or trispyrazole[62–65] ligands in the past years. In addition, the use of Ag as metal node gives the possibility to explore different systems modifying the solvents, the anions, the ligand-metal ratio and the non-covalent interactions involved in the crystal[66]. Previously, our research group explored the possibility to build architectures based on Ag-S coordination bond between bispyrazolyl ligands and silver salts[67–71]. The systems obtained showed permanent microporosity due to $Ag^{+}\cdots(PF_6^{-})\cdots Ag^{+}$ interactions. In this chapter, we show new ligands based on bispyrazolyl moiety functionalized with different halogen atom (I, Br) and the following synthesis of silver coordination complexes with these organic ligands. The aim of this work is to investigate weak interactions such as halogen bond or π-π stacking, instead of strong interactions explored in previous works, in order to build potentially porous three-dimensional networksbased on weak interactions. [72]

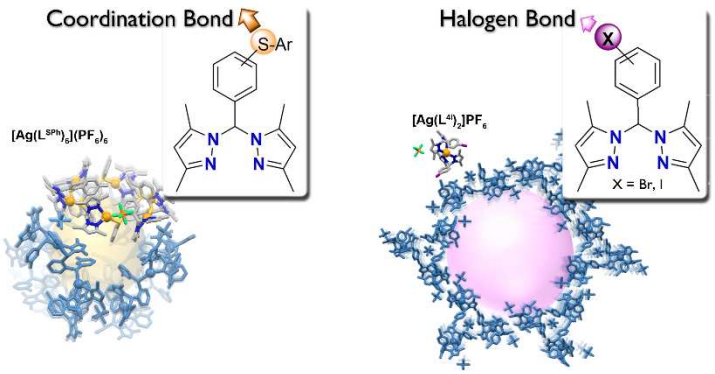

2.1 Introduction

2.1.1 Crystal Engineering

We cannot start our journey into potentially porous materials and crystalline architectures without taking into consideration the relationship between their structure and properties and how their stability is based on specific interactions: coordination and covalent bonds, hydrogen bonds, halogen bonds, and so on. Indeed, the rational design of 2D or 3D architectures has witnessed an increasing importance in the last twenty years, giving birth to a new branch of chemistry: the crystal engineering. This discipline was defined by Desiraju, Ramanan and Vittal in 1988 as "the understanding of intermolecular interactions in the context of crystal packing and the utilization of such understanding in the design of new solids with desired physical and chemical properties." [73] Inspired by nature, crystal engineering investigates how to include a well-defined molecular conformation or/and functionality into a multi-dimensional architecture to ensure a specific functionality.

Covalent and non-covalent interactions are both present in crystalsand, given a certain molecular structure, how we can determine/predict the crystal structure? The relationship between these two features is not so simple, as a matter of fact, every functional group position in the crystal depends on the nature and the disposition of all other moieties of the molecule. This concept can be applied either to simple molecules or complex organic and metal organic architectures.[74]

In order to simplify the problem of prediction of crystal structure, crystal engineering based its studies on supramolecular synthons,[75] which are are well defined structural units. Supramolecular synthons can be assembled using intermolecular interactions and ultimately define the crystal structure.

For example, robust synthons are formed by strong and directional interactions, as hydrogen bonds. These types of interactions tend not to break easily and they are usually formed next to other weaker synthons that involve less directional

interactions in the crystal. With this concept in mind, we can build the entire crystal structure as a network of node (molecules) and connectors (interactions).

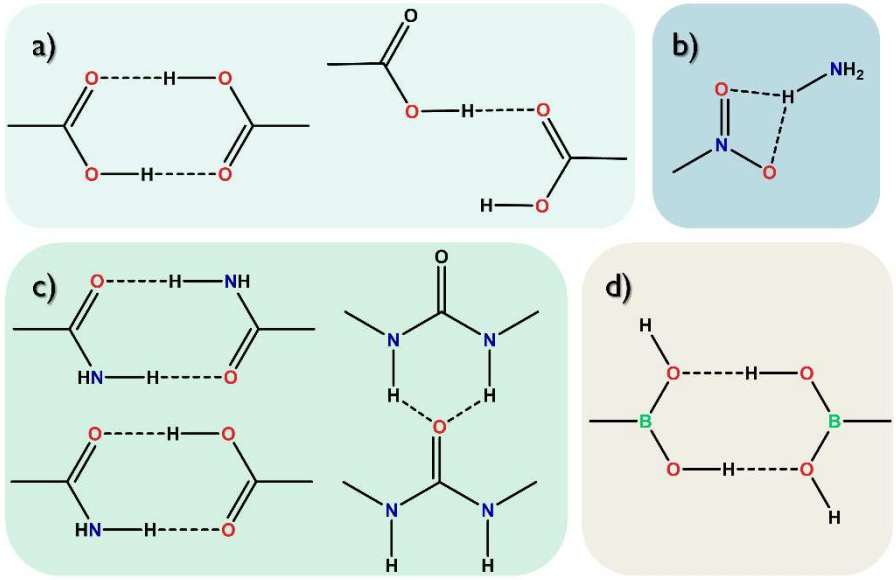

Figure 11. Some examples of supramolecular synthons: a) Synthons of carboxylic acids, b) nitro---amino synthon, c) typical synthons of biological systems, d) synthon of boronic acids.[73]

2.1.2 Coordination networks

The design of new architectures combining metals centers and ligands, is one the most important topics in today's chemistry. In the past years much attention was given to mixed systems built on metal-ligand coordination bond such as coordination polymers (CPs) or porous coordination networks (PCPs) also called metal-organic frameworks. Combining metal and organic moieties in the same structure is very useful to synthetize materials with various applications. Indeed, metal centres can act as reactivity centres towards specific external stimuli as light, or act as catalyst (Figure 13). The organic ligands also play a key role in the building of the network. Usually, ligands with bridging functionality are used to bond two or more metal centers. The length of the organic ligands and the directionality of their functional groups can control the properties of the final product.

Therefore, the discovery of new coordination polymers starts with the design of novel multitopic organic ligand that can bind to a specific metal and, secondly on the choice of metal node. Coordination number, geometry, electronic properties and dimensions are some of the factors that can influence the selection. Tuning these properties allowed to design polymeric or oligomeric species with one, two or three dimentional structures based on non-covalent interactions (Figure 13). As mentioned at the beginning of this chapter, silver has been extensively used in coordination polymers in the last twenty years as depicted in Figure 12.

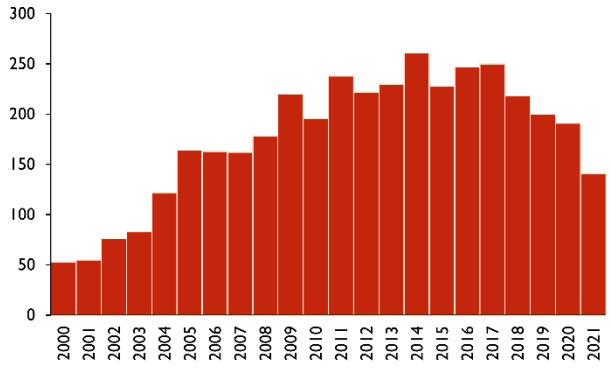

Figure 12. Number of papers cointaing the keywords "Ag" and "coordination polymers". Source Web of Science, December 2021.

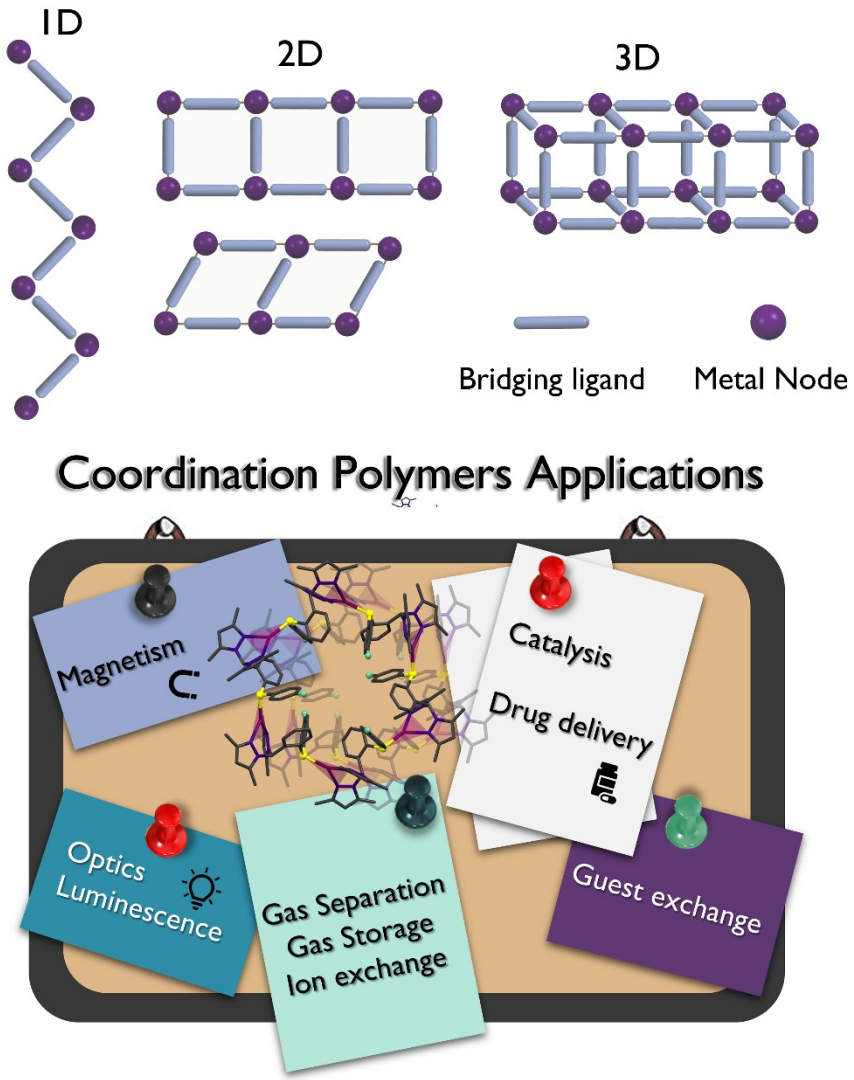

Figure 13. Structure of 1D, 2D, 3D coordination polymers (top), Coordination polymers applications (down).

The interest in CP based on silver is mainly due to their intrinsic structures diversity, resulting in both *low-dimentional Ag coordination polymers* as well as *architectures with higher dimensionality* also supported by weak interactions.

The first group are formed with di- or multitopic N-donor ligands based mainly on silver-ligand interactions. In these structures, Ag(I) ion can adopt different geometries from linear to octahedral, affording the opportunity to explore how the crystal structure obtained can be influenced by the synthesis and crystallization conditions. This family includes 1D coordination polymers with linear or zigzag topology, ladder and helical architectures; 2D coordination polymers with honeycomb or square grids; 3D diamondoid or octahedral networks and so on (Figure 14).

The high dimensional silver coordination networks are formed with the addition of supramolecular interactions, as hydrogen bonds, halogen bonds and argentophilic interactions.[76]

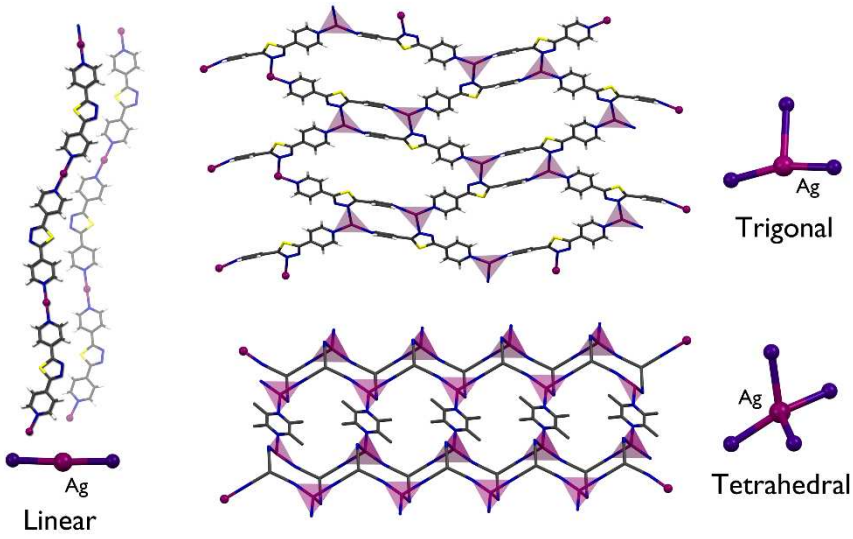

Figure 14. More common silver geometries and 1D, 2D or 3D silver coordination polymers. Color Code Ag [Violet], N [Blue], C[Grey], S [Yellow]. Refcode CCDC: ESEVAZ, ESETOL, TABPUI.

2.1.3 The Halogen Bond

Weak interactions can be used to build coordination assemblies with desired structural features. Non-covalent interactions are the "glue" that held together molecules in the crystals. We can describe a specific interaction such as halogen bonds or π-π stacking by its strength, its geometric directionality and by its distance dependence.

The strength is one of the first features that we use to distinguish interactions. Strong interactions are usually associated with covalent bonds (75-125 kcal/mol). On the contrary, the majority of weak interactions are associated with energy of 1 to 15 kcal/mol. However, most of the time, this distinction is very subjective. As a matter of fact the strongest halogen bonds between $[HF_2]^-$ anions, is around 50 kcal/mol while the energy of the weakest covalent bond (C-I), is about 30 kcal/mol.[73] Another characteristic of interactions is their directionality since there are isotropic interactions and anisotropic ones. The first types are dispersive-repulsive force, usually weak and responsible for the packing motives in the crystal (dipole-dipole and London forces). Instead, the anisotropic interactions are fundamental to design crystals and they have a specific directionality in the three-dimensional space that arise from a unique electronic distribution. Hydrogen bonds (HB), halogen bonds (XB), picnogen bonds are just a few examples of anisotropic interactions.

Among the many weak interaction in porous crystals, in this chapter we will focus on only one type of anisotropic interaction, the halogen bond.[77]

Usually, halogen atoms are considered as nucleofilic sites, due to their high electronegativity and high electron density. Nevertheless, their electronic distribution is not isotropic when halogen is covalently bound to other atoms. Beside the negative zone of electrostatic potential orthogonal to the covalent bond, there is a region with positive electrostatic potential on the elongation of the covalent bond. This region of lower electron density is called sigma hole (σ-hole) and it is responsible for the halogen bond interaction.

In 2013 IUPAC defined the halogen bond as a weak interaction between an electrophilic region present on a halogen atom (sigma-hole) and a nucleophilic region (mainly due to electronegative atoms such as F^-, Cl^-, N, O, S etc.) on the

same or different molecular entity[78] (Figure 15). This weak interaction is highly directional due to the presence of a sigma-hole, on the opposite side of the R-X sigma bond and it is mainly evident in atoms such as bromine and iodine, characterized by low electronegativity and high polarizability.

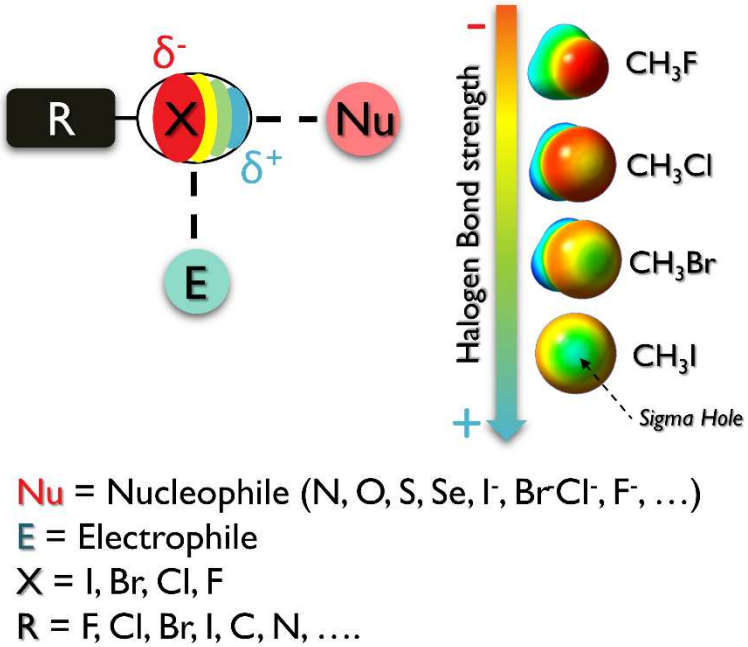

Figure 15. Schematic representation of the anisotropic distribution of the electrostatic potential around the halogen atom X and possible interactions of the halogen atom: halogen bond interaction $X^{\delta+}$---Nu, and orthogonal interaction between the negative corona of X with an electrophile $X^{\delta-}$---E (left). Representation of the electrostatic potential surfaces calculated at an isoelectronic density value of 0.004 for compounds of formula CH_3X, in which X is a halogen atom (right).

Herein we illustrate some of the main features of halogen bond:

a) **Directionality.** Halogen bond is more directional than HB, due to the spot-like size of the sigma hole. Usually the RX-Nu angle is close to 180°. Moreover, when the interaction between Nu with lone-pairs, the XB lies along the axis of lone-pairs of the nucleophile.[79]

b) **Tunability.** As depicted in Figure 15, XB donor ability increases with the polarizability of the halogen atoms and decreases with its electronegativity. So, iodine has more prominent σ-hole and tends to

form stronger XB then bromine or chlorine. Fluorine is the poorest XB donor; however, when fluorine is bound to strong electron-withdrawing groups or atoms, it is possible to observe a fluorine sigma-hole.[80] The XB strength can be modulated, also, by changing the hybridization of the carbon bound to the XB donor site. The greater the s-component the greater is the XB strength, so C(sp)−X > C(sp^2)−X > C(sp^3)−X. For instance, haloalkynes, as diiodoacetylene and (iodoethynyl)-benzene, are very good halogen bond donors.[81,82]

c) **Hydrophobicity.** Halogen atoms are usually employed to increase the hydrophobicity of a specific molecule. The halogen bond XB can be considered as a more lipophilic synthon of HB and can be used to tune the hydrophilic/lipophilic properties of the final molecule.

d) **Energy.** XB can have a wide range of energy from 2-3 kcal/mol for weak XBs, to 40 kcal/mol for the strong ones.

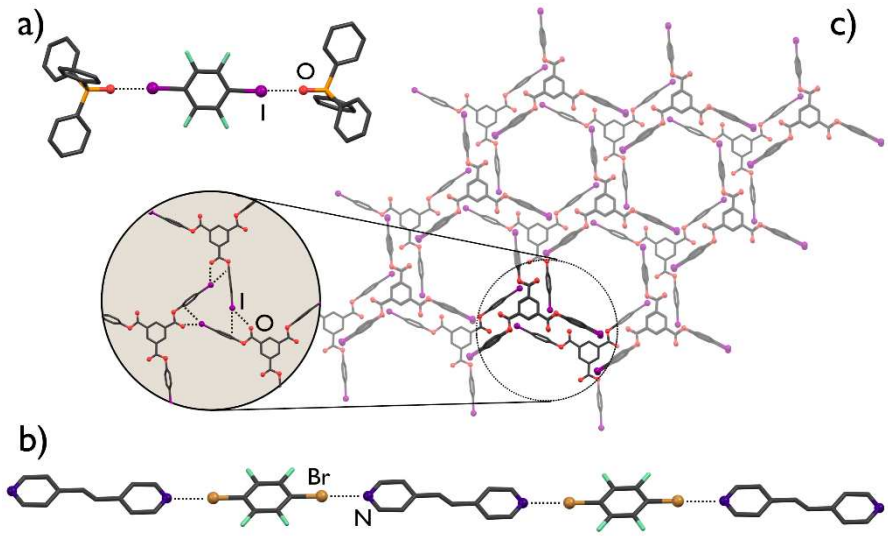

Figure 16. a) Molecular complex based on XB between iodine and oxygen atoms of triphenylphosphine oxide;[83] b) Linear 1D-chain formed by XB between trans-by(pyridinyl)ethene and 1,4-dibromotetrafluorobenzene molecules;[84] c) 3D architecture with honeycomb structure based on I---O and I---π XBs.[85]

Halogen bond interactions can cooperate with other XBs or HBs to obtain supramolecular systems via self-assembled synthesis. It is only in the past years that crystal engineering has focussed its studies on this type of interaction.

Since the definition of XB in 2013, several examples have been developed from zero-dimensional aggregates (i.e. co-cystrals involving XB donors and acceptors) to mono-, di-, and tri-dimensional networks (coordination polymers based on XBs) as illustrated in Figure 16.

2.2 Aim of the work

In this study we focus on the design of supramolecular architectures by esploring different type of weak interaction, in particular the highly directional halogen bonds. Six different phenyl(bispyrazolyl)methane ligands were prepared (see Section 2.4.1) with different functionalization on the phenyl ring, using iodine or bromine halogen atoms. The intent was to investigate the influence of the functionalization on the strengh, and directionality of the halogen bond interactions formed in the final architecture. Silver(I) was used as metal, and in addition we studied the influence of the counter ion in the resulted structure, using two different silver salts, namely $AgPF_6$ and $AgCF_3SO_3$. These two different counteranions could also act as XB acceptors, but they can also provide a coordination bond with a metal center.

2.3 Experimental Section

2.3.1 General remarks

All commercially available reagents and solvents were used without further purification. Anhydrous solvents were dried and stored over molecular sieves (3 Å) after activation (250°C, 24 hours). Reactions performed under an inert atmosphere (N_2) were carried out using standard Schlenk glassware. Flash column chromatography was performed using silica gel (230-400 mesh). Iodomorpholine[86] and Bis(3,5-dimethyl-1H-pyrazol-1-yl)methanone[87] was synthetized according known procedure.

NMR Experiments: NMR experiments were performed on either a Brüker Avance 300 or 400 MHz instruments at 298 K. Chemical shifts are expressed in ppm relative to tetramethylsilane, using the solvent residual peak of $CDCl_3$ (δH 7.26, δC 77.00) as a reference standard.

Differential Scanning Calorimetry (DSC) and Thermal gravimetric analyses (TGA): Fresh crystals were taken from mother liquor and quickly dried over filter paper (sample mass 2-8 mg). DSC were performed in 50 µL perforated aluminum crucibles on a PerkinElmer DSC 6000 with a heating rate of 5 °C min^{-1} from 25 to 180 °C or from 25 to 280 °C using nitrogen (20 mL min^{-1}) as flowing gas. Thermograms were collected on PerkinElmer TGA 8000, heating from 25 to 310 °C at atmospheric pressure, with a temperature ramp of 10 °C min^{-1} under nitrogen flux (30 mL min^{-1}).

Other Measurements: Infrared (IR) spectra were obtained with a Thermo Scientific Nicolet 5PCFT-IR-ATR spectrometer (diamond crystal or Zr-Se crystal for alkyne compounds) in the 4000-400 cm^{-1} interval. Electrospray mass spectral analyses (ESI-MS) were performed with an electrospray ionization time-of-flight Micromass 4LCZ spectrometer after solubilization of the samples in methanol or acetonitrile. Elemental analyses of silver complexes (sample mass 3 mg) were performed on Thermo Fischer Scientific FlashSmart CHNS.

Single crystal X-ray diffraction (SCXRD): Single crystal measurements were performed with a Bruker D8 PhotonII or a Smart Breeze area detector diffractometer (Mo Kα: λ = 0.71073 Å) and complete datasets were obtained by merging several series of exposure frames[88]. The crystals of **9**-phase-2, **10**-phase-2 and **12** were non-merohedrally twinned, and two different components were taken into account during data integration and scaling, which was performed with the TWINABS program.[89] For the remaining structures, an absorption correction was applied with the program SADABS.[90] The structures were solved with ShelxT[91] and refined on F2 with full-matrix least squares,[92] using the Olex2 software package.[93] **10**·DCM and **10**-phase-3 were refined with suitable twin-matrixes. The hydrogen atoms were placed at their calculated positions. Compounds **9**-phase-1 and **10**-phase-1 exhibited large cavities occupied by solvent molecules. For **10**-phase-1, four THF molecules were refined with site occupancy factors (s.o.f.) of 0.25 each (1 THF overall). Towards the centre of the cavity the solvent was modelled by using the Platon-squeeze program,[94] which gave a void of 4470 A^3/cell containing 943 electrons/cell. This corresponds approximately to 24 THF molecules/cell. The long prismatic crystals of **9**-phase-1 were significantly thinner than those of **10**-phase-1 and the dataset did not allow to identify the solvent molecules close to the channel surface. The residual electron density was therefore modelled with the Platon-squeeze program, which gave a void of 7450 A^3/cell containing 2257 electrons/cell. Graphical images was prepared with the Mercury[95] and TOPOSPro[96] programs. CCDC 1902455-1902465 and 1968843-1968848 contain the supplementary crystallographic data.

Powder X-ray diffraction (PXRD): Data were collected by using Rigaku Smartlab XE diffractometer equipped with a 2D HyPix3000 detector operating in 1D mode. The X-rays incident beam (Cu Kα = 1.5046 Å) was parallelized in order to minimize the sample roughness effects related to the specific preparation. Indeed, a lump of crystals was placed together with some mother liquor on a zero-background sample holder and rapidly covered with a thin Mylar sheet sealed at the boundaries of the zero background with silicon grease in order to prevent solvent evaporation. Data collections were carried out in continuous in the 2θ x-y° range, step size 0.01° and scan speed 1 °/min.

2.3.2 Synthesis of the ligands

General procedure A for the synthesis of bispyrazolyl ligands L^X

Funclionalized bispyrazolyl ligands $\mathbf{L^X}$ were prepared from bispyrazolyl ketone and the corresponding benzaldehydes in a standard procedure depicted in **Scheme 1**.

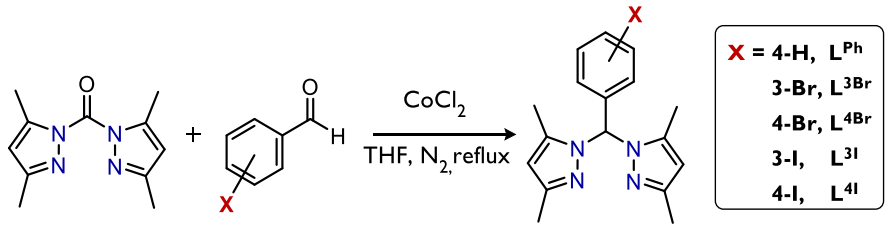

Scheme 1. General synthetic route for the phenyl(bispyrazolyl)methane ligands L^{Ph}, L^{3Br}, L^{4Br}, L^{3I}, L^{4I}.

Bis(3,5-dimethyl-1H-pyrazol-1-yl)methanone (5 mmol, 1 eq), the desired benzaldehyde (1.15 eq.), $CoCl_2 \cdot 6\ H_2O$ (0.05 eq.) and dry tetrahydrofuran (0.20 mol/L) were added in a two-neck round bottom flask previously dried in the oven. The blue solution was brought to reflux and stirred until the reaction was complete (24 hours). After this period, distilled water was added, and the product was extracted with dichloromethane three times. The organic phase was washed with saturated K_2CO_3 and brine and then dried over anhydrous Na_2SO_4. The organic solvent was removed *via* rotary evaporation. The crude product was purified by flash chromatography on silica or by recrystallization yielding $\mathbf{L^x}$ as a white crystalline powder.

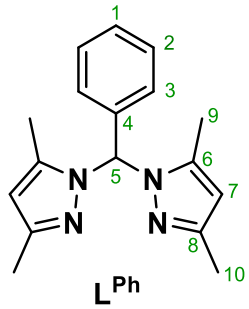

1,1'-((phenylmethylene)bis(3,5-dimethyl-1H-pyrazole) (L^{Ph}). This coumpound was synthetized following the *general procedure A*. The solid obtained after evaporation was recrystallised was washed with hexane (3 mL), filtered, and then recrystallized using hexane, yielding $\mathbf{L^{Ph}}$ as a white crystalline powder (yield 14 %).

^{1}H NMR (400 MHz, $CDCl_3$) δ (ppm): 7.66 (s, H_5), 7.32-7.37 (m, H_1, H_2), 6.92-6.95 (m, H_3), 5.88 (s, H_7), 2.24 (s, H_{10}), 2.22 (s, H_9);

^{13}C NMR (100 MHz, $CDCl_3$) δ (ppm): 148.35 (C_8), 141.09 (C_6), 136.84 (C_4), 128.52 (C_3), 128.38 (C_2), 126.83 (C_1), 106.85 (C_7), 73.92 (C_5), 13.75 (C_{10}), 11.85 (C_9);

ESI-MS (p.i., CH_3CN, m/z): 185.16 $[(Me_2Pz)PhCH]^+$, 281.30 $[H(L)]^+$, 303.27 $[Na(L)]^+$, 320.26 $[K(L)]^+$;

IR (cm^{-1}): 2987w, 2946w, 2917m, 1599w, 1553s, 1495m, 1447s, 1411m, 1373m, 1359m, 1305s, 1262m, 1212w, 1179w, 1129w, 1109w, 1079w, 1030m, 971w, 874m, 860m, 835m, 797s, 779m, 747m, 729vs, 702m, 693m, 666w, 632w, 612m, 583w, 488m, 472m.

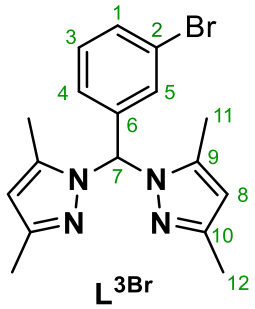

1,1'-((3-bromophenyl)methylene)bis(3,5-dimethyl-1H-pyrazole) (L^{3Br}). This coumpound was synthetized following the *general procedure A*. The solid obtained after evaporation was recrystallised was washed with hexane (3 mL), filtered, and then recrystallized using hexane, yielding L^{3Br} as a white crystalline powder (yield 41%).

^{1}H NMR (400 MHz, $CDCl_3$) δ (ppm): 7.56 (s, H_7), 7.46 (dt, J_1 = 8 Hz, J_2 = 1.2 Hz, H_1), 7.19 (t, J = 8 Hz, H_3), 7.09 (s, H_5), 6.85 (dd, J_1 = 8 Hz, J_2 = 0.8 Hz, H_4), 5.86 (s, H_8), 2.21 (s, H_{11}, H_{12});

^{13}C NMR (100 MHz, $CDCl_3$) δ (ppm): 148.31 (C_{10}), 141.00 (C_9), 139.05 (C_6), 131.60 (C_1), 130.04 (C_5), 130.03 (C_3), 125.68 (C_4), 122.74 (C_2), 107.11 (C_8), 73.13 (C_7), 13.74 (C_{12}), 11.82 (C_{11});

ESI-MS (p.i., CH_3CN, m/z): 359.20 $[H(L)]^+$, 381.90 $[Na(L)]^+$;

IR (cm^{-1}): 2919wbr, 2879wbr, 1596w, 1560m, 1464w, 1417m, 1372m, 1341w, 1298m, 1250w, 1213w, 1186w, 1073w, 1028m, 996w, 858m, 818m, 775s, 750m, 689s, 677m, 662w, 625m.

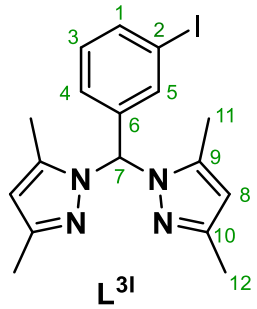

L^{3I}

1,1'-((3-iodophenyl)methylene)bis(3,5-dimethyl-1H-pyrazole) (L^{3I}). This coumpound was synthetized following the *general procedure A*. The solid obtained after evaporation was recrystallised was washed with hexane (3 mL), filtered and then recrystallized using hexane, yielding **L^{3I}** as a white crystalline powder (yield 12 %).

^{1}H NMR (400 MHz, $CDCl_3$) δ (ppm): 7.66 (dd, J_1 = 8 Hz, J_2 = 0.8 Hz, 1H, H_1), 7.54 (s, H_7), 7.29 (s, H_5), 7.06 (t, J = 8 Hz, H_3), 6.87 (dd, J_1 = 8 Hz, J_2 = 0.8 Hz, H_4), 5.86 (s, 2H, H_8), 2.21 (s, $H_{11,}$ H_{12});

^{13}C NMR (100 MHz, $CDCl_3$) δ (ppm): 148.72 (C_{10}), 141.11 (C_9), 138.07 (C_6), 137.68 (C_1), 135.96 (C_5), 130.28 (C_3), 126.42 (C_4), 107.22 (C_8), 94.45 (C_2), 72.07 (C_7), 13.68 (C_{12}), 11.96 (C_{11});

ESI-MS (p.i., CH_3CN, m/z): 311.06 $[(Me_2Pz)PhICH]^+$, 407.16 $[H(L)]^+$, 429.14 $[Na(L)]^+$, 835.34 $[Na(L)_2]^+$;

IR (cm^{-1}): 2943m, 2916m, 2849m, 1590w, 1559s, 1465m, 1415m, 1372m, 1340w, 1295s, 1248w, 1212w, 1187w, 1159w, 1132w, 1106w, 1066w, 1029m, 994w, 972w, 915w, 893w, 859m, 819m, 802w, 788m, 775s, 763s, 748s, 700w, 686m, 674m, 663w, 648w, 624m, 588w, 506w, 479w, 436w, 418w.

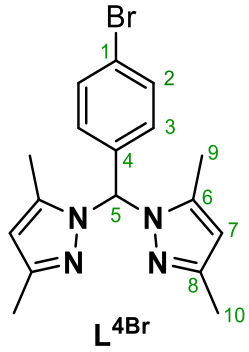

L^{4Br}

1,1'-((4-bromophenyl)methylene)bis(3,5-dimethyl-1H-pyrazole) (L^{4Br}). This coumpound was synthetized following the *general procedure A*. The solid obtained after evaporation was recrystallised was washed with hexane (3 mL), filtered and then recrystallized using hexane, yielding L^{4Br} as a white crystalline powder (yield 35 %).

^{1}H NMR (400 MHz, $CDCl_3$) δ (ppm): 7.54 (s, H_5), 7.45 (dd, J_1 = 8.5 Hz, J_2 = 1.8 Hz, H_2), 6.81 (dd, J_1 = 8.5 Hz, J_2 = 1.8 Hz, H_3), 5.86 (s, 2H, H_7), 2.20 (s, 6H, H_9), 2.19 (s, H_{10});

^{13}C NMR (100 MHz, $CDCl_3$) δ (ppm): 148.54 (C_8), 141.02 (C_6), 135.87 (C_2), 131.67 (C_4), 128.72 (C_3), 122.60 (C_1), 107.06 (C_7), 73.44 (C_5), 13.71 (C_{10}), 11.79 (C_9);

ESI-MS (p.i., CH_3CN, m/z): 361.21 $[H(L)]^+$, 381.21 $[Na(L)]^+$, 741,49 $[Na(L)_2]^+$;

IR (cm^{-1}): 2943m, 2923m, 2866w, 1596w, 1557m, 1486m, 1462m, 1415mbr, 1372w, 1345w, 1301s, 1251m, 1214w, 1178w, 1147w, 1130w, 1071m, 1028m, 1009s, 974w, 885w,.862m, 840m, 829m, 802m, 748s, 775m, 745m, 735w, 704m, 678w, 661w, 640w, 622w, 490s, 439w, 413w.

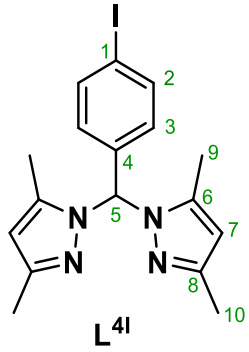

L^{4I}

1,1'-((4-iodophenyl)methylene)bis(3,5-dimethyl-1H-pyrazole) (L^{4I}). This coumpound was synthetized following the *general procedure A*. The crude product was purified by flash chromatography on silica with hexane/ethyl acetate (8:2) as eluent yielding L^{4I} as a white crystalline powder (yield 64%).

^{1}H NMR (400 MHz, $CDCl_3$) δ (ppm): 7.66 (d, J = 8.0 Hz, 2H, H_2), 7.54 (s, H_5), 6.67 (d, J = 8.0 Hz, H_3), 5.86 (s, H_7), 2.22 (s, H_9), 2.19 (s, H_{10});

^{13}C NMR (100 MHz, $CDCl_3$) δ (ppm): 148.54 (C_8), 141.01 (C_6), 137.63 (C_2), 136.57 (C_4), 128.89 (C_3), 107.04 (C_7), 94.35 (C_1), 73.52 (C_5), 13.71 (C_9), 11.79 (C_{10});

ESI-MS (p.i., CH_3CN, m/z): 311.04 $[(Me_2Pz)PhICH]^+$, 407.14 $[H(L)]^+$, 429.14 $[Na(L)]^+$, 835.34 $[Na(L)_2]^+$;

IR (cm^{-1}): 2953m, 2921m, 2856w, 1559s, 1452m, 1412m, 1391m, 1371m, 1343m, 1304s, 1257m, 1214w, 1135w, 1061w, 1030m, 1001s, 879m, 865s, 842m, 781vs, 747m, 707m, 675w, 622w, 490m, 480m, 436w, 411w.

Synthetic strategy for the synthesis of bispyrazolyl ligands L^{4CCI}.

The ligand L^{4CCI} was prepared from L^{4I} through Sonogashira coupling followed by deprotection of the trimethylsilane (TMS) group and subsequent iodination of alkyne (**Scheme 2**).

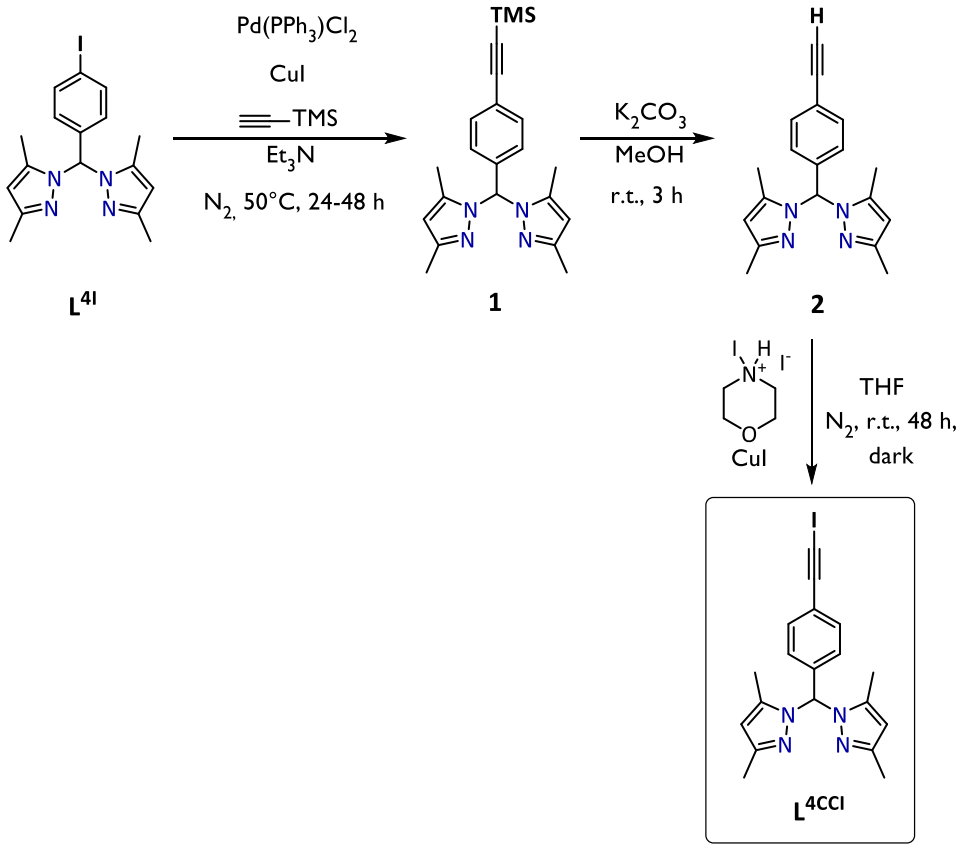

Scheme 2. Synthesis of the ligand L^{4CCI}.

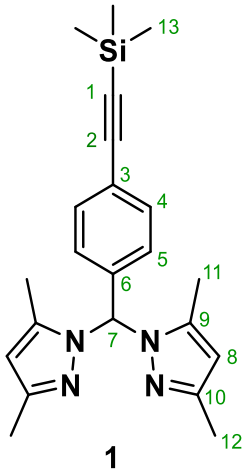

1

1,1'-((4-((trimethylsilyl)ethynyl)phenyl)methylene)bis(3,5-dimethyl-1H-pyrazole) (1). Aryl iodide **L^{4I}** (122 mg, 0.30 mmol, 1 eq.), trimethylsilylacetylene (50 µL, 0.36 mmol, 1.2 eq.), CuI (2.9 mg, 0.015 mmol, 0.05 eq.) $Pd(PPh_3)_2Cl_2$ (6.6 mg, 0.015 mmol, 0.05 eq.), anhydrous triethylamine (3 mL) were added in a schlenk flask under inert atmosphere and stirred at 50°C for 24 hours. The reaction was quenched with saturated aqueous $NaHCO_3$ (5 mL). The aqueous layer was estracted with ethyl acetate (3 x 10 mL) and the organic layer were dried over anhydrous Na_2SO_4 and the suspension was filtred over celite pad and then evaporation of solvent left a yellow solid which was purified by column chromatography on silica (AcOEt:Hx, 20:80) to get the trimethylsilyl derivative (**1**) (94 mg, 0.25 mmol, 83 % yield).

^{1}H NMR (400 MHz, $CDCl_3$) δ (ppm): 7.58 (s, H_7), 7.40-7.42 (m, H_4), 6.91-6.81 (m, H_5), 5.85 (s, H_8), 2.20 (s, H_{12}), 2.18 (s, H_{11}), 0.24 (s, H_{13});

^{13}C NMR (100 MHz, $CDCl_3$) δ (ppm): 148.48 (C_{10}), 141.06 (C_9), 137.14 (C_6), 132.12 (C_4), 126.85 (C_5), 123.35 (C_3), 107.00 (C_8), 104.58 (C_2), 95.06 (C_1), 73.71 (C_7), 14.27 (C_{12}), 11.87 (C_{11}), 0.00 (C_{13}).

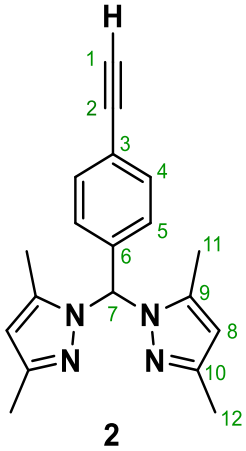

2

Synthesis of 1,1'-((4-ethynylphenyl)methylene)bis(3,5-dimethyl-1H-pyrazole) (3). Trimethylsilyl derivative (**1**) (116 mg, 0.30 mmol, 1 eq.), was dissolved in MeOH (10 mL) and stirred with K_2CO_3 (128 mg, 3 eq.) for 2.5 h. The complection of the reaction was monitored by TLC (EtOAc:Hx, 30:70). After the completion, methanol was removed under reduced pressure and water (10 mL) was added. The product was extracted with ethyl acetate (3 x 10 mL) and the combined organic layers were dried over anhydrous Na_2SO_4 and then the solvent was removed *via* rotary evaporation. The crude product (2) was obtained as a white solid and used for the next synthetic step without further purification (91 mg, 0.29 mmol, 97 % yield).

^{1}H NMR (300 MHz, $CDCl_3$) δ (ppm): 7.60 (s, H_7), 7.45 (d, J_1 = 8.7 Hz, H_4), 6.89 (d, J_1 = 8.7 Hz, H_5), 5.86 (s, H_8), 3.08 (s, H_1), 2.21 (s, H_{12}), 2.19 (s, H_{11});

^{13}C-NMR (75 MHz, $CDCl_3$) δ (ppm): 148.53 (C_{10}), 141.08 (C_9), 137.51 (C_6), 132.30 (C_4), 127.00 (C_5), 122.37 (C_3), 107.06 (C_8), 83.19 (C_2), 77.98 (C_1), 73.69 (C_7), 13.76 (C_{12}), 11.85 (C_{11}) ppm.

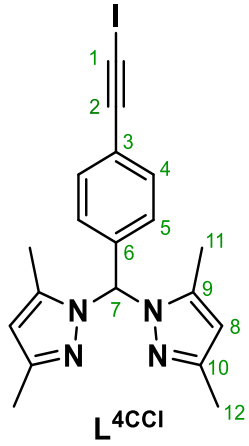

L^{4CCl}

Synthesis of 1,1'-((4-(iodoethynyl)phenyl)methylene)bis(3,5-dimethyl-1H-pyrazole) (L^{4CCl}). Alkyne compound (**2**) (127 mg, 0.417 mmol) and CuI (8 mg, 0.10 eq.) were dissolved in anhydrous tetrahydrofuran (28 mL) under nitrogen atmosphere and the pale-yellow solution was stirred at room temperature for 30 minutes in the dark. Subsequently N-iodomorpholine (286 mg, 0.834 mmol, 2 eq.) was added and the red solution was stirred at R.T. for 2 days in the dark. Afterwards 10 mL of a saturated solution of ammonium chloride was added and then extracted with diethylether (3 x 10 mL). The organic phases were washed with a saturated solution of $Na_2S_2O_3$ (2 x 10 mL) and then dried over Na_2SO_4. The solvent was removed via rotary evaporator to obtaind $\mathbf{L^{4CCl}}$ as a pale-yellow solid (162 mg, 0.376 mmol, 90%).

^{1}H NMR (400 MHz, $CDCl_3$) δ (ppm): 7.58 (s, H_7), 7.38 (d, J_1 = 8.27 Hz, H_4), 6.87 (d, J_1 = 8.27 Hz, H_5), 5.85 (s, H_8), 2.20 (s, H_{12}), 2.19 (s, H_{11});

^{13}C-NMR (100 MHz, $CDCl_3$) δ (ppm): 148.58 (C_{10}), 141.09 (C_9), 137.40 (C_3), 132.51 (C_4), 126.89 (C_5), 123.60 (C_6), 107.08 (C_8), 93.55 (C_2), 73.59 (C_7), 13.84 (C_{12}), 11.92 (C_{11}), 8.35 (C_1);

ESI-MS (p.i., CH_3OH, m/z): 335.04 $[(Me_2Pz)PhC{\equiv}CICH]^+$, 431.10 $[H(L)]^+$, 453.10 $[Na(L)]^+$, 469.04 $[K(L)]^+$, 883.26 $[Na(L)_2]^+$;

IR (cm^{-1}): 2923m, 2851w, 2164w, 1559s, 1506m, 1461m, 1414s, 1382m, 1324m, 1313m, 1253s, 1175m, 1116m, 1022s, 972s, 872s, 857m, 820s, 784s, 724w, 703m, 698w.

Synthesis of tripyrazolyl L^{TrisI}

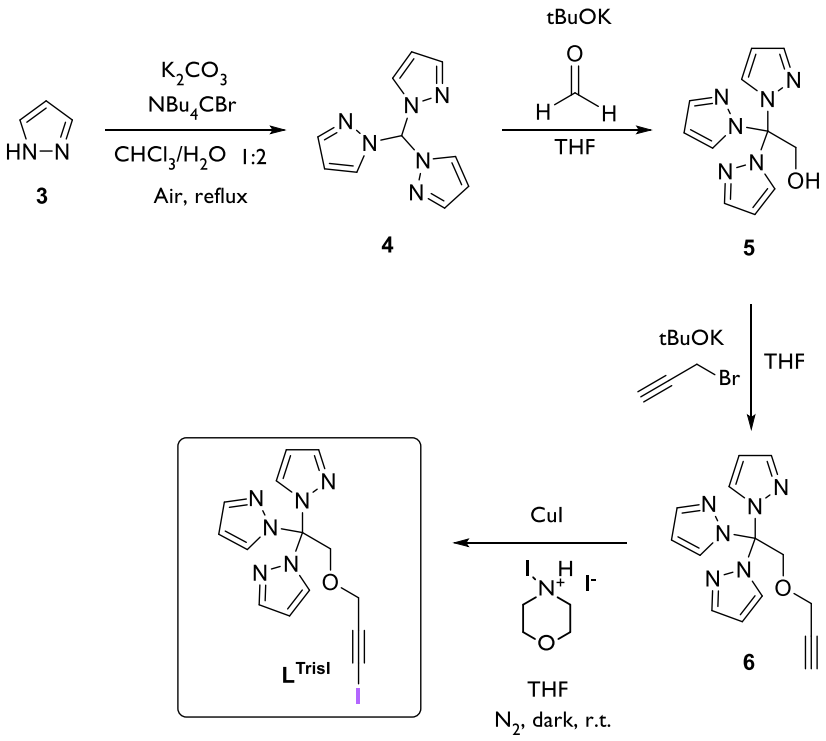

Scheme 3. Synthetic strategy to yield ligand $\mathbf{L^{TrisI}}$.[97]

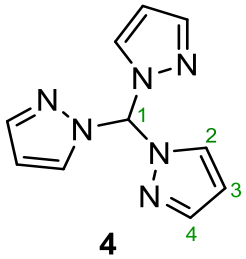

4

Tri(1H-pyrazol-1-yl)methane (4). Distilled water (147 ml) was added to a 500 ml round bottom flask containing a mixture of pyrazole (**3**) (10.0 g, 147 mmol, 1 eq.) and tetra-n-butylammonium bromide (2.46 g, 7 mmol, 7 eq.). With vigorous stirring, potassium carbonate (93 g, 677 mmol) was added gradually to the reaction mixture. After cooling to room temperature, chloroform (73 ml) was added and the mixture was heated at reflux for 72 h.

The mixture was then filtered to remove the excess of K_2CO_3. To the filtrate was added diethyl ether (100 ml) and H_2O (100 ml). The organic layer was separated, and the aqueous layer extracted with diethyl ether several times. The combined organic layers were then washed with saturated brine solution (100 ml). The organic layer was dried over sodium sulfate and the solvent removed by rotary evaporation. The resulting pale-yellow solid was crystallized in diethyl ether/Hx at -20°C in order to remove the catalyst NBu_4CBr, (7.00 g, 32 mmol, 66%).

^{1}H NMR (300 MHz, $CDCl_3$) δ (ppm): 8.41 (s, H_1), 7.68 (dd, J = 1.8, 0.7 Hz, H_4), 7.58 (dd, J = 2.6, 0.7 Hz, H_2), 6.38 (dd, J = 2.6, 1.8 Hz, H_3).

^{13}C NMR data are consistent with literature.[97]

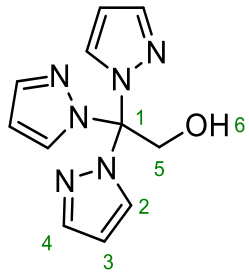

5

2,2,2-tri(1H-pyrazol-1-yl)ethan-1-ol (5) Tris(pyrazol-1-yl)methane (**4**) (1.50 g, 7 mmol), paraformaldehyde (0.841 g, 28 mmol) and potassium tert-butoxide (3.93 g, 35 mmol) were dissolved in anhydrous tetrahydrofuran (100 ml) and the brown-orange solution stirred for 3 days at r.t. Subsequently, water was added (60 ml) and the mixture was then extracted with diethylether/AcOEt (3 x 70 ml). The combined organic phases were dried over Na_2SO_4 and the solvent evaporated under reduced pressure. Recrystallisation of the yellowish residue from methanol at -20°C yielded a white crystalline solid (**5**) (1.35 g, 5.5 mmol, 78%).

^{1}H NMR (400 MHz, $CDCl_3$) δ (ppm): 7.70 (dd, J = 1.8, 0.6 Hz, H_4), 7.11(dd, J = 2.6, 0.6 Hz, H_2), 6.36 (dd, J = 1.8, 0.6 Hz, H_3), 5.08 (s, H_5), 4.90 (br, H_6).

^{13}C NMR data are consistent with literature.[97]

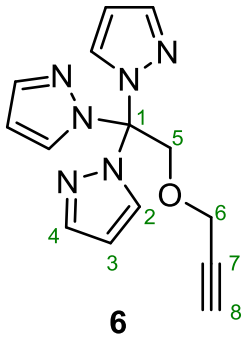

6

1,1',1''-(2-(prop-2-yn-1-yloxy)ethane-1,1,1-triyl)tris(1H-pyrazole) (6) A 50 mL flask equipped with a pressure equalized addition funnel was charged with 155 mg potassium tert-butoxide (1.29 mmol, 1.05 eq.) and 6 mL of anhydrous THF, then placed under inert atmosphere (N_2). 300 mg (1.23 mmol) of (**5**), dissolved in 6 mL of anhydrous THF and added dropwise at 0°C to the mixture over 15 minutes, then stirred at room temperature for additional 1.50 h after which propargyl bromide was added (0.150 mL, 1.29 mmol, 1.05 eq.). The system was stirred at reflux for 72 h. Afterwards, 10 mL of water was added, and the solution obtained was extracted with AcOEt. The organic phases were washed with additional water and the organic phase was dried over Na_2SO_4. The organic solvents were removed using rotary evaporator. The white solid (**6**) (350 mg, 1.23 mmol, 99 %) was used without further purification.

^{1}H NMR (400 MHz, $CDCl_3$) δ (ppm): 7.66 (dd, J = 1.7, 0.6 Hz, H_4), 7.41 (dd, J = 2.6, 0.6 Hz, H_2), 6.34 (dd, J = 2.7, 1.7 Hz, H_3), 5.20 (s, H_5), 4.17 (d, J = 2.4 Hz, H_6), 2.50 (t, J = 2.4 Hz, H_8).

^{13}C NMR data are consistent with literature.[97]

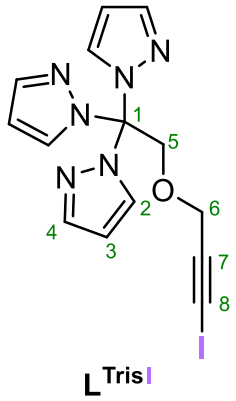

L^{TrisI}

1,1',1''-(2-((3-iodoprop-2-yn-1-yl)oxy)ethane-1,1,1-triyl)tris(1H-pyrazole) (L^{TrisI}) (6) (334 mg, 1.22 mmol) and CuI (19 mg, 0.07 eq., 0.7 mmol) were dissolved in anhydrous THF (28 ml) under nitrogen atmosphere and the pale-yellow solution was stirred at r.t. for 30 minutes in the dark. Subsequently N-iodomorpholine (837 mg, 2.44 mmol, 2 eq.) was added and the red solution was stirred at r.t. for 72 h. Afterwards 20 mL of a saturated solution of ammonium chloride was added and then extracted with diethylether (3 x 15 ml). The organic phases were washed with a saturated solution of $Na_2S_2O_3$ (2 x 20 mL) and the organic phase was dried over Na_2SO_4, the organic solvents were removed using rotary evaporator. The red-brown solid was recrystallized in DCM/Hx at -20°C to yield a pale-yellow crystalline solid (L^{TrisI}) (224 mg, 0.597 mmol, 49%).

^{1}H NMR (300 MHz, $CDCl_3$) δ (ppm): 7.66 (dd, J = 1.8, 0.7 Hz, H_4), 7.39 (dd, J = 2.6, 0.7 Hz, H_2), 6.34 (dd, J = 2.6, 1.7 Hz, H_3), 5.18 (s, H_5), 4.30 (s, H_6);

^{13}C NMR (75 MHz, $CDCl_3$) δ (ppm): 141.43 (C_4), 130.83 (C_2), 106.63 (C_3), 89.56 (C_1), 89.27 (C_7), 73.00 (C_5), 60.82(C_6), 5.17 (C_8);

ESI-MS (p.i., CH_3OH, m/z): 839 $[2L+Na]^+$, 447 $[L+K]^+$, 431 $[L+Na]^+$, 409 $[L+H]^+$, 341 [TrisI-$C(pz)_2$+ $H]^{\bullet+}$, 214 $[C(pz)_3+H]^{\bullet+}$;

IR (cm^{-1}): 3121w, 2845w, 2184w, 1722w, 1513w, 1423w, 1386m, 1351w, 1321m, 1200m, 1110m, 1095s, 1070w,1045m, 946m, 909m, 861m, 786m, 754s, 686m, 640m, 583w.

2.3.3 Synthesis of the silver complexes

General procedure B for the synthesis of silver complexes

The desired ligand $\mathbf{L^x}$ (0.14 mmol) and silver salt ($AgPF_6$ or $AgCF_3SO_3$, 0.5 eq.) were mixed together in acetone (7 mL). The colourless solution was stirred at room temperature for 1 h and then concentrated via rotary evaporation. The product was precipitated by adding hexane and then filtered yielding a white crystalline powder.

Synthesis of $[Ag(L^{Ph})_2](PF_6)$. The complex was synthetized according to the *general procedure B* with $\mathbf{L^{Ph}}$ (80 mg, 0.28 mmol) and $AgPF_6$ (36 mg, 0.14 mmol) yielding a white crystalline powder (85 mg, 0.10 mmol, yield 72%). The compound can be recrystallized stratifying diethyl ether over an acetone solution of the complex yielding colorless crystals of $[Ag(L)_2](PF_6)$ (**1**).

^{1}H NMR (400 MHz, $CDCl_3$) δ (ppm): 7.34-7.38 (m, H_1, H_2, H_5), 6.54 (d, J = 6.8 Hz, 2H, H_3), 6.00 (s, H_7), 2.50 (s, H_{10}), 1.56 (s, H_9);

ESI-MS (p.i., CH_3CN, m/z): 185.20 $[(Me_2Pz)PhCH]^+$, 281.29 $[H(L)]^+$, 303.26 $[Na(L)]^+$, 387.21 $[Ag(L)]^+$, 669.46 $[Ag(L)_2]^+$;

IR (cm^{-1}): 3031w, 2019w, 1560m, 1498w, 1451m, 1418m, 1389m, 1370w, 1313m, 1296w, 1256m, 1240m, 1186w, 1160w, 1125w, 1033m, 1001w, 980w, 922w, 873m, 837sbr, 828vs, 743s, 702s, 691m, 671w, 654w, 629w, 619m, 592w, 557s, 492w, 470w, 450w;

Elemental Analysis [Calc. for $C_{34}H_{40}N_8AgPF_6$] (%): **C**, 50.19; **H**, 4.96; **N**, 13.77; [Found] (%): **C**, 49.93; **H**, 4.76; **N**, 13.54.

Synthesis of $[Ag(L^{Ph})_2](CF_3SO_3)$. The complex was synthetized according to the *general procedure B* with $\mathbf{L^{Ph}}$ (126 mg, 0.45 mmol) and $AgCF_3SO_3$ (60 mg, 0.23 mmol) yielding a white crystalline powder (130 mg, 0.16 mmol, yield 69%). The compound can be recrystallized stratifying diethyl ether over an acetone solution of the complex yielding colorless crystals of $[Ag(L)_2](CF_3SO_3)$(**2**).

^{1}H NMR (400 MHz, $CDCl_3$) δ (ppm): 7.34-7.38 (m, H_1, H_2, H_5), 6.53 (d, J = 7.2 Hz, , H_3), 5.99 (s, , H_7), 2.50 (s, , H_{10}), 1.56 (s, H_9) ppm;

ESI-MS (p.i., CH_3CN, m/z): 106.88 $[Ag]^+$, 387.18 $[Ag(L)]^+$, 667.41 $[Ag(L)_2]^+$;

IR (cm^{-1}): 1558m, 1497w, 1461m, 1451m, 1419w, 1391w, 1327w, 1314w, 1297w, 1266vs, 1243m, 1224m, 1187w, 1160m, 1148s, 1124w, 1113w, 1033s, 1004w, 982w, 870m, 852w, 830m, 804m, 754w, 746m, 741m, 701s, 691w, 674w, 637vs, 620m, 592w, 572w, 518m, 490w, 450w;

Elemental Analysis [Calc. for $C_{35}H_{40}N_8AgF_3SO_3$] (%): **C**, 51.41; **H**, 4.93; **N**, 13.70; **S**, 3.92 ; [Found] (%): **C**, 51.62; **H**, 5.13; **N**, 13.51, **S**, 4.09.

Synthesis of $[Ag(L^{3Br})_2](PF_6)$. The complex was synthetized according to the *general procedure B* with $\mathbf{L^{3Br}}$ (100 mg, 0.24 mmol) and $AgPF_6$ (35 mg, 0.14 mmol) yielding a white powder (70 mg, 0.07 mmol, yield 52%). The compound can be recrystallized stratifying hexane over a dichloromethane solution of the complex yielding colorless crystals of $[Ag(L^{3Br})_2](PF_6)\cdot CH_2Cl_2$ (**3**·DCM).

^{1}H NMR (400 MHz, $CDCl_3$) δ (ppm): 7.53 (d, J = 8.4 Hz, H_1), 7.34 (s, H_7), 7.26 (t, J = 8.4 Hz, H_3), 6.72 (s, H_4), 6.52 (d, J = 7.5 Hz, H_5), 6.02 (s, H_8), 2.51 (s, H_{12}), 1.61 (s, H_{11});

ESI-MS (p.i., CH_3CN, m/z): 107.87 $[Ag]^+$, 383.15 $[Na(L)]^+$, 467.10 $[Ag(L)]^+$, 825.29 $[Ag(L)_2]^+$;

IR (cm^{-1}): 1558m, 1461w, 1424m, 1389w, 1319w, 1245w, 1185w, 1133w, 1075w, 1033w, 976w, 834vsbr, 775s, 708m, 694m, 675m, 662w, 618w, 556s, 494w;

Elemental Analysis [Calc. for $C_{34}H_{38}Br_2N_8AgPF_6$] (%): **C**, 42.04; **H**, 3.94; **N**, 11.54; [Found] (%): **C**, 42.28; **H**, 4.07; **N**, 11.77.

Synthesis of $[Ag(L^{3Br})_2](CF_3SO_3)$. The complex was synthetized according to the *general procedure B* with $\mathbf{L^{3Br}}$ (81 mg, 0.23 mmol) and $AgCF_3SO_3$ (60 mg, 0.22 mmol) yielding a white crystalline powder (105 mg, 0.11 mmol, yield 58%). The compound can be recrystallized stratifying hexane over a dichloromethane solution of the complex yielding colorless crystals of $[Ag(L^{3Br})_2](CF_3SO_3)$ (**4**).

^{1}H NMR (400 MHz, $CDCl_3$) δ (ppm): 7.53 (d, J = 8 Hz, H_1), 7.39 (s, H_7), 7.26 (t, J = 8 Hz, H_3), 6.72 (s, H_4), 6.52 (d, J = 8 Hz, H_5), 6.03 (s, H_8), 2.52 (s, H_{12}), 1.58 (s, H_{11});

ESI-MS (p.i., CH_3CN, m/z): 106.85 $[Ag]^+$, 467.02 $[Ag(L)]^+$, 826.14 $[Ag(L)_2]^+$;

IR (cm^{-1}): 2969w, 2917w, 1560m, 1461m, 1424m, 1389w, 1320w, 1260sbr, 1222s, 1159s, 1075w, 1026vs, 996w, 887w, 858m, 776m, 709w, 693w, 675w, 635vs, 572w, 516s, 429m;

Elemental Analysis [Calc. for $C_{35}H_{38}Br_2N_8AgF_3SO_3$] (%): **C**, 43.10; **H**, 3.93; **N**, 11.49; **S**, 3.29 ; [Found] (%): **C**, 43.39; **H**, 3.74; **N**, 11.23, **S**, 3.46.

Synthesis of $[Ag(L^{3I})_2](PF_6)$. The complex was synthetized according to the *general procedure B* with $\mathbf{L^{3I}}$ (56 mg, 0.14 mmol) and $AgPF_6$ (17 mg, 0.07 mmol) yielding a white crystalline powder (48 mg, 0.05 mmol, yield 67%). The compound can be recrystallized stratifying hexane over a dichloromethane solution of the complex yielding colorless crystals of $[Ag(L^{3I})_2](PF_6)\cdot CH_2Cl_2$(**5**·DCM).

^{1}H NMR (400 MHz, $CDCl_3$) δ (ppm): 7.73 (d, J = 7.6 Hz, H_1), 7.32 (s, H_7), 7.13 (t, J = 7.6 Hz, H_3), 6.93 (s, H_4), 6.56 (d, J = 8 Hz, H_5), 6.02 (s, H_8), 2.51 (s, H_{12}), 1.64 (s, H_{11});

ESI-MS (p.i., CH_3CN, m/z): 311.06 $[(Me_2Pz)PhICH]^+$, 407.20 $[H(L)]^+$, 429.15 $[Na(L)]^+$, 513.08 $[Ag(L)]^+$, 919.31 $[Ag(L)_2]^+$;

IR (cm^{-1}): 1560 w, 1459w, 1420w, 1388w, 1318w, 1254w, 1182w, 1121w, 1068w, 1029w, 994w, 976w, 834vsbr, 802m, 784m, 773m, 709m, 688m, 673m, 659w, 648w, 617w, 557s, 482w;

Elemental Analysis [Calc. for $C_{34}H_{38}I_2N_8AgPF_6$] (%): **C**, 38.33; **H**, 3.60; **N**, 10.52; [Found] (%): **C**, 38.63; **H**, 3.75; **N**, 10.77.

Synthesis of $[Ag(L^{3I})_2](CF_3SO_3)$. The complex was synthetized according to the *general procedure B* with $\mathbf{L^{3I}}$ (45 mg, 0.11 mmol) and $AgCF_3SO_3$ (15 mg, 0.06 mmol) were mixed in acetone (7 mL) yielding a white crystalline powder (22 mg, 0,02 mmol, yield 37%). The compound can be recrystallized stratifying

hexane over a THF solution of the complex yielding colorless crystals of $[Ag(L^{3I})_2](CF_3SO_3)$)·0.5 THF (**6**).

^{1}H NMR (400 MHz, $CDCl_3$) δ (ppm): 7.76 (d, J = 8 Hz, H_1), 7.39 (s, H_7), 7.13 (t, J = 8 Hz, H_3), 6.94 (s, H_4), 6.58 (d, J = 8 Hz, H_5), 6.01 (s, H_8), 2.52 (s, H_{12}), 1.65 (s, H_{11});

ESI-MS (p.i, CH_3CN, m/z): 429.09 $[Na(L)]^+$, 513.08 $[Ag(L)]^+$;

IR (cm^{-1}): 2971w, 2921w, 1590w, 1560m, 1462m, 1420m, 1390m, 1320w, 1262vsbr, 1223m, 1184w, 1152mbr, 1068w, 1030s, 993w, 976w, 884w, 862m, 788m, 780m, 754w, 709m, 869m, 674m, 660w, 647w, 636s, 618w, 572m, 517m, 484w, 426w;

Elemental Analysis [Calc. for $C_{35}H_{38}I_2N_8AgF_3SO_3$] (%): **C**, 39.31; **H**, 3.58; **N**, 10.48; **S**, 3.00 ; [Found] (%): **C**, 39.11; **H**, 3.83; **N**, 10.73, **S**, 2.88.

Synthesis of $[Ag(L^{4Br})_2](PF_6)$. The complex was synthetized according to the *general procedure B* with $\mathbf{L^{4Br}}$ (50 mg, 0.14 mmol) and $AgPF_6$ (18 mg, 0.07 mmol) yielding a white powder (58 mg, 0.06 mmol, yield 85%). The compound can be recrystallized stratifying hexane over a dichloromethane solution of the complex yielding colorless crystals of $[Ag(L^{4Br})_2](PF_6)$ (**7**).

^{1}H NMR (400 MHz, $CDCl_3$) δ (ppm): 7.45 (dd, J_1 = 8.5 Hz, J_2 = 1.8 Hz, H_2), 7.33 (s, H_5), 6.41 (dd, J_1 = 8.5 Hz, J_2 = 1.8 Hz, H_3), 6.01 (s, H_7), 2.51 (s, H_{10}), 1.61 (s, H_9);

ESI-MS (p.i., CH_3CN, m/z): 106.89 $[Ag]^+$, 467.06 $[Ag(L)]^+$, 826.23 $[Ag(L)_2]^+$; **IR** (cm^{-1}): 1558m, 1489w, 1460m, 1421w, 1392w, 1321m, 1301w, 1257w, 1184w, 1133w, 1078w, 1032w, 1014m, 979w, 870m, 846s, 831s, 814s, 797s, 714m, 703m, 680w, 663w, 637w, 623w, 556s, 500w, 491m, 462w, 423m;

Elemental Analysis [Calc. for $C_{34}H_{38}Br_2N_8AgPF_6$] (%): **C**, 42.04; **H**, 3.94; **N**, 11.54; [Found] (%): **C**, 42.45; **H**, 4.12; **N**, 11.78.

Synthesis of $[Ag(L^{4Br})_2](CF_3SO_3)$. The complex was synthetized according to the *general procedure B* with $\mathbf{L^{4Br}}$ (50 mg, 0.14 mmol) and $AgCF_3SO_3$ (18 mg, 0.07 mmol) yielding a white crystalline powder (62 mg, 0.06 mmol, yield 91%). The compound can be recrystallized stratifying of hexane over a dichloromethane solution of the complex yielding colorless crystals of $[Ag(L^{4Br})_2](CF_3SO_3)$ (**8**).

^{1}H NMR (400 MHz, $CDCl_3$) δ (ppm): 7.50 (dd, J_1 = 8.5 Hz, J_2 = 1.8 Hz, H_2), 7.32 (s, H_5), 6.40 (dd, J_1 = 8.5 Hz, J_2 = 1.8 Hz, H_3), 6.05 (s, H_7), 2.51 (s, H_{10}), 2.04 (s, H_9);

ESI-MS (p.i., CH_3CN, m/z): 106.88 $[Ag]^+$, 467.03 $[Ag(L)]^+$, 826.22 $[Ag(L)_2]^+$;

IR (cm^{-1}): 1560m, 1490w, 1461w, 1419w, 1394w, 1263s, 1226m, 1183w, 1153m, 1142m, 1076w, 1030s, 1013m, 981w, 882w, 869m, 841w, 830w, 801s, 755w, 717w, 705w, 636s;

Elemental Analysis [Calc. for $C_{35}H_{38}Br_2N_8AgF_3SO_3$] (%): **C**, 43.10; **H**, 3.93; **N**, 11.49; **S**, 3.29 ; [Found] (%): **C**, 43.55; **H**, 4.08; **N**, 11.33, **S**, 2.96.

Synthesis of $[Ag(L^{4I})_2](PF_6)$. The complex was synthetized according to the *general procedure B* with $\mathbf{L^{4I}}$ (26 mg, 0.06 mmol) and $AgPF_6$ (8 mg, 0.03 mmol) yielding a white crystalline powder (20 mg, 0.02 mmol, yield 59%). The compound can be recrystallized by stratifying hexane over a dichloromethane solution of the complex yielding colorless crystals of $[Ag(L^{4I})_2](PF_6)$ (**9**-phase-3), by stratifying hexane over a dichloroethane solution of the complex yielding colorless crystals of $[Ag(L^{4I})_2](PF_6)\cdot 1.5C_2H_4Cl_2$ (**9**·DCE), or stratifying hexane over a tetrahydrofuran solution of the complex yielding colorless crystals of $[Ag(L^{4I})_2](PF_6)\cdot$n(THF) (**9**-phase-1).

^{1}H NMR (400 MHz, $CDCl_3$) δ (ppm): 7.64 (d, J = 8.8 Hz, H_2), 7.28 (s, H_5), 6.24 (dd, J_1 = 8.8 Hz, H_3), 5.99 (s, H_7), 2.48 (s, H_{10}), 1.52 (s, H_9);

ESI-MS (p.i. CH_3CN, m/z): 513.07 $[Ag(L)]^+$, 919.29 $[Ag(L)_2]^+$;

IR (cm^{-1}): 1558m, 1483w, 1457w, 1418w, 1321w, 1241w, 1032w, 1006w, 836vsbr, 795s, 714w, 707m, 556s;

Elemental Analysis [Calc. for $C_{34}H_{38}I_2N_8AgPF_6$] (%): **C**, 38.33; **H**, 3.60; **N**, 10.52; [Found] (%): **C**, 38.73; **H**, 3.79; **N**, 10.84.

Synthesis of $[Ag(L^{4I})_2](CF_3SO_3)$. The complex was synthetized according to the *general procedure B* with $\mathbf{L^{4I}}$ (26 mg, 0.06 mmol) and $AgCF_3SO_3$ (9 mg, 0.03 mmol) yielding a white crystalline powder (22 mg, 0.02 mmol, yield 63%). The

compound can be recrystallized by stratifying hexane over a dichloromethane solution of the complex yielding colorless crystals of $[Ag(L^{4I})_2](CF_3SO_3)\cdot 1.5CH_2Cl_2$ (**10**·DCM), or by stratifying hexane over a tetrahydrofuran solution of the complex yielding colorless crystals of $[Ag(L^{4I})_2](CF_3SO_3)\cdot n(THF)$ (**10**-phase-1).

^{1}H NMR (400 MHz, $CDCl_3$) δ (ppm): 7.64 (d, J = 8.4 Hz, H_2), 7.35 (s, H_5), 6.24 (dd, J_1 = 8.4 Hz, H_3), 5.98 (s, H_7), 2.50 (s, H_{10}), 1.53 (s, H_9);

ESI-MS (p.i., CH_3CN, m/z): 311.05 $[(Me_2Pz)PhICH]^+$, 407.13 $[H(L)]^+$, 429.13 $[Na(L)]^+$, 513.09 $[Ag(L)]^+$, 919.32 $[Ag(L)_2]^+$;

IR (cm^{-1}): 2981w, 2916w, 1558m, 1486w, 1461w, 1417w, 1390w, 1325w, 1256sbr, 1223m, 1151sbr, 1063w, 1030s, 1006m, 983w, 870m, 795s, 754w, 708m, 636vs, 572w, 517m, 489w, 462w;

Elemental Analysis [Calc. for $C_{35}H_{38}I_2N_8AgF_3SO_3$] (%): **C**, 39.31; **H**, 3.58; **N**, 10.48; **S**, 3.00 ; [Found] (%): **C**, 39.26; **H**, 3.62; **N**, 10.24, **S**, 2.96.

Synthesis of $[Ag(L^{4CCl})_2](PF_6)$. The complex was synthetized according to the *general procedure B* with $\mathbf{L^{4CCl}}$ (32 mg, 0.07 mmol) and $AgPF_6$ (8.8 mg, 0.035 mmol) yielding a pale-yellow powder (28 mg, 0.03 mmol, yield 72%). The compound can be recrystallized by stratifying hexane over a tetrahydrofuran solution of the complex yielding colorless crystals of $[Ag(L^{4CCl})_2](PF_6)\cdot THF$ (**12**).

^{1}H NMR (400 MHz, $CDCl_3$) δ (ppm): 7.36 (d, J = 8.3 Hz, H_4), 7.31 (s, H_7), 6.47 (d, J_1 = 8.3 Hz, H_5), 5.99 (s, H_8), 2.48 (s, H_{12}), 1.52 (s, H_{11});

ESI-MS (p.i., CH_3OH, m/z): 335.06 $[(Me_2Pz)PhC{\equiv}ClCH]^+$, 431.14 $[H(L)]^+$, 453.13 $[Na(L)]^+$, 883.31 $[Na(L)_2]^+$, 967.27 $[Ag(L)_2]^+$;

IR (cm^{-1}): 2920w, 2852w, 2169w, 1559m, 1506w, 1461w, 1416w, 1383w, 1253m, 1178w, 1121w, 1031w, 977w, 873w, 838s, 819m, 721w, 708w, 695w;

Elemental Analysis [Calc. for $C_{38}H_{38}I_2N_8AgPF_6$] (%): **C**, 40.99; **H**, 3.44; **N**, 10.06; [Found] (%): **C**, 41.24; **H**, 3.88; **N**, 9.88.

Synthesis of $[Ag(L^{4CCl})_2](CF_3SO_3)$. The complex was synthetized according to the *general procedure B* with $\mathbf{L^{4CCl}}$ (32 mg, 0.070 mmol) and $AgCF_3SO_3$ (8.9 mg, 0.035 mmol) yielding a pale-yellow powder (25 mg, 0.02 mmol, yield 64%). The compound can be recrystallized in THF/Hx or acetone yielding colorless crystals of $[Ag(L^{4I})_2](CF_3SO_3)$ (**11**·THF).

^{1}H NMR (400 MHz, $CDCl_3$) δ (ppm): 7.37 (s, H_7), 7.36 (d, J = 8.3 Hz, H_4), 6.48 (d, J = 8.3 Hz, H_5), 5.98 (s, H_8), 2.49 (s, H_{12}), 1.54 (s, H_{11} overlapped with water);

ESI-MS (p.i., CH_3OH, m/z): 335.17 $[(Me_2Pz)PhC{\equiv}ClCH]^+$, 431.14 $[H(L)]^+$, 453.13 $[Na(L)]^+$, 883.31 $[Na(L)_2]^+$, 967.24 $[Ag(L)_2]^+$;

IR (cm^{-1}): 2921w, 2854w, 2169w, 1698 w, 1559m, 1507w, 1460w, 1417w, 1382w, 1322w, 1307w, 1249s, 1223m, 1156m, 1028s, 980w, 873m, 819m, 797m, 755w, 720w, 708m, 694m, 668m, 636s;

Elemental Analysis [Calc. for $C_{39}H_{38}I_2N_8AgF_3SO_3$] (%): **C**, 41.92; **H**, 3.43; **N**, 10.03; **S**, 2.87 ; [Found] (%): **C**, 42.15; **H**, 3.68; **N**, 9.89, **S**, 2.67.

2.4 Results and discussion

2.4.1 Synthesis

In order to explore the halogen bond interactions to sustain the formation of multidimensional networks, we synthetized a family of phenyl-bis(pyrazolyl)methane ligands with iodine or bromine atoms on the phenyl ring in both para and meta positions. Due to the greater sigma hole present on iodine than on bromine, we expected to find an increased tendency to form halogen bonds in structures with L^{3I} and L^{4I} ligands. Functionalized bispyrazolyl ligands $\mathbf{L^X}$ were prepared from bispyrazolyl ketone and the corresponding benzaldehydes in a stardard procedure using $CoCl_2$ as catalyst as depicted in Scheme 1.

Initially, the reaction was performed in anhydrous THF at 70 °C for 24 hours and the crude product was purified from residual reagents by recrystallization in hexane. The crystallization yield was about 35-40% for L^{3Br} and L^{4Br}, and about 10-15 % for L^{Ph}, L^{3I} and L^{4I}. Despite the reaction is favoured with electron-withdrawing groups (EWG) on the aldehyde, we were able to improve the yield of iodine substituted products by purification of the crude mixure with column chromatography. L^{4I} was obtained as a white crystalline powder using hexane/ethyl acetate (8:2) as eluent and the yield of reaction was improved from 10% to 64%.

We also synthetized the ligand L^{4CCI} to increase the XB donor ability according to the presence of an alkyne moiety between the phenyl ring and iodine atoms. The alkyne group, due to its EWG nature, enhances the sigma hole on the halogen atom.

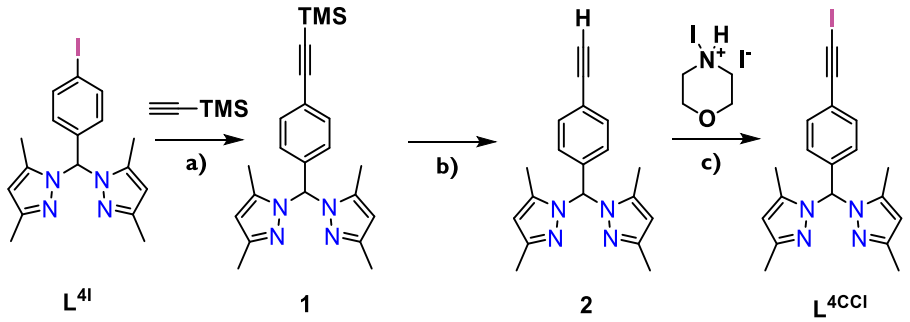

Scheme 4. Synthesis of the ligand L^{4CCl}. a) $Pd(PPh_3)Cl_2$ (0.05 eq.), CuI (0.05 eq.), trimethylsilylacetylene (1.2 eq.), dry Et_3N, 50°C, 24 h, N_2; b) K_2CO_3 (3 eq.), MeOH, r.t. 3 h; c) N-iodomorpholine (2 eq.), CuI (0.10 eq.), dry THF, r.t. 48 h, dark, N_2.

The first step of the synthesis (**Scheme 4**) involved the Sonogashira coupling of the iodo-derivate L^{4I} with trimethylsilylacetylene. It was necessary to protect the free alkyne hydrogen during the coupling to avoid the side reaction between two molecules of L^{4I} with one molecule of non-protected alkyne (acetylene). The trimethylsilyl protecting group could be easily removed in mild conditions with potassium carbonate, to give the free alkyne function with quantitative yield. Finally, we choose to introduce the iodine atoms with N-iodomorpholine iodination reagents. N-iodomorphiline had to be freshly synthetized from iodine and morpholine prior to use. Indeed, with this chelating substrate it was mandatory to avoid the use of metal salts such as $AgNO_3$ which contain metals that could potentially bind to the N-chelating function of the pyrazole moieties[98–100]. The overall yield of three synthetic steps is about 73% yielding L^{4CCl} as off-white crystalline solid.

The silver complexes were preparared by treating equimolar amounts of ligands L^x with silver salts ($AgPF_6$, $AgCF_3SO_3$) in acetone for 1 hour. We choose these two different silver salts to investigate the possible influence of the anions in the resulting supramolecular assembly. The hexafluorophosphate moiety is usually a non-coordinating anion, on the contrary, the $CF_3SO_3^-$ usually behaves as a O-monodentate.[101] The choice of counter-ion is also important given the presence of electronegative atoms (fluorine or oxygen), which can act as halogen-bond acceptors.

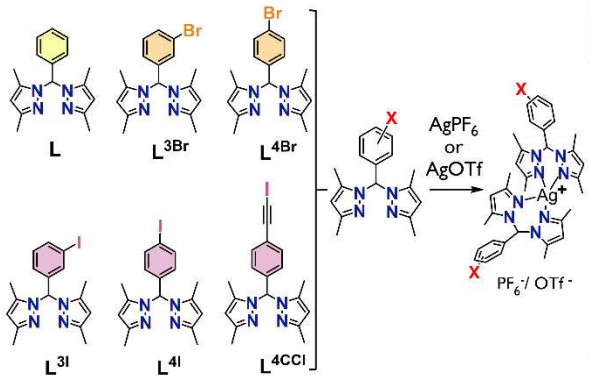

Ligand	$AgPF_6$ Complex	$AgCF_3SO_3$ Complex
L^{Ph}	**1**	**2**
L^{3Br}	**3** · DCM	**4**
L^{3I}	**5** · DCM	**6**
L^{4Br}	**7**	**8**
L^{4I}	**9**-phase-I	**10**-phase-I
	9-phase-2	**10**-phase-2
	9-phase-3	**10**-phase-3
	9 · DCE	**10** · DCE
L^{4CCl}	**11** · THF	**12**

Figure 17. Ligands $\mathbf{L^X}$ obtained and silver complexes synthetized in this study.

The silver complexex **1**-**11** were isolated by precipitation by adding hexane to the reaction mixture and they were subsequently recrystallized in different solvent systems. In particular, for the complexes of L^{4I} ligand, the solvent systems used for crystallization were: THF/Hx, MeCN/Et_2O, Ac/Et_2O and DCM/Hx, DCE/Hx. Single crystals suitable for the XRD analysis were obtained with all these systems, except for acetone-Et_2O. The crystals obtained in acetonitrile-Et_2O were affected by twinning, which made data analysis difficult. The unit cell was however different from those obtained by the crystallization in the other solvent systems. A summary of the results obtained by the solvent screening is listed in Table 1.

Table 1. Results of solvent screening for $[Ag(L^{4l})_2]PF_6$ and $[Ag(L^{4l})_2]CF_3SO_3$ complexes.

Solvent Systems	$[Ag(L^{4l})_2]PF_6$	$[Ag(L^{4l})_2]CF_3SO_3$
THF/Hx	**9**-phase-1 Space group P-3 Crystal system Trigonal Potentially porous structure (1D cavity diameter of 30 Å) with THF in the cavities	**10**-phase-1 Space group P-3 Crystal system Trigonal Potentially porous structure (1D cavity diameter of 30 Å) with THF in the cavities
DCE/Hx	**9**-DCE Space group $P2_1/n$ Crystal system Monoclinic Solvate of DCE Layered structure	-
DCM/Hx	**9**-phase-3 Crystal system Monoclinic Space group $P2_1/c$ High Packed structure	**10**-DCM Space group $Pca2_1$ Orthorhombic High Packed structure
MeCN/Et_2O	Twinned crystals. Not suitable for SCXRD analysis.	-
Ac/Et_2O	Not suitable for SCXRD analysis.	No suitable for SCXRD analysis.

2.4.2 Analysis of crystal structures

The complexes show very similar coordination geometries: the silver adopt a linear geometry distorted toward a tetrahedral one. To describe this geometry is useful to consider τ_4 indexes, [102,103] which are calculated as follows:

$$\tau_4 = \frac{360° - (\alpha + \beta)}{360° - 2\theta} \qquad \tau_4{}' = \frac{\beta - \alpha}{360° - \theta} + \frac{180° - \beta}{180° - \theta} \qquad \theta = 109.5°$$

Where α and β are the coordination angles with α < β. τ_4 values varies between 0 and 1, where 0 represents an ideal square planar geometry and 1 the tetrahedral geometry. In all structures, τ_4 and $\tau_4{}'$ indexes are comprised between 0.70-0.61 and 0.65-0.46, respectively, which indicate an intermediate situation between the limiting geometries. Moreover, since two Ag-N coordination bonds are always longer (2.34-2.49 Å range) and two are shorter (2.21-2.31 Å range), the the coordination environment can be considered as intermediate between the tetrahedral and the linear ones, and it is usually conserved (see Appendix I).

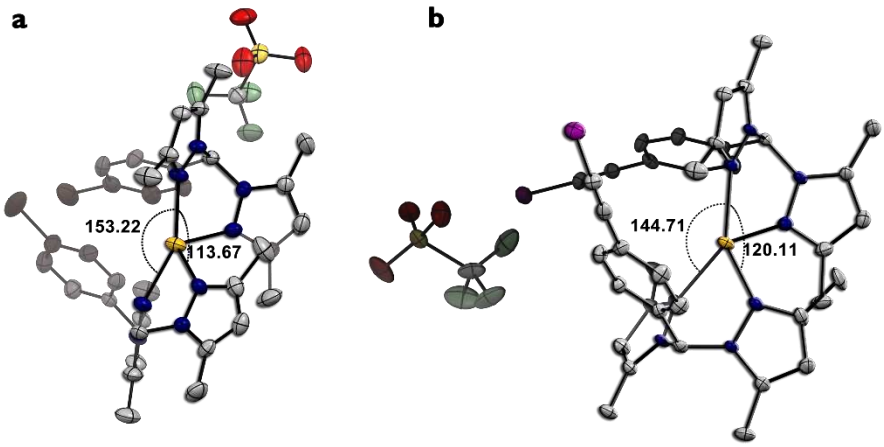

Figure 18. a) Asymmetric unit of $[Ag(L^{4Br})_2](CF_3SO_3)$ (**8**), with thermal ellipsoids at the 30% probability level. b) Asymmetric unit of $[Ag(L^{4CCl})_2](CF_3SO_3)$ (**12**) with thermal ellipsoids at the 30% probability level. a-b) Highlight of α and β coordination angles (α<β) useful to calculate τ_4 and $\tau_4{}'$ values.

As far as the halogen bond interaction is concerned, we observed that $[Ag(L^X)_2]^+$ could be considered as a a supramolecular synthon. Indeed, it was characterized by a pre-organized aromatic group with respect to the bis-pyrazole moiety. Therefore, the halogen bond interactions were purely determined by the substitution in meta or in para positions on the phenyl ring. When the substitution was in meta position, the angles between the carbon-halogen vector can be quite different, resulting in the diverse orientations of two halogen atoms on the phenyl rings (Figure 19 top). Instead, the substitution in para gives rise to a fixed orientation of the halogen with C-X angles approximately around 90° (Figure 19 bottom). In conclusion, the alkyne group in L^{4CCI} preserve the same spatial orientation of the halogen atom with respect to the L^{4I} system.

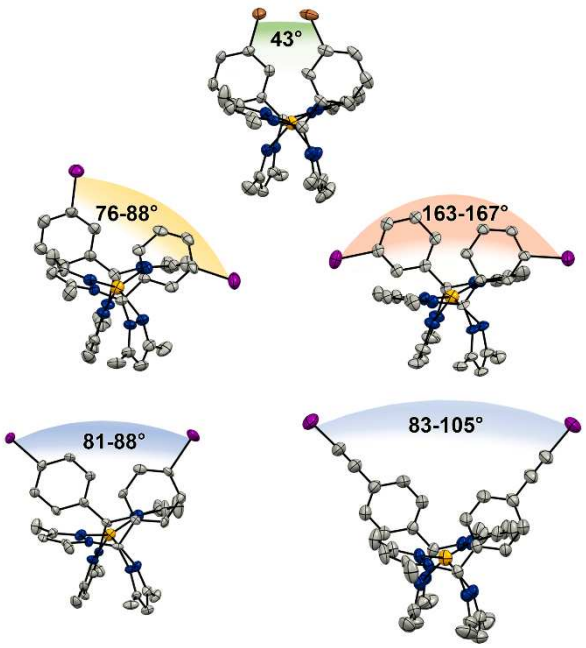

Figure 19. Schematic representation of the multiple experimental orientations, which can be experienced by the halogen atoms after the formation of the Ag complex. The indicated values refer to the observed angles between the C-halogen vector (color codes: C, gray; N, blue; Br, light brown; P, orange; and I, purple). Reprinted with permission from Inorg. Chem. 2020, 59, 6, 4140–4149. Copyright 2020 American Chemical Society.

Moreover, the halogen atoms in para position gives rise to two different types of interactions, in which the counter-anion is the halogen bond acceptor. In the first

type, the halogen atom is both XB donor toward the anion and XB acceptor toward a second halogen atom (Figure 20h). In the second type, the counter-anion acts as a bridge between two different halogen atoms (Figure 20i, l).

Figure 20 summarizes all the halogen bond interactions found in the study concerning compounds **1-12.** In summary, bromine and iodine atoms can act as XB acceptor towards other halogens of the ligands or as XB donor toward electronegative atoms of anion, other halogens, or oxygen atoms of the solvent.

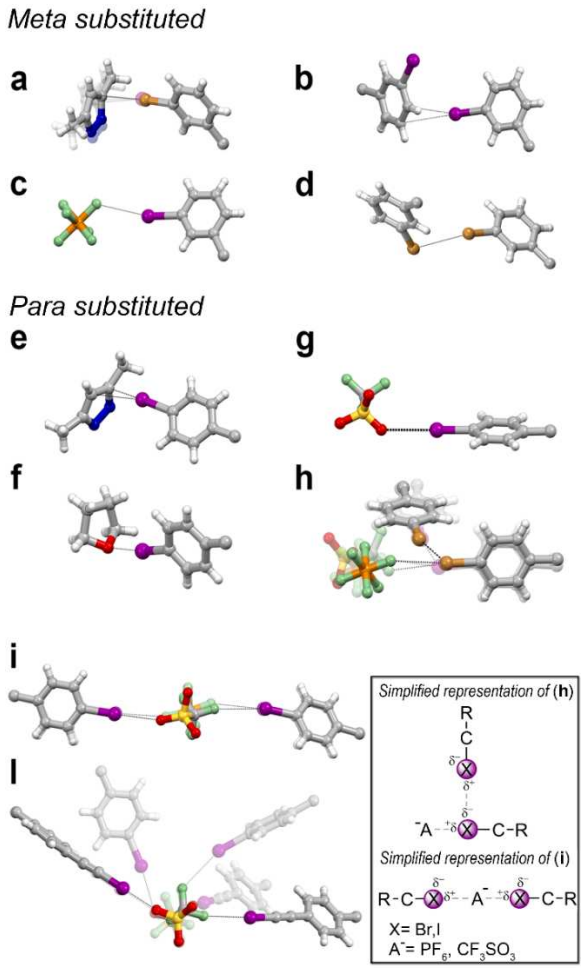

Figure 20. Summary of the XB interactions exchanged by the halogen atoms in the reported structures. The inset describes a schematic representation of XB between two halides and anion (color codes, C, gray; N, blue; O, red; H, white; F, green; S, yellow; Br, light brown; P, orange; I, purple). Reprinted with permission from Inorg. Chem. 2020, 59, 6, 4140–4149. Copyright 2020 American Chemical Society.

2.4.3 Solvates

As illustrated in **Table 1** the complexes $[Ag(L^{4I})_2]PF_6$ and $[Ag(L^{4I})_2]CF_3SO_3$ were crystallized in different solvent systems, resulting in different solvates.

In the structure obtained from DCE/Hx system (**9**·DCE) the complex entities are arranged layers formed by two different arrays of molecules. The crystal packing is sustained by the pyrazole-anion interaction ($CH_{ligand}\cdots F_{anion}$), and by two iodine-carbon interactions involving only I3 (Figure 21). The second iodine atom point toward chlorine atoms of DCE.

$[Ag(L^{4I})_2]CF_3SO_3$ was also crystallized in DCE/Hx (**10**·DCM) yielding a structure with interstitial cavities filled with DCM. The solvent interacts in the pocket by CH···F, CH···O and CH···π interactions with the anions and the π system of the pyrazole rings. The interactions in the crystal are dominated by bridging halogen bonds between the anion and two distinct iodine atom I6 and I12. In both cases the iodine-oxygen distances are in the range 3.018-3.090 Å.

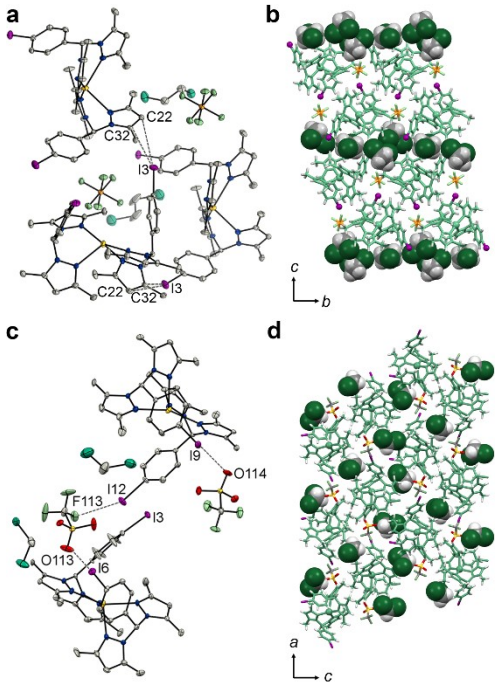

Figure 21. a) Interactions in **9**·DCE. b) Packing **9**·DCE in which solvent layer and the complex molecules layer are alternated. c) d) Crystal packing **10**·DCM, highlighting the pocket-like interstitial cavities filled by dichloromethane solvent molecules.

Tetrahydrofuran/hexane system gave isostructural compound for both $[Ag(L^{4I})_2]PF_6$ and $[Ag(L^{4I})_2]CF_3SO_3$ complexes. These two species, namely **9**-phase-1 and **10**-phase-1 were subject to a phase transition to generate two different new phases (see next section).

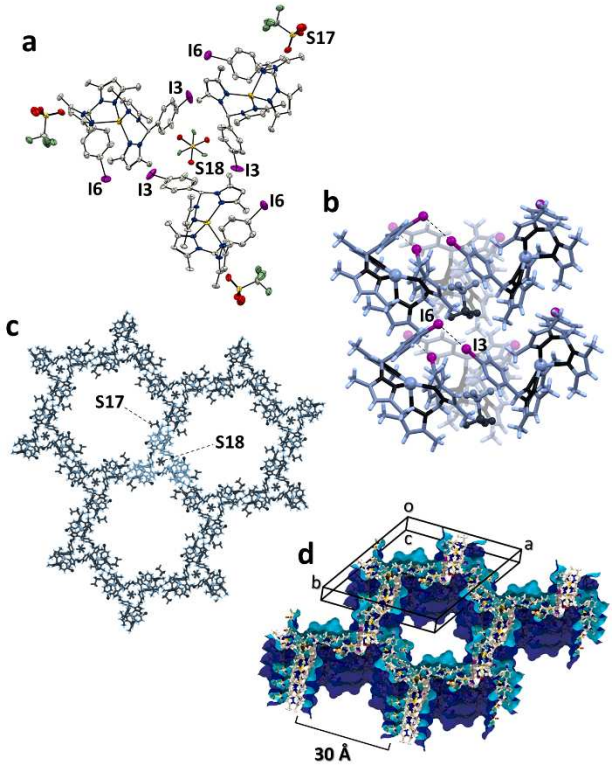

Figure 22. Crystal structure of **10**-phase-1 crystallized in THF/Hx. a) Supramolecular trimer. b) Trimeric units piled along the c-axis. c) Expansion of the trimeric unit in the ab crystallographic plane. d) Crystal packing highlighting the 1D channels. Reprinted with permission from Inorg. Chem. 2020, 59, 6, 4140–4149. Copyright 2020 American Chemical Society.

9-phase-1 and **10**-phase-1 exhibit long prismatic crystals, which are stable in the presence of the crystallization solvent or at temperature below 200 K. According to SCXRD characterization, they form large 1D hexagonal cavities occupied with solvent of crystallization (Figure 22). The crystal lattice is based on weak interactions involving the aromatic rings and the anions. More specifically, PF_6^- or $CF_3SO_3^-$ are surrounded by three molecular units, through CH···F or CH···O contacts. There are also iodine-iodine weak contacts (I6···I3 4.5 Å) in which the sigma hole on I6 point toward the δ^- of the iodine I3 with the C-I6···I3 angle of

160°. Supramolecular trimers, running along the c-axis, are then stacked one over the other (Figure 22b). In addition, the anions (P17/S17), through CH···F interactions, promote the expansion of trimers stacking along the crystallographic plane *ab* (Figure 22c). The final arrangement is a honeycomb structure with hexagonal 1D cavities along c-axis, filled with THF molecules. Performing the X-ray collection at low temperature allowed only to indentify THF close to the surface of the channel. In particular, solvent molecules interact with I3 atom through XB (I3···O1s 3.24 Å) as shown in Figure 20f.

The supramolecular assembly obtained is potentially porous with a cavity volume of 7300 $Å^3$/cell c (56% of the unit cell volume), and a cavity diameter of about 30 Å (Figure 22d).

2.4.4 Phase transitions

As mentioned above, **9**-phase-1 and **10**-phase-1 were not stable without mother liquor. For both systems, we could observe a phase-1 to phase-2 transition, using hot-stage microscopy with polarized light (Figure 23). The whole process took less than 1 minute and led to the complete conversion of the crystals with needle-like morphology into the plate-like crystals of phase 2. In this section, for simplicity we will describe the phase transitions of **10**-phase-1 as a representative example of both systems.

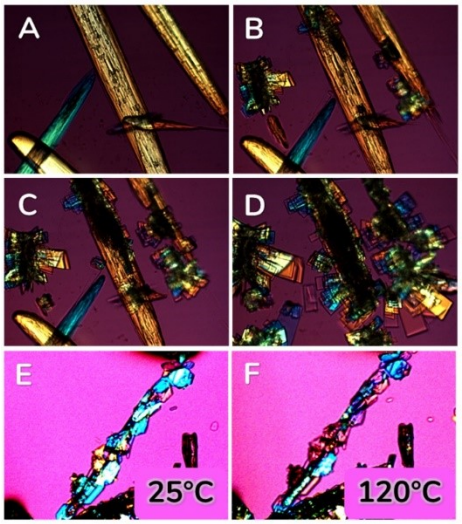

Figure 23. (A-D) Polarized microscopy images collected at different points in time showing the phase transition from **10**-phase-1 (needles) to **10**-phase-2 (plates) at RT. (E-F) Hot-stage microscopy images showing the phase transition from **10**-phase-2 to **10**-phase-3. Reprinted with permission from Inorg. Chem. 2020, 59, 6, 4140–4149. Copyright 2020 American Chemical Society.

The **10**-phase-2 crystals have a small channel-like cavity (5Å diameter) containing one THF molecule per $[Ag(L^{4l})_2]CF_3SO_3$ complex. Iodine atoms interacts with fluorine and oxygen atoms of $CF_3SO_3^-$ anion through halogen bonds. Usually, iodine-fluorine distances are longer than iodine-oxygen ones, with values of 3.27/3.38 Å and 2.97/2.99 Å, respectively (Figure 24a,b).

This second phase is stable at room temperature but we could observe a second phase transition when crystals of **10**-phase-2 were heated above 120°C, giving **10**-phase-3 (Figure 23e,f).

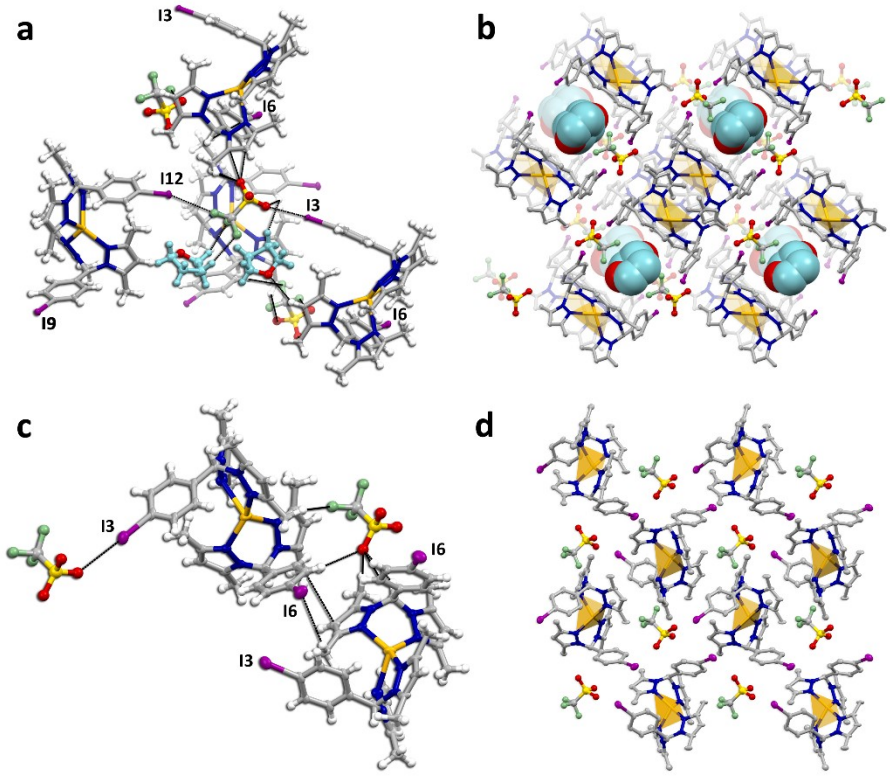

Figure 24. Intermolecular interactions (a) and crystal packing (b) of **10**-phase-2. THF molecules in the channel in light blue. Intermolecular interactions (c) and crystal packing (d) of **10**-phase-3.

The single-crystal X-ray structure shows that the system underwent a significant structural rearrangement, resulting in a new anhydrous form of the silver complex. In this more compact foIrm, only iodine I3 interact with the oxygen atom of trifluoromethanesulphonate anion (Figure 24c,d). Instead I6 atom interact with methyl group of pyrazole moiety via its negatively charged corona. Interestingly, the system with PF_6^-, namely **9**-phase-2, underwent a phase transition after heating the crystals at 120 °C, but the formed **9**-phase-3 was not isostructural to **10**-phase-3.Indeed, **9**-phase-3 and **10**-phase-3 exhibited different

PXRD patterns , Figure 25. The **9**-phase-3 system is also an anhydrous form, and the mayor supramolecular interaction involves I3 that act simultaneously as XB donor and acceptor towards fluorine atom of the anion and I6, respectively (see Figure 20h).

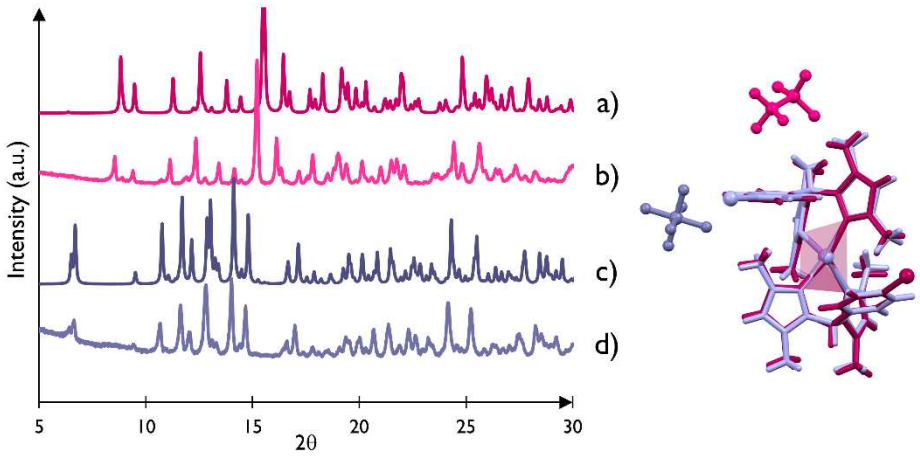

Figure 25. Simulated (a) and experimental (b) PXRD pattern of **10**-phase-3. Simulated (c) and experimental (d) PXRD pattern of **9**-phase-3. Structure overlay of **10**-phase-3 [violet] and **9**-phase-3 system [light blue].

Phase transitions from phase-1 to phase-3 were also investigated with PXRD, which confirmed the matching between single-crystal data and the bulk composition of the system, despite the strong preferential orientation due to the needle-like or plate-like shape of the crystals.

Due to their metastable nature, phase-1 of both systems were the most difficult to characterize. To avoid the immediate conversion to phase-2 a specific experimental setup was conceived. Specifically, a lump of crystals of phase-1 was placed together with some mother liquor on a zero-background sample holder, and rapidly covered with a thin Mylar sheet sealed at the boundaries with silicon grease in order to prevent solvent evaporation. Moreover, the crystals were not grounded to prevent the phase transition. When the Mylar film was removed from the sample holder the complete conversion of phase-1 into phase-2 was observed within 30 seconds. The PXRD pattern of phase-3 was recorded after exposing the crystal at 120°C in oven for 5 minutes followed by the XRD measurements. These conditions allowed to record the PXRD patterns of all three phases as shown in Figure 26.

The thermal experiments were performed on **10**-phase-2 crystals dried prior the analysis to remove the solvent on the crystals (Figure 27). The DSC showed the presence of a broad endothermic peak below 100 °C associated with the desolvation process between phase-2 and phase-3. This behaviour was confirmed also by TGA analysis with a weight loss below 100°C of about 1.92 %.

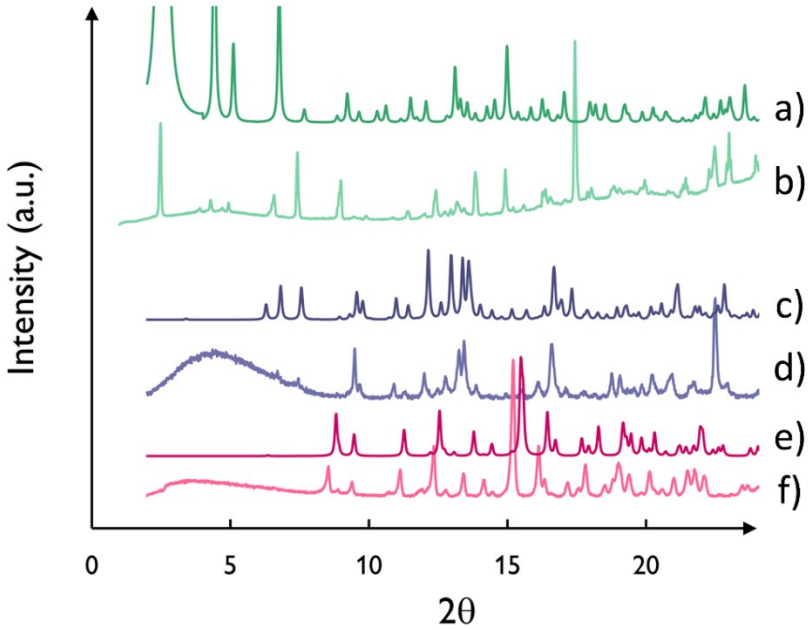

Figure 26. Overlap between the simulated and experimental XRD of **10**-phase-1 (a,b), **10**-phase-2 (c,d), **10**-phase-3 (e,f).

The endo/eso peak at 113°C (T_{onset}) is indicative of the phase transition. The endo event is most likely due to the desorption of the residual THF, which is located in the channels of **10**-phase-2 and the immediate spatial reorganization. Moreover, both TGA and DSC profile confirm the degradation peak of the anhydrous form around 225°C.

As far as the **9** system (PF_6^-) is concerned the DSC scan showed two endothermic peaks at 111 and 264 °C. The first event derives by the loss of the THF molecules into the small channels, and then, to the phase conversion into the more stable anhydrous form. The desolvation process at 111 °C is confirmed by a 5% weight loss in the TGA profile, which is consistent with 1 molecule of THF per $[Ag(L^{4I})_2]PF_6$ (theoretical value of 6%) (Appendix II, Figure B18).

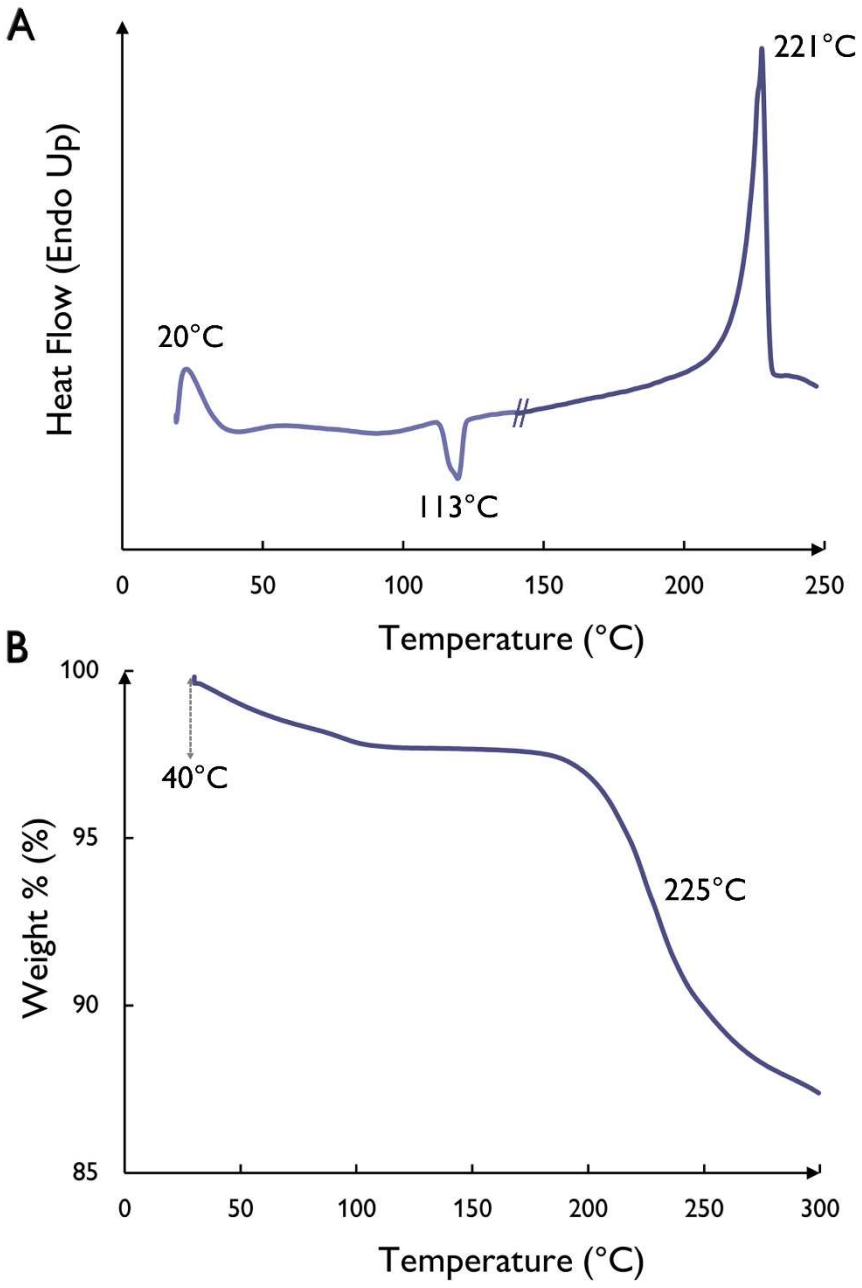

Figure 27. (A) DSC and (B) TGA profile of **10**-phase-2.

2.4.5 Tuning σ-hole strength with longer synthon

With the aim to have a more pronounce σ-hole we have synthetized a system with iodoalkyne moiety, resulting in $[Ag(L^{4CCI})_2](PF_6)\cdot THF$ (**11**·THF) and $[Ag(L^{4CCI})_2](CF_3SO_3)$ (**12**), illustrated in Figure 29. The crystal packing of both compounds shows the formation of supramolecular chains, based on the bridging halogen bond interaction between anion and two peripheral iodine atoms ($X^{\delta+}\cdots Anion\cdots{}^{+\delta}X$). However, the structural packing of **12** and **11**·THF is not the same. In fact, in the first system, the chains are more interwoven, having a structure with no voids. In the second system, 1D cavities are occupied by disordered THF molecules.

In summary, by comparing the XB distances for all of the systems, there is a significant decrease of XB distances from L^{Br} to L^{4CCI}, due to a more pronounced σ-hole on L^{4CCI} with respect to L^{4I} and L^{Br}. Hence, we might expect to have gained a significant control over the formation of the supramolecular architecture due to more robust and directional halogen bond interactions. It is instructive to analyse the XB interactions for the various systems. It can be appreciated in Figure 12 as the trifluoromethanesulfonate anion and the L^{4CCI} ligand led to the shortest, hence strongest XBs among the cases here described.

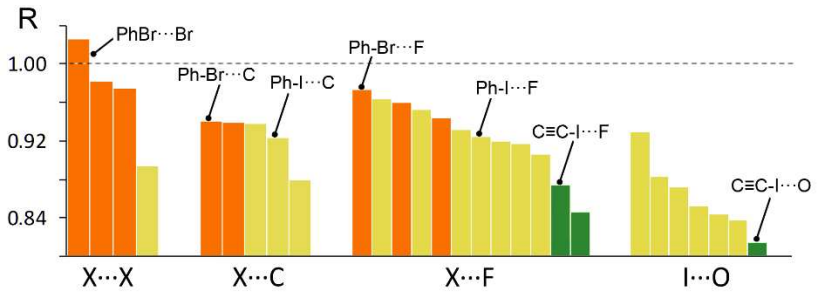

Figure 28. Histogram of the normalized distance R for halogen bonds. A value of 1 corresponds to an XB donor-acceptor distance equal to the sum of the v.d.W. radii.

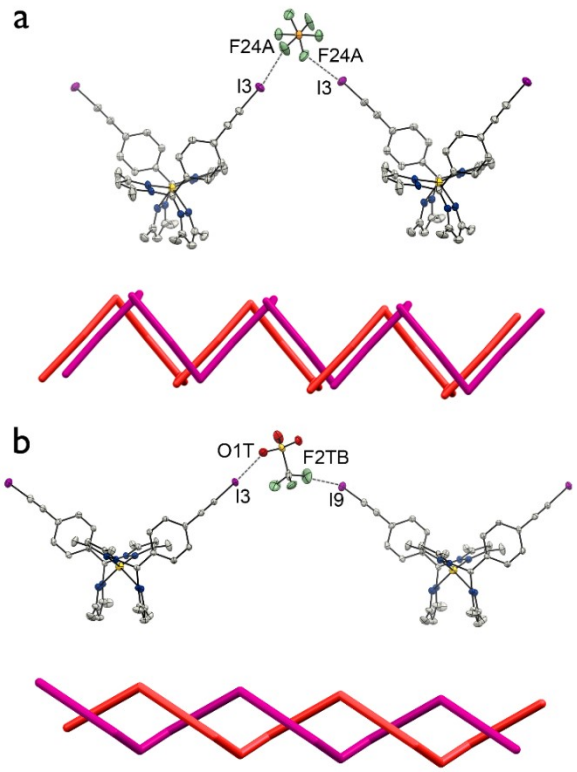

Figure 29. XB interactions and supramolecular chains rapresentation for **11**·THF (a) and **12** (b) systems.

2.4.6 Design of coordination polymer sustained by XB interaction

We also explored the possibility to build different silver coordination polymers based on halogen bond interactions[104] through the design of a new ligand with a greater conformational mobility and an enhanced σ-hole. We focused on the synthesis of a tridentate ligand based on tris(pyrazolyl)methane moiety[63,105] with a mobile iodo-alkyne chain as depicted in Figure 30. This new ligand L^{TrisI} can potentially act as tridentate ligand (κ^3) or bidentate one (κ^2). Moreover, L^{TrisI} can act a κ^2-κ^1 ligand as bridge between two different silver metals, leading to the formation of coordination polymers. In addition, the presence of iodo-alkyne

function introduced a potentially strong XB donor system to to sustain the polymeric chain.

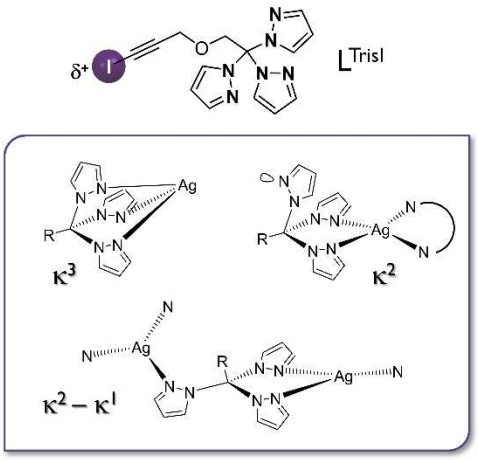

Figure 30. Tridentate L^{TriI} ligand synthetized. The inset shows the possible coordination mode of $[HC(pz)_3]$ moiety in silver compounds[63].

The synthesis of L^{trisI} started from the preparation of trispyrazole followed by the subsequent addition of paraformaldehyde yielding trispyrazolyl-ethanol **5** with a 78% yield. The etherification reaction with propargyl bromide and potassium tert-butoxide as a base allowed to introduce the alkyne moiety in **6** in quantitative yield. The last step of the synthesis was the iodination of the alkyne hydrogen with iodomorpholine in the same condition used for the ligand L^{4CCI}. In this case, it was necessary to add a purification step via recrystallization at -20 °C with DCM/Hx as solvent, to remove unreacted compounds. The yield of this synthetic step is strongly influenced by the purity of iodomorpholine reagent and to ensure good yield it had to be prepare just before use.

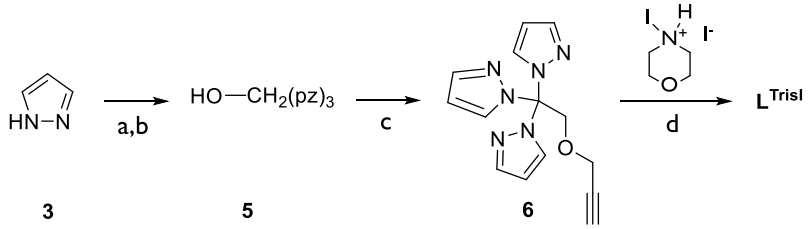

Scheme 5. Synthetic path of ligand L^{TrisI}.The detailed experimental conditions are described in the experimental section[97].

2.5 Conclusion

In this study we synthetized different bispyrazolyl ligands characterized by a N-N chelating system towards silver metal ions, and which can form directional supramolecular interactions due to the presence of halogen atoms in meta or para position in the phenyl ring. The silver assemblies obtained exhibit the same coordination geometry (distorted tetrahedral), resulting in a pre-organized XB donor moiety, whose directionality depends exclusively on the position of the halogen functionalization. Solvent screening was performed for the system involving ligand L^{4I}, and different solvates were obtained in DCE/Hx, DCM/Hex and THF/Hx solvent mixtures. In THF/Hx, three phases were identified. The phase-1 to phase-3 conversion takes place with the decrease of the THF content and was observed both by PXRD and by hot-stage microscopy (Figure 23). Phase 1 has a honeycomb structure with a cavity diameter of 30 Å, which is occupied by the THF molecules. However, the supramolecular interactions are not strong enough to sustain the assemblies. Hence, when the solvent was removed, the system underwent a spatial reorganization resulting in a new phase with a low content of crystallization solvent. Phase-2 is stable at room temperature, and it could be transformed in phase-3 heating the system above 110°C.

The design of L^{4CCl} ligands resulted in a more pronounced sigma hole (see Section 2.4.5), and more robust XB interactions could be formed in this case.

In conclusion, the studied systems have expanded the panorama of possible supramolecular synthons involving XBs, for the construction of supramolecular architectures.

Chapter 3

3. Phosphine oxide porous organic polymers

In the last decade functional materials and in particular porous materials have been investigated due to their wide range of applications such as catalysis, gas storage and gas adsorption. Their properties are usually determined by their chemical functions and structure but also by their large accessible surface area and the size, shape, and distribution of their inner pores. In this chapter, we focused our interest in the preparation of a series of phosphorus-based porous organic polymers (POPs) using different synthetic methods. The inclusion of the phosphorous atom had the scope to introduce a chemical functionality that could capture specific metal ions. Different types of Friedel-Craft polymerization were employed, using two Lewis acid catalysts: $FeCl_3$ and $AlCl_3$, yielding six different knitted aromatic polymers. $AlCl_3$-POPs displayed low surface area (100-200 m^2/g) with high microporosity. On the other hand, $FeCl_3$-POPs exhibited higher surface area (400-600 m^2/g) with both mesoporosity and microporosity. Post-synthetic modification allowed the impregnation of polymers with metals as cobalt(II), nickel(II), iron(II) and molibedenum (III). Finally, the electrochemical properties of the functionalized POPs were characterized to explore the possibility of future applications in the field of hydrogen evolution reaction (HER) catalysis.

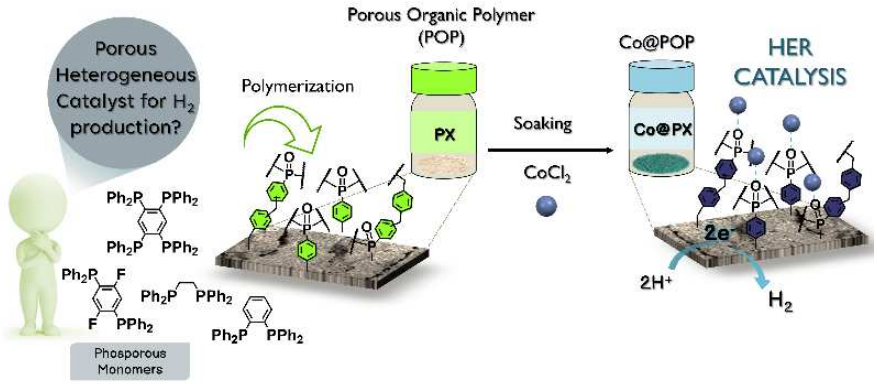

3.1 Introduction

3.1.1 Porous Organic Frameworks

The main families of amorphous porous organic polymers (POPs) are hyper-cross-linked polymers (HCPs), porous aromatic frameworks (PAFs), polymers of intrinsic microporosity (PIMs) and conjugated microporous polymers (CMPs). Classification of amorphous POPs is quite subjective and usually it depends on the perspective of the authors. Generally, they are all synthesized from rigid aromatic monomers and linkers and have an amorphous disordered structure which can be both porous and non-porous depending strongly on the synthetic conditions performed. To obtain high microporosity, angled and rigid molecules should be used as monomers, and additionally, it is necessary to avoid that side chains in the structure block the pores, for example with using too conformationally flexible monomers. In the next table are depicted the adsorption properties and the main applications of these families of POFs.

Table 2. Outlook of POFs adsorption properties and their main applications in chemistry.

Polymers	BET Surface area (m^2/g)	Pore Size (Å)	Applications
CMPs	522-1018	10 - 50	Gas storage, photoconductors, sensors, batteries, phototherapy.
PIMs	450-1760	5 - 15	Gas storage, catalysis, gas permeation.
HCPs	600-2090	10 - 50	Gas storage, adsorption, water harvesting, catalysis.
PAFs	851-6461	5 - 50	Gas storage, gas separation, molecular rotors, photocatalysis, sensors.

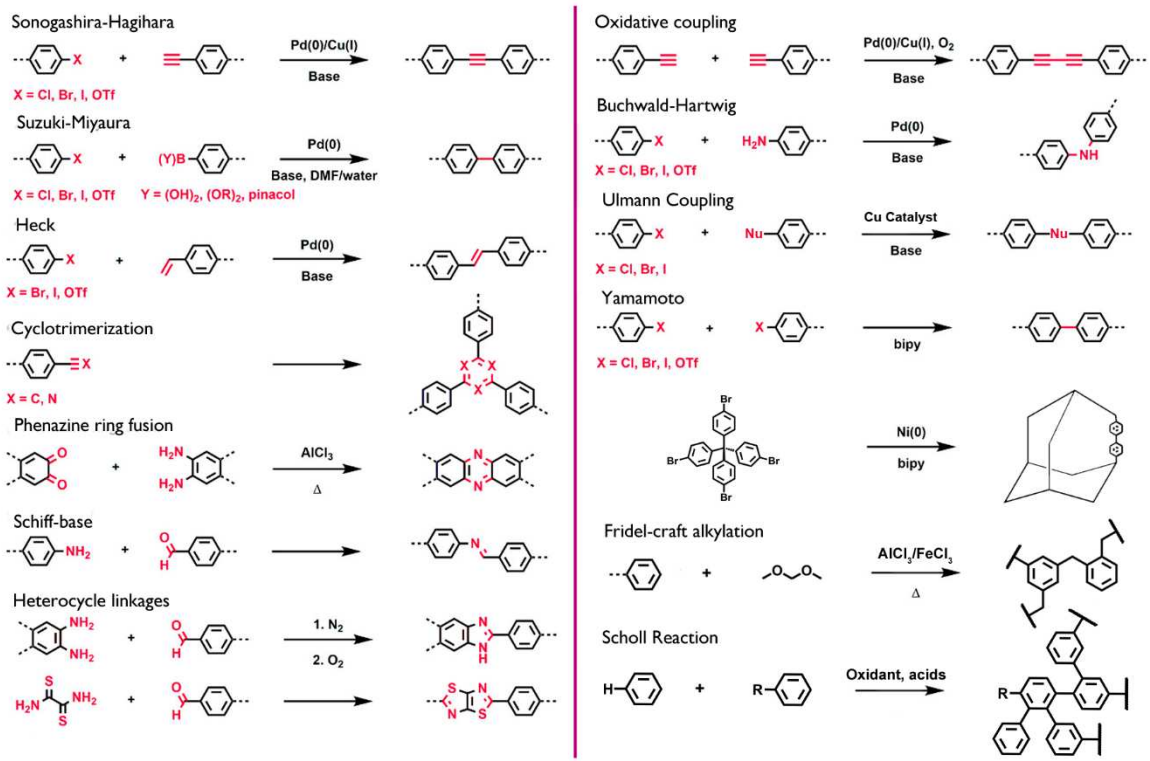

Figure 31. Overview of the synthetic metodologies used for synthetized POFs.

Herein we illustrated the main features of these families of POPs:

1. Coniugated mycroporous polymers

Coniugated mycroporous polymers (CMPs) have a π-conjugated structure built from C-C coupling reaction as Sonogashira, Suzuki or Heck type (Figure 31). CMPs are usually characterized by permanent microporosity due to their conjugated π structure, low solubility, and high conductivity (Figure 32). The synthetic diversity available results in a wide range of amorphous materials with extremely diverse functionality that have a lot of applications such as energy storage and adsorption, chemosensors, heterogeneous catalysis and phototherapy.[106]

Microporous poly(aryleneethynylene) network (CMP-1) was the first example of CMP synthetized in 2007 by J.M. Lee and A. Cooper.[107] It possesses a BET surface area up to 834 m^2/g, and it was formed by Sonogashira-Hagihara cross-coupling.

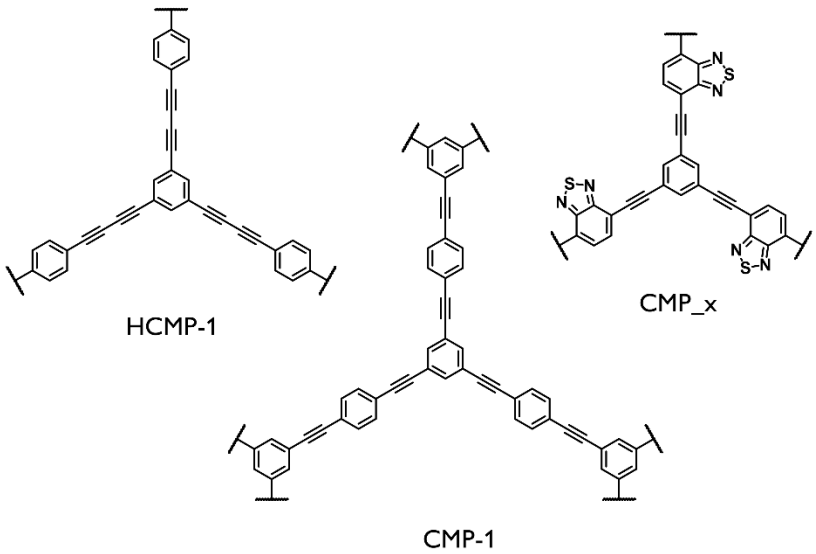

Figure 32. Some examples of CMPs.

2. Porous Aromatic Frameworks

Porous aromatic frameworks (PAFs) is a class of POPs, closely related to CMPs that are formed using similar coupling reactions, but PAFs do not possess extended π-conjugation because they are mainly linked by tetrahedral tetraphenylmethane nodes to build 3D porous structure. Monomers used for PAFs synthesis are usually rigid and with a well-defined topology that led to materials with local ordered structure (Figure 33).

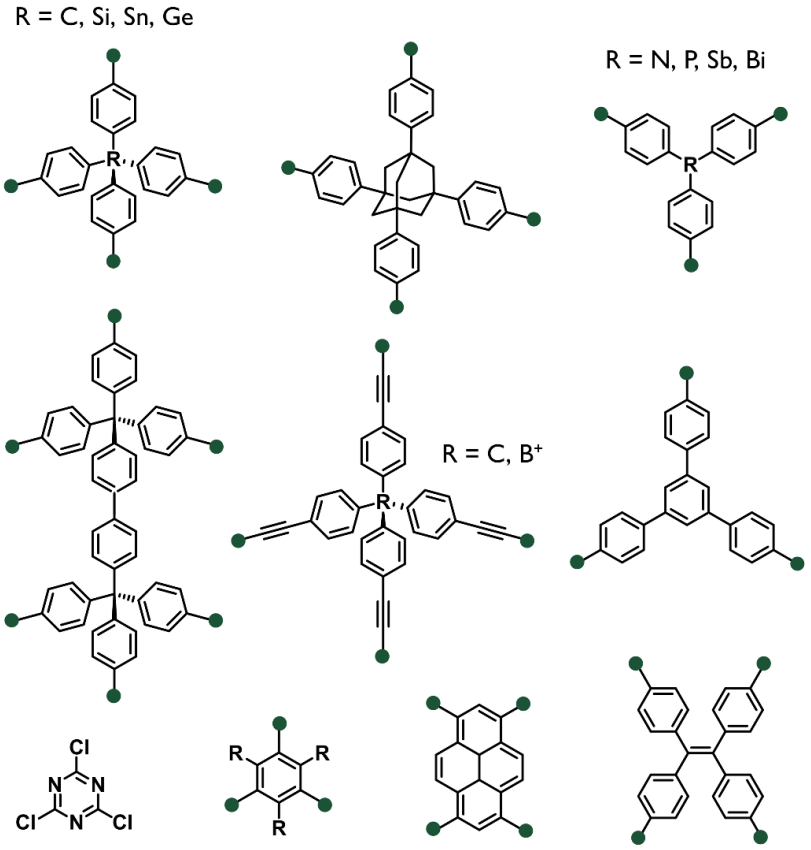

Figure 33. Some of building units used to form PAFs architectures. In green are represented the preferential site for generate the connettivity.[108]

In addition to monomers containing only carbon atoms, precursors with heteroatoms such as P, N, Si, Ge, Sn and Bi, have been used, too.

These specific type of PAFs are called element organic frameworks (EOFs) and were developed by Kaskel's group. As PAFs they show high hydrophobicity and porosity, good thermal and chemical stability. In this case, elements like silicon, bismuth, boron or phosphorus are integrated in the structure and used as connecting units. EOFs can be generated either by multiple lithiation of multidentate bromo-arylic ligands and subsequent lithium-element-exchange or via Suzuki coupling. A well-known example is EOF-2, one of the first species found, which was obtained by the twofold lithiation of 4,4'-dibromobiphenyl followed by the reaction with tetraethylorthosilicate (TEOS).[109,110]

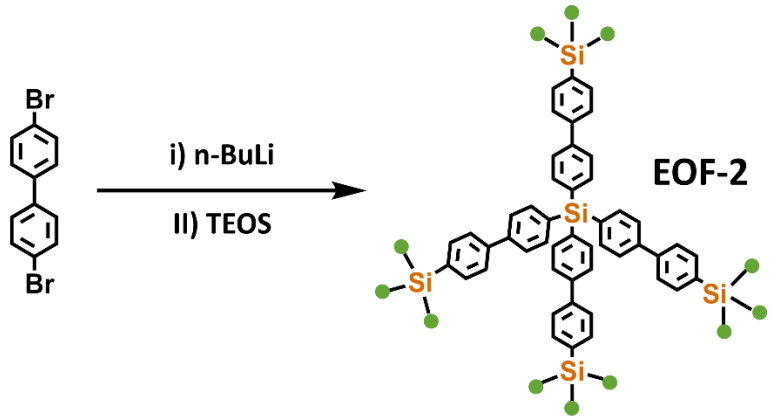

Figure 34. Synthesis of EOF-2.

The main methodologies used to prepare PAFs are irreversible coupling reactions such as Yamamoto, Ullmann, Suzuki and Sonogashira (Figure 31). These reactions create strong C-C covalent bonds, ensuring a stable framework with a microporous/mesoporous structure, resistant to harsh chemical treatments. Powder X-ray diffraction (PXRD) technique pointed out that the coupling reaction leads to the formation of an amorphous framework. Even so, PAFs show quite a regular design because they are not properly the result of random connection of monomers but instead, they ensue from rigid building units with predesigned geometries. PAFs have the higher surface area among POFs (up to 7100 m^2/g), and also possess several distinct advantages. Indeed, they can be synthesized from different building units with distinct shapes and sizes via various coupling reactions thus providing a huge number of

porous frameworks having different surface area, pore volume and pore size. Moreover, PAFs contain aromatic compounds that both ensure the rigidity of the building units and allow enough reactivity for further modification. Finally, they are chemically resistant to harsh acidic, alkaline, and humid environments, crucial to their applications in industry. These characteristics make PAFs very useful for adsorption and gas separation applications, catalysis, sensing, photocatalysis, electrochemistry, and to build stimuli-responsive materials. For example, PAF-1 synthetized by Teng and co-workers in 2009 from tetrakis(4-bromophenyl)methane, have a BET surface area of 5600 m^2/g.[111] PAF-1 have one of the highest values of adsorption for amorphous materials of about 10.7 wt% for H_2 adsorption at 77 K/48 bar and 1300 mg/g (298 K, 40 bar) for carbon dioxide uptakes. Moreover PAF-1 have excellent capacity to adsorb organic pollutants such as benzene and toluene (Figure 35).

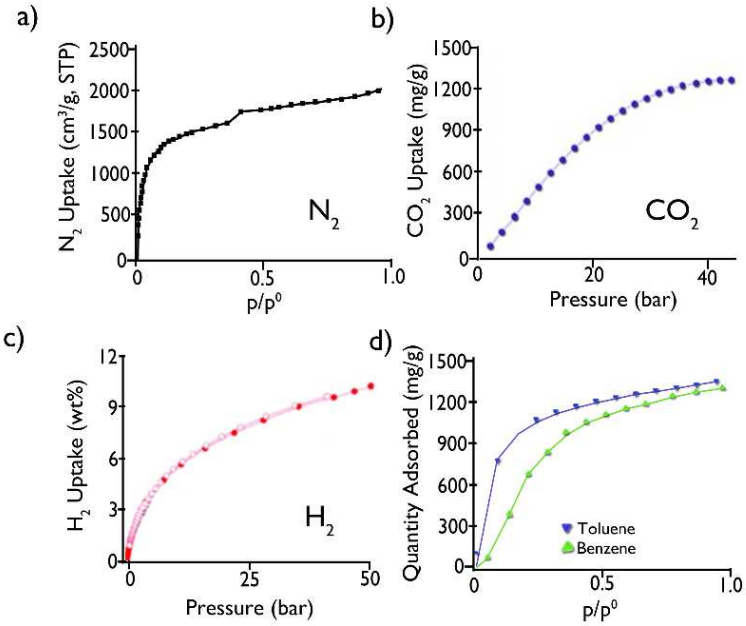

Figure 35. a) N_2 adsorption isotherm of PAF-1 at 77 K. b) High-pressure carbon dioxide adsorption isotherm at 298 K; c) High-pressure hydrogen sorption isotherms at 77 K. d) Toluene and benzene vapor adsorption isotherms at 298 K.[111]

3. Hyper-crosslinked polymers[112,113]

Hyper-crosslinked polymers (HCPs) are grown by subsequent C-H activations of aromatic monomers, using Lewis acid catalyst in Friedel-Craft polymerization reaction. There are two main methodologies to form HCPs:

I. Post-crosslinking of highly solvated polymer chains by Friedel–Crafts alkylation.
II. Knitting of rigid aromatic building blocks using external linkers obtaining knitting aromatic polymers (KAPs).

The first methodology was the oldest, developed in 1970s from Davankov and Tsyurupa to build the so called "Davankov polystyrene resins" or hypercrosslinked polystyrene. These HCPs were obtained by crosslinking of polystyrene chains with chlorinated solvents. The linear styrene was filled with solvent, to separate the chain due to the swelling process. Then catalysts as $SnCl_4$, $FeCl_3$, $AlCl_3$ are used to cross-link the polymer chain and then, after the cross-polymerization, the solvent was removed, resulting in a permanent porous material.

The second methodology is the one-step polymerization of small molecules linked together by elimination of small functional group, usually via Friedel Craft alkylation reaction (see Figure 31).[114] The final properties of the polymer depend on the ratio between monomer, linker, and catalyst and on the synthetic conditions, such as temperature, time of polymerization and solvent choice. This route allows to extend the variety of polymeric structures with a simple method that does not necessarily require highly functionalized precursors. This novel strategy to generate hyper-crosslinked polymer was firstly introduced in 2011 by Tan's group.[115] Aromatic monomers such as benzene, phenol, biphenyl, 1,3,5-triphenylbenzene, methylbenzene and chlorobenzene were crosslinked through methylene bonds using a Lewis acid catalyst and formaldehyde dimethyl acetal (FDA) as external crosslinker.

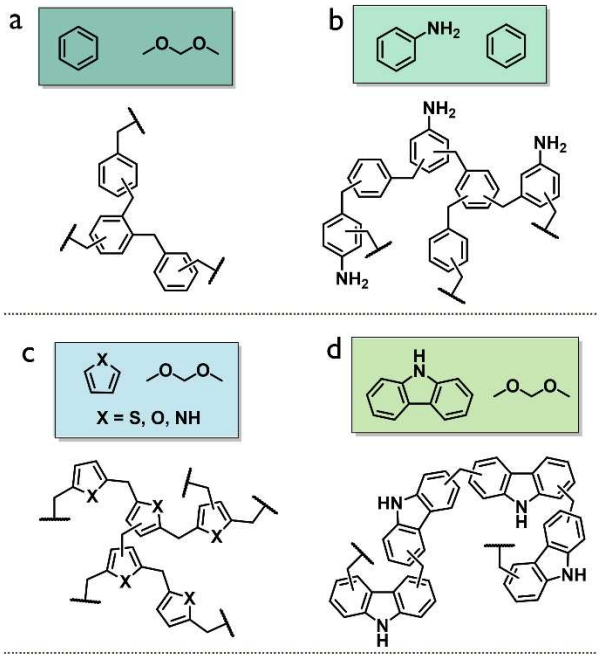

Figure 36. Knitted aromatic polymers and respective monomers. a,b) From benzene-type monomers;[115,116] c,d) From heterocyclic monomers.[117,118]

4. Polymers of intrinsic microporosity[119]

Unlike HCPs and PAFs, polymers with intrinsic microporosity (PIMs), are soluble porous polymers obtained with non-reversible condensation reactions, introduced in 2004 by Budd and Mc Keown.[27,120] Their solubility made PIMs useful to make membrane, coatings and sensors. PIMs have a ladder-like structure which give them an unpacked solid-state arrangement. The design strategy for the synthesis of porous PIMs consists in the use rigid monomers with at least one site of contortion (e.g. spiro-carbon, chiral carbon etc.). If two planar monomers are used instead, non-porous compounds will be obtained.

As illustrated in Figure 37, three distinct types of reactions can be used to obtain PIMs:

⇒ Formation of dibenzodioxin;

⇒ Tröger's base synthesis;

⇒ Imide synthesis.

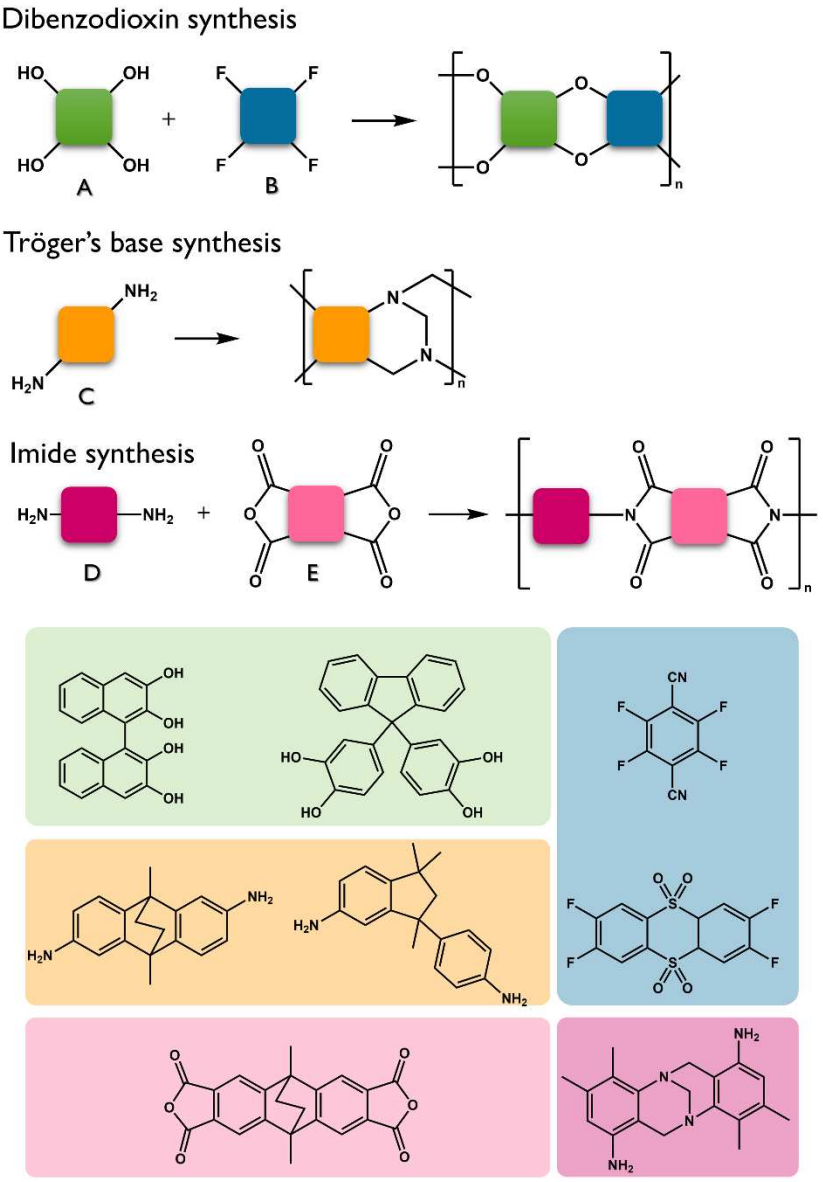

Figure 37. Different synthetic methods to prapare porous PIMs (top). Examples of monomers for the synthesis of PIMs (down).

3.1.2 Single atom catalyst

The design of new highly efficient and selective heterogeneous catalysts, which can work under mild reaction conditions and are derived from less-expensive raw materials is one of the most challenges of the modern era. The catalytic activity and selectivity of a catalyst rely on the accessibility of the active site, the type of interactions with the substrate and the overall structure of the material.[121] A relatively recent route to develop new active catalyst was introduce in 2005 by Thomas *et al*. with the so-called single atom catalysts (SACs) or single-site heterogeneous catalysts (SSHCs). However, the concept of single-site catalyst was already proposed by H.S. Taylor in 1925 with nickel hydrogenation catalyst.[122]

Single site catalyst could be defined as a "catalysts in which all of the active metal species exist as isolated single atoms, or ions stabilized by the support of or by alloying with another metal".[123] This catalytically active center may consist of one or more atoms spatially isolated from one another, which are structurally well-characterized. SACs are different from nanoparticle (NP) catalysts because they do not contain metal–metal bonds and they are usually positively charged. These unique electronic and geometric features bring substantial differences of the type of interactions between SAC and the other components during catalysis, leading to enhance the activity and/or selectivity of the process. The introduction of SACs is particularly attractive because it allows to limit the use of noble metals and enhance stability, activity and selectivity for various reactions as oxidation, water–gas shift and hydrogenation, due to the low-coordination environment of metals as well as the improved strong metal–support interactions. SSHCs can be divided in three main chategories:

1. Only individual isolated ions, atoms or molecular complexes on a support
2. Single site isolated atoms incorporated into a fremeworkframework with high surface area as zeolites, MOFs, PAFs etc.
3. Isolated catalytic molecular entities (or organometallic complexes) are entrapped on a surface or inside a framework.

Apart from the difficulties in the synthesis and stabilization of SACs, their characterization is also not trivial since it is necessary to use expensive and advanced techniques (Figure 38). A first approach is the imaging of single metal atoms dispersed on the supports, with spectroscopy such as EXAFs (X-ray Absorption Near Edge Structure) and XANES (Extended X-ray Absorption Fine Structure). Moreover, sub-angstrom resolution high-angle annular dark-field STEM (HAADF-STEM) has been utilized to directly visualized the SACs surface. Due to its high spatial resolutions, this technique allows the precise determination of the distribution of the single metals and also provide structural information of the support. The main applications of SACs in catalysis concern the "Oxygen Reduction Reaction" (ORR)[124–126] to replace the expensive Pt catalyst, "Hydrogen Evolution Reaction" (HER)[127] using N-doped carbon as support for SACs and other electrochemical reactions.[128] SACs materials are also used in organic synthesis (hydrogenation, oxydation reaction etc.) and in the field of environmental remediation as photocatalyst for CO_2 reduction and removal of pollutants.[129]

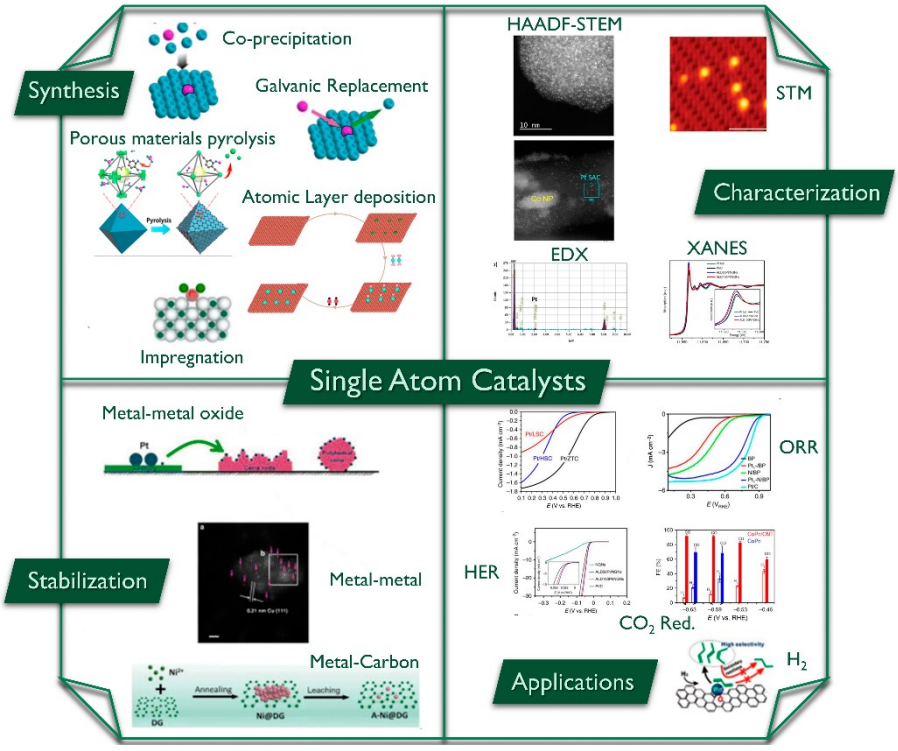

Figure 38. Overview of SACs: Synthesis, characterization techniques, methods of stabilization and some applications.[130,131]

Synthesis of SACs

There are several methods for the synthesis of SACs such as wet and dry impregnation methods, atomic layer deposition (ALD), co-precipitations and carbonization of porous support (Figure 38). A common prerequisite of these methods is to disperse the well-isolated single metal atoms into an appropriate support. Anyway, SAC preparation is still a challenge due to the tendency of metal atoms to preferential form aggregates during synthesis. To our scope, herein it will be given only a brief description of the SACs synthesis from the carbonization of porous materials. This strategy prevents the agglomeration of single atoms by adsorption of suitable metal precursors inside porous materials such as MOFs, COFs, POPs and zeolites. The porous structure acts as template for the synthesis of SACs. Li *et al.*[124] for example reported a pyrolysis of zinc and cobalt MOF at 800°C with the formation of single cobalt atom on N-doped porous carbon. Another research group[132] applied this procedure with UiO-66-NH_2 MOF. This MOF possess amine groups linked to the terephthalic acid linkers that act as Lewis base to stabilize $RuCl_3$. Embedding this ruthenium salts during the synthesis of crystalline MOFs allowed to form a material with confined Ru atoms in the pore of the frameworks. Following, the pyrolysis of the material at 700°C built in situ a porous carbon with ZrO_2 crystals which could easily be etched by adding HF solution. This procedure results in the synthesis of Ru single atoms within the N-doped porous carbon (0.30 wt % of Ru loading). Nitrogen-doped carbon support could also be prepared by other types of porous structures as hypercrosslinked polymers.[133,134] Porous carbons have high surface areas (> 1000 m^2/g) and good chemical, thermal and mechanical stability, together with high conductivity. Their synthesis from HCPs is beneficial due to the tunability of this type of polymers, their easily and inexpensive synthesis and their wide range of applications. The pyrolysis of HCPs allowed to obtain various porous carbon but also enhanced the properties of these materials. For examples Cooper *et al*. synthetized three porous carbons from HCPs derived by the polymerization of thiophene, pyrrole and benzene. The HCPs polymers have BET surface areas of 1382 m^2/g for HCP-Ben, 484 m^2/g for HCP-Th, and 322 m^2/g for HCP-Py. Carbonization process with KOH resulted in increased both the microporosity and the mesoporosity of the materials with higher BET surface areas of 3105 m^2/g, 2682 m^2/g and 4334 m^2/g obtained respectively from HCP-Ben, HCP-Th, HCP-Py using different carbonization conditions.

3.2 Aim of the work

In this studied were synthetized seven different phosphine oxide porous organic polymer (POPs) which can bind active metal centers towards the activation of small molecules. Among that, four POPs, namely $\mathbf{P1}_{Fe}$, $\mathbf{P4}_{Fe}$, $\mathbf{P6}_{Fe}$ and $\mathbf{P7}_{Fe}$ were synthetized using a simple and well-known polymerization reaction as Friedel Craft alkylation that used iron trichloride as Lewis acid. We also explored the possibility to use $AlCl_3$ as Lewis acid catalyst in the polymerization reaction, resulting in $\mathbf{P2}_{Al}$ and $\mathbf{P5}_{Al}$ POPs. Moreover, $\mathbf{P3}_{Li}$ polymer was generated by lithiation of bromoarylic monomer and the following polymerization with PCl_3 to generate a more ordered structure with amorphous nature. The materials were characterized by thermal methods and with solid state NMR (^{1}H, ^{13}C, ^{31}P) and N_2 adsorption isotherms at 77 K were measured to evaluate their porous architecture. Transition metals were also loaded in the seven polymers with the aim to design a heterogeneous catalyst which can potentially have activity towards electrochemical reactions as hydrogen evolution reaction (HER) in more enviromentally benign conditions (pH=7). Furthermore, the metallated M@POPs were also used to synthetized single atom catalysts through pyrolysis at high temperature as an easy way to obtaine more active catalysts and enhanced the properties of this porous materials such as their conductivity and robustness.

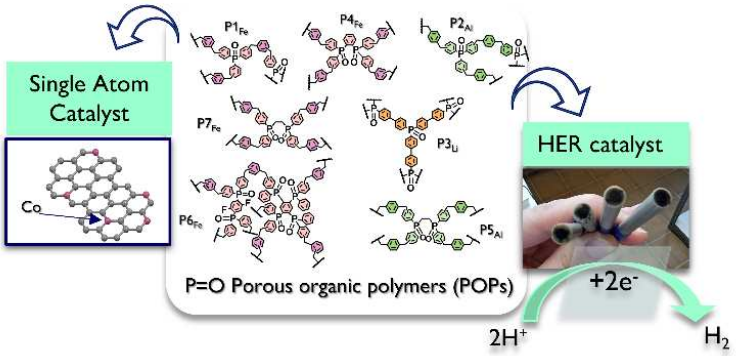

3.3 Experimental Section

3.3.1 General remarks

All commercially available reagents and solvents were used without further purification. Anhydrous solvents were dried and stored over molecular sieves (3 Å) after activation (250°C, 24 hours). Reactions performed under an inert atmosphere (N_2) were carried out using standard Schlenk glassware. Flash column chromatography was performed using silica gel (230-400 mesh). Anhydrous iron (III) chloride and anhydrous aluminium (III) chloride were purchased from Sigma Aldrich and stored in glove box under nitrogen. Triphenylphosphine (TPP), 1,2-bis(diphenylphosphaneyl)ethane (DPPE), and 1,2-bis(diphenylphosphaneyl)benzene (DPPB) are commercially avaiable and were used as received.

NMR Experiments: NMR experiments were performed on a Brüker Avance 400 MHz instruments or JEOL 600 MHz ECZ600R instrument at 298 K. Chemical shifts are expressed in ppm relative to tetramethylsilane, using the solvent residual peak of $CDCl_3$ (δH 7.26, δC 77.00) as a reference standard.

Solid State NMR: ^{1}H, ^{13}C, ^{31}P and ^{19}F solid-state NMR experiments were carried out with a Bruker Avance 300 instrument operating at a static field of 7.04 T equipped with a 4 mm double resonance MAS probe and high-power amplifiers (1 kW). ^{1}H-MAS NMR spectra (single-pulse excitation SPE) were performed at a spinning speed of 12.5 kHz using a recycle delay of 20 s. The ^{1}H chemical shift was referenced to adamantane.^{13}C-MAS NMR spectra (single-pulse excitation SPE) were performed at a spinning speed of 12.5 kHz using a recycle delay of 60 s.$^{13}C\{^{1}H\}$ ramped-amplitude Cross Polarization (CP) experiments were performed at a spinning speed of 12.5 kHz using a contact time of 2 ms and 0.05 ms and recycle delay of 5 s. The 90° pulse for proton was 2.5 µs. Crystalline polyethylene was taken as an external reference at 32.8 ppm from TMS. Quantitative solid-state $^{31}P\{^{1}H\}$ ramped-amplitude CP experiments were performed at a spinning speed of 12.5 kHz using a recycle delay of 5 s and contact time of 8.5 ms. $\mathbf{P6_{Fe}}$ ^{19}F-MAS NMR spectrum was performed at a spinning speed of 12.5 kHz using a recycle delay of 20 s. The ^{19}F chemical shift was referenced to NaF. The 90° pulse for fluorine was 2.5 µs. Phase-modulated

Lee−Goldburg (PMLG) heteronuclear ^{1}H-^{13}C correlation (HETCOR) experiments coupled with fast magic angle spinning allowed the recording of the 2D spectra with a high resolution in both hydrogen and carbon dimensions. Narrow hydrogen resonances, with line widths on the order of 1−2 ppm, were obtained with homonuclear decoupling during t1; this resolution permits a sufficiently accurate determination of the proton species in the system. The two dimensional ^{1}H - ^{13}C PMLG HETCOR spectra were run with an LG period of 18.9 μs. The efficient transfer of magnetization to the carbon nuclei was performed by applying the RAMP-CP sequence. Quadrature detection in t1 was achieved by the time proportional phase increments method (TPPI). The carbon signals were acquired during t2 under proton decoupling by applying the two-pulse phase modulation scheme (TPPM). The 2D ^{1}H-^{13}C PMLG HETCOR NMR spectrum of $\mathbf{P4_{Fe}}$ were conducted at 298 K under magic angle spinning (MAS) conditions at 12.5 kHz with a contact time of 2 ms.

Gas adsorption measurements: N_2 adsorption isotherms at 77 K were collected on a sorption analyzer Micromeritics® ASAP 2020. The polymer samples were treated overnight at 100 °C under high vacuum before adsorption experiments ($p < 5$ μbar). Surface area were calculated from the N_2 adsorption isotherm at 77 K using the data in the pressure range $p/p°$ from 0.015 to 0.1, according to the Brunauer-Emmett-Teller (BET) and Langmuir models. Total pore volume was calculated from the N_2 adsorption isotherms at 77 K by the NLDFT method with the carbon slit pore model up to $p/p°$ 0.98.

Scanning electron microscopy (SEM): SEM experiments were performed using an ESEM instrument Quanta 250 FEG (FEI, Hillsboro, OR) equipped with an energy-dispersive spectrometer (EDS) for X-ray microanalysis (Bruker Nano GmbH, Berlin, Germany). The EDS is equipped with a QUANTAX XFlash® 6 | 30 detector with energy resolution ≤ 126 eV FWHM at Mnkα. The spectra were collected and analysed using ESPRIT 1.9 software (Bruker Nano GmbH).

Inductively coupled plasma atomic emission spectrometry (ICP-AES): ICP analyses were performed with an ULTIMA 2 instrument JOBIN YVON in radial configuration, with a JY 2501 monochromator calibrated against carbon lines. The optical path was continuously purged with nitrogen (2 L/min). Samples of the functionalized polymers were dissolved in 2 mL of a mixture of HNO_3 65% and H_2O_2 30% and then heated by microwave irradiation (Milestone,

MLS-1200 MEGA, equipped with TFM inner vessels) using the conditions reported in the following table:

Step	Time (min)	Power (W)
1	2.00	250
2	2.00	0
3	6.00	250
4	5.00	400
5	5.00	650

Calibration was performed with standard solutions 10% of HNO_3 on six different metal concentration levels, ranging from 0.5 mg/L to 100 mg/L. No significant spectral interferences were detected. Data were acquired by considering the following emission lines: Co 228.616 nm, Fe 238.204 nm, Mo 202.030 nm. Data acquisition and processing were performed using the ICP JY v 5.4.2 software (Jobin Yvon).

Single crystal X-ray diffraction (SCXRD): Data collection for **DFDPPB** was performed at 200 K with a Bruker D8 diffractometer equipped with Photon II area detector, using a CuKα microfocus radiation source (λ = 1.54184). The data collection strategy covered the sphere of reciprocal space. Absorption corrections were applied using the program SADABS.[90] The structure was solved with the SHELXT code.[91] Fourier analysis and refinement were performed by the full-matrix least-squares methods based on F2 using SHELXL-2014,[92] implemented in Olex2.[93] All the non-H atoms were refined with anisotropic displacement parameters. The CCDC code for DFDPPB is 2100398.

Other Measurements: Thermogravimetric analysis was performed with a PerkinElmer TGA 8000, heating the frameworks (0.5-3 mg) from 30 to 600/800 °C in atmospheric pressure, with a T-ramp of 5°C min^{-1} under oxygen flux (30 mL min^{-1}). Infrared (IR) spectra were obtained with a Perkin Helmer Spectrum Two FT-IR spectrometer (diamond crystal, in ATR mode) in the 4000-400 cm^{-1} interval at room temperature.

Electrochemical measurements: Electrochemical measurements were performed using an electrochemical workstation (Metrohm-Autolab potentiostat/galvanostat, PGSTAT100N) with a standard three-electrode setup, with Ag/AgCl (in 3.5 M KCl solution) as the reference electrode, a platinum plate as the counter electrode, and a glassy carbon electrode (GC, 3 mm in

diameter) coated with the as-prepared catalysts as the working electrode. All the measurements were carried out in 0.1 M phosphate buffer (pH 6.93),and conducted in an argon-saturated solution at ambient temperature. In a typical experiment, 5 mg of target material and 5 mg of carbon black powder (Vulcan XC 72R) were dispersed in 950 µL of isopropanol and 50 µL of Nafion solution (5 wt %). The mixture was vigorously sonicated for about 1h to form a "homogeneous" ink suspension. The obtained ink (5 µL) was drop-casted onto a glassy carbon electrode (3 mm diameter, mass loading of ~90 µg cm^{-2}), previously polished with diamond paste, sonicated in water for 10 mins, washed with acetone and oven-dried (Figure S1).

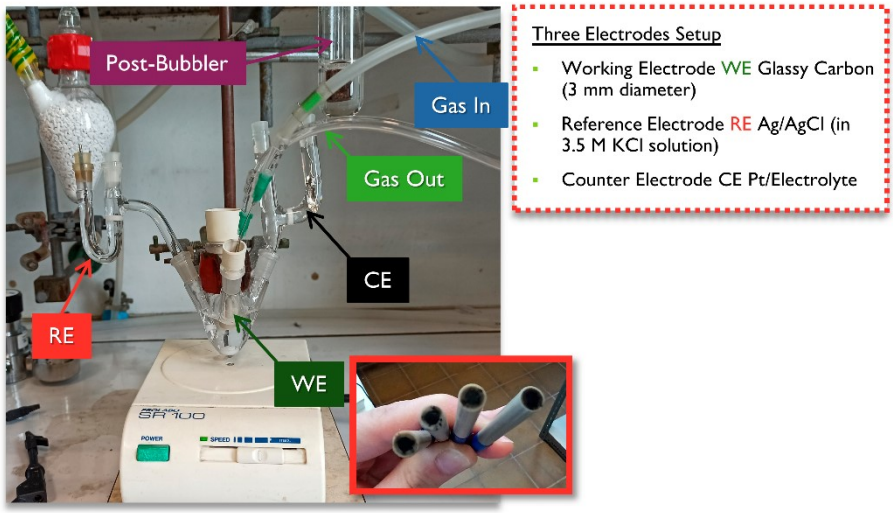

Figure S1. Experimental setup for LSV characterizations. In the inset are pictured glassy carbon electrodes functionalized with POPs inks.

All the measurements were referred to the reversible hydrogen electrode (RHE) by using the following equation:

$$E(RHE) = E(Ag/AgCl) + E_0(Ag/AgCl) + 0.059\ V \times pH$$

Each newly prepared electrode was first stabilized by cyclic voltammetry (CV) between 0 V and -1.18 V vs RHE at a scan rate of 50 $mV \cdot s^{-1}$ until the CV curves remain roughly stable (10 cycles). After this step, linear sweep voltammetry (LSV) experiments were carried out at a scan rate of 5 mV s^{-1} in the same potential window. The linear portions of the Tafel plots (i.e. overpotential vs.

log(|j|) plot), as derived from iR-corrected LSV curves, were analysed by the fitting Tafel equation:

$$\eta = b*\log(|j|) + A$$

where j is the current density ($mA \cdot cm^{-2}$), η is the overpotential vs RHE, b is the Tafel slope and A is the intercept of the linear regression. For H_2 quantification, a custom-made 4-necks cell was used and equipped with rubber septa allowing for the introduction of the three electrodes as well as gas inlet and outlet tubing. The counter electrode (Pt) was separated from the working electrode compartment with a glass frit. The free volume of the closed cell after fitting the septa and electrodes was determined (38.0 mL) and the electrolyte (15.0 mL, 0.1 M phosphate buffer) was introduced. The electrolyte was purged with N_2 (10 mL min^{-1}) for 30 min before conditioning the working electrode (3 mm GC, coated with the desired material) as mentioned above. The electrolyte was further purged with N_2 for 5 min before running 8h-long controlled potential electrolysis (CPE) at –0.68 V vs RHE. The quantification of produced H_2 was done using a Perkin Elmer Clarus 580 Gas Chromatograph. CPE were run under constant N_2 purging (5 mL min^{-1}) and automated injections were programmed to sample the composition of the exhausting gas mixture every 2 minutes. The instant production of H_2 could therefore be monitored over time and the total quantity of H_2 produced during the CPE was determined upon integration over the 8h of the experiments.

Pyrolysis procedure: carbonization of the synthetized polymers and Co@Px polymers was performed in Nabertherm tube furnace equipped with a quartz tube and a quartz crucible in which ~200 mg of polymers where placed. The system was purged with nitrogen gas flow for 30 minutes prior the analysis, heated to 900°C at a scan rate of 5 °C/min, held at the set temperature for 2 hours and finally gradually cooled to r.t. overnight under N_2.

3.3.2 Synthesis of the monomers

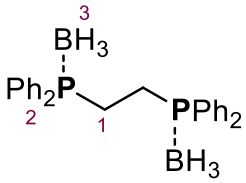

DPPE-BH_3

Synthesis of 1,2-bis(diphenylphosphaneyl)ethane DPPE-BH_3. In a 100 mL three neck round-bottom flask, DPPE (1.00 g, 6.17 mmol, 5 eq.) was solubilized in 15 mL of dry THF, under inert atmosphere. Then a 1.0 M solution of BH_3 in THF (15 mL, 15 mmol, 6 eq.) was added dropwise at 0°C. The mixture was stirred at room temperature overnight, and then ethanol was added dropwise. The solvent was removed in vacuum to afford DPPE-BH_3 as a white solid (0.959 g, 90% yield).

^{1}H NMR (400 MHz, $CDCl_3$) δ (ppm): 7.68 – 7.58 (m, H_2), 7.54 – 7.39 (m, H_2), 2.37 (d, J = 3.3 Hz, H_1), 1.61 – 1.33 (m, H_3); **^{31}P-NMR (162 MHz, $CDCl_3$) δ (ppm):** 18.08 (brs, **P**-BH_3); **IR (cm^{-1}):** 3057wbr, 2919wbr, 2379sbr, 2338mbr, 1483w, 1435s, 1416w, 1179w, 1107w, 1055s, 998w, 754w, 734s, 691s, 594w, 505w, 491w, 468m.

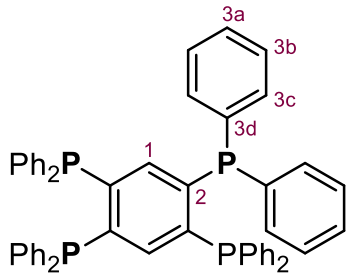

TPPB

Synthesis of 1,2,4,5-tetrakis(diphenylphosphaneyl)benzene TPPB (adapted from Miller *et al.*[135]). 1,2,4,5-tetrafluorobenzene (0.224 mL, 2.00 mmol) was slowly added dropwise to a solution of 18-crown-6 (2.159 g, 8.00 mmol, 4 eq.) and potassium diphenylphosphide ($KPPh_2$, 0.5 M/THF) (20 mL, 10.00 mmol, 5 eq.) in 5 mL of dry THF, under inert atmosphere. The system was stirred at room temperature for 10 min, and then heated under reflux for 48 hours. Then, the THF was removed under vacuum, giving a white sticky solid and the excess phosphide was hydrolysed by heating the system at 70°C for 2 h in degassed ethanol (40 mL). After cooling, the resulting solid was recovered by filtration, and purified by recrystallization from $CHCl_3$: MeOH (5:1 ratio) to yield TPPB as a crystalline white solid (0.932 g, 1.14 mmol, 57% yield). Single crystals of TPPB suitable for SCXRD experiments were obtained from a $CHCl_3$/MeOH mixture directly from the recrystallization step of the crude reaction products.

^{1}H NMR (400 MHz, $CDCl_3$) δ (ppm): 7.15 (m, 8H, H_{3a}), 7.06 (dd, J_1=11.3 Hz, J_2= 4.0 Hz, 16H, H_{3b}), 6.92 (dtt, J_1=7.4 Hz, J_2= 5.0 Hz, J_3= 2.4 Hz, 18H, H_1, H_{3c}); **^{31}P-NMR (162 MHz, $CDCl_3$) δ (ppm):** -14.88 (s, 4P); **^{13}C-NMR (100 MHz, $CDCl_3$) δ (ppm):** 144.48 (m, J= 9 Hz, C_{3d}), 139.98 (pstt, J= 3 Hz, C_2), 136.53 (pstt, J=3 Hz, C_1), 133.84 (t, J = 10.61 Hz, C_{3c}) 128.43 (s, C_{3a}), 128.33 (t, C_{3b}); **IR (cm^{-1}):** 2987wbr, 2901wbr, 1582w, 1478w, 1433w, 1393wbr, 1241wbr, 1066wbr, 908wbr, 740w, 691w.

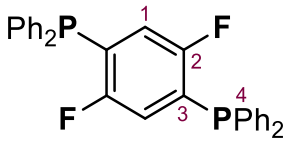

DFDPPB

Synthesis of (2,5-difluoro-1,4-phenylene)bis(diphenylphosphane) DFDPPB (adapted from Miller *et al.*[135]). 1,2,4,5-tetrafluorobenzene (0.440 mL, 3.93 mmol) was added dropwise to a solution of potassium diphenylphosphide ($KPPh_2$) 0.5 M in THF (16 mL, 8.25 mmol, 2.1 eq.) under inert atmosphere. The system was stirred at room temperature for 1 h, and then heated under reflux overnight. Then, the THF was removed under vacuum, which gave a sticky white solid and the excess phosphide was hydrolysed by heating the system at 70°C for 4 h in degassed methanol (30 mL). After cooling, the white solid obtained was recovered by filtration, and purified by recrystallization from $CHCl_3$: MeOH (5:1 ratio) to yield DFDPPB as a crystalline white solid (0.924 g, 3.93 mmol, 49 % yield). Single crystals of DFDPPB suitable for SCXRD experiments were obtained from a $CHCl_3$: MeOH mixture directly from the recrystallization step of the crude reaction products.

^{1}H NMR (400 MHz, $CDCl_3$) δ (ppm): 7.43 – 7.29 (m, 20H, H_4), 6.50 – 6.36 (m, 2H, H_1); **^{31}P-NMR (162 MHz, $CDCl_3$) δ (ppm):** -18.09 – (-18.65) (m, 2P); **^{19}F-NMR (565 MHz, $CDCl_3$) δ (ppm):** 18.04 (dp, J = 48.8, 6.7 Hz).

3.3.3 Synthesis of the frameworks

The polymers **P1**$_{Fe}$[136], **P2**$_{Al}$[137] and **P3**$_{Li}$[110] were prepared according to published procedures.

General procedure C for the synthesis of the Fe-polymers Px$_{Fe}$.

Organophospine monomer (M), formaldehyde dimethyl acetal (FDA), benzene (B), anhydrous $FeCl_3$, and anhydrous 1,2-dichloroethane were mixed together in glove box (N_2). The ratio between the reactants depends on the number of aromatic rings present in the corresponding monomer. If *x* is the number of aromatic rings of M, the *ratio* is *x* **FDA**: *0.5x* **B**: *x* **$FeCl_3$**. The mixture was stirred at 45°C for 24 h and then at 80°C for the required time to complete the polymerization. The polymers were then washed with Soxhlet equipment using MeOH and DCM as washing solvents. The resulting brown powder were then dried at 60°C under vacuum for 48 hours.

General procedure D for the synthesis of the Al-polymers Px$_{Al}$

P5$_{Al}$, was prepared by reacting the organophospine monomer (M, 2.5 mmol), 1,4-bis(bromomethyl)benzene (1.5 eq.), anhydrous $AlCl_3$ (6 eq.), and anhydrous 1,2-dichloroethane (10 mL/mmol) in a schlenk flask under nitrogen atmosphere. The mixture was stirred at 80°C for 72 hours. The polymer was then washed with Soxhlet equipment using MeOH and DCM as washing solvents. The resulting brown powder were then dried at 60°C under vacuum for 48 hours.

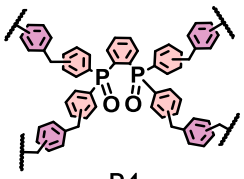

P4$_{Fe}$

Synthesis of P4$_{Fe}$. Polymer **P4$_{Fe}$** was prepared according to the *general procedure C* with 1,2 bis(diphenylphosphino)benzene (0.5 g, 1.12 mmol), $FeCl_3$ (1.00 g, 6.17 mmol, 5 eq.), 18 mL of dry DCE, FDA (0.495 mL, 5.60 mmol, 5 eq.) and benzene (0.200 mL, 2.24 mmol, 2 eq.). The mixture was initially heated under

reflux at 45 °C overnight, and then at 80 °C for 6 days. **P4$_{Fe}$** was obtained as a dark brown powder (197 mg).

IR (cm^{-1}): 2987wbr, 2901wbr, 1601wbr, 1494w, 1436wbr, 1263w, 1188w, 1066wbr, 727w, 724w, 695w.

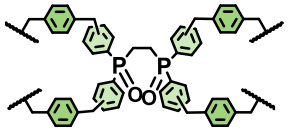

P5$_{Al}$

Synthesis of P5$_{Al}$. Polymer **P5$_{Al}$** was prepared according to the *general procedure D* with 1,2-bis(diphenylphosphino)ethane (1.00 g, 2.51 mmol), $AlCl_3$ (2.10 g, 15.06 mmol, 6 eq.), 25 mL of dry DCE, and 1,4-bis(bromomethyl)benzene (0.996 g, 3.76 mmol, 1.5 eq.) yielding **P5$_{Al}$** as brown powder (526 mg).

IR (cm^{-1}): 3342wbr, 2908wbr, 1608wbr, 1436w, 1375w, 1237w, 1162w, 1027w, 877w, 740w, 695w.

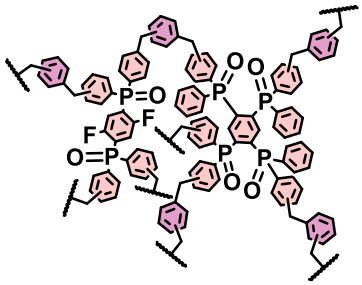

P6$_{Fe}$

Synthesis of P6$_{Fe}$. Polymer **P6$_{Fe}$** was prepared according to the *general procedure C* with TPPB (0.606 g, 0.744 mmol), DFPPB (0.294 g, 0.610 mmol), anhydrous $FeCl_3$ (2.32 g, 14.3 mmol, 12.9 eq.), 16 mL of dry DCE, FDA (1.24 mL, 14.0 mmol, 12.7 eq.), benzene (0.556 mL, 6.22 mmol, 5.6 eq.). The mixture was initially heated under reflux at 45 °C overnight, and then at 80 °C for 6 days. **P6$_{Fe}$** was obtained as a dark brown powder (647 mg).

IR (cm^{-1}): 2987wbr, 2901wbr, 1436wbr, 1406wbr, 1337wbr, 1250wbr, 1229w, 1075w, 1066w, 1056wbr, 894wbr, 692w.

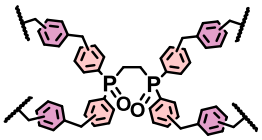

$P7_{Fe}$

Synthesis of $P7_{Fe}$. Polymer $P7_{Fe}$ was prepared according to the *general procedure C* with BH_3-dppe (0.850 g, 1.99 mmol), anhydrous $FeCl_3$ (1.67 g, 10.3 mmol, 5.17 eq.), 20 mL of dry DCE, FDA (0.885 mL, 10.0 mmol, 5 eq.) and benzene (0.360 mL, 4.0 mmol, 2 eq.). The resulting mixture was initially heated under reflux at 45 °C overnight, and then at 80 °C for 6 days. $P7_{Fe}$ was obtained as a light brown powder (0.275 g).

IR (cm^{-1}): 3660wbr, 2988mbr, 2901mbr, 1603w, 1494mbr, 1434mbr, 1075mbr, 806w, 735m, 695m, 481mbr.

3.3.4 Functionalization of the frameworks

Functionalization with Co(II): Under inert atmosphere $CoCl_2 \cdot 6H_2O$ (250 mg; 1.05 mmol) in dry THF (6 mL) was added to 40-50 mg of porous polymers **P1-6**, forming a light blue reaction mixture. The system was stirred at r.t. for 48 h then was washed with THF and centrifuged until the supernatant became colourless. The solvent was then discarded, and the solid was dried under vacuum for 4 days.

Functionalization with Fe(II): Under inert atmosphere $FeCl_2 \cdot 4H_2O$ (278 mg; 1.40 mmol) in degassed DMF (7 mL) was added to 40 mg of porous polymers **P1-6**, forming a brown-red reaction mixture. The system was stirred at 80°C for 72 h then was washed with DMF (2x), THF (3x) until the supernatant became colourless. Finally, the brown solid was dried under vacuum for 4 days.

Functionalization with Mo(III): Under argon atmosphere, $MoCl_3(THF)_3$ (50 mg, 120 μmol) was dissolved in 16 mL of anhydrous THF and then 120 mg of polymer **P1, P3** were added. Three cycles of freeze-pump-thaw of 10 min. each were applied to the system. The pink mixture obtained was then stirred at 50 °C overnight. After that time, the reaction mixture was washed with anhydrous THF and centrifuged until the supernatant was colourless. The solvent was removed in glovebox with a syringe and the pink solid obtained was dried under vacuum overnight.

Functionalization with Ni(II): Under inert atmosphere $Ni(NO_3)_2 \cdot 6H_2O$ (800 mg; 2.75 mmol) in degassed acetone (5 mL) was added to 60 mg of porous polymers **Px**. The system was stirred at r.t. for 72 h then was washed with acetone four times until the supernatant became colourless. Finally, the solid was dried under vacuum at 60°C for 3 days.

3.4 Results and discussion

3.4.1 Synthesis

In this study, a series of phosphine oxide porous organic polymers were synthetized and loaded with metals such as cobalt, nickel, iron and molybdenum to obtain hybrid materials with potentially electrocatalytic applications.

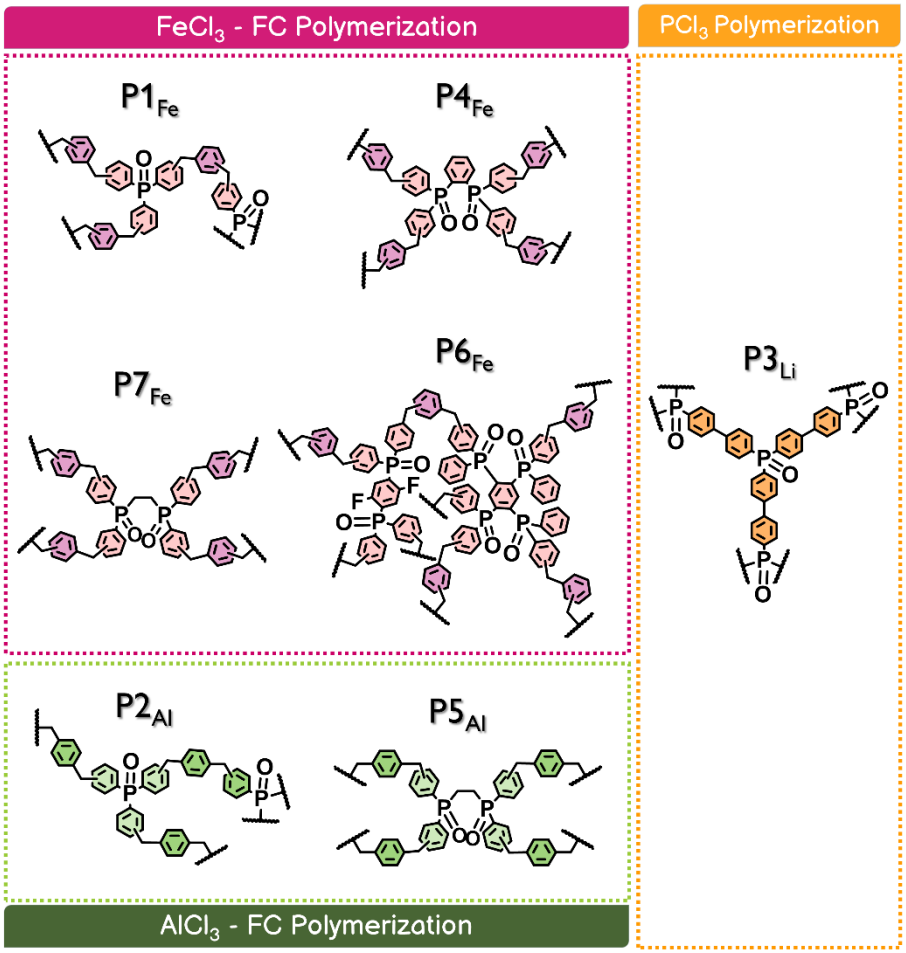

Figure 39. Phosphine-oxide porous organic polymers synthetized via Friedel-Craft polymerization (purple and green box) and via two-step method with PCl_3 (orange box).

Among all possible polymerizations, we have chosen two methods:1) a two-step polymerization with thrichlorophosphine and 2) Friedel-Craft alkylation on phenylphosphines. The former method was previously used by Kaskel and co-workers in 2013 to synthetized element organic frameworks (EOFs).[110] In this case, the framework $\mathbf{P3_{Li}}$ was obtained through the lithiation of 4,4-dibromobiphenyl with butyllithium in anydrous tetrahydrofuran at low temperatures. The following PCl_3 polymerization of the lithiated biphenyl intermediate formed covalent phosphorus–carbon bonds (Figure 40). The stoichiometry between 4,4-dibromobiphenyl, n-BuLi and PCl_3 was 1:2:0.67, respectively, and it allowed to obtain a three-dimensional cross-linked network, which presents defects in variable quantities, mainly due to the presence of residual bromine as a result of the incomplete polymerization. Increasing the equivalents of n-BuLi or PCl_3 does not allowed to make substantial changes to the structure of the framework.

To synthetize $\mathbf{P1_{Fe}}$, $\mathbf{P2_{Al}}$, $\mathbf{P4_{Fe}}$, $\mathbf{P5_{Al}}$ and $\mathbf{P6_{Fe}}$ polymers, Friedel-Craft alkylation was used. This well-known reaction is widely used for the synthesis of highly cross-linked polymers with great thermal and chemical stability, and it is an easily and inexpensive way which could be used also in industry.

Friedel-Crafts reaction requires a phophine aromatic monomer, an external linker as benzene, dimethoxymethane (FDA) or 1,3-bis(bromomethyl)benzene and a Lewis acid (LA) to catalyse the polymerization. In this LA-catalyzed electrophilic aromatic substitution, the interaction between the alkyl halide (our crosslinker) and the Lewis acid activate the arene and could eventually lead to the polyalkylation on the same aromatic ring. The degree of cross-linking could be tuned by modyfing the ratio between the reagents and LA catalyst, but with this method there is no complete control over the final amorphous POPs structure.

In literature, knitting polymers were obtained by Friedel-Craft methods using both aromatic and heteroaromatic monomers. Among aromatic monomers, different types of substituted benzene were used such as phenols, anilines, triphenylmethanol and triphenylamine. As far as phosphorus-based aromatic compounds are concerned, only triphenylphosphine was used by Li[136] and Zhu[137] in 2012 and 2019, respectively. Hence, our interest focused on the possibility to introduce $R_3P{=}O$ structural motif into the robust architecture of the amorphous

framework, using both rigid monodentate (TPP, DFDPPB) and bidentate P-donor monomors (DPPE, DPPB, TPPB). The presence of two donor functions properly oriented allowed the possibility to design a preorganized framework which could chalete a metal center.

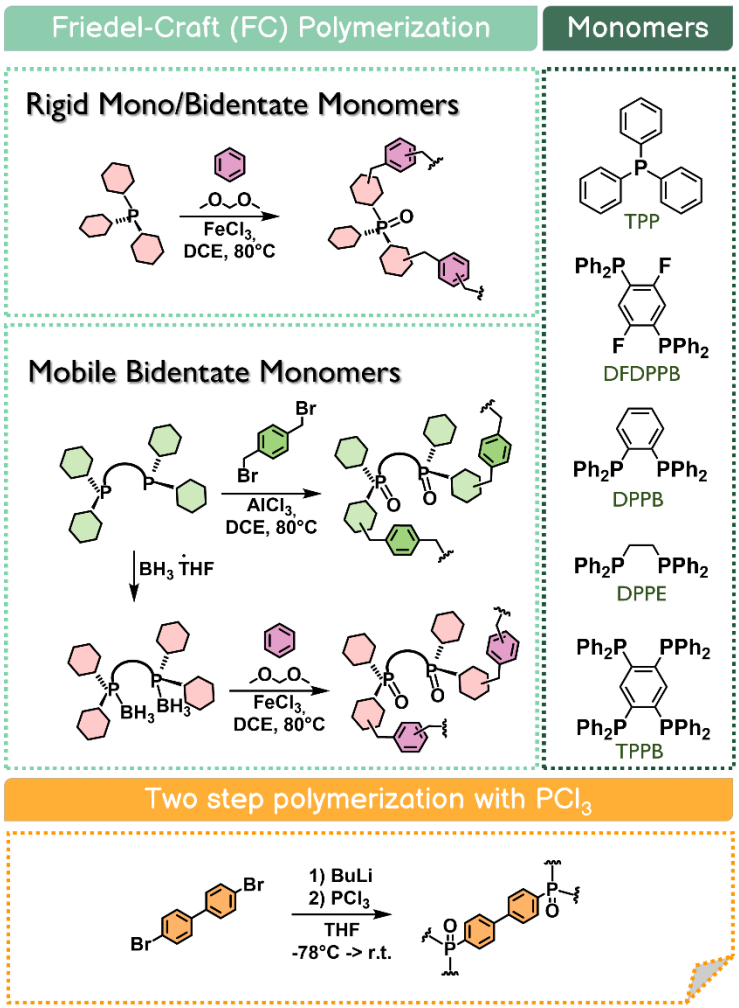

Figure 40. Synthetic methods used in this study: Friedel-Craft polymerizations (light blue box) and two step procedure with PCl_3 (orange box).

As illustrated in Figure 41 two types of acid catalysts were used in the FC polymerization, anydrous $FeCl_3$ and $AlCl_3$. The outcome of the synthesis yielded an extremely similar, yet different, frameworks. $AlCl_3$-POPs such as $P5_{Al}$ displayed low surface area (100-200 m^2/g) with high microporosity. On the other hand, $FeCl_3$-POPs usually exhibited higher surface area (400-600 m^2/g)

with both mesoporosity and microporosity. Moreover, in $P5_{Al}$ the desorption and absorption branches were not overlapping at lower pressures implying a more swellable nature of the $AlCl_3$–based polymers. The extended characterization of these two types of polymers will be discussed in the next section.

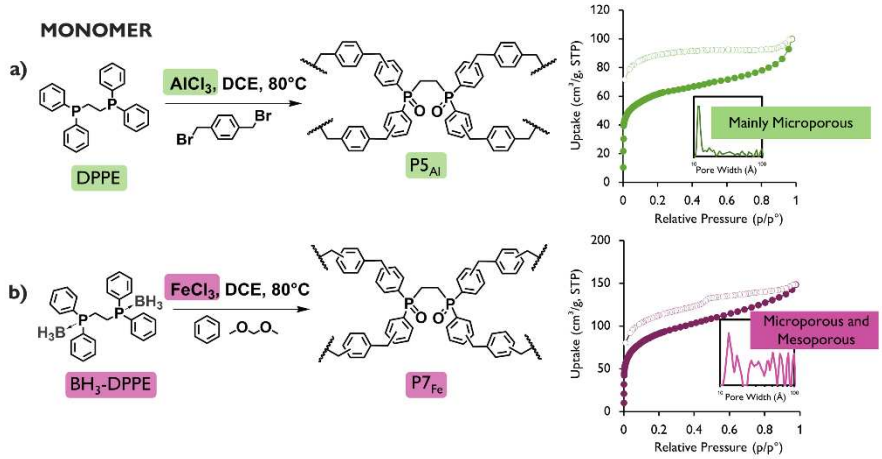

Figure 41. Comparison between the different types of Friedel-Craft polymerization used in this study.

Moreover, the reaction conditions needed to be adapted especially for certain monomers depending on their different nature and the way they were combined with various types of crosslinkers. The central idea common to all the $FeCl_3$ catalysed syntheses was to use a ratio between the catalyst, FDA and benzene (B), which depends on the number of aromatic rings of the monomer M used. If *x* is the number of aromatic rings of M, the *ratio* is approximately *x* **FDA**: *0.5x* **B**: *x* **$FeCl_3$**. In some cases, an excess of $FeCl_3$ was used, mainly because Lewis acids are extremely sensitive to the presence of water in the reaction environment, which leads to the inactivation of the catalyst, lowering the reaction yield (Table 3).

On the other hand, for the syntheses catalysed by $AlCl_3$, the number of catalyst equivalents were doubled or sometimes simply added in excess when compared to the number of the aromatic rings of the monomer, because of $AlCl_3$ lower catalyst activity with respect to $FeCl_3$. Both $\mathbf{P2_{Al}}$ and $\mathbf{P5_{Al}}$ polymerization required six equivalents of LA and 1.5 eq. of cross-linker with respects to 1 eq. of monomer.

Table 3. Summary of the ratio between reagents used to synthetized $FeCl_3$-FC polymers in this work.

KAPs	Number of Aromatic rings in the monomer (*x*)	FDA eq.	Benzene eq.	$FeCl_3$ eq.
P1$_{Fe}$	3	3	1	3
P4$_{Fe}$	5	5	2	5
P6$_{Fe}$	12	17.7	5.6	12.9
P7$_{Fe}$	4	5	2	5.2

It is interesting to note that mobile bidentate monomer such as DPPE does not lead to any crosslinking with $FeCl_3$ catalytic system, and this type of monomers was at first only polymerized with with 1,4-bis(bromomethyl)benzene yielding **P5$_{Al}$** (Figure 40). The protection of phosphorus atom with BH_3 prevented the scavenging effect of phosphine groups and allowed the synthesis of **P7$_{Fe}$** using $FeCl_3$-FC conditions. As outlined in Figure 42 the polymer obtained has the same properties of KAPs derived from iron catalyst and the boron protection is lost during polymerization. Indeed, the FT-IR spectra of **P7$_{Fe}$** does not show the signal around 2300 cm^{-1} due to the presence of B-H stretching vibrations. The deprotection is also confirmed by the shift of ^{31}P-NMR signal from 18 ppm of dppe-BH_3 monomer to 26.4 ppm typical of oxidized phosphorus in the resulting network.

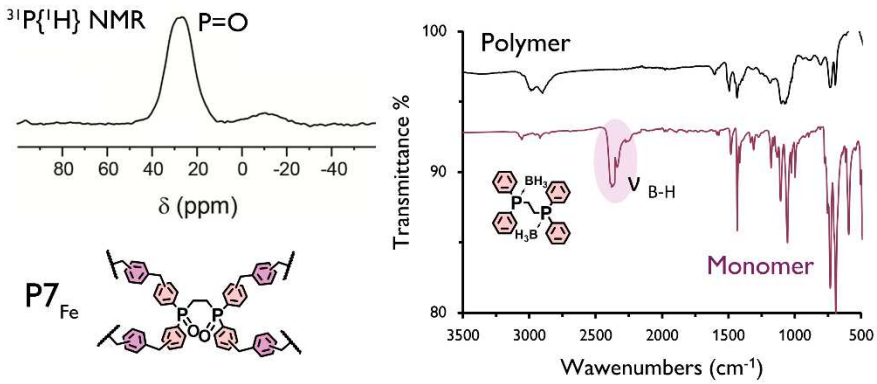

Figure 42. P7$_{Fe}$ characterization: $^{31}P\{^1H\}$ CP MAS spectra performed at a spinning speed of 12.5 kHz and contact time of 8.5 ms; comparison between FT-IR spectra of P7$_{Fe}$ and the corresponding monomer.

Synthesis of $P6_{Fe}$ monomers

All of the above-discussed polymerizations, aside from $\mathbf{P6_{Fe}}$ and $\mathbf{P7_{Fe}}$, were synthetized from commercial monomers. To obtain $\mathbf{P6_{Fe}}$, we synthetized both tetrakis(diphenylphosphino)benzene (TPPB) and (2,5-difluoro-1,4-phenylene)bis(diphenylphosphane) (DFDPPB) by the reaction between the corresponding fluoride precursor and a 0.5 M solution of potassium diphenylphosphine in THF. Poly(diphenylphosphanyl)benzene ligands are versitile ligands which could act as multidentate ligands in coordination chemistry, however they have been barely explored due to their difficult synthesis. Mc Farlane and co-workers were the first to explore their synthesis in 1988 from the fluoroarene derivate, PPh_3, liquid ammonia and sodium metal.[138]

The synthesis of this ligands was later improved by a Miller[135] and Ferrer,[139] in 2008 and 2017 respectively, by using potassium diphenylphosphide ($KPPh_2$) instead of PPh_3, sodium metal and ammonia.

They applied this procedure to other arylphosphine, especially starting from 1,3,5-trifluorobenzene as reagent. On the contrary we focused on TPPB and DFDPPB and how to adjust the reaction conditions to yield one product with respect to the other. To obtain TPPB we started from Miller's conditions: 4.1 equivalents of $KPPh_2$ solution with respect to tetrafluorobenzene, which was refluxed overnight in THF followed by the hydrolysis of the excess of $KPPh_2$ in MeOH for 4 hours. Despite $KPPh_2$ was used in stoichiometric quantity, ^{1}H- and ^{31}P-NMR characterization revealed the presence of two species: the desired tetrasubstituted and the unexpected disubstituted one in 1:0.82 ratio, respectively (Figure 43ii). With this almost equimolar mixture of TPPB and DFDPPB products, the purification step by recrystallization did not allow to isolate the pure products. An attempt was made by using flash chromatography, since thin layer chormatography in DCM-Hx (60:40) hightlighted the precence of two distinctive spots of TPPB ($R_f = 0.75$) and DFDPPB ($R_f = 0.50$). The yield of this purification method was also low due to the partial oxidation of the phosphine in the column. For this reason, we decided to change the reaction conditions, with the aim to obtain only the TPPB product.

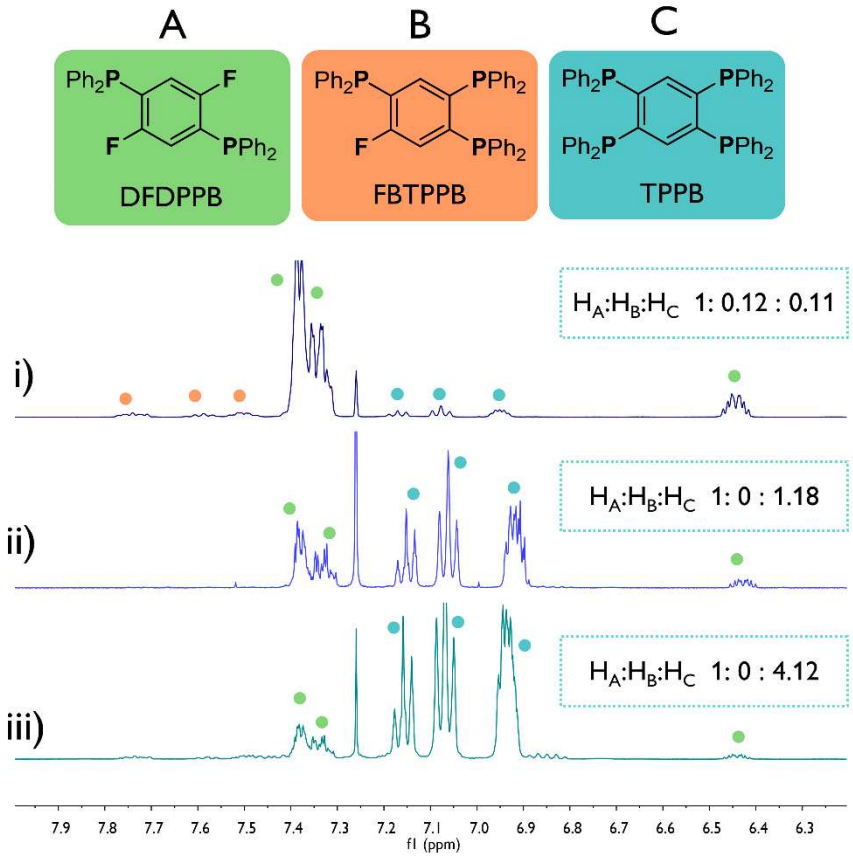

Figure 43. ^{1}H-NMR stacked spectra in $CDCl_3$ (400 MHz) obtained from different reaction conditions: i) 2.1 eq. $KPPh_2$ (0.5 M/THF), 80°C, 24 h. ii) 4.1 eq. $KPPh_2$ (0.5 M/THF), 80°C, 24 h. iii) 5.1 eq. $KPPh_2$ (0.5 M/THF), 80°C, 48 h. Inset represents the ratio between DFDPPB (A) FBTPPB (B), and TPPB (C) products.

We performed the reaction with 5 eq. of $KPPh_2$ at 80 °C for two days instead of 24 hours and we could obtain maily TPPB product as shown in Figure 43iii. The ratio between TDPPB and DFDPPB allowed the isolation of the pure tetrasubstituted products by simple recrystallization in $CHCl_3$/DCM (5:1 ratio). The pure disubstituted product could be obtained by the reaction of tetrafluorobenzene with 2.1 eq. of $KPPh_2$ at 80°C overnight. In this conditions only a low quantity of TPPB and of the trisubstituted product (5-fluorobenzene-1,2,4-triyl)tris(diphenylphosphane) (FBTPPB) were formed (H_A:H_B:H_C 1:0.12:0.11 ratio , see Figure 43i). The isolation of DFDPPB could be easily

performed by the same method used for TPPB, yielding the pure product as white crystalline solid.

Both TPPB and DFDPPB were fully characterized with ^{1}H, ^{13}C, ^{19}F and ^{31}P- NMR spectroscopy (where these data were not present in literature) and single crystals suitable for SCXRD experiments were obtained from a chloroform/methanol mixture (5:1) directly from the recrystallization step of the crude reaction products. TPPB was previously describe by G. Hogarth et *al.*[140] whereas DFDPPB molecular structure is shown in Figure 44.

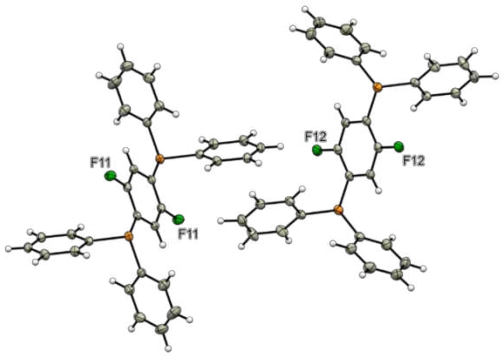

Figure 44. Molecular structure of **P6$_{Fe}$**-monomer (2,5-difluoro-1,4 phenylene)bis(diphenylphosphane), (thermal ellipsoids are drawn at 30% probability level), hydrogen atoms are omitted for clarity. Colour code: C, gray; P, orange; F, green; H, white. The asymmetric unit comprises two half molecules of DFDPPB.

3.4.2 Characterization of POPs

In order to assess whether we managed to obtain porous polymeric structure, the organic polymers Px were characterized through a series of targeted analytical techniques. Before characterizations, all the polymers were washed in Soxhlet equipment using MeOH (24 h) and DCM (24 h) as washing solvent. After washing, the POPs were thermally activated at 60°C for 48 hours under high vacuum ($5 \cdot 10^{-5}$ atm) yielding brown powder for **P1**$_{Fe}$, **P2**$_{Al}$, **P4**$_{Fe}$, **P5**$_{Al}$, **P6**$_{Fe}$, **P7**$_{Fe}$ and off-white powder for **P3**$_{Li}$.

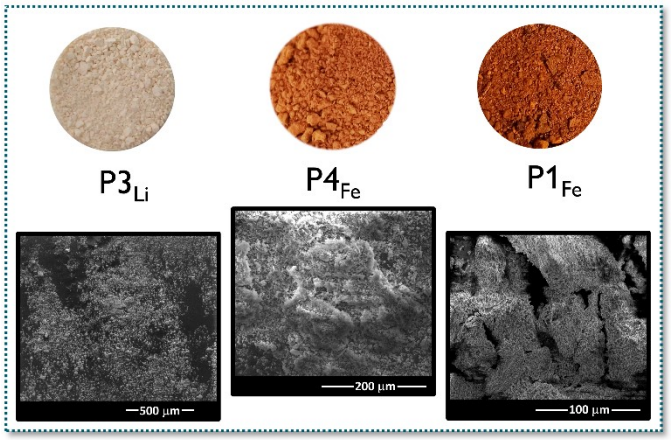

Figure 45. Representative material of synthetized POPs and the corresponding SEM image, showing their amorphous morphology.

Regarding Al-FC-based POPs, the purification step did not remove all of the $AlCl_3$ catalyst and EDX analysis on synthetized polymer highlighted the residual aluminium for both **P2**$_{Al}$ and **P5**$_{Al}$ as shown in Figure B27 and Figure B30, Appendix II. The difficulties in the purification step were mainly due to the poor solubility of this Lewis acid in organic solvents. On the contrary, the Soxhlet extraction managed to remove all the $FeCl_3$ from the Fe-FC-based polymers as confirmed by EDX analysis (Figure B26-B32, Appendix II).

FT-IR

The preliminary investigation was done with infrared spectroscopy (FT-IR), by comparing the IR profile of the starting materials with that of the POPs. In our case, the main difference between polymeric and monomeric structures lied in the diverse extent of their IR absorption bands. Indeed, polymeric bands are

usually broader than the monomeric ones. All the FT-IR spectra of Friedel-Craft KAPs showed adsorption bands corresponding to the stretching of C-H aromatic bond (ca. 3058 cm^{-1}) and C-H bond of the methylene bridge (around 2900 cm^{-1}) (see Figure 47e). Regarding $\mathbf{P3_{Li}}$, the FT-IR is accordance with the data report by Kaskel and co-workers and shows a pure aromatic structure. The IR spectra of the polymers, as well as of the corresponding monomers, were reported in Figure B11-17, Appendix II.

Thermal Analysis

The polymeric behaviour of a compound can be further investigated through thermogravimetric analysis. Polymeric materials can be easily recognized as their massive weight loss occur at higher temperature (around 450-600°C) compared to that of the monomers, due to their reticular structure. All the Friedel-Crafts products have a similar one-step decomposition curve with comparable degradation temperatures ranging from 520°C to 588°C (Table 4, Figure 47c).

Table 4. Weight loss (%) and the corrisponding temperature of degradation for polymer **P1**-**P7**.

Polymer	Weight loss (%)	T_{max} (°C)
$\mathbf{P1_{Fe}}$	5.6	49
	90.4	520
$\mathbf{P2_{Al}}$	14.1	112
	72.8	549
$\mathbf{P3_{Li}}$	7.0	52
	49.1	455
	40.6	637
$\mathbf{P4_{Fe}}$	99.0	538
$\mathbf{P5_{Al}}$	3.4	44
	96.8	534
$\mathbf{P6_{Fe}}$	4.9	92
	90.6	588
$\mathbf{P7_{Fe}}$	1.4	140
	90.8	559

In some cases, is also present a weight loss at low temperature due to the presence of residual solvent entrapped in the porous structure of the polymers, even though it was dried for days under high vacuum. This assumption is also confirmed by EDX analysis on activated polymer (Figure 46).

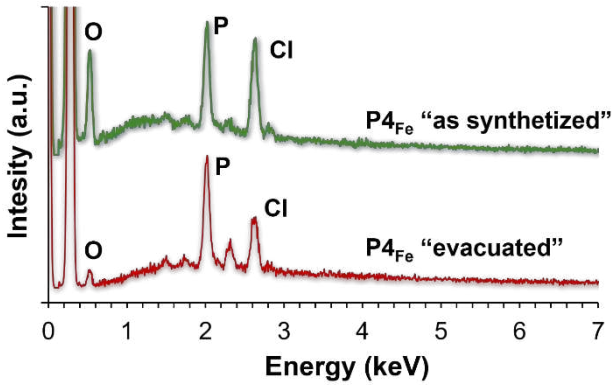

Figure 46. Comparison between EDX of $\mathbf{P4_{Fe}}$ after simple evacuation at r.t. (green) and EDX of $\mathbf{P4_{Fe}}$ treated overnight at 100 °C under high vacuum ($p < 5$ μbar) (red). The chlorine signal due to the presence of residual DCE from synthesis is decreased. The presence of the residual chlorine signal after applying a high vacuum may correspond to the presence of chlorine-containing pendant groups formed during the FC reaction, as previously observed for the polymers described Bracco *et al.*[141] The initial fraction of the chlorine signals is most likely due to solvent trapped in the polymer cavities as a result of non-homogeneous pore size distribution of $\mathbf{P4_{Fe}}$.

$\mathbf{P3_{Li}}$ profile is characterized by a multistage decomposition since the compound experienced a first weight loss (49 %) between 300 and 455 °C and a second weight loss (40%) from 530°C and 637°C (Table 4). These marked differences are most likely be the result of the structural diversity that characterises the two types of polymers. Despite being amorphous as the obtained FC-POPs, $\mathbf{P3_{Li}}$ appears to possess a more ordered structure.

Solid-State NMR characterizations

Monodimensional and 2D NMR spectroscopy were used to determine the structural organization of the synthetized networks. The aromatic nature of the polymers, due to the aromatic rings of the monomeric units, is easily described by both ^{1}H and ^{13}C NMR spectra. Indeed, ^{13}C spectra showed peaks between 110 and 150 ppm, the characteristics region of aromatic carbon signals. The presence of aromatic moieties is also confirmed by ^{1}H signals in the aromatic region around 7 ppm. In $\mathbf{P3_{Li}}$ these types of signals dominated the spectra, encompassing the C-C signal of diphenyl connecting group.[110]

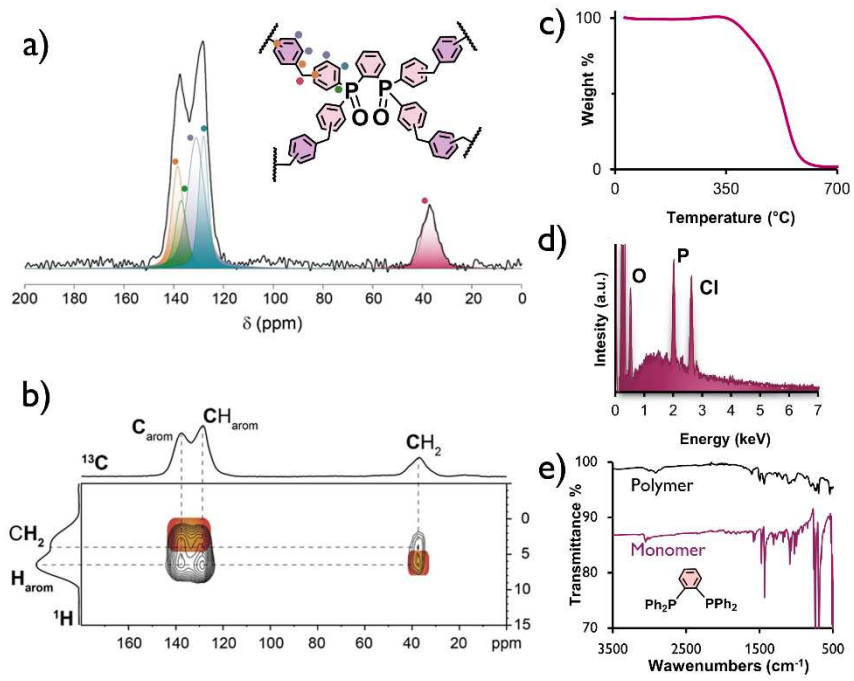

Figure 47. Characterizations of $\mathbf{P4_{Fe}}$ polymer. a) Quantitative $^{13}C\{^{1}H\}$ MAS spectrum performed at a spinning speed of 12.5 kHz and a recycle delay of 60 s. b) 2D ^{1}H-^{13}C PMLG HETCOR NMR spectrum performed at 12.5 kHz and contact time of 2 ms. The space interactions between the aromatic ring and methylene moiety are shown by the cross peaks in red. c) TGA from 25°C to 700°C under oxygen flux with a scan rate of 10°C/min. d) EDX spectrum: chlorine signal from residual DCE solvent. e) FT-IR spectra of the polymer (black) and the corresponding monomer (purple).

For Friedel–Crafts reaction polymers, additional signals were present in the aliphatic region. These signals are mainly ascribed to the bridging methylene group after Friedel-Craft polymerization (δ_C = 37 ppm). The resulting complex pattern was the result of the multiple alkylation of the aromatic rings. The connectivity of methylene groups was also studied by 2D ^{1}H-^{13}C NMR spectra, which highlights the spatial proximity between hydrogen and carbon nuclei. As pointed out in **P4$_{Fe}$** spectra (Figure 47a,b) the aromatic hydrogens of the main network (δ_H = 6.5 ppm) are correlated to the carbons of the methylene groups (δ_C = 37.3 ppm). Additionally, the CH_2 hydrogens (δ_H= 4.0 ppm) are correlated with the aromatic carbons, confirming the knitting of the monomers by the methylene linkers. Regarding $AlCl_3$-FC-POPs (**P2$_{Al}$** and **P5$_{Al}$**), we also observed methylene bridging groups and CH_3 pendants in benzyl position (Figure B7-8, Appendix II).

In ^{13}C-NMR measurements there are also minor alkyl and alkoxy signals (CH_3, CH_2-O and CH_3-O at δ = 16.8-18.7, 56.5 and 73.0 ppm) attributed by pendant groups as already observed in KAPs.[141] At 40-44 ppm, together with ph-CH_2-ph broad signal centered at 37 ppm it is also possible to observe minor signals due to chlorine pendant groups due to the FC polymerization in accordance with EDX spectra of the polymer (see Figure 46).

The ^{31}P solid state NMR spectra confirmed the presence of the P=O moiety, resonating at about 30 ppm. In **P3$_{Li}$**, **P7$_{Fe}$**, and **P6$_{Fe}$** there are also minor peaks at δ=-7.2, -10.5 and -14.8 ppm, respectively, due to some not oxidized aryl phosphorus (Figure B9, Appendix II).
Furthermore, the ^{19}F solid state NMR demonstrates the co-polymerization of both monomers into **P6$_{Fe}$** polymer, showing a fluorine peak due to the DFDPPB monomer in the framework (Figure B10, Appendix II).

Adsorption Measurements

The adsorption properties of the frameworks were investigated by N_2 adsorption isotherms at 77 K, which exhibited a sharp slope in the adsorption branch at very low pressures and a continuous rise at higher pressures. This behaviour reflected the presence of both micro- and meso-pores in the frameworks. The nitrogen physisorption isotherms of the vacuum dried polymers are shown in Figure 48.

The highest surface area was achieved by polymerizing rigid monomers as DPPB in which four aromatic rings are connected to two phosphorus atoms, providing the expansion of the network in all directions. Indeed, $\mathbf{P4_{Fe}}$ displays Langmuir and BET surface areas of 1125 and 990 m^2/g, respectively. If the monomer contained a flexible ethyl group connecting two phosphorus atoms the resulting framework ($\mathbf{P7_{Fe}}$) have low surface area (331 m^2/g), due to the conformational freedom of the building block. High surface area of 640 m^2/g was also obtained in the case of $\mathbf{P1_{Fe}}$ where the monomer PPh_3, with three phenyl rings, is also rigid. It is interesting to point out that a higher number of phenyl rings give rise to frameworks with lower surface area and lower pore capacity respect to $\mathbf{P4_{Fe}}$. Indeed, $\mathbf{P6_{Fe}}$ displays a surface area of about 678 m^2/g as a result of the overcrowded knitting that led to a closed structure. Hysteresis loops were observed between the adsorption and desorption branches. This behaviour was usually observed in soft polymeric materials and it was due to swelling of the network during sorption for capillary condensation in the mesopores.[142]

Regarding POPs derived by aluminium-based FC polymerization, their more disordered structure resulted in a lower surface area of about 220 m^2/g and with higher microporosity. Their low surface area could also be attributed to the residue of catalyst that blocked the pore as pointed out from EDX spectra (see Appendix II, Figure B26-B32).

Together with the adsorption isotherms, we also obtained information about how the structure of the polymer impacted on the pore sizes. We observed that for the same type of linkers (benzene and FDA), the use of the bidentate monomer DPPB provided cavities having a major volume as compared with monodentate monomers as TPP (0.920 cm^3/g for $\mathbf{P4_{Fe}}$ total pore volume vs 0.377 cm^3/g for $\mathbf{P1_{Fe}}$ pore volume). This could be due by the different number

and position of the aromatic rings in the DPPB that allowed the formation of wider openings.

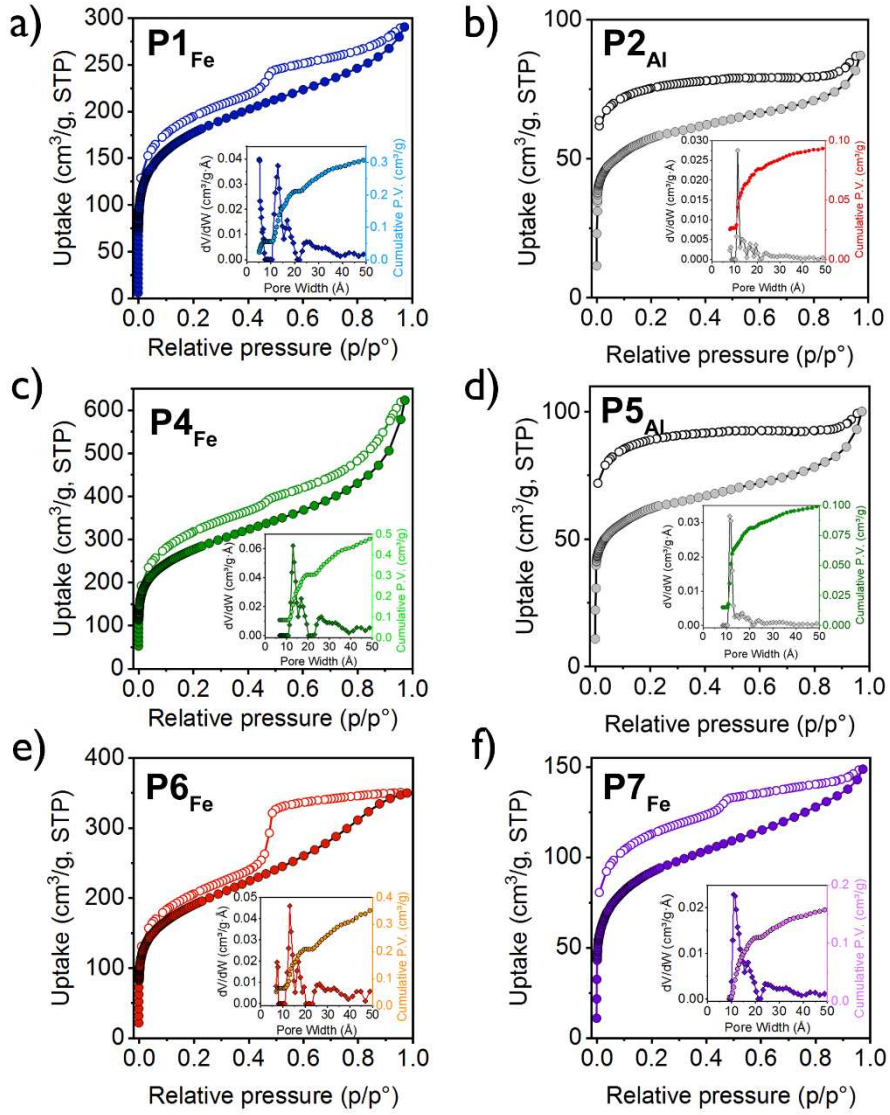

Figure 48. N_2 physisorption isotherms at 77 K (adsorption, ●; desorption, ○) for $\mathbf{P1}_{\mathbf{Fe}}$ (a), $\mathbf{P2}_{\mathbf{Al}}$ (b), $\mathbf{P4}_{\mathbf{Fe}}$ (c), $\mathbf{P5}_{\mathbf{Al}}$ (d), $\mathbf{P6}_{\mathbf{Fe}}$ (e), and $\mathbf{P7}_{\mathbf{Fe}}$ (f). Insets: differential and cumulative pore size distributions between 0 and 50 Å.

3.4.3 Complexation with metal ions

The inclusion of the phosphorus oxide functionalities had the aim to introduce binding sites that could promote the complexation of specific metal ions. Specifically, P=O donor functions are suitable for hard transition metal ions such as first row transition metals or lanthanides.[143–146] Porous organic frameworks have been succesfully applied in the field of catalysis[7,114,136,137] and metal-doped porous organic polymers (M-POPs)[147] (with M = Fe, Co, Ni, Cu, Mn) could be a valid replacement of noble and expensive metals such as Pt, Pd, Au and Ag. Moreover, introducing this type of metal enhance the electrochemical properties and stability compared with simple POPs.[148]

Hence, we started our study focusing on Co(II) ions and we loaded cobalt in the frameworks by soaking for 72 h with $CoCl_2 \cdot 6H_2O$ in THF under nitrogen atmosphere. After this soaking, the coloured solid was isolated through repeated centrifugation and washings with THF until the excess of free metal was completely removed and the supernatant become colourless. The loading of the materials could be easily appreciated by colour change from white to light blue for **Co@P3$_{Li}$** (Figure 49), whereas for FC-based polymers tonality changes were not easily detectable due to their brownish colour (Figure 45).

In order to assess the effective presence of the metals inside the polymers and to determine the metal content, energy dispersive X-ray spectroscopy (EDX) and inductively coupled plasma atomic emission spectroscopy (ICP-AES) were performed. EDX confirmed the presence of cobalt within the phosphorous-based polymers as shown in Figure 49c from the peak of k_α of cobalt and chlorine at 6.92 keV and 2.62 keV, respectively. From ICP analysis the amount of cobalt in the frameworks was about for 4.5 % w/w for **Co@P3$_{Li}$** and between 0.8 % and 4.2 % w/w for the other polymers (Appendix II, Table B3 and B4).

In addition, we investigated the adsorption properties of the functionalized **Co@P3$_{Li}$** sample, to determine if the inclusion of metal ions produced an occlusion of the pore of the network. In Figure 49 are reported the N_2 adsorption isotherm at 77 K of **P3$_{Li}$** (green) and **Co@P3$_{Li}$** (blue). If the native polymer exhibited both micro- and mesoporosity with a notable swellability and a total pore volume of 0.293 cm^3/g, the cobalt functionalized polymer had a lower

surface area and a microporous structure, resulting in a lower total pore volume of about 0.169 cm^3/g. Therefore, the inclusion of the cobalt ions did not lead to an occlusion of the inner cavities, and the materials was still able to adsorbe small molecules which could reach metal centers inside the amorphous network.

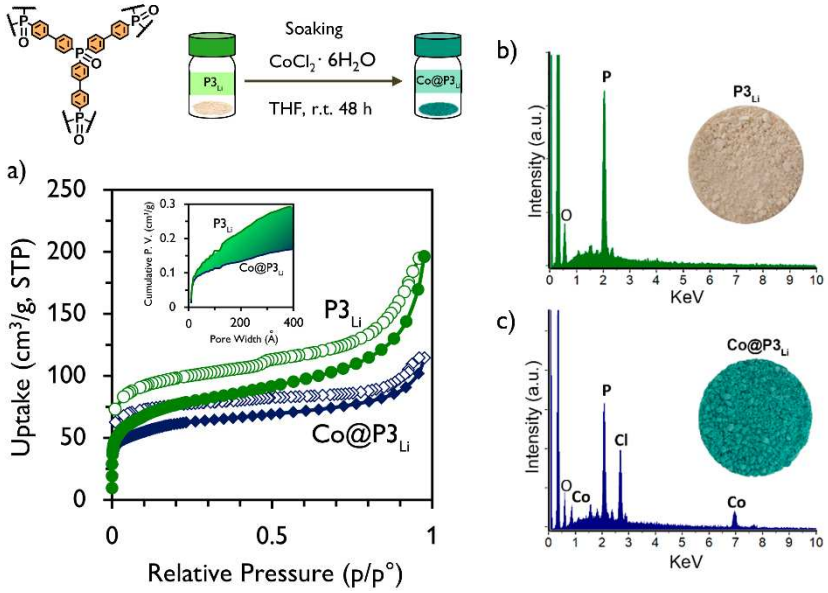

Figure 49. a) N_2 adsorption isotherm at 77 K of $\mathbf{P3_{Li}}$ (green) and $\mathbf{Co@P3_{Li}}$ (blue). Inset: cumulative pore size distributions. b) EDX of $\mathbf{P3_{Li}}$ (green) and c) EDX of $\mathbf{Co@P3_{Li}}$ (blue).

Incorporation of other non-noble transition metals

We also explored the incorporation of other non-noble transition metals for $\mathbf{P3_{Li}}$ polymer. Specifically, we incorporated more abundant metals such as nickel and iron. The choice of the metal precursor was influenced by the solubility of the metal precursors in organic solvents. It was also considered preferable to avoid the use of harmful and high-boiling point solvents, such as DMSO or DMF.

To continue the series of metal chloride salts, we initially used $FeCl_2 \cdot 4H_2O$ precursor to introduce iron in the framework (Figure 50a). In this case we had to use DMF, as soaking solvent at high temperature to improve the solubility and then washing the resulting powder with DMF and THF, until the supernatant became colourless. On the contrary, nickel nitrate in acetone was used as metal

precursor for Ni(II) due to the poor solubility of the chloride salt in other organic solvents (Figure 50b).

It was also interesting to investigate the incorporation of an active metal as molybdenum. This metals and its complexes had important catalityc activity toward nitrogen conversion to ammonia as pointed out in numerous reviews.[149,150] For this reason we chose Mo(III)$Cl_3(THF)_3$ complex as metal precursor. This pink complex was extremely sensible to oxygen and the loading on **P3$_{Li}$** was performed in gloveblox under argon atmosphere at 50°C (Figure 50c). The complexation and the subsequent washing step was done under argon yielding pink amorphous powder of **Mo(III)@P3$_{Li}$**. It was interesting to note that if the material is not stored under inert atmosphere it changes colour from pink to light blue, probably due to the oxidation of Mo(III) ions.

The loading of these metal in **P3$_{Li}$** framework could be observed by the color change from off-white of native polymer to dark yellow for **Ni@P3$_{Li}$**, light brown for **Fe@P3$_{Li}$** and to pink for **Mo(III)@P3$_{Li}$**. EDX and ICP-AES analysis performed on functionalized materials provided the evidence that the materials can be loaded with various metal precursors, and possibly expanding the number of catalytic processes that can be addressed.

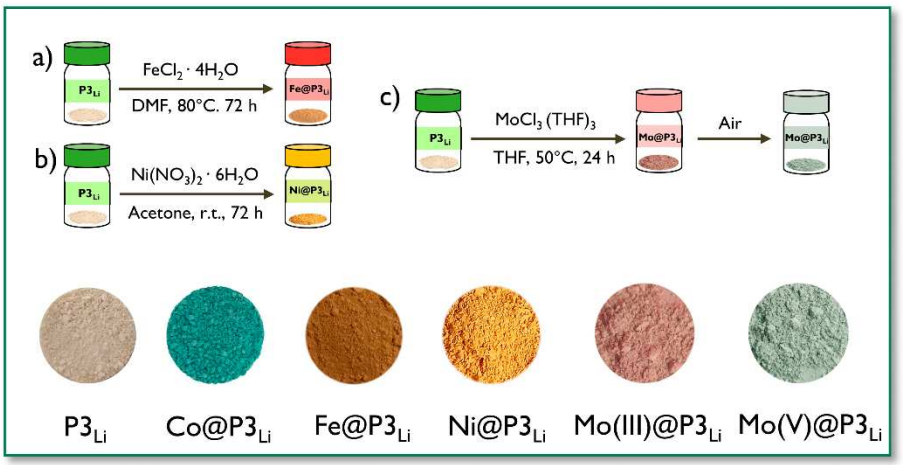

Figure 50. Incorporation of transition metals: a) Fe(II), b) Ni(II) and c) Mo(III). Below are also represented the colored powder of sample **P3$_{Li}$** and corrisponding functionalized **Co@P3$_{Li}$**, **Fe@P3$_{Li}$**, **Ni@P3$_{Li}$**, **Mo(III)@P3$_{Li}$**, **Mo(V)@P3$_{Li}$**.

3.4.4 Electrocatalytic studies

After having confirmed the accomplishment of the applied loading procedure and defined the amount of cobalt, the functionalized **Co@Px** (x = 1, 3, 4, 6) materials, were tested as electrocatalyst for Hydrogen Evolution Reaction (HER), by linear sweep voltammetry (LSV).

The functionalized POPs were deposited on glassy carbon (GC) working electrode (3 mm diameter) via drop casting technique, using an ink, including each target polymers (5 mg), nafion (50 μL) and carbon black (5 mg) in isopropanol (950 μL). LSV performed in aqueous phosphate buffer at neutral pH (from 0 V to -1.18 V vs RHE potential) at 5 mV.s-1 scan rate highlighted a significant increase of current density between ~-0.4 to -0.9 V vs RHE range in the case of $\mathbf{P1}_{Fe}$, $\mathbf{P4}_{Fe}$, $\mathbf{P6}_{Fe}$ and $\mathbf{P3}_{Li}$ derivatives with respect to the metallated materials. (Figure 51, half-wave potentials = -0.62 V for $\mathbf{P3}_{Li}$, -0.75 V for $\mathbf{P1}_{Fe}$, -0.74 V for $\mathbf{P4}_{Fe}$, -0.76 V for $\mathbf{P6}_{Fe}$). This suggests the catalytic HER activity of the cobalt functionalized materials was induced by the metal inside the inner cavities of the frameworks and it could be associated with the reduction of Co(II) to Co(0) nanoparticles. However, a detailed mechanistic study would be required to gain further insights on the nature of the reduced species, which would not be trivial, and this type of study can be addressed in the future to investigate the behavior of these systems and a possible future application.

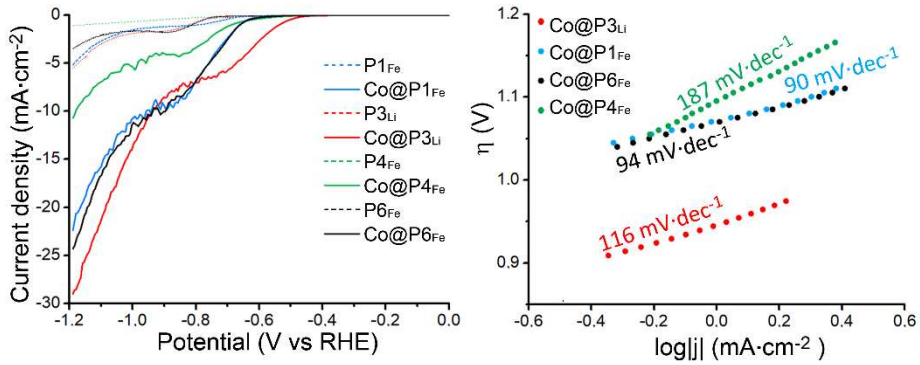

Figure 51. LSV curves of selected **Co@PX** vs **PX** materials (x = 1, 3, 4, 6), and corresponding Tafel plots (linear region, Tafel slopes are indicated).

Furthermore, we found that **Co@Px** materials had generally high overpotentials to reach a current density of 1 $mA \cdot cm^{-2}$, maybe due to low density of catalytic

sites, low electrical conductivity or the low wettability of the samples. For examples the overpotentials for **Co@P4$_{Fe}$** and **Co@P3$_{Li}$** are 0.68 V and 0.53 V, respectively and 0.66 V for **Co@P1$_{Fe}$** and **Co@P6$_{Fe}$**. These data are relatively high related to other HER electrocatalysts working at neutral pH[151,152] and porous materials such as MOFs [54,153]and COFs,[154,155] which however worked under strongly acidic or basic conditions, which are kinetically more favourable (lower ohmic loss and higher ionic concentration) compared to neutral pH conditions. To our knowledge, the only described non-carbonized POP-based material for HER electrocatalysis contained highly active platinum nanoparticles. [156]

To explore the inherent catalytic mechanism of the electrocatalyst, Tafel plots of the catalysts were fitted based on Tafel equation and Tafel slopes. An inherent index of the rate-limiting step of HER, were determined to be in the 90-187 $mV \cdot dec^{-1}$ range (Figure 51), in agreement with the Volmer step (i.e. the adsorption of H atoms) being globally the rate-determining one.

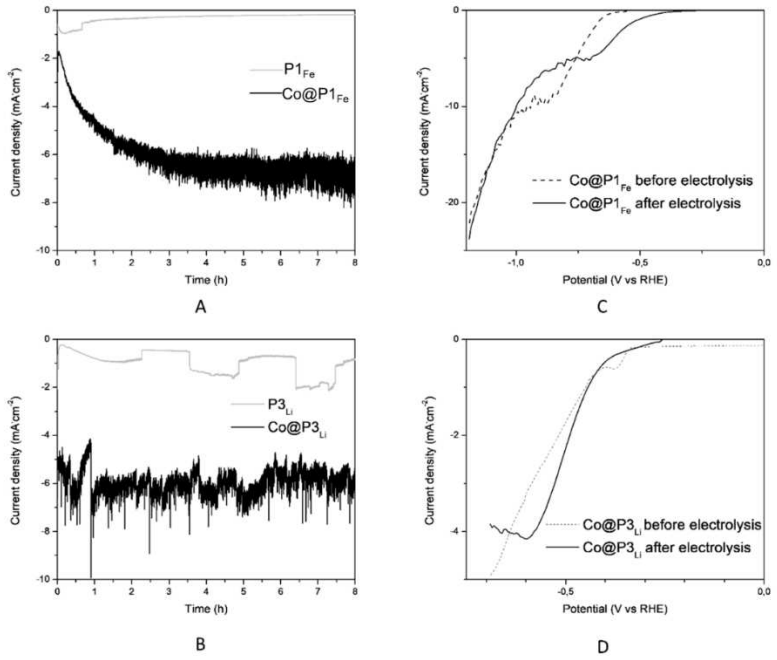

Figure 52. CPE experiments carried out at -0.68 V vs RHE for **Co@P1$_{Fe}$** (A) and **Co@P3$_{Li}$** (B) HER catalysts. LSVs curves recorded before and after electrolysis are shown in (C) for **Co@P1$_{Fe}$** and in (D) for **Co@P3$_{Li}$**.

Controlled potential electrolysis (CPE) experiments were carried out on the metallated polymer vs the respective metal-free **Px** (x= 1,3,4,6) materials at –0.68 V vs RHE for 8 hours, to evaluate the robustness of the catalysts and to confirm the effect of metallation on the HER performances on a longer timescale.

As reported in Figure 52 significant differences of current densities between the Co-containing and the native polymers were observed for the $\mathbf{P1}_{\mathbf{Fe}}$ and $\mathbf{P3}_{\mathbf{Li}}$ systems, but not for $\mathbf{P4}_{\mathbf{Fe}}$ and $\mathbf{P6}_{\mathbf{Fe}}$ ones. This indicates that only $\mathbf{P1}_{\mathbf{Fe}}$ and $\mathbf{P3}_{\mathbf{Li}}$ materials could have a potentially durable HER application.

The amounts of produced H_2 were measured by gas chromatograph (Appendix II, Figure B34), every two minutes over the 8 hours timescale. The HER faradaic efficiency found was 82% for $\mathbf{Co@P1}_{\mathbf{Fe}}$ ($4.76.10^{-5}$ mol H_2 per 11.25 C) and 95% for $\mathbf{Co@P3}_{\mathbf{Li}}$ ($5.81.10^{-5}$ mol H_2 per 11.76 C). If each single cobalt center behaves as an active catalyst, turnover numbers (TONs) and frequencies (TOFs) could be calculated as reported in the following table, by considering the %Co in the materials as derived by ICP (4.22% and 4.51% w/w for $\mathbf{Co@P1}_{\mathbf{Fe}}$ and $\mathbf{Co@P3}_{\mathbf{Li}}$, respectively), the electrode mass loading (~90 μg cm^{-2}) and the geometric electrode surface (0.07 cm^2).

Table 5. Turnover numbers (TONs) and frequencies (TONs) for most interesting materials $\mathbf{Co@P1}_{\mathbf{Fe}}$ and $\mathbf{Co@P3}_{\mathbf{Li}}$.

	TON	TOF (h^{-1})
$Co@P1_{Fe}$	$1.1{\cdot}10^4$	$1.4{\cdot}10^3$
$Co@P3_{Li}$	$1.2{\cdot}10^4$	$1.5{\cdot}10^3$

Even if the overpotentials are not competitive, these catalytic parameters demonstrate a good activity of each single active cobalt center and a reasonable catalyst stability.

3.4.5 Porous carbon synthesis

As mentioned in the previous section, **Co@P1$_{Fe}$** and **Co@P3$_{Li}$** have shown an electrocatalytic HER activity under environmentally friendly conditions (pH=7) and they represent a rare example of HER electrocatalysts based on non-carbonized POPs. Although due to their high overpotentials, the catalytic performances of these materials can be improved with future investigations by tuning their properties as increasing of the density of active centers or improve their electrical conductivity. A strategy to improve the conductivity of the functionalized POPs could be the synthesis of single atom catalyst (SAC) from the carbonization of the functionalized polymers. In a preliminary study the most representative materials between the seven synthetized, were pyrolyzed in an oven using the temperature scan program depicted in the graph below (Figure 53a). **Co@P1$_{Fe}$** and **Co@P3$_{Li}$** and the corresponding native polymers were heated at 5°C/min from r.t. to 900°C in quartz crucible under a constant flux of nitrogen gas. The sample was kept at 900°C for 2 h, to pyrolyze all the organic structure of the POPs and then was cooled to r.t. overnight. The apparatus used is shown in Figure 53b.

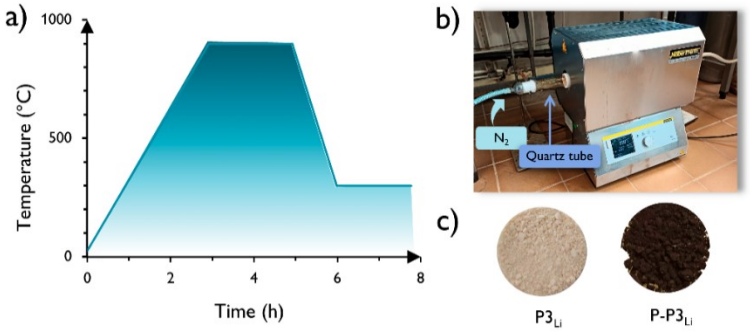

Figure 53. a) Temperature programme used to pyrolyzed the samples: temperature scan at 5°C/min from 30°C to 900°C, then 900°C for 2 hours and cooling under N_2 to RT overnight.

The obtained pyrolyzed sample show a remarkable colour change as reported in Figure 53c for **P3$_{Li}$** and for the corresponding carbonized **P-P3$_{Li}$** material. The yield of the pyrolysis is about 26% w/w for **P3$_{Li}$** family and 50% w/w for FC polymers.

3.5 Conclusion

In summary, we explored the possibility to design amorphous heterogeneous catalysts for electrocatalytic applications, and more specifically for the hydrogen evolution reaction (HER) at neutral pH. In order to do so, we used different synthetic strategies to generate seven porous aromatic polymers. Friedel Craft reaction with $FeCl_3$ led to high surface area polymers such as **P4$_{Fe}$**, which has a BET surface area of 990 m^2/g. This method was not successful in the case of DPPE monomer most likely due to the scavenging effect of the phosphine groups towards the metal of the catalyst. Nevertheless, this monomer could be polymerized through its protection with BH_3 prior polymerazation, resulting in the synthesis of **P7$_{Fe}$**.

The strategy adopted opened the possibility to obtain a wide range of POPs using an easy and low-cost method that allowed to tune the final properties of the frameworks by simply changing the phosphine building blocks.

The presence of P=O moiety allowed to functionalize the POPs with different metals such as cobalt, nickel, iron and molybdenum. In particular, Co@POPs were characterized by EDX and ICP methods and the cobalt amount was about 4.5% for Co@P3Li polymer and between 0.8 % and 4.2 % w/w for the other polymers. For these metallated materials the electrocatalytic HER activity was finally explored. Although the catalytic performances of these materials are currently limited due to their high overpotentials, their properties such as porosity, density of binding sites, wettability can be easily tuned. Moreover, a way of tuning the properties of this materials could be also trough the generation of single atom catalyst. This was investigated in the final part of the work, where pyrolysis conditions were applied with the aim to generate a single atom catalyst based on this polymer and having cobalt as single site.

Chapter 4

4. Phosphorous and Sulphur based metal organic frameworks

In this chapter we will describe the synthesis and characterization of a novel metal organic framework with UIO-68 topology, using sulphur functionalized linkers. In addition, we developed different synthetic methodologies to prepare various carboxylate linkers functionalized both with phosphines and thioether with the aim to bind soft transition metals (Figure 54).

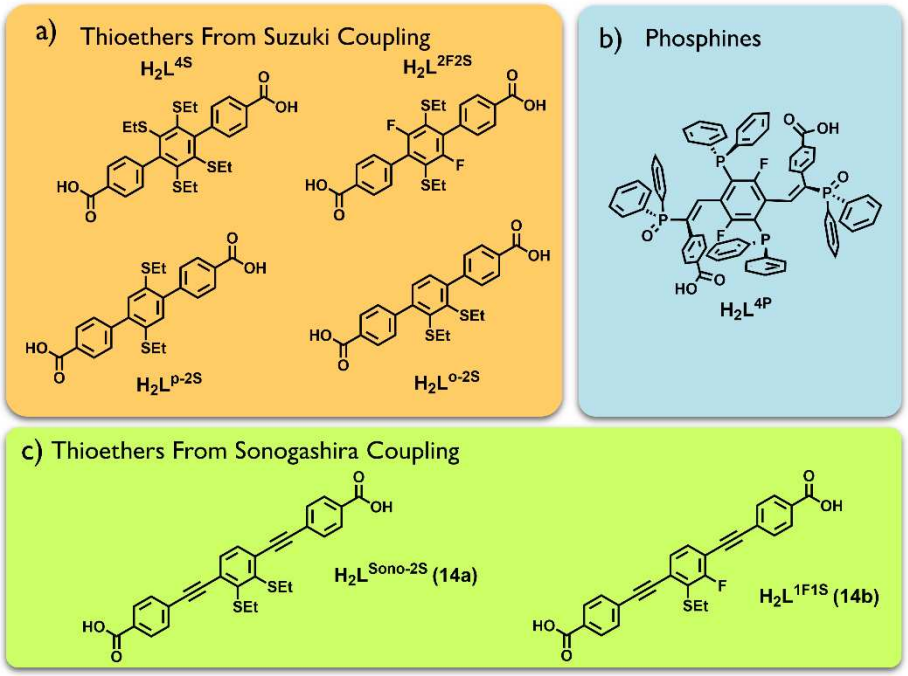

Figure 54. Organic linkers prepared in this work.

4.1 Introduction

4.1.1 Metal organic framework

Metal organic frameworks are a class of porous crystalline materials with 2D or 3D structure, which are constructed by joining metal-containing units with organic linkers through strong coordination bonds. The inorganic building blocks of MOFs are called secondary building units (SBUs) and various metal ions were employed for this purpose. The most common SBUs are formed from zirconium, zinc, copper, iron and aluminium ions. More recently, also lanthanides MOFs were studied due to the optical properties of the rare-earth metals.[157,158] The organic ligands are molecules with multiple coordinating functionality such as carboxylates, amine or imidazolates (Figure 55). In the last twenty years this interesting field of chemistry has shown an exponential growth due to the various combination between SBUs and organic linkers that gave rise to a huge amount of new crystalline structure and opened the way to an accurate tuning of the topology and adsorption properties of the final product. This relatively new field of chemistry is based on the principle of "reticular chemistry" (from the latin word "reticularis" meaning "little net"), a term introduced by Yaghi and co-workers in the early years of this century to describe the "linking of molecular building units by strong bonds to make crystalline, extended structures".[159]

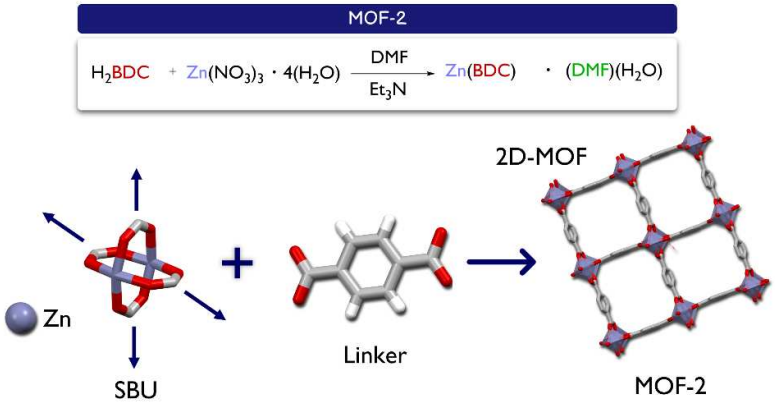

Figure 55. 2D-MOF-2 building block and synthesis.[160]

One of the main features of MOFs is their permanent porosity with BET surface area up to 7000 m^2/g. This characteristic opened the way to use them for a wide range of applications. MOFs are used today as adsorbent, for gas separation and storage, they also in some case possess specific optical or magnetic properties.I In addition, MOFs are used as heterogeneous catalyst or as host-guest systems to encapsulate small molecules.[161]

4.1.2 Isoreticular family of UiO metal organic frameworks

Another fundamental concept that we had to consider is the "isoreticular principle" by which different network can be constructed by the simple use of the same SBUs and using organic linkers with different length. The resulting family of MOFs have the same topology but different porous properties, pore size and surface area. Examples of isoreticular series are the IRMOF (from IsoReticular Metal-Organic Framework)[22] and UiO (from University of Oslo)[162] families.

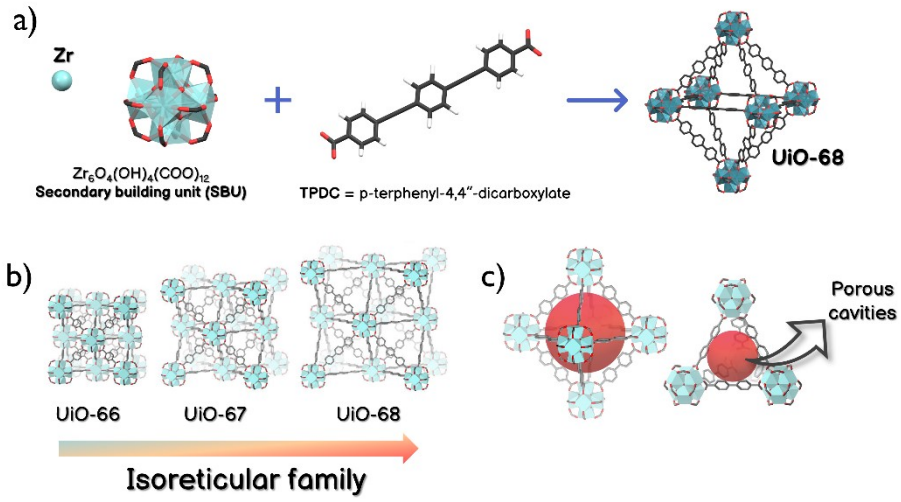

Figure 56. UiO-68 building blocks (a). Isoreticular series of UIO metal organic framework (b). Pore cavities in UiO frameworks (c).

UIO are formed by zirconium oxo cluster (with six Zr atoms) and dicarboxylate ligands based on thereftalic acid block. The main interesting properties of these solids are their thermal stability and high porosity due to the presence of large cavities inside the structure. This series was synthetized in 2008 by Lillerud *et al*.[163] The stability of these MOFs is mainly due to the strength of the zirconium-oxygen bonds, which are stable to hydrolysis unlike zinc-oxo bonds. In addition, the UiO series (and all MOFs with fcu topology) display two tetrahedral, and one octahedral, cages per zirconium cluster as shown in Figure 56c.

4.1.3 Sulphur-based Metal Organic Frameworks

The design of new metal organic framework does not involve only the studies of the new topologies but also the incorporation of new functional groups such as amines, thiols, alcholic functions, and so on. Tuning the functional groups allows to specifically prepare a MOFs for a specific application. Nowadays, the presence of sulphur-based functional groups is widely explored due to the tendency of sulphur to form strong coordination bond with transition metals. This heteroatom has a soft and polarizable nature and in the MOFs structure it could bind to soft metal ions such as Cu^{+}, Ag^{+}, Mn^{2+}, Pd^{2+}, Pt^{2+} without interfering with the metal of the SBUs due to the hard nature of these ions (e.g. Zr^{4+}, Al^{3+}, Eu^{3+}). For example, Z. Xu *et al*. developed a metal organic framework that combined the luminescent properties of lanthanides such as europium with the soft and polarizable properties of copper. This second metal is bound to the framework through a coordination bond with the thiother functions of the ligand. In this architecture, the sulphur functionalization interacts only the soft metal ions and not with the hard europium ions.

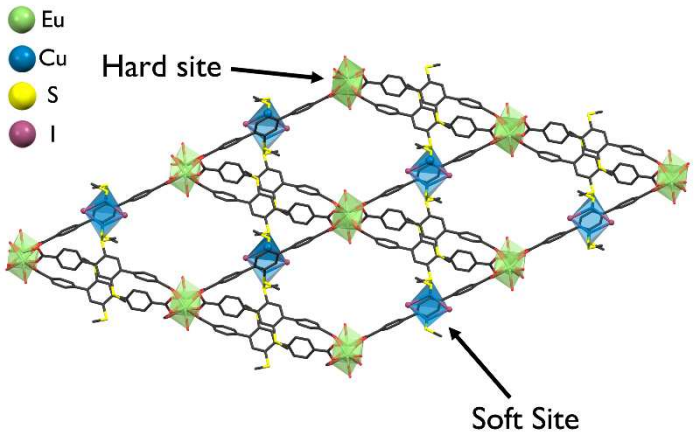

Figure 57. Bimetallic MOF of europium and copper, highlighting the different types of metal site in the framework. Refcode CCDC: TUZVUH.[164]

The use of this sulphur function is also interesting because it could be a starting point to synthetized new multifunctional system in which thiols and thioether are transformed into new functionality after the synthesis of the network. There are three main strategies to prepare sulphur-based MOFs:

1. Direct synthesis using a specific linker functionalized with sulphur.
2. Post-synthetic modification in which the sulphur functionality is introduce in the framework
3. Incorporation of sulphur functionality with the design of hybrid materials.

Focusing on the direct synthesis of sulphur MOFs, several ligands have been used to this purpose. As far as the dicarboxylate linker are concerned, both thiols and thioether groups have been successfully incorporated in a framework (Figure 58). Usually, the dicarboxylate linker posseses a monodentate sulphur atoms. Only one linker was reported with a terephthalic acid-based skeleton having a bidentate thioether functions.[165]

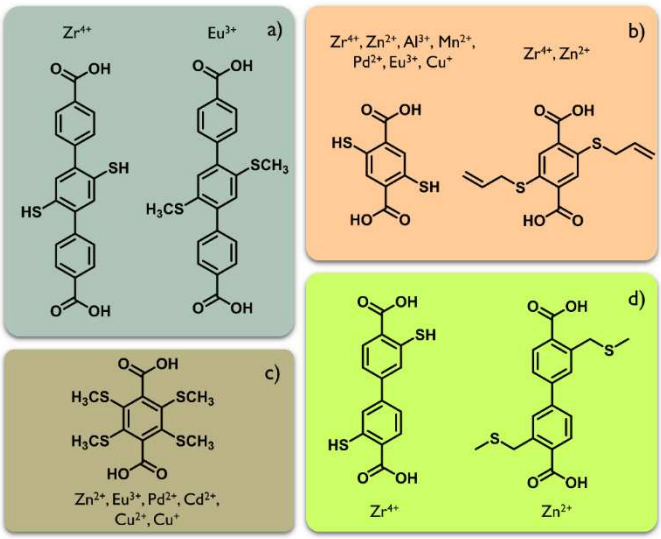

Figure 58. Sulphur-based organic linkers and the corrisponding metal used in the synthesis of metal organic frameworks. a) Triphenyl-4,4′-dicarboxylic acid-based ligands. b) Terephthalic acid-based linkers with monodentate sulphur groups. c) Terephthalic acid-based linkers with bidentate sulphur groups. d) Biphenyl-dicarboxylic acid linkers.[165]

4.2 Aim of the work

After exploring amorphous materials such as phosphorous POPs, we focused our attention on crystalline materials with the aim to design a stable heterogeneous catalyst for electrochemical reactions. Our choice fell on a particular class of inorganic and organic porous materials, namely Metal Organic Frameworks. Their crystalline nature allowed to determine their structure and so to have a better control over fundamental properties that are important in catalysis: porosity, pore size and active sites. Our strategy involved the synthesis of linkers functionalized with a chelating group able to bind an active transition metal such as palladium, platinum, nickel or cobalt. We investigated two classes of chelating groups: aryl phosphines (P,P donor system) as previously done for POPs, and thioethers (S,S donor system). Usually S,S donor systems in MOFs are formed by thiols. There are some examples of thiols functionalized MOFs to incorporate palladium and platinum metal ions, due to their tendency to form strong coordination bonds.[166] However, this fuctional group is strongly subject to oxidation, compromising the stability of the final porous framework and its applicability on the large scale and in various operative conditions. Instead, the thiother group is significantly more stable to oxidation, and it is still able to bond soft transition metals,[167,168] even though it forms weaker coordination bond than the thiol moiety. After the synthesis of the caboxylate ligands we optimized the MOFs synthesis and then we characterized the resulting materials with PXRD, TGA, and N_2 and H_2 adsorption isotherm. Some conditions were also investigated to incorporate transition metals by soaking the porous MOFs with palladium or platinum precursor.

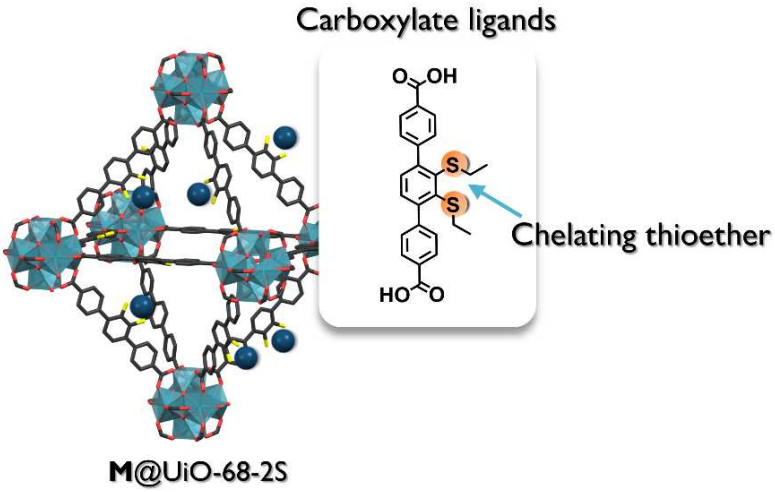

Figure 59. Example of Zr-MOFs materials investigated in this chapter.

4.3 Experimental Section

4.3.1 General remarks

All commercially available reagents and solvents were used without further purification. Anhydrous solvents were dried and stored over molecular sieves (3 Å) after activation (250°C, 24 hours). Reactions performed under an inert atmosphere (N_2) were carried out using standard Schlenk glassware. Flash column chromatography was performed using silica gel (230-400 mesh). Potassium diphenylphosphide solution (0.5 M/THF) was purchased from Sigma Aldrich and stored under nitrogen. (2,3-difluoro-1,4-phenylene)bis(trimethylsilane)(**10**)[169] $Pd(PPh_3)Cl_2$[170], $Pd(COD)Cl_2$[171] and *cis*-$Pt(MeCN)Cl_2$[172] were synthetized by known procedure.

NMR Experiments: NMR experiments were performed on a Brüker Avance 400 MHz instruments or JEOL 600 MHz ECZ600R instrument at 298 K. Chemical shifts are expressed in ppm relative to tetramethylsilane, using the solvent residual peak of $CDCl_3$ (δH 7.26, δC 77.00) as a reference standard.

Gas adsorption measurements: Gas Sorption isotherms (0-1.0 bar) were measured by a volumetric method using Micromeritics Tristar-II instruments. The samples (35 mg) were evacuated by heating at 135 °C under dynamic vacuum for 6 h before adsorption experiments. For hydrogen sorption isotherms, H_2 gas (99.99 % purity) was generated by Yanaco RHG-200 hydrogen generator. Nitrogen gas sorption isotherms at 77 K were measured in liquid nitrogen. Brunauer, Emmett and Teller (BET) surface areas were determined from N_2 adsorption data at 77 K using Micromeritics software.

Scanning electron microscopy (SEM): SEM experiments were performed using an ESEM instrument QuantaTM 250 FEG (FEI, Hillsboro, OR) equipped with an energy-dispersive spectrometer (EDS) for X-ray microanalysis (Bruker Nano GmbH, Berlin, Germany). The EDS is equipped with a QUANTAX XFlash® 6 | 30 detector with energy resolution ≤ 126 eV FWHM at Mnkα. The

spectra were collected and analysed using ESPRIT 1.9 software (Bruker Nano GmbH).

Inductively coupled plasma atomic emission spectrometry (ICP-AES): ICP analyses were performed with an ULTIMA 2 instrument JOBIN YVON in radial configuration, with a JY 2501 monochromator calibrated against carbon lines. The optical path was continuously purged with nitrogen (2 L/min).

2/3 mg of MOFs samples were dissolved in 4 mL of HNO_3 65% and 1 mL of H_2O_2 30% and then heated by microwave irradiation (Milestone, MLS-1200 MEGA, equipped with TFM inner vessels) using the conditions reported in the following table:

Step	Time (min)	Power (W)
1	2.00	250
2	2.00	0
3	6.00	250
4	5.00	400
5	5.00	650

After mineralization the final solution were brought to a final volume of 25 mL in water H_2O Millipore. Calibration was performed with standard solutions 10% of HNO_3 on eight different metal concentration levels, ranging from 0.5 mg/L to 100 mg/L. No significant spectral interferences were detected. Data were acquired by considering the following emission lines: Co 228.616 nm, Zn 213.856 nm, Ni 221.647 nm, Pt 265.945 nm, Zr 339.198 nm and Pd 340.458 nm. Data acquisition and processing were performed using the ICP JY v 5.4.2 software (Jobin Yvon).

Single crystal X-ray diffraction (SCXRD): Data collection for the ligands was performed at 200 K with a Bruker D8 diffractometer equipped with Photon II area detector, using a CuKα (λ = 1.54184) or MoKα (λ = 0.71073) as microfocus radiation source. The data collection strategy covered the sphere of reciprocal space. Absorption corrections were applied using the program SADABS.[90] The structure was solved with the SHELXT code.[91] Fourier analysis and refinement were performed by the full-matrix least-squares methods based on F^2 using SHELXL-2014,[92] implemented in Olex2.[93] All the non-H atoms were refined with anisotropic displacement parameters.

Single-crystal X-ray diffraction experiment for [$Ag_2L^{p\text{-}2F}$] were carried out at the BL02B1 of SPring-8 synchrotron. A wavelength of $\lambda = 0.41190$ and a single crystal of 0.01 x 0.01 x 0.005 mm^3 were used. The crystal was attached to the tip of a MiTeGen MicroMount. All frame images (Dectris) were collected at 100 K and converted to SFRM format by the Henkankun-R. Data reduction was performed using Bruker SAINT. Structure was solved by SHELXT [91] and refined against F^2 by weighted full matrix least-squares (SHELXL[92]).

Power X-ray diffraction (PXRD): PXRD data were were collected on a Thermo Scientific ARL X'TRA diffractometer in θ-θ Bragg Brentano geometry with CuKα radiation. The samples were placed on zero background sample holder and exposed to radiation ($3° < 2\theta < 40°$) with a scan of 0.1 °/min.

Electrochemical measurements: Electrochemical measurements were performed using an electrochemical workstation (Ivium technology potentiostat/galvanostat, compactStat) with a standard three-electrode setup, with Ag/AgCl (in 3.5 M KCl solution) as the reference electrode, a platinum plate as the counter electrode, and a glassy carbon electrode (GC, 3 mm in diameter) coated with the as-prepared catalysts as the working electrode. The measurements were carried out in 0.1 M solutions of either phosphate buffer, $KHCO_3$, H_2SO_4 or KOH, previously saturated with Ar or CO_2 at ambient temperature. In a typical experiment, 5 mg of target material and 5 mg of carbon black powder (Vulcan XC 72R) were dispersed in 950 µL of isopropanol and 50 µL of Nafion solution (5 wt %). The mixture was vigorously sonicated for about 1 hour to form a "homogeneous" ink suspension. The obtained ink (5 µL) was drop-casted onto a glassy carbon electrode (3 mm diameter, mass loading of ~90 µg cm^{-2}), previously polished with diamond paste, sonicated in water for 10 minutes, washed with acetone and oven-dried. All the measurements were referred to the reversible hydrogen electrode (RHE) by using the following equation:

$$E(\text{RHE}) = E(\text{Ag/AgCl}) + E_0(\text{Ag/AgCl}) + 0.059\ \text{V} \times \text{pH}$$

Each newly prepared electrode was first stabilized by cyclic voltammetry (CV) between 0 V and -1.18 V vs RHE at a scan rate of 100 $mV \cdot s^{-1}$ until the CV curves remain roughly stable (10 cycles). After this step, linear sweep voltammetry (LSV) experiments were carried out at a scan rate of 5 mV s^{-1} in the same potential window.

Other Measurements: Thermogravimetric analysis was performed with a PerkinElmer TGA 8000, heating MOFs (0.5-3 mg) from 30 to 600/800 °C in atmospheric pressure, with a T-ramp of 10°C min^{-1} under oxygen flux (30 mL min^{-1}). Electrospray mass spectral analyses (ESI-MS) were performed with an electrospray ionization time-of-flight Micromass 4LCZ spectrometer after solubilization of the samples in methanol or acetonitrile. Infrared (IR) spectra were obtained with a Perkin Helmer Spectrum Two FT-IR spectrometer (diamond crystal, in ATR mode) in the 4000-400 cm^{-1} interval at room temperature. Elemental analyses of MOFs (sample mass 3 mg) were performed on Thermo Fischer Scientific FlashSmart CHNS.

4.3.2 Synthesis of the ligands

Synthesis of phosphorous ligand H_2L^{4P}

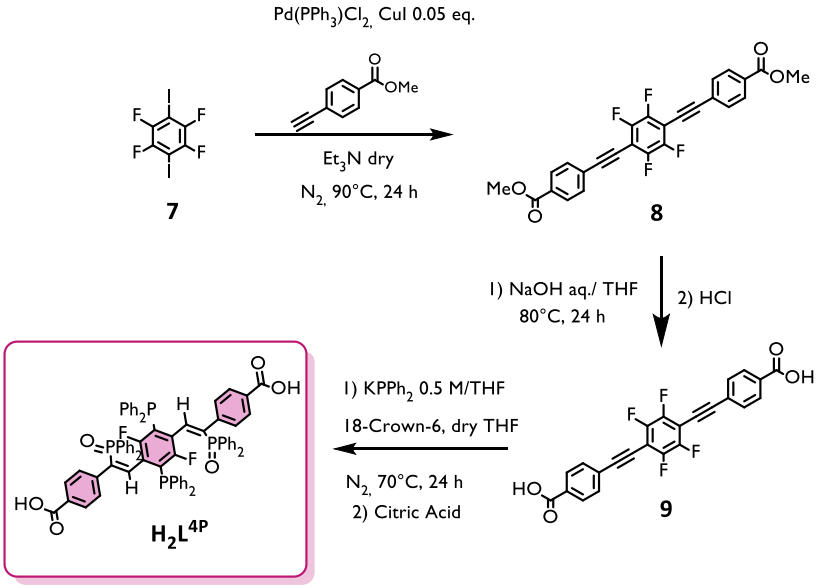

Scheme 6. Synthesis of the phosphorous carboxylate ligand $\mathbf{H_2L^{4P}}$.

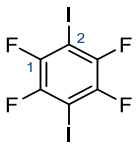

1,2,4,5-tetrafluoro-3,6-diiodobenzene (7) In a three-neck round-bottom flask 1,2,4,5-tetrafluorobenzene (2.50 mL, 22.39 mmol) was diluted in 100 mL of anydrous THF. The system was cooled to -78°C and a solution of *n*-butyllithium (2.0 M/cyclohexane, 29 mL, 29 mmol, 2.6 eq.) was added dropwise over 30 minutes. After 40 minutes 15.34 g of iodine was added portionwise. The system was stirred a r.t. overnight and then the reaction was quenched at 0°C with 40 mL of water. The solution was extracted three times with DCM (3 x 70 mL) and washed two times with $Na_2S_2O_3$ to remove the excess

of iodine. The organic phase was dried with Na_2SO_4 and then the solvent was removed under reduced pressure, yielding a yellow solid than was recrystallized in Hx:DCM at -20°C to obtain the desired product **(7)** (6.44 g, 16 mmol, 72 %)

^{13}C NMR (151 MHz, $CDCl_3$) δ (ppm): 148.02 – 145.39 (m, C_1), 72.97 (d, J = 16.1 Hz, C_2); **^{19}F NMR (565 MHz, $CDCl_3$) δ (ppm):** -117.92 (s, 4F). **IR** (cm^{-1}): 2957w, 1458brs, 1429m, 1355w, 1229m, 1247m, 1214m, 1180m, 968w, 939s, 827s, 757s, 649m, 562m.

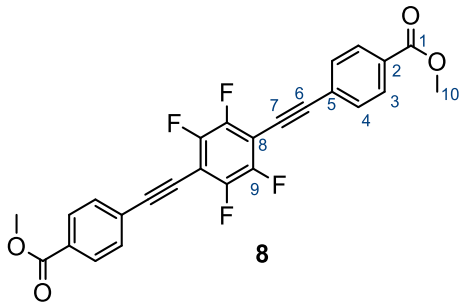

8

dimethyl4,4'-((perfluoro-1,4-phenylene)bis(ethyne-2,1 diyl))dibenzoate (8)[173] $Pd(PPh_3)_2Cl_2$ (47 mg, 0.67 mmol, 0.03 eq.), CuI (13 mg, 0.67 mmol, 0.03 eq.), methyl 4-ethynylbenzoate (825 mg, 5.15 mmol, 2.3 eq.) and 1,4-diiodo-2,3,5,6-tetrafluorobenzene (**7**) (900 mg, 2.24 mmol) were added in a 250 mL schlenk flask. The system was degassed three times after that 59 mL of dry triethylamine were added. The system was stirred a 90°C overnight and then the reaction was quenched with 40 mL of water. The off-white solid was isolated by vacuum filtration and washed with water and acetone. Finally, was dried under vacuum. The pure product (**8**) was obtained by recrystallization of crude product in hot chloroform, yielding a crystalline bright solid (0.671 g, 1.44 mmol, crystallization yield 64 %)

^{1}H NMR (600 MHz, $CDCl_3$) δ (ppm): 8.07 (d, *J* = 8.0 Hz, H_3), 7.67 (d, *J* = 7.8 Hz, H_4), 3.95 (s, H_{10}); **^{19}F NMR (565 MHz, $CDCl_3$) δ (ppm):** -136.33 (s, 4F); **IR** (cm^{-1}): 2956w, 1722s, 1604m, 1518w, 1486s, 1433s, 1405w, 1273s, 1180w, 1105s, 978s, 956m, 857m, 767s, 691m.

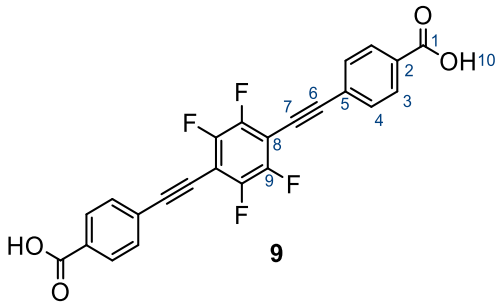

9

4,4'-((perfluoro-1,4-phenylene)bis(ethyne-2,1-diyl))dibenzoic acid (9) 4F-diester (**8**) (509 mg, 1.09 mmol), sodium hydroxide (671 mg, 16.8 mmol, 15 eq.), THF (130 mL) and water (30 mL) were added in a 250 mL round bottom flask. The system was refluxed overnight after which the product was precipitated adding concentrated HCl until the pH was three. The pure product (**8**) was isolated by centrifugation and washed with water and acetone, yielding white solid (0.442 g, 1.02 mmol, 92 %)

^{1}H NMR (400 MHz, DMSO-d_6) δ (ppm): 13.36 (brs, H_{10}), 8.03 (d, J = 7.9 Hz, H_3), 7.78 (d, J = 8.3 Hz, H_4); **^{19}F NMR (565 MHz, DMSO-d_6) δ (ppm):** -136.75 (s, F_9); **IR** (cm^{-1}): 3050 brw, 1681s, 1605m, 1558w, 1480s, 1406m, 1314m, 1281s, 1177w, 1017w, 977s, 858s, 768s, 736m, 690m, 522m.

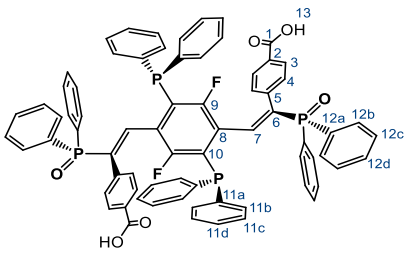

H_2L^{4P}

4,4'-(2,5-bis(diphenylphosphaneyl)-3,6-difluoro-1,4phenylene) bis(1-(diphenylphosphoryl)ethene-2,1-diyl))dibenzoic acid (H_2L^{4P}).[174] In a dry three-neck round bottom flask under nitrogen atmosphere were added 18-crown-6 (929 mg, 3.51 mmol, 5.17 eq.) diacid-4F (**9**) (298 mg, 0.680 mmol) and 15 mL of anhydrous THF. The system was evacuated three times and then $KPPh_2$ 0.5 M/THF (6 mL, 3.00 mmol, 4.50 eq.) was added

dropwise with a syringe at 0°C. The system was stirred at reflux for 24 hours. The conversion of the reagents was controlled by TLC using DCM/MeOH 90:10 as eluent. After that time the excess of phophide was hydrolyzed with MeOH following by the removal of solvent under high vacuum. Then dicloromethane was added (40 mL) and the clear bright yellow solution has been acidified with a saturated solution of citric acid (25 mL). The organic phase was separated and washed with 25 mL of acqueous citric acid, 25 mL of water and brine. The organic phase was dried with Na_2SO_4 and then the solvent was removed under reduced pressure, following with a washing step with degassed EtOH to remove byproducts and the crown ether. The desired ligand ($\mathbf{H_2L^{4P}}$) was obtained as bright yellow solid with 59 % yield (0.470 g, 0.400 mmol). The ligand $\mathbf{H_2L^{4P}}$ is soluble in chlorinated solvents and its behavior changes with the oxidation state of the phosphorous groups.

^{1}H NMR (400 MHz, CD_2Cl_2) δ (ppm): 7.71 (d, *J* = 8.3 Hz, H_3), 7.55 – 7.20 (m, H_{11}-H_{18}), 6.98 (d, *J* = 8.0 Hz, H_4), 6.38 (d, *J* = 4.5 Hz, H_7). **^{13}C NMR (101 MHz, $CDCl_3$) δ (ppm):** 172.9 (s, C_1), 158.8 – 154.1 (m, C_9), 146.0 (dd, *J* = 20.7, 4.1 Hz, $C_{6,10}$), 145.7 (d, *J* = 20.7 Hz, $C_{11a,12a}$), 135.3 (d, *J* = 21.0 Hz, $C_{11b\text{-}d,12b\text{-}d}$), 134.9 (d, *J* = 11.0 Hz, C_8), 131.1 (dd, *J* = 15.0, 8.8 Hz, C_7), 130.1 (s, C_3), 129.3 (d, *J* = 8.8 Hz, C_4), 129.08 (s, $C_{11b\text{-}d,12b\text{-}d}$), 129.02 (s, $C_{11b\text{-}d,12b\text{-}d}$), 128.42 (s, $C_{2,5}$).

^{31}P-NMR (162 MHz, CD_2Cl_2) δ (ppm): 6.68 s (s, P_6), -14.21 (d, *J* = 9.9 Hz, P_{10});

^{19}F NMR (565 MHz, $CDCl_3$) δ (ppm): -100.80 (s, F_9). **IR (cm^{-1}):** 3373mbr, 3055w, 2971w, 1692s, 1604w, 1479w, 1434m, 1390w, 1261s, 1176w, 1092w, 1044m, 1026w, 911w, 804w, 739s, 692s, 623w, 502m.

Synthesis of Sonogashira-based linkers

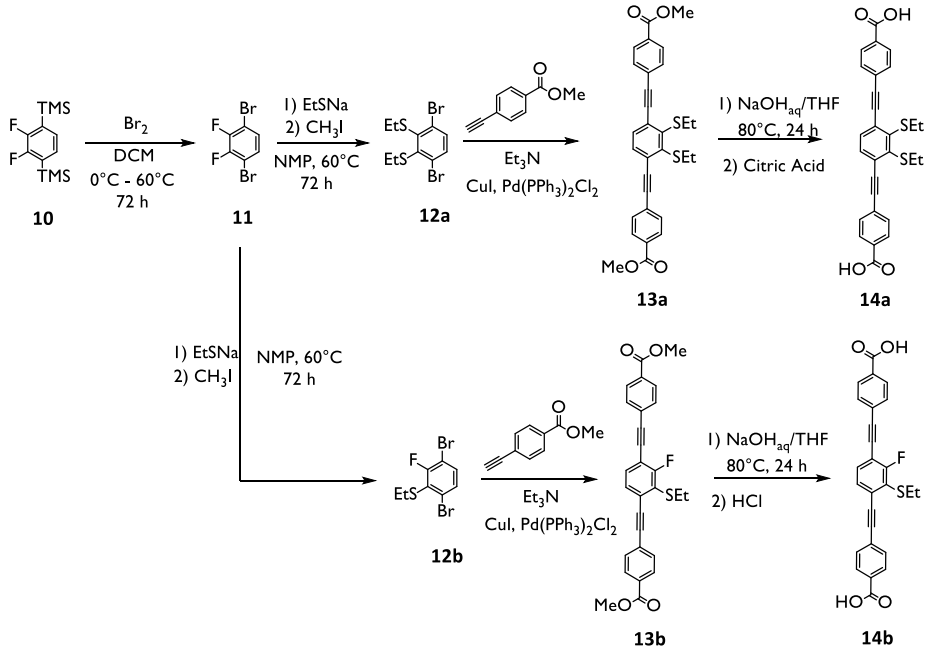

Scheme 7. Synthetic paths for **14a** and **14b** linkers.

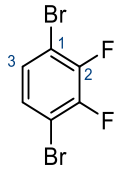

11

1,4-dibromo-2,3-difluorobenzene (11).[175] The trimethylsilane derivate (**10**) (5.00 g, 19.4 mmol) was dissolved in 15 mL of dichloromethane in a three-neck round-bottom-flask under nitrogen, then a solution of bromine (8 mL, 0.053 M in DCM, 7.8 eq.) was added slowly (25 minutes) at 0°C. Then, the mixture was heated to reflux for 1 days and then another 1 mL of bromine was added to complete the reaction. The reaction was monitored by TLC chromatography with Hx 100% as eluent (R_f = 0.71). The system was refluxed for two additional days and then the reaction was quenched at 0°C with saturated solution of $Na_2S_2O_{3\,aq}$. The aqueous phase was extracted with dichloromethane twice. The combined organic phases were washed with brine and then were dried

over anhydrous Na_2SO4. After removing the solvent, the crude product was purified by distillation under vacuum (ΔT_B 96°-100°C/< 10^{-3} Torr) to give a colorless oil (3.40 g, 12.51 mmol, 65%).

^{1}H NMR (400 MHz, $CDCl_3$) δ (ppm): 7.24 - 7.23 (m, H_3). **^{19}F NMR (565 MHz, $CDCl_3$) δ (ppm):** -125.8 (m, F_2).

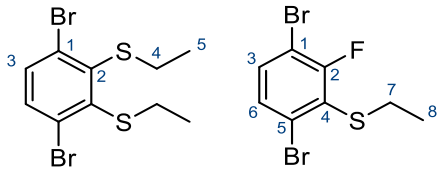

12a **12b**

(3,6-dibromo-1,2-phenylene)bis(ethylsulfane) (12a) and (3,6-dibromo-2-fluorophenyl)(ethyl)sulfane (12b). In a 100 mL schlenk flask were added sodium ethantiolate (1.57 g, 18.7 mmol, 3.05 eq.), 30 mL of anhydrous N-metil-2-pirrolidone (NMP) in order to solubilize the thiolate (purple solution). After the compound (**11**) (1.66 g, 6.11 mmol) was added at 0°C (dark purple solution). The system was stirred at 60°C for 72 h than CH_3I 99% (1.20 mL, 19.0 mmol, 3.25 eq.) was added (dark grey solution). The system was stirred for 10 minutes and than water was added at 0°C to quench the reaction. The acqueous phase was extracted with diethyl ether three times and then the organic phase was washed with water (2x) and brine (1x). The resulting Et_2O phase was dried over sodium sulfate, and evaporated in vacuo to yield a pale yellow oil (crude mixture of **12a** + **12b**). The two products (**12a**) and (**12b**) were isolated by flash chromatography (eluent from 100:0 to 80:20 Hx:DCM) (Rf_{12a} =0.5; Rf_{12b} =0.63 (100% Hx) with 35% and 29% yield, respectively.

(**12a**) (0.735 g, 2.11 mmol, 35%)

- **^{1}H NMR (400 MHz, $CDCl_3$) δ (ppm):** 7.45 (s, H_3), 3.01 (q, *J* = 7.4 Hz, H_4), 1.23 (t, *J* = 7.4 Hz, H_5).**^{13}C NMR (101 MHz, $CDCl_3$) δ (ppm):** 143.5 (C_2), 134.0 (C_3), 131.2 (C_1), 31.5 (C_4), 14.4 (C_5).

(**12b**) (0.551 g, 1.75 mmol, 29%)

- **^{1}H NMR (400 MHz, CD_2Cl_2) δ (ppm):** 7.38 – 7.30 (m, H_3, H_6), 2.97 (qd, *J* = 7.4, 0.8 Hz, H_7), 1.25 (td, *J* = 7.3, 0.7 Hz, H_8). **^{13}C NMR (101 MHz, $CDCl_3$) δ (ppm):** 159.7 (d, *J* =248 Hz, C_2), 133.3 (C_3), 129.27 (C_4) 129.26 (C_6), 125.9 (d, *J* = 21.6 Hz, C_5), 108.8 (d, *J* = 24.6 Hz, C_1), 29.40 (d, *J* = 5.1 Hz, C_7), 14.92 (C_8). **^{19}F NMR (565 MHz, CD_2Cl_2) δ (ppm):** -92.06 (d, *J* = 6.3 Hz, F_2).

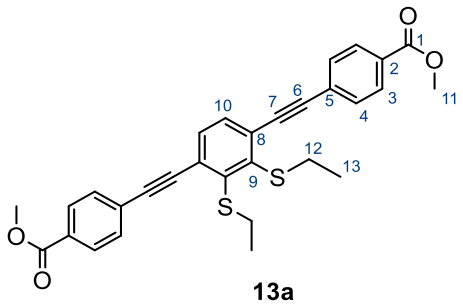

13a

Dimethyl 4,4'-((2,3-bis(ethylthio)-1,4-phenylene)bis(ethyne-2,1-diyl))dibenzoate (13a). $Pd(PPh_3)_2Cl_2$ (179.53 mg, 0.26 mmol, 0.08 eq.), CuI (50.14 mg, 0.26 mmol, 0.08 eq.), methyl 4-ethynylbenzoate (1.11 g, 6.95 mmol, 2.10 eq.) and (**12a**) (1.090 g, 3.06 mmol) were added in a 100 mL schlenk flask. The system was degassed three times after that 45 mL of dry and degassed triethylamine were added. The system was stirred a 90°C for 24 h and then the reaction was quenched with 20 mL of water. The solid was isolated by vacuum filtration and washed with water. Finally, the yellow solid was dried under vacuum, yielding the (**13a**) (0.516 g, 1.0 mmol, 32%). Single crystal suitable for SC-XRD analysis was obtained from Et_2O:Hx (1:1) mixture.

^{1}H NMR (400 MHz, $CDCl_3$) δ (ppm): 8.05 (d, *J* = 8.4 Hz, H_3), 7.62 (d, *J* = 8.3 Hz, H_4), 7.52 (s, H_{10}), 3.94 (s, H_{11}), 3.13 (q, *J* = 7.4 Hz, H_{12}), 1.27 (t, *J* = 7.4 Hz, H_{13}). **^{13}C NMR (101 MHz, $CDCl_3$) δ (ppm):** 166.5 (s, C_1), 143.19 (s, C_9), 132.44 (s, C_{10}), 131.53 (s, C_3), 129.90 (s, C_2), 129.62 (s, C_4), 129.40 (s, C_5), 127.64 (s, C_8), 94.89 (s, C_6, C_7), 91.58 (s, C_6, C_7), 52.32 (s, C_{11}), 30.98 (s, C_{12}), 14.91 (s, C_{13}). **IR (cm^{-1}):** 2949w, 2922w, 1714s, 1602s, 1505w, 1433s, 1403m, 1270s, 1189m, 1014m, 965w, 853m, 821s, 763s, 691s, 522w.

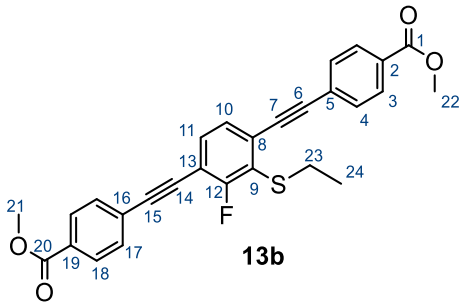

13b

Dimethyl 4,4'-((2-(ethylthio)-3-fluoro-1,4-phenylene)bis(ethyne-2,1-diyl))dibenzoate (13b). $Pd(PPh_3)_2Cl_2$ (60.0 mg, 0.82 mmol, 0.05 eq.), CuI (15.9 mg, 0.82 mmol, 0.05 eq.), methyl 4-ethynylbenzoate (554 mg, 3.45 mmol, 2.11 eq.) and (**12b**) (515 mg, 1.64 mmol) were added in a 50 mL schlenk flask. The system was degassed three times after that 25 mL of dry and degassed triethylamine were added. The system was stirred a 90°C overnight and then the reaction was quenched with 20 mL of water. The grey solid was isolated by vacuum filtration and washed with water and acetone. Finally, the solid was dried under vacuum, yielding the product (**13b**) with 90% yield (0.700 g, 1.48 mmol).

^{1}H NMR (400 MHz, CD_2Cl_2) δ (ppm): 8.03 (dd, J = 8.3, 2.7 Hz, H_3, H_{18}), 7.64 (dd, J = 8.2, 5.1 Hz, H_4, H_{17}), 7.46 (dd, J = 8.1, 6.7 Hz, H_{11}), 7.39 (d, J = 8.1 Hz, H_{10}), 3.91 (s, H_{22} , H_{21}), 3.07 (q, J = 7.3 Hz, H_{23}), 1.28 (t, J = 7.4 Hz, H_{24}). **^{13}C NMR (101 MHz, CD_2Cl_2) δ (ppm):** 166.19 (C_1), 166.16 (C_{20}), 162.9 (d, *J* = 250 Hz, C_{12}), 132.3 (C_{11}), 131.6 (C_4), 130.28 (C_8), 129.48 (C_3), 128.4 (C_{10}), 127.21 (C_2, C_{19}), 126.96 (C_5, C_{16}), 125.3 (C_9), 112.3 (C_{13}), 95.7 (C_6/C_{15}), 95.4 (C_7/C_{14}), 90.0 (C_7/C_{14}), 85.0 (C_6/C_{15}), 52.15 (C_{22},C_{21}), 29.19 (C_{23}), 14.97 (C_{24}). **^{19}F NMR (565 MHz, $CDCl_3$) δ (ppm):** -101.2 (d, *J* = 6.7 Hz, F_{12}). **IR (cm^{-1}):** 2950w, 1715s, 1603s, 1506w, 1433m, 1403m, 1271s, 1189m, 1107s, 1015m, 854m, 821m, 763s, 691s, 522w.

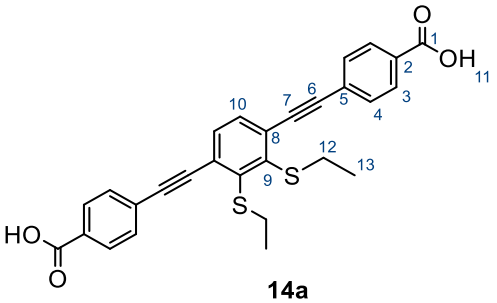

14a

4,4'-((2,3-bis(ethylthio)-1,4-phenylene) bis (ethyne-2,1diyl)) dibenzoic acid (14a) The diester (**13a**) (349 mg, 0.68 mmol), sodium hydroxide (303 mg, 7.49 mmol, 11.0 eq.), THF (85 mL) and water (12 mL) were added in a 250 mL round bottom flask. The system was refluxed overnight after which the product was precipitated adding saturated citric acid until the pH was three. The pure product (**14a**) was isolated by centrifugation and washed with water and acetone and dicloromethane, yielding a grey solid (0.108 g, 0.222 mmol, 33 %).

^{1}H NMR (400 MHz, DMSO-d_6) δ (ppm): 13.18 (s, H_{11}), 8.01 (d, J = 8.4 Hz, H_3), 7.69 (d, J = 8.3 Hz, H_4), 7.67 (s, H_{10}), 3.12 (q, J = 7.3 Hz, H_{12}), 1.18 (t, J = 7.3 Hz, H_{13}). **IR (cm^{-1}):** 29625w, 2812w, 2663w, 2537w, 1681s, 1602s, 1556w, 1419s, 1312m, 1279s, 1170m, 1109w, 1015w, 924m, 856m, 800w, 768s, 690m, 556m, 519m. **^{13}C NMR (101 MHz, DMSO-d_6) δ (ppm):** 166.6 (s, C_1), 142.5 (s, C_9), 132.7 (s, C_{10}), 131.5 (s, C_3), 131.0 (s, C_2), 129.7 (s, C_4), 128.7 (s, C_5), 126.3 (s, C_8), 94.7 (s, C_6, C_7), 91.0 (s, C_6, C_7), 30.0 (s, C_{12}), 14.7 (s, C_{13}). **IR (cm^{-1}):** 2965w, 2812w, 2662w, 2536w, 1681s, 1603s, 1556w, 1419s, 1312m, 1279s, 1170m, 1109m, 1015w, 924w, 856m, 799w, 769s, 690m, 519m.

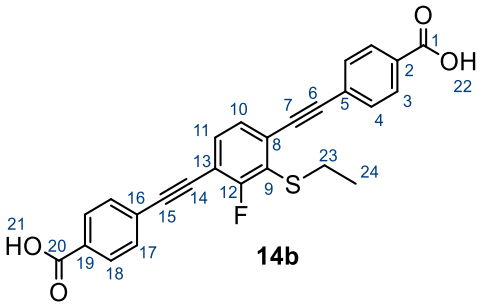

14b

44,4'-((2-(ethylthio)-3-fluoro-1,4-phenylene)bis(ethyne-2,1-diyl))dibenzoic acid (14b) The diester (**13b**) (371 mg, 0.79 mmol), sodium hydroxide (366 mg, 9.15 mmol, 11.6 eq.), THF (90 mL) and water (15 mL) were added in a 250 mL round bottom flask. The system was refluxed overnight after which the product was precipitated adding concentrated HCl until the pH was three. The pure product (**14b**) was isolated by centrifugation and washed with water and acetone, yielding a light brown solid (0.240 g, 0.529 mmol, 69 %)

^{1}H NMR (400 MHz, DMSO-d$_6$) δ (ppm): 13.15 (s, $H_{21,}$ H_{22}), 8.01 (dd, J = 8.3, 4.1 Hz, H_3,H_{18}), 7.71 (dd, J = 8.3, 3.5 Hz, H_4,H_{17}), 7.67 - 7.55 (overlapped m, $H_{10,}$ H_{11}), 3.07 (q, J = 7.3 Hz, H_{23}), 1.20 (t, J = 7.3 Hz, H_{24}). **^{13}C NMR (101 MHz, DMSO-d$_6$) δ (ppm):** 167.09 (C_1), 167.06 (C_{20}), 162.54 (d, *J* = 249 Hz, C_{12}), 133.4 (C_{11}), 132.2 (C_4), 131.7 (C_8), 130.2 (C_3), 129.44 (C_2, C_{19}), 129.3 (C_{10}), 126.2 (C_5, C_{16}), 124.9 (C_9), 112.1 (C_{13}), 96.3 (C_6, C_{15}), 96.0 (C_7, C_{14}), 90.0 (C_7, C_{14}), 85.0 (C_6, C_{15}), 29.0 (C_{23}), 15.5 (C_{24}). **^{19}F NMR (565 MHz, DMSO-d$_6$) δ (ppm):** -102.0 (d, *J* = 5.7 Hz, F_{12}). **IR (cm^{-1}):** 2972brw, 2872brw, 2669brw, 2550brw, 1686s, 1605s, 1467w, 1421m, 1313m, 1283m, 1172m, 1093w, 857w, 769s.

Synthesis of Suzuki-based linkers

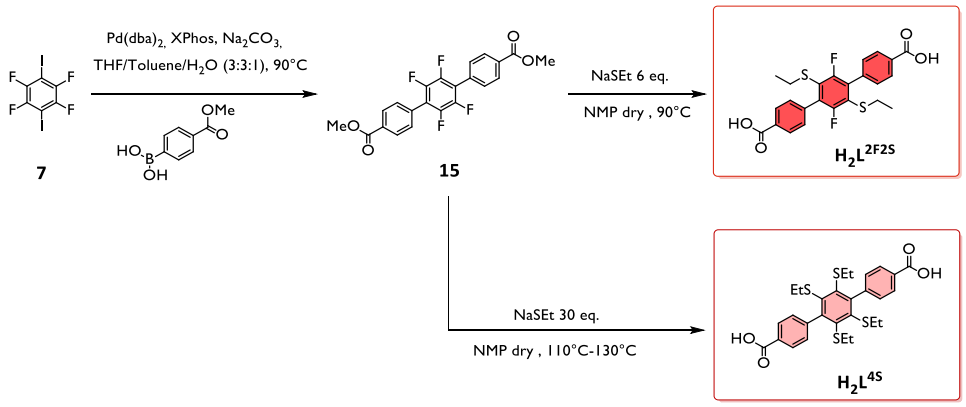

Scheme 8. Synthetic pathways for the synthesis of H_2L^{4S} and H_2L^{2F2S} linkers.

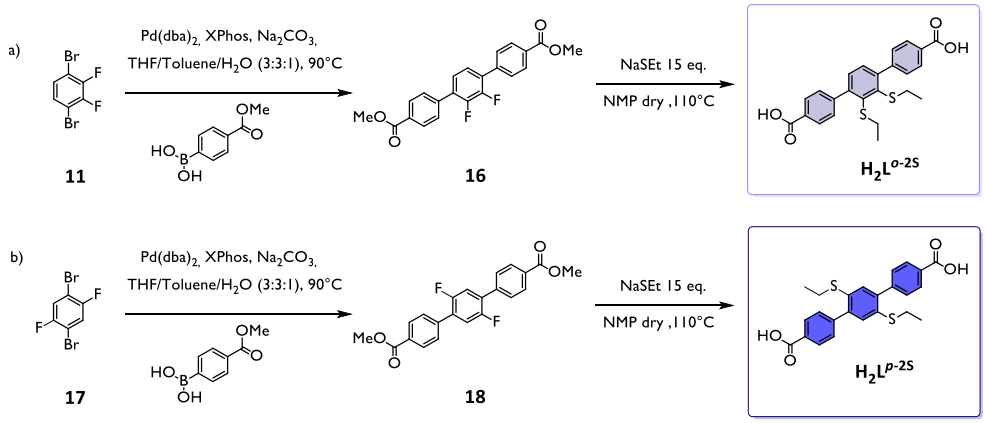

Scheme 9. Synthetic pathways for the synthesis of $H_2L^{o\text{-}2S}$ and $H_2L^{p\text{-}2S}$ linkers.

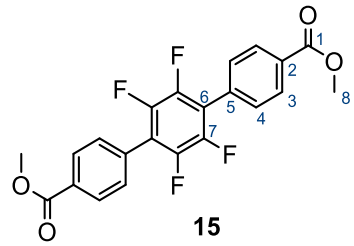

15

Dimethyl 2',3',5',6'-tetrafluoro-[1,1':4',1''-terphenyl]-4,4''-dicarboxylate (15).[176] Under an nitrogen atmosphere 2-dicyclohexylphosphino triisopropylbiphenyl (XPhos) (110 mg, 0.224 mmol, 0.09 eq.), $Pd(dba)_2$ (28.49 mg, 0.049 mmol, 0.02 eq.), Na_2CO_3 (569 mg, 5.35 mmol, 2.15 eq.), 4(methoxycarbonyl)phenyl-boronic acid (0.904 g, 5.02 mmol, 2.02 eq.) and 1,4-diiodotetrafluorobenzene (**7**) (1.010 g, 2.49 mmol), were added to 10 mL toluene, 10 mL THF and 3 mL of water (3:3:1 ratio), previously degassed for 30 minutes. The reaction mixture was heated to 95 °C and stirred for 72 hours. Crystals were formed during the reaction. After cooling to room temperature, the reaction mixture was filtered, the crystals were washed with water, hexane and a little quantity of THF to eliminite the residual of the catalytic system, and dryng under vacuum to yield the pure product (**15**) as white crystals (671 mg, 1.60 mmol, 65%).

^{1}H NMR (400 MHz, $CDCl_2$) δ (ppm): 8.21 (d, J = 8.4 Hz, H_3), 7.64 (d, J = 8.1 Hz, H_4), 3.99 (s, H_8). **^{13}C NMR (101 MHz, $CDCl_3$) δ (ppm):** 166.5 (s, C_1), 145.5-142.7 (m, C_7), 131.82 (s, C_2), 130.86 (s, C_6), 130.27 (s, C_3), 129.84 (s, C_4), 52.39 (s, C_8). **^{19}F NMR (565 MHz, $CDCl_3$) δ (ppm):** -143.23 (s, F_7). **IR (cm^{-1}):** 3025w, 2963w, 1721s, 1613m, 1568w, 1471s, 1428s, 1399s, 1315m, 1277s, 1187m, 1123w, 1105s, 1020m, 960m, 957m, 853s, 804m, 766s, 709s, 666m, 509m.

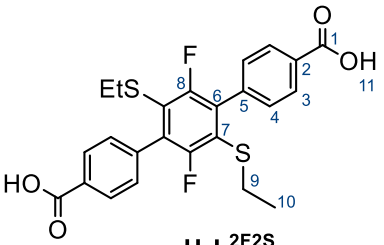

H_2L^{2F2S}

2',5'-bis(ethylthio)- 3',6'-difluoro - [1,1':4',1''-terphenyl] -4,4''-dicarboxylic acid (H_2L^{2F2S}). Under nitrogen atmosphere, sodium ethanethiolate (100 mg, 1.2 mmol, 10.6 eq.) was dissolved in 4 mL of anhydrous NMP. 4F-diester (**15**) (47 mg, 0.113 mmol) was added. The reaction mixture was then stirred and heated at 70 °C for 72 hours and then the reaction mixture was poured into 5 mL of water, and HCl was added slowly (pH=2). The precipitate formed was isolated by centrifugation and washed with water yielding the pruduct H_2L^{2F2S} (45 mg, 0.094 mmol, 84 %). Single crystal suitable for SCXRD analysis was obtained from DMSO:DCM (2:8).

^{1}H NMR (600 MHz, DMSO-d_6) δ (ppm): 8.06 (d, J = 8.2 Hz, H_3), 7.51 (d, J = 8.3 Hz, H_4), 2.70 (q overlapped, H_9), 1.02 (t, J = 7.3 Hz, H_{10}). **^{19}F NMR (565 MHz, DMSO-d_6) δ (ppm):** -108.6 (s, F_8).

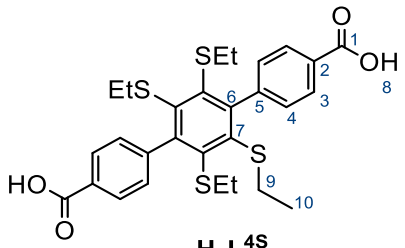

H_2L^{4S}

2',3',5',6' - tetrakis(ethylthio) - [1,1':4',1''-terphenyl] -4,4''-dicarboxylic acid (H_2L^{4S}). Under nitrogen atmosphere, 4F-diester (**15**) (158 mg, 0.360 mmol) reacted with sodium ethanethiolate in 13 mL of anhydrous NMP at 135°C for 72 hours. The sodium ethanethiolate (0.904 g, 10.8 mmol, 30 eq.) was added portionwise during the 72 h for a total amount of 30 equivalents respect to **15**. After the required time water was added (10 mL) and HCl to protonate the carboxylates. The precipitate formed was isolated by

centrifugation and washed with water and acetone yielding a mixture of $\mathbf{H_2L^{2F2S}}$ and $\mathbf{H_2L^{4S}}$ (determined from ^{1}H-NMR). Single crystal of $\mathbf{H_2L^{4S}}$ suitable for SCXRD analysis was obtained from slow evaporation (DMSO:Acetone ratio 2:8).

^{1}H NMR (400 MHz, DMSO-d_6) δ (ppm): 13.10 (brs, H_8), 7.99 (d, J = 8.2 Hz, H_3), 7.35 (d, J = 8.3 Hz, H_4), 2.60 (q, J = 7.4 Hz, H_9), 0.92 (t, J = 7.4 Hz, H_{10}).

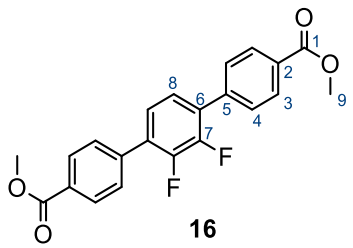

16

Dimethyl 2',3'-difluoro-[1,1':4',1''-terphenyl]-4,4''-dicarboxylate (16). Under an nitrogen atmosphere 2-dicyclohexylphosphino triisopropylbiphenyl (XPhos) (175 mg, 0.367 mmol, 0.10 eq.), $Pd(dba)_2$ (35.0 mg, 0.060 mmol, 0.02 eq.), Na_2CO_3 (871 mg, 8.22 mmol, 2.13 eq.), (4-(methoxycarbonyl)phenyl)boronic acid (1.41 g, 7.83 mmol, 2.03 eq.) and 1,4-dibromo-2,3-difluorobenzene (**11**) (1.055 g, 3.86 mmol), were added to 12 mL toluene, 12 mL THF and 4 mL of water (3:3:1 ratio), previously degassed for 30 minutes. The reaction mixture was heated to 95 °C and stirred for 72 hours. After cooling to room temperature, white crystals were formed and were filtered and washed with water, hexane and a little quantity of THF to eliminite the residual of the catalytic system. The crystals were dried under vacuum to yield the pure product (**16**) (1.327 g, 3.47 mmol, 90%).

^{1}H NMR (400 MHz, $CDCl_3$) δ (ppm): 8.15 (d, J = 8.4 Hz, H_3), 7.68 (d, J = 8.1 Hz, H_4), 7.36 – 7.30 (m, H_8), 3.96 (s, H_9). **^{13}C NMR (101 MHz, $CDCl_3$) δ (ppm):** 166.7 (s, C_1), 149.9-147.2 (m, C_7), 138.9 (s, C_2), 129.94(s, C_5), 129.92(s, C_3), 129.50 (m, C_6), 128.88(s, C_4), 124.86 (t, J=3.4 Hz, C_8), 52.3 (s, C_9). **^{19}F NMR (565 MHz, $CDCl_3$) δ (ppm):** -141.79 (s, F_7). **IR (cm^{-1}):** 3028w, 1718s, 1609m, 1461m, 1400m, 1314w, 1277brs, 1181m, 1106brs, 1019m, 958m, 860m, 817m, 761s, 705s, 698s, 615m, 482w.

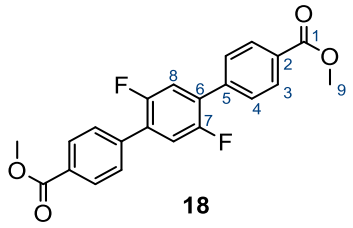

18

Dimethyl 2',5'-difluoro-[1,1':4',1''-terphenyl]-4,4''-dicarboxylate (18). Under an nitrogen atmosphere 2-dicyclohexylphosphino triisopropylbiphenyl (XPhos) (113 mg, 0.26 mmol, 0.09 eq.), $Pd(dba)_2$ (23.0 mg, 0.039 mmol, 0.01 eq.), Na_2CO_3 (551 mg, 5.25 mmol, 2.00 eq.), (4-(methoxycarbonyl)phenyl)boronic acid (0.933 g, 5.18 mmol, 1.97 eq.) and 1,4-dibromo-2,5-difluorobenzene (**17**) (0.714 g, 2.63 mmol), were added to 10 mL toluene, 10 mL THF and 4 mL of water (3:3:1 ratio), previously degassed for 30 minutes. The reaction mixture was heated to 95 °C and stirred for 48 hours. After cooling to room temperature, white crystals were formed and were filtered and washed with water, hexane and a little quantity of THF to eliminite the residual of the catalytic system. The crystals were dried under vacuum to yield the pure product (**18**) (0.725 g, 1.90 mmol, 72%).

^{1}H NMR (400 MHz, $CDCl_3$) δ (ppm): 8.14 (d, *J* = 8.4 Hz, H_3), 7.67 (d, *J* = 8.1 Hz, H_4), 7.31 (t, *J* = 8.4 Hz, H_8), 3.96 (s, H_9). **^{13}C NMR (101 MHz, $CDCl_3$) δ (ppm):** 166.7 (s, C_1), 156.9-154.5 (m, C_7), 138.7 (s, C_2, C_5), 129.9 (s, C_3), 128.9 (s, C_4), 128.7 (m, C_6), 117.9-117.5 (m, C_8), 52.3 (s, C_9). **^{19}F NMR (565 MHz, $CDCl_3$) δ (ppm):** -122.5 (s, F_7). **IR** (cm^{-1}): 3058w, 2990w, 2951w, 1715s, 1608m, 1525w, 1489m, 1435m, 1393m, 1318w, 1281s, 1191w, 1179m, 1194s, 1014w, 914w, 854m, 794m, 768s, 705s, 632w.

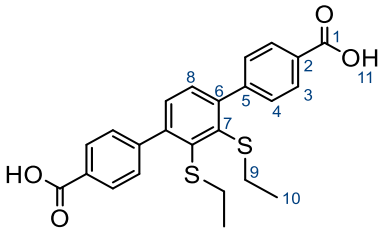

$H_2L^{o\text{-}2S}$

2',3'-bis(ethylthio)-[1,1':4',1''-terphenyl]-4,4''-dicarboxylic acid ($H_2L^{o\text{-}2S}$). Under nitrogen atmosphere, sodium ethanethiolate (0.732 g, 25.3 mmol, 10.7 eq.) was dissolved in 30 mL of anhydrous NMP. When NaSEt was completely dissolved in NMP, diester (**16**) (0.403 g, 1.05 mmol) was added. The reaction mixture was then stirred and heated at 110 °C for 24 hours and then a second addition of NaSEt was done (0.542 g, 6.44 mmol, 2.7 eq.). The system was heated at 110°C for two more days and then the reaction mixture was poured into 20 mL of water, and citric acid was added slowly with vigorous stirring (pH=2). The resultant solid was isolated by centrifugation, was washed with water and acetone, and dried under vacuum. The white solid product $\mathbf{H_2L^{o\text{-}2S}}$ obtained was pure and was used for the synthesis of MOFs (0.375 g, 0.855 mmol, 81%). The scale-up synthesis of $\mathbf{H_2L^{o\text{-}2S}}$ was done with 900 mg of compound (**16**) and 20 equivalents of freshly synthetized NaSEt with three additions over the three days of reaction. Single crystals of $\mathbf{H_2L^{o\text{-}2S}}$ suitable for SCXRD analysis were obtained with slow evaporation method from DMSO or from DMF.

^{1}H NMR (400 MHz, DMSO-d_6) δ (ppm): 13.04 (brs, H_{11}), 8.02 (d, J = 8.3 Hz, H_3), 7.58 (d, J = 8.4 Hz, H_4), 7.37 (s, H_8), 2.51 (overlapped q, H_9), 0.91 (t, J = 7.4 Hz, H_{10}). **^{1}H NMR (400 MHz, Acetone-d_6) δ (ppm):** 11.32 (brs, H_{11}) 8.12 (d, J = 8.4 Hz, H_3), 7.63 (d, J = 8.4 Hz, H_4), 7.40 (s, H_8), 2.60 (q, J = 7.4 Hz, H_9), 0.99 (t, J = 7.4 Hz, H_{10}). **^{13}C NMR (101 MHz, DMSO-d_6) δ (ppm):** 167.63 (s, C_1), 146.3 (s, C_2), 146.2 (s, C_5), 139.2 (s, C_7), 130.5 (s, C_8), 130.0 (s, C_6), 129.9 (s, C_4), 129.5 (s, C_3), 30.4 (s, C_9), 14.6 (s, C_{10}). **ESI-MS (p.i., CH_3OH, m/z): 437.0 $[M\text{-}H]^-$, 875.3 $[2M\text{-}H]^-$. IR** (cm^{-1}): 2962w, 2925w, 2669w, 2552w, 1678s, 1606s, 1567m, 1423s, 1374w, 1319m, 1296s, 1182m, 1133w, 1105w, 1014w, 938brm, 869m, 826m, 789s, 705s, 550m, 535m.

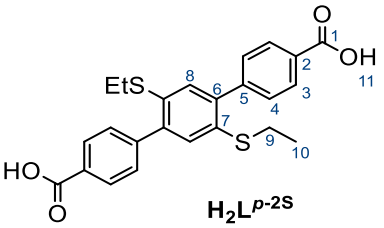

$H_2L^{p\text{-}2S}$

2',5'-bis(ethylthio)-[1,1':4',1''-terphenyl]-4,4''-dicarboxylic acid ($H_2L^{p\text{-}2S}$). Under nitrogen atmosphere, sodium ethanethiolate (1.02 g, 12.2 mmol, 11.6 eq.) was dissolved in 30 mL of anhydrous NMP. When NaSEt was completely dissolved in NMP, diester (**18**) (0.400 g, 1.05 mmol) was added. The reaction mixture was then stirred and heated at 110 °C for 72 hours and then the reaction mixture was poured into 20 mL of water, and citric acid was added slowly with vigorous stirring (pH=2). The precipitate formed was isolated by centrifugation and washed with water. The crude mixture was purified with an extraction with acetone to separate the unreacted species (insoluble in acetone) from the pruduct $H_2L^{p\text{-}2S}$ (soluble in acetone). The resulting organic phase was dried under vacuum to yield a yellow solid. Single crystal suitable for SCXRD analysis was obtained from DMSO:Acetone mixture (2:8).

^{1}H NMR (400 MHz, DMSO-d_6) δ (ppm): 13.04 (brs, H_{11}), 8.02 (d, J = 8.3 Hz, H_3), 7.57 (d, J = 8.3 Hz, H_4), 7.26 (s, H_8), 2.87 (q, J = 7.3 Hz, H_9), 1.14 (t, J = 7.4 Hz, H_{10}). **^{13}C NMR (101 MHz, DMSO-d_6) δ (ppm):** 167.05 (s, C_1), 143.80 (s, C_6), 140.26 (s, C_5), 132.09 (s, C_7), 130.01 (s, C_2), 129.46 (s, C_3), 129.14 (s, C_4), 128.77 (s, C_8), 26.34 (s, C_9), 13.57 (s, C_{10}),. **IR** (cm^{-1}): 2971brw, 2670brw, 1683s, 1608m, 1524w, 1422m, 1393w, 1319m, 1288s, 1168w, 1014m, 856m, 769s, 705m, 552m.

4.3.3 UiO-68 synthesis

UiO-68-2S. Benzoic acid (376 mg, 3.08 mmol, 30 eq.), zirconyl chloride octahydrate (0.031 g, 0.102 mmol, 1 eq.) and DMF (4 ml) were added to a 20 ml PYREX tube and sonicated for 15 minutes. H_2L^{o2S} (0.045 g, 0.102 mmol) and 5.56 mmL of H_2O (0.308 mmol, 3 eq.) were added and were sonicated until all the ligand was solubilized. The pyrex tube is heated at 120 °C in the bath oil for 4 days and then was slowly cooled to room temperature. The bulk microcrystalline powder was isolated by centrifugation and washed twice with fresh DMF and three times with acetone, before being activated under vacuum at 60°C per 48 hours. UiO-68-2S material was obtained as off-white microcrystalline powder with 42% of yield. The detailed tests done are explained in Appendix III.

IR (cm^{-1}): 2960w, 2924w, 1596m, 1549m, 1408s, 1258w, 1180w, 1150w, 1016w, 781m, 707s, 683s, 551w, 454s.

UiO-68-2S2F. Benzoic acid (80 mg, 0.655 mmol, 22 eq.), $ZrCl_4$ (6.99 mg, 0.030 mmol, 1 eq.) and DMF (1 mL) were added to a 10 ml PYREX tube and sonicated for 15 minutes. H_2L^{2F2S} (14.23 mg, 0.030 mmol) was added and the vessel was sonicated until all the ligand was solubilized. The pyrex tube is heated at 120 °C in the bath oil for 48 hours and then was slowly cooled to room temperature. The microcrystalline powder was isolated by centrifugation and washed twice with fresh DMF and three times with acetone, before being activated under vacuum at 670°C per 24 hours. UiO-68-2F2S material was obtained as pale-yellow microcrystalline powder.

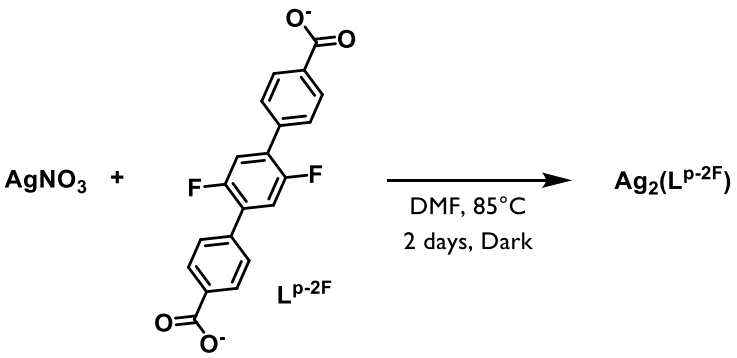

Ag coordination polymer [Ag_2L^{p-2F}]. In a 30 mL sealed tube were added 9.34 mg of L^{p-2SF} (0.025 mmoL), 15.96 mg of $AgNO_3$ (0.8 mmol, 3 eq.) and 5 mL of DMF. The mixure was sonicated in order to solubilize the ligand and the sealed tube was placed in oven at 80°C for 48 hours in the dark. After that time, the system was cooled at 10°C/min to return to room temperature. Single crystal suitable for X-ray diffraction were found in the mother liquid and analyzed with synchrotron facility.

4.3.4 UiO-68 functionalization

Functionalization with transition metals

General Procedure: In 20 mL-schlenk tube under nitrogen 10 mg of UiO-68-2S were added. A solution of the desidered metal (0.158 mmol) were added (3-4 mL). The system was evacuated with three freeze and thaw cycles and were stirred at r.t. for 3 days. The resulting solid were isolated for centrifugation and washed with DMF and a volatile solvent. The solid was dried under vacuum at 60°C for 3 days. For the metal precursor used see Appendi III, Figure C28.

4.4 Results and discussion

4.4.1 Synthesis of phosphorous-based ligands

The large majority of the MOFs described in literature are assembled from rigid linkers, usually synthesized by Suzuki, Sonogashira or Buchwald-Hartwig coupling reactions; indeed, the use of more flexible ligands is much less investigated (Figure 60). Moreover, the presence of unsaturated alkene can also be used as reactive sites for postsynthetic modification of MOFs.

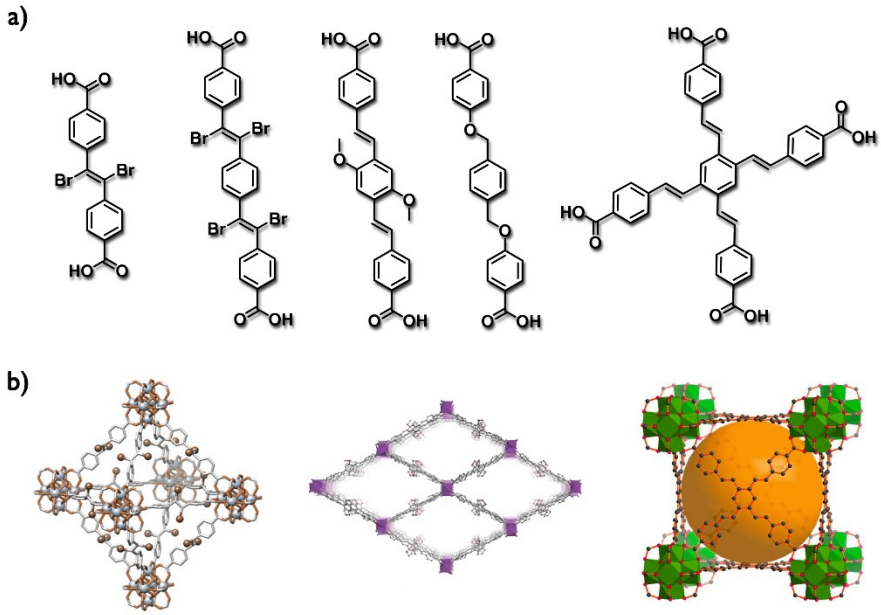

Figure 60. a) Example of flexible carboxylic ligands used in MOF synthesis. b) Zirconium and Yb^{3+}-based MOFs with alkene as ligands.[177–180]

Interestingly, only few examples of phosphines functionalization in MOFs have been reported to our knowledge.[181] Falkowski *et al.* developed in 2014 a chiral MOFs for asymmetric catalysis in which the ligand is a BINAP-derived dicarboxylate molecule (Figure 61). Post-synthetic modification allowed then to incorporate ruthenium and rhodium metals exploiting the P,P donor system of BINAP.

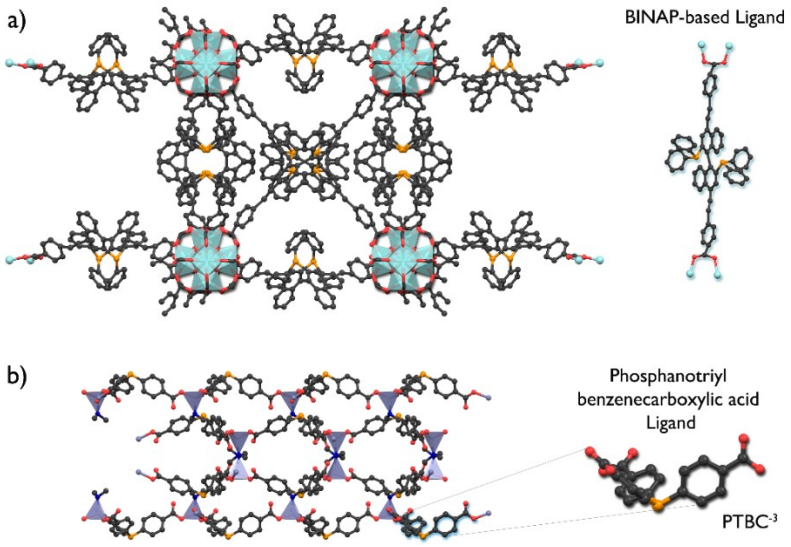

Figure 61. Examples of phosphine-based metal organic frameworks. a) BINAP-based chiral zirconium MOFs. b) PPh_3-based zinc MOFs.[182,183]

Inspired by the work of Falkowski *et al.* we decided to focus our attention on dicarboxylate ligands bearing chelating phenyphosphine groups such as BINAP. Our synthetic strategy involved the synthesis of the dicarboxylate scaffold by Sonogashira coupling of 1,2,4,5-tetrafluoro-3,6-diiodobenzene with the methyl 4-ethynylbenzoate (see Figure Scheme 6 and Scheme 10), followed by the deprotection of the ester groups in quantitative yield.

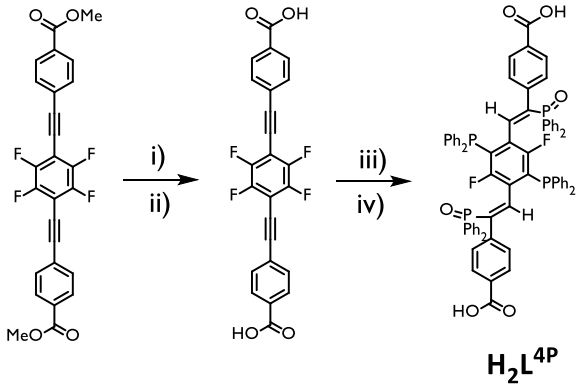

Scheme 10. Synthetic plan for $\mathbf{H_2L^{4P}}$ ligand. i) NaOH (15 eq.); THF, H_2O, 80°C, 24 h, ii) HCl conc.; iii) 18-Crown-6 (5.17 eq.), $KPPh_2$ 0.5M/THF (4.5 eq.), anhydrous THF, 80°C, 24 h; iv) Citric Acid (pH=2).

The functionalization of the phosphines to the scaffold was accomplished with a nucleophilic aromatic substitution using $KPPh_2$ as nucleophile as previously done for phosphine monomers of $\mathbf{P6_{Fe}}$ polymer (see Section 3.4.1). It has to be pointed out that using 4.5 equivalents of potassium diphenylphosphide did not led to the tetrasubtituted product, in which all fluorine are replaced by PPh_2 groups. Instead, due to the large steric hindrance of the phenyl groups, only two fluorine atoms on the central aromatic ring were substituted. The excess of $KPPh_2$ reacted with the alkyne moieties of the molecule, yielding $\mathbf{H_2L^{4P}}$ ligand in which two alkene and four aryl phosphine functionalities are present. This second reactivity of $KPPh_2$ has been observed by other research groups mainly involving the nucleophilic addition of phosphines to alkynes,[184–186] catalysed by a base or with activated phosphine oxides (Figure 62a).

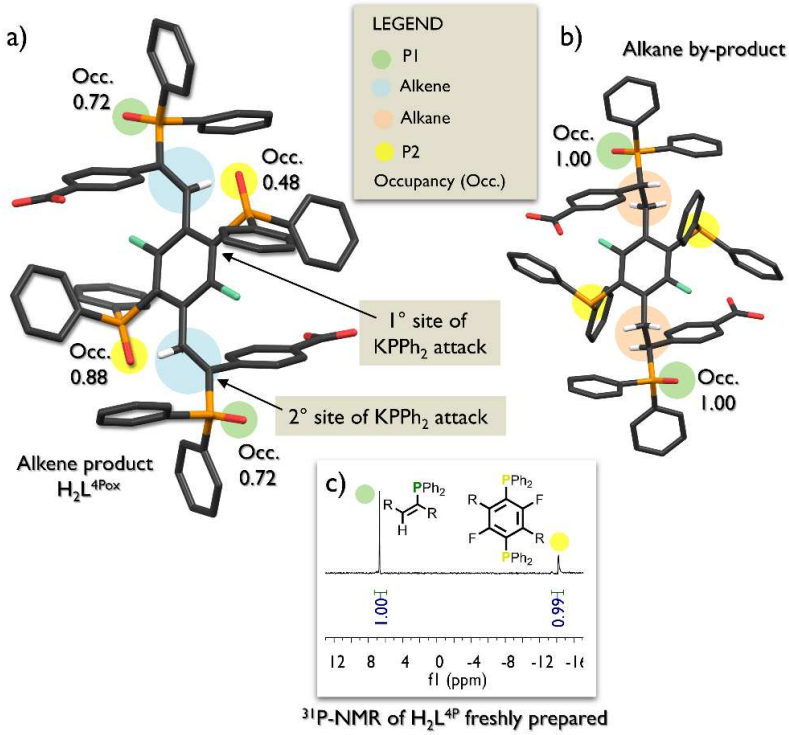

Figure 62. Schematic representation of the reactivity of $KPPh_2$ in this study. a) Main product $\mathbf{H_2L^{4P}}$ showing the partial oxidation of phosphine groups. b) Alkane by-product from the reduction of alkynes. c) ^{31}P-NMR (162 MHz, CD_2Cl_2) of freshly prepared $\mathbf{H_2L^{4P}}$ (and stored under N_2). Colour Code P [Orange], F [Green], O [Red], S [yellow], C[Black].

The $\mathbf{H_2L^{4P}}$ ligand structure was investigated by ^{31}P-, ^{1}H, ^{13}C- NMR and also with single crystal X-ray diffraction (see Appendix III). ^{31}P-NMR of the freshly prepared and stored under nitrogen atmosphere ligand shows the presence of two peaks at -14.24 ppm and +6.68 ppm (Figure 62c). In analogy of DFDPPB moiety (that shows a multiplet at -18 ppm), the first peak could be assigned to the reduced phosphorous(III) atoms on the central phenyl ring, observed also by shape of the peak (multiplet) due to coupling with fluorine. Instead, the singlet peak at +6.68 ppm was assigned to the phosphorous(III) atoms on the alkenes.

If the compound is handled under normal laboratory conditions (and not under inert atmosphere), especially in solution, the phosphine groups on the alkenes are easily oxidized, followed by the oxidation of the phosphines on the central aromatic ring. The partial oxidation of the phosphines with time could be observed by the different occupancy of the oxygen atoms in the SCXRD structure, that is not equal to 1 (Figure 62a).

Moreover, the $KPPh_2$ reactivity on this system could also involve the double reduction of the alkyne to generate the alkane. In fact, we were able to find in solution a little amount of the alkane by-product, which was then crystallized from absolute ethanol. The SCXRD stucture revealed the alkane functionality and the fully oxidized peripheral P-atoms (P1, Figure 62b), implying that the oxidation of the P2 atoms is promoted when the ligand is in solution (e.g. in the crystallization solvent: EtOH or DMSO) and not during the synthesis. The fully characterization of the ligand $\mathbf{H_2L^{4P}}$ can be found in the Appendix III Figure C1-6.

The single crystal structure of the ligand in its partially oxidized form was investigated. Crystals suitable for analysis were obtained from slow evaporation of a solution of the ligand in DMSO/DCM. The analysis showed that, with respect to the alkyne reagent, the compound has lost its rigid and linear structure as shown in Figure 63b.

A preliminary study was done to evaluate the tendency of this ligand to form complexes with metal ions. In particular, we preliminary investigated the interaction with zinc. The results are shown in Appedinx III-Figure C26, and the PXRD analysis confirmed the formation of a crystalline compound between H_2L^{4P} and $Zn(NO_3)_2 \cdot 6H_2O$ as metal precursor.

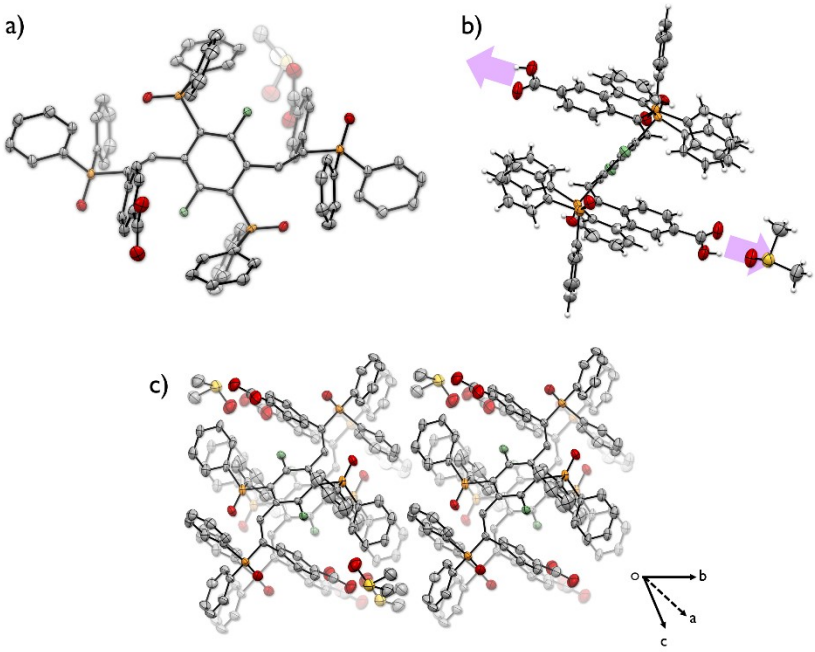

Figure 63. a) Molecular unit of fully oxydized $\mathbf{H_2L^{4P}}$ ligand. b) View of $\mathbf{H_2L^{4P}}$ highlighting the carboxylic site of potential binding with metal ions. c) Packing of $\mathbf{H_2L^{4P}}$. Hydrogen atoms are omitted for clarity. Color Code P [Orange], F [Green], O [Red], S [yellow], C[Grey].

4.4.2 Synthesis of sulphur-based ligands

With the purpose to explore different sulphur-based linker for the synthesis of sulphur functionalized MOFs, we focused our attention on two typologies of skeleton characterized by different lengths between the two carboxylic functions. The first type involves a scaffold built from Sonogashira coupling incorporating two alkyne moieties. The second type is built from Sukuki coupling giving a triphenyl-4,4′-dicarboxylic acid-based ligands (Figure 64).

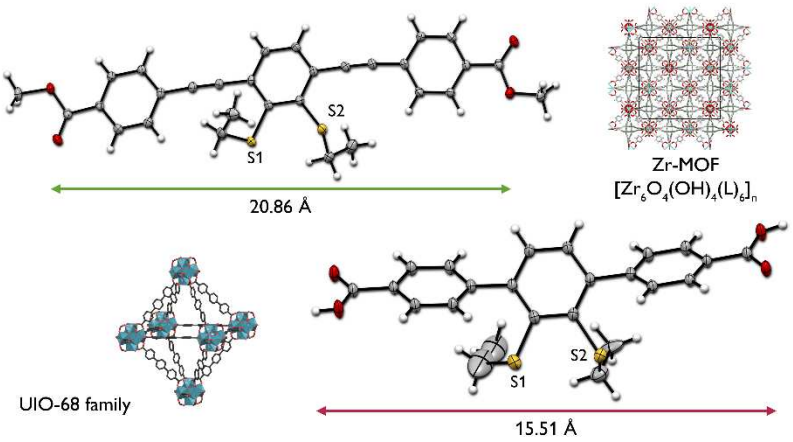

Figure 64. Sonogashira-derived linker precursor and the corresponding zirconium MOFs family (above). Suzuki-derived linker and the corresponding UiO-68 family of MOFs (below).

Sonogashira-based ligands

Sonogashira-based ligand synthetized in this study are illustrated in Figure 65 and the overall synthetic pathway are reported in Scheme 7. Both **14a** and **14b** linkers were obtained from the addition of sodium ethanethiolate to 1,4-dibromo-2,3-difluorobenzene and the following Sonogashira coupling to synthetize the main scaffold. Different synthetic conditions were explored to perform the coupling in order to avoid the formation of the homocoupling by-product and to increase the yield. We eventually selected the $Pd(PPh_3)_2Cl_2$/CuI catalytic system with Et_3N as solvent and base. The presence of sulphur on the central aromatic ring makes this type of coupling very difficult to perform, with a consequent decrease

of the total yield of the reaction, compared to the same reaction but with electron-withdrawing group (EWG) substituents such as four fluorine atoms. Nevertheless, the introduction of the thioether functions after the coupling reaction is not possible due to the attack of the triple bonds by the sulphur moiety, as previously observed with $KPPh_2$ as ucleofile.

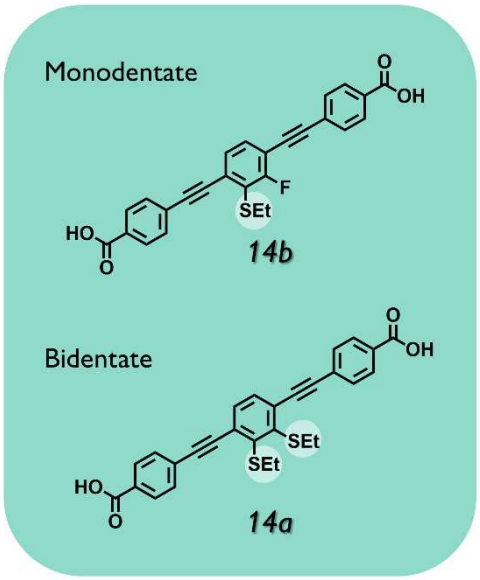

Figure 65. Sonogashira-based ligands with monodentate (**14b**) and bidentate (**14a**) functional group synthetized in this study.

Suzuki-based ligands

The above-mentioned syjthetic problem, derived from the alkyne incompatibility with sodium ethanethiolate, could be avoided by the design of a different scaffold. In particular, we prepared a carboxylate linker composed from three phenyl rings, in which the central one is functionalized with different thioether functions. Even in this case, we explored both monodentate and bidentate functionality as illustrated in Figure 66. The synthetic strategy involved the Suzuki coupling between the 1,4-dibromo-2,3-difluorobenzene and a boronic acid to prepare the corrisponding diester, followed by the one-pot saponification and nucleophilic aromatic substitution to introduce the thiother and the free acids. The retrosynthetic strategy followed is depicted in the Figure 66.

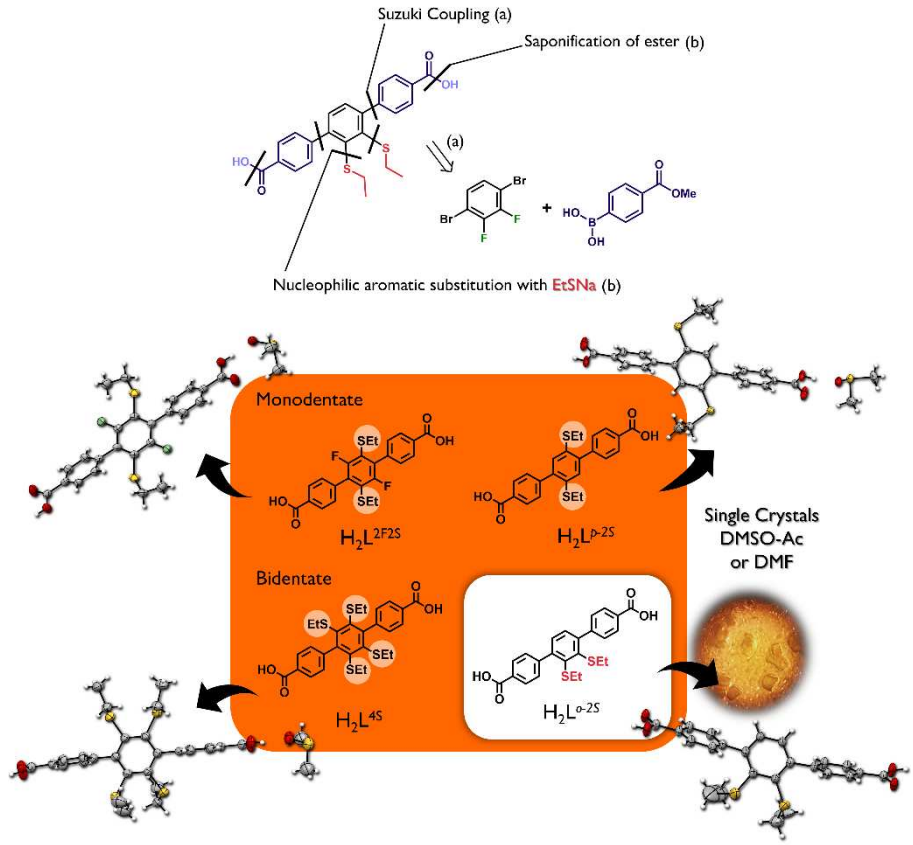

Figure 66. Retrosynthetic route to prepare Suzuki-based linkers (up). Linkers with monodentate (**H_2L^{2F2S}** and **$H_2L^{p\text{-}2S}$**) and bidentate (**H_2L^{4S}** and **$H_2L^{o\text{-}2S}$**) functional group synthetized in this study (down).

The orange panel above showed the 4 linkers synthetized in this study. Among these four ligands the $H_2L^{o\text{-}2S}$ has been obtained with a total yield of 72 % (calculated on 2 steps). Single crystals of thiother linkers were obtained from slow evaporation of the solution of the corresponding ligand and DMSO, using acetone or dichloromethane as anti-solvent. In all the structures it is possible to observe the linear and pre-organized geometry of this ligand with flexible pendant ethylthioether groups. Crystallographic tables are reported in Appendix III.

$H_2L^{o\text{-}2S}$ and H_2L^{2F2S} ligands have been used to obtained UiO-68-2S (see next section) and UiO-68-2F2S (Appendix III, Figure C27) MOFs, respectively.

4.4.3 Synthesis and characterization of UiO-68-2S

In this section we focused on the synthesis of zirconium metal organic framework based on the bidentate linker $H_2L^{o\text{-}2S}$. The framework belongs to the UiO-68 family of MOFs and was named UiO-68-2S according to previous examples of other functionalized UiO-68 materials.[187–189]

UiO-68-2S was initially synthesized according to the procedure reported by Schaate *et al.*[189] for the synthesis of compound UiO-68-NH_2 . In order to increase the dimensions of the crystals, several variations of the solvothermal conditions were performed. Zirconium chloride octahydrate was selected as the metal precursor over zirconium chloride, and the addition of small amount of water showed an increase of the crystallinity of the final product. The optimized experimental conditions involved the solvothermal synthesis at 120°C in sealed tube for 4 days, using 30 eq. of benzoic acid as modulator and 1 eq. of zirconium chloride octahydrate to build the SBU (Figure 67a).

In these conditions, we obtained an off-white microcrystalline powder. The scanning electron microscopy image of the MOF reveals the prismatic microstructure characteristic of UiO architecture. The PXRD analysis showed the successful synthesis of a crystalline material by the comparison between the experimental pattern with the literature data of the same family of UIO-68 MOFs. Characteristic peaks were found at 4.7, 5.4, 7.7, 8.9, 9.4 and 14.2 values of 2θ. The sample was not ground and some preferential orientation was observed, even though the PXRD pattern is comparable with the reference system (Figure 67b).

The material characterization was also performed with infrared spectroscopy (Figure 67c) and thermogravimetric analysis (Figure 67d). The comparison between the FT-IR spectra of the free $H_2L^{o\text{-}2S}$ ligand and the metal organic framework showed the disappearance of the broad O-H stretching band around 3000 cm^{-1} of the acid and the shifting to lower frequencies of the C=O asymmetrical stretching band. Moreover, the coordination to the framework was highlighted by the appearance of the typical carboxylate vibrations between 1596

and 1407 cm^{-1}, as previously observed for the same topologies of UiO-68 frameworks.[190]

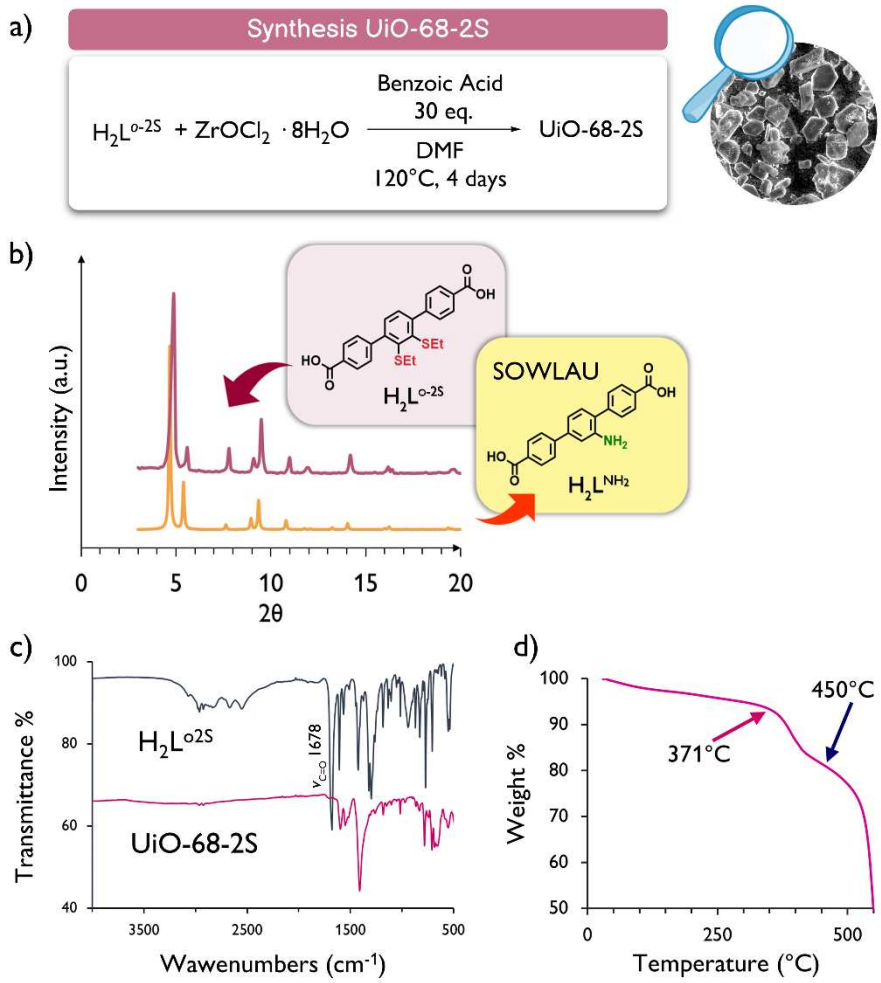

Figure 67. UiO-68-2S framework. a) Solvothermal synthesis of microcrystalline powder. b) Comparison between the experimental PXRD pattern and the simulated one from literature (CCDC refcode SOWLAU). c) Comparison between FT-IR spectra of UiO-68-2S and the corresponding linker. d) TGA (30-550°C, 10°C/min, oxygen flux) analysis of activated material.

The thermal behaviour of UiO-68-2S is characterized by an initial weight loss (3.5%) at low temperature due to the residual solvent inside the pores. The degradation of the organic fraction occurred by two steps degradation at high temperatures. The onset temperature of the first step was about 371°C with a

weight loss of 13 % and the second step started at 428°C with a weight loss of 33% below 550°C. Therefore, the TGA analysis showed the stability of the synthetized network up to 370°C, typical of UIO-68 family.

Adsorption properties of UiO-68-2S

Adsorption properties of the new MOF were investigated through the evaluation of nitrogen and hydrogen uptake at 77 K. UiO-68 analogues usually possess high porous cavities with a total pore volume of about 1.82 cm^3/g [191] with a BET (nitrogen adsorption) surface area of about 2815 m^2/g (UiO-68[192]).

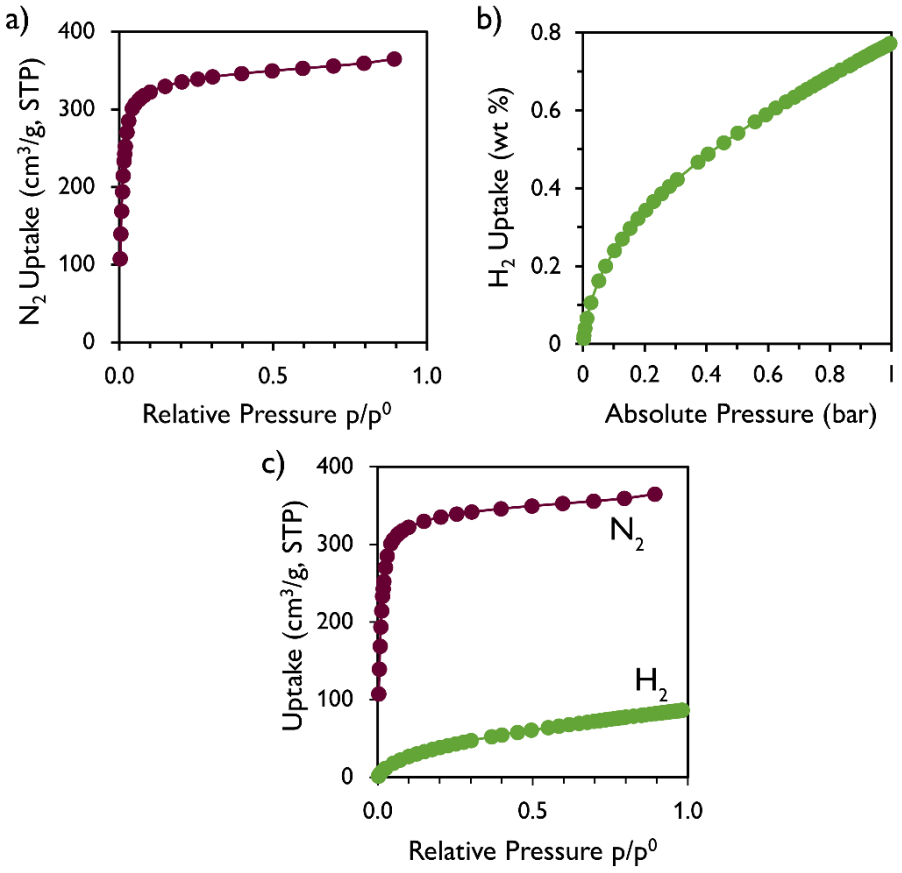

Figure 68. Adsorption properties of UiO-68-2S material. a) N_2 adsorption isotherm at 77 K. b) H_2 low pressure adsorption isotherm at 77 K. c) Comparison between nitrogen and hydrogen uptake at 77 K.

N_2 adsorption isotherm of the sample is reported in Figure 68a. UiO-68-2S displays a type-I N_2 adsorption isotherm with a BET surface area of 1442 m^2/g. This value is lower that the value reported for the parent UiO-68, most probably due to the steric hindrance of the thiother substituents on the central aromatic ring of the linker and for the different activation conditions. However, the high surface area confirmed the porous structure of our materials.

Low pressure H_2 adsorption measurements reveal modest uptake at 77 K of about 0.78 wt% at the pressure of 1 bar (Figure 68b). This value is slightly lower with respect to other type of MOFs such as Al-TCPBP (1.53 wt%)[193], MOF-177 (1.36 wt%)[194] or MOF-5 (1.46 wt%)[195] at similar pressure and temperature. It is interesting to note the comparison between the volumetric amount of nitrogen and hydrogen adsorbed for the same network (Figure 68c). The total amount of hydrogen gas at low pressure is much less that the corresponding quantity of N_2 as shown the reported isotherms. The American department of energy (DOE) established the target value of H_2 adsorption of about 7 wt% at 298 K and 2 bar of pressure in order to be abke to use these materials for hydrogen storage.[196] UiO-68 family of MOFs seems to have quite good behaviour at 77 K but when the hydrogen uptake is measured at room temperature its efficiency is significantly reduced. Interestingly, it is worth noting that even at higher pressure (150 bar), the parent UiO-68 shows only a 0.45 wt% of H_2 uptake at room temperature.[197] These data showed a quite different behaviour of UiO-68 MOF towards nitrogen and hydrogen gas uptake.

4.4.4 UiO-68-2S functionalization with transition metals

As previously investigated for POPs, we evaluated the possibility to incorporate soft transition metals within the cavities of the novel **UIO-68-2S** MOFs. In particular, we focused on palladium, platinum, cobalt and nickel metal ions to bind to the thiother functionality. The schematic strategy performed is depicted in Figure 69a. The impregnation method used involves the freeze and thaw technique and the following soaking of the MOF powder in a solution of metal ions. We tried different metal salts or complexes (see Appendix III for the functionalizations). The counter ion plays a fundamental role in the solubility of the chosen metal precursor, and consequently in the effectiveness of the soaking protocol. For this reason, we used metal salts that are quite soluble in organic solvents such as nickel nitrate (soluble in acetone), or different cobalt salts such as cobalt chloride, nitrate and acetate.

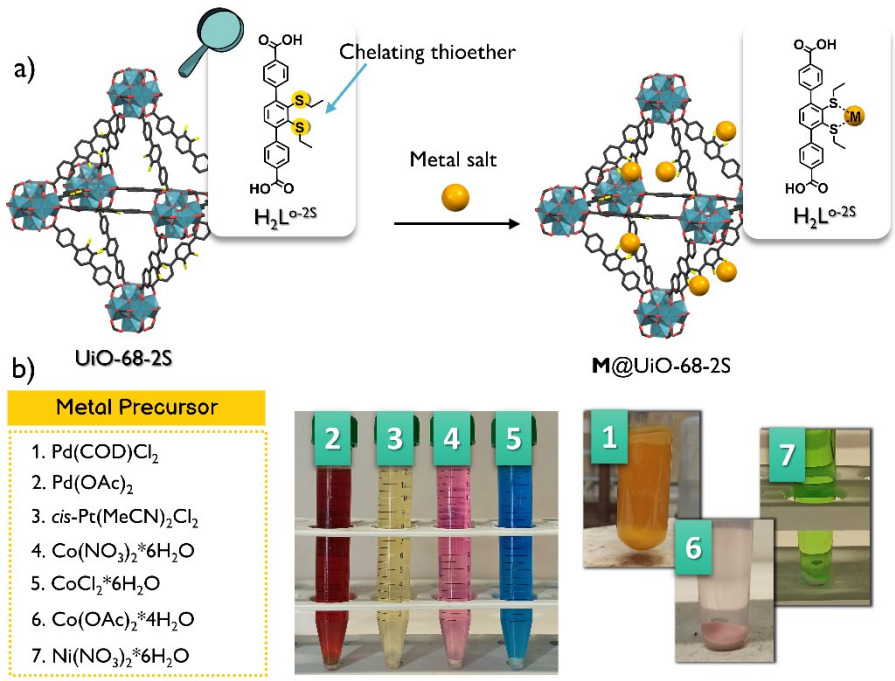

Figure 69. a) Post- synthetic strategies to functionalize **UiO-68-2S** with different transition metal ions. b) Metal precursor used and pictures of the functionalized **M@UiO-68-2S** materials.

As far as palladium and platinum precursor were concerned, we choose *cis* complexes to bind to the chelating system of the thioethers. In particular, $Pd(COD)Cl_2$ and *cis*-$Pt(MeCN)Cl_2$ were synthetized in the laboratory and freshly used for the impregnation method. Another advantage of this complexes was their higher solubility in organic solvents with respect to the correspondent chloride salts. The detailed synthetic conditions are reported in the experimental section and in the Appendix III, Figure C28.

Moreover, a prior evaluation of the functionalized MOFs could be done by the simple observation of the colour change of the powder (Figure 69b). More specifically, the **UiO-68-2S** frameworks changed from white to brownish for **Pd**@UiO-68-2S or to pink for **Co**$(OAc)_2$@UiO-68-2S (Appendix III, Figure C29).

The metal content was investigated through EDX and ICP-AES analyses (see also Appendix III section 3.7 and 3.8). The comparison between the native UiO-68-2S framework and examples of functionalized materials is reported in the figure below.

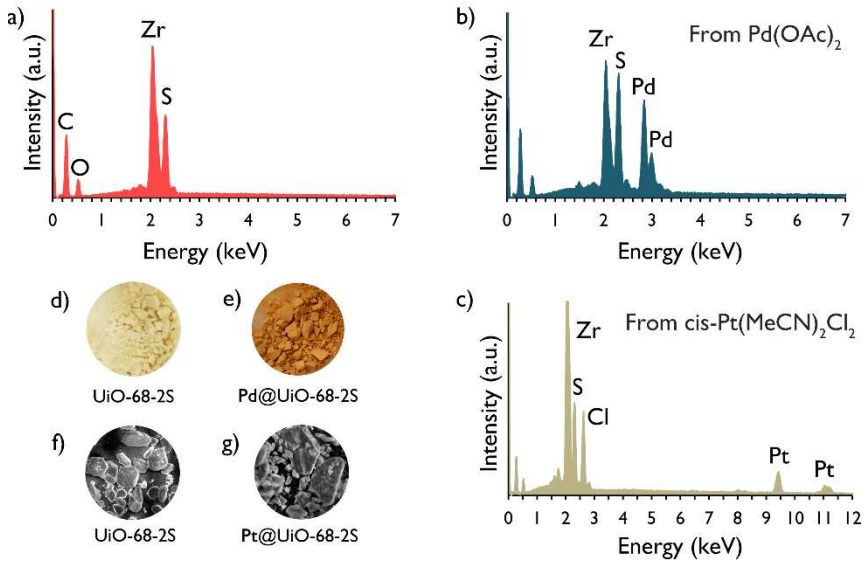

Figure 70. EDX spectra of native **UiO-68-2S** (a), **Pd@UiO-68-2S** (b) and **Pt@UiO-68-2S** (c). **UiO-68-2S** (d) and **Pd@UiO-68-2S** (e) powder. SEM images of **UiO-68-2S** (f) and **Pt@UiO-68-2S** (g).

The EDX spectra showed the presence of zirconium and sulphur peaks, characteristic of the metal cluster and the sulphur functionalization of the linker. Furthermore, in **Pd**@UiO-68-2S, distinctive peaks associated with the $L\alpha$ and $L\beta$ of palladium ions are presents, evidence of the successful incorporation of the metal within the network. This assumption is also confirmed by the ICP analysis that report an amount of palladium of about 4.66 % (w/w) for this sample.

The same was observed for platinum functionalized material (Figure 70c). In this case characteristic peak of platinum are observed at 9.4 ($L\alpha$) and 11.1 keV($L\beta$) with a loading of 5.50 % (w/w).

According to the EDX and ICP results, palladium and platinum ions showed more tendency to be incorporated in the UiO-68-2S materials. Indeed, in the case of cobalt, the ratio between Zr and Co was higher, meaning a lower loading and in the case of nickel the loading was only of 0.5 % (w/w). The low loading was also observed by the pale colour of the functionalized materials (Appendix III, EDX section).

4.4.5 Preliminary results of the electrochemical studies

We evaluated the stability and the activity of the metallated MOFs in electrochemical conditions. We initially focused on the **$Ni(NO_3)_2$@UiO-68-2S** system and investigated its activity toward two main process: 1) hydrogen evolution reaction (HER) and 2) carbon dioxide reduction reaction (CO2RR). When investigating the HER, it is important to explore the reaction at various pH values. Indeed, up to now, the majority of the HER catalysts work in acidic media (high proton concentration) and with noble metals such as Pt, Pd, Ag, Ru. The HER activity in basic conditions is less studied but it can actually open the possibility to investigate more abundant and cheaper transition metals.[198]

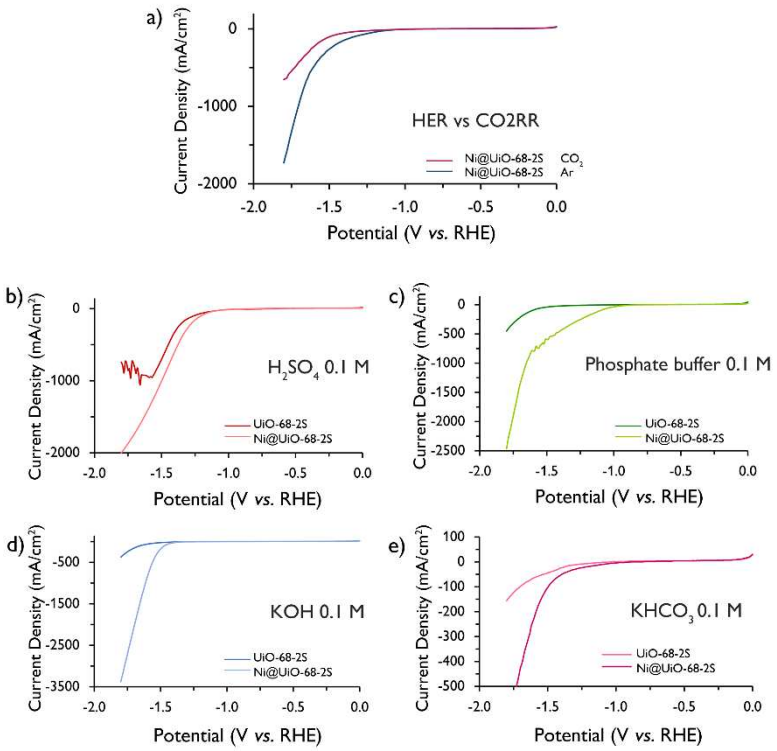

Figure 71. LSV measurements of **UiO-68-2S** and **$Ni(NO_3)_2$@UiO-68-2S**. HER activity at pH 1 (b), pH 7 (c) and pH 11 (d) in argon. CO2RR activity in $KHCO_3$ 0.1 M under CO_2 (e) and comparison between the HER and the CO2RR process in 0.1M $KHCO_3$ (a).

The HER performance was carried out in argon atmosphere at three different pH using H_2SO_4, phosphate buffer and KOH 0.1 M as electrolytes. As it is shown in Figure 71, the linear-sweep voltammetry (LSV) of the **Ni(NO$_3$)$_2$@UiO-68-2S** and the native MOFs were measured. Ni@MOFs diplays no difference from the native **UiO-68-2S** at low pH in H_2SO_4. On the contrary at neutral and basic pH in argon, there is a significant difference between **UiO-68-2S** vs **Ni@UiO-68-2S**, especially at basic pH. However, the overpotential is still high. A possible application of this material in basic condition may therefore be evaluated in the next future.

As far as CO2RR is concerned, this electrochemical transformation is extremely important to reduce the CO_2 level in the air and to convert the huge amount of CO_2 produced into new useful chemicals. One of the main problems related to that process is the selectivity. In aqueous conditions the HER process is also present, especially at low overpotential for several materials.[199] Another challenge is related to the possible products, which can be formed in the CO2RR reaction. For example, from the electron transfer of two electrons we can produce formic acid or carbon monoxide, resulting in a different mechanism of the process that can led to more complex molecules such as alcohols and hydrocarbons. This pathway is difficult to achieve but it is the most desirable from the industrial point of view. The initial CO2RR catalysts were mainly molecular materials or metal-based ones, but in recent years more and more examples of single atom catalyst based on abundant metals or metal organic frameworks are studied. Different topologies of MOFs were investigated, in particular H-KUST1 family that showed promising results toward the formation of more energetic carbon compounds. In our case, the CO2RR performance was carried out under CO_2 in $KHCO_3$ 0.1 M as electrolyte. As is shown from Figure 71d, the linear-sweep voltammetry of the **Ni(NO$_3$)$_2$@UiO-68-2S** and the native MOFs were measured. This primary evaluation showed a difference in the behaviour of the metallated MOF vs the native one, therefore this material could potentially be applied for this transformation. However, as shown in Figure 71a, the main issue seems to be that the materials display higher current under argon then under CO_2. The selectivity of the process seems to go towards hydrogen evolution reaction with respect to CO2RR. The selectivity of the CO_2 reduction process and the Faradaic efficiency through controlled potential electrolysis and with gas chromatography still need to be investigated.

4.5 Conclusion

In the last project, we focused on the design and preparation of metal organic frameworks for electrochemical application. The linker explored were dixarboxylate molecules of different length and geometry, bearing on the central ring different donor systems such as aryl phosphines or thiothers. Some of them was used to build zinc or zirconium frameworks. In particular with the $\mathbf{H_2L^{o\text{-}2S}}$ linker, we successfully synthetized a microcrystalline **UIO-68-2S** porous network with a BET surface area of 1442 m^2/g. The structure, the thermal and adsorption properties of the resulting materials were evaluated showing a stability up to 350°C. In addition, the post synthetic functionalization with different metal ions were performed to generate **Pd**@UiO; **Pt**@UiO, **Co**@UiO and **Ni**@UiO materials, highlighting a different tendency of these metals to be incorporated in the pores exploiting the S,S-donor system of the linkers. Finally, a preliminary investigation of their activity towards HER and CO2RR were studied for **Ni**@UIO-68-2S resulting in an active material, mainly for the HER catalysis.

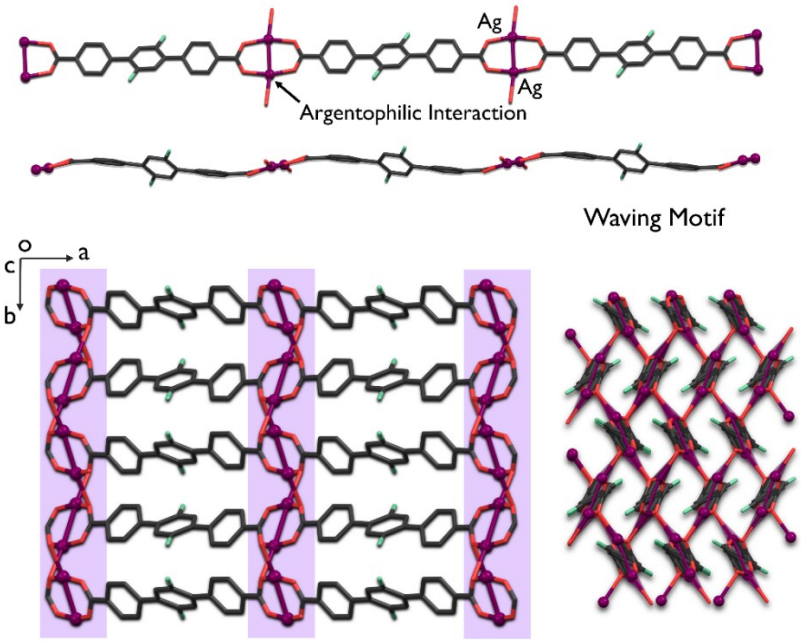

Figure 72. Silver coordination polymer with $\mathbf{L^{p\text{-}2F}}$ ligand exibiting a rod-like topology of the SBUs.

In this study we used mainly the functionalized linkers to form stable structure with zirconium and zinc precursor. Another possibility could be the formation of coordination polymers with these dicarboxylate linkers as reported previously by Sumby *et al.*[200] In particular, using silver combines the interesting luminescent and antimicrobial properties of this metal with the stability of metal organic frameworks due to the use of ligands that can form strong coordination bonds. In particular, rod-like SBUs were employed to obtaine stable structure in the past. Likewise, using one of the linkers synthetized, namely the dicarboxylate $L^{P\text{-}2F}$ we explored this possibility and synthetized a silver coordination polymer based on this rod-like topology (Figure 72). The SCXRD hightlighted the argentophilic interaction between two Ag metal ions and the wave-like organization in the space of the linkers. The silver atom did not present a linear geometry (see Figure 14) but it exhibited a T geometry and bound by three different linker molecules, giving rise to a 3D structure.

5. CONCLUDING REMARKS

In conclusion, in this work we explored crystalline and amorphous materials with the aim to build a catalyst for electrochemical applications. We started from the synthesis and the study of silver complexes organized in architectures with have large channels filled with crystallization solvent, even though without permanent porosity (after the removal of the solvent). We then focused on more stable materials, such as porous organic polymers with amorphous nature and functionalized with cobalt, nickel, molybdenum and iron. These systems are useful as heterogeneous catalyst because they are insolubile in water and in common organic solvents and they are easily to synthetize. The major drawbacks are related to their amorphous nature and consequently to the inability to strictly control their pore size. In the last part we focused on crystalline materials such as MOFs, in which the controlled synthesis allowed to obtain a well-defined framework suitable to interact with transition metal centers, for small molecules electrocatalitic convertion.

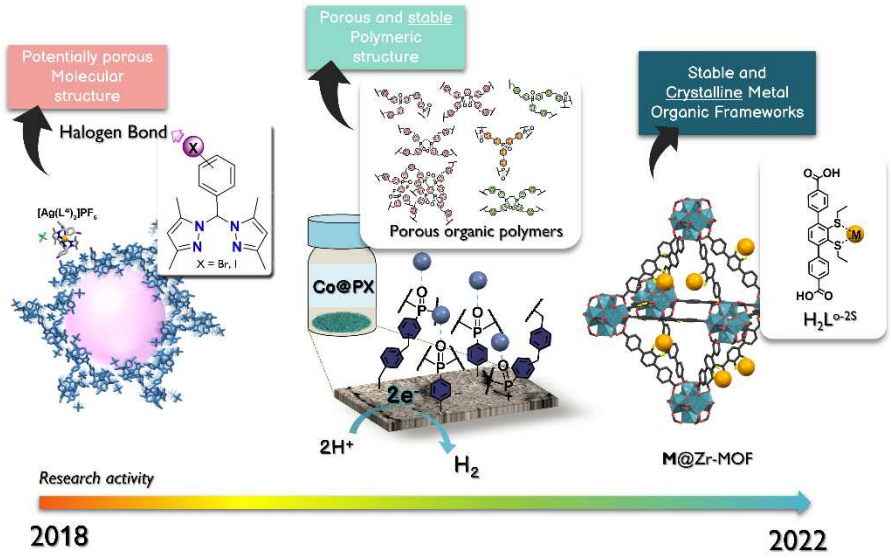

6. BIBLIOGRAPHY

1 M. E. Davis, *Nature*, 2002, **417**, 813–821.

2 F. Schüth and W. Schmidt, *Adv. Mater.*, 2002, **14**, 629–638.

3 F. Fajula, A. Galarneau and F. Di Renzo, *Microporous Mesoporous Mater.*, 2005, **82**, 227–239.

4 H. Furukawa, K. E. Cordova, M. O'Keeffe and O. M. Yaghi, *Science*, 2013, **341**, 1230444.

5 Y. Cui, B. Li, H. He, W. Zhou, B. Chen and G. Qian, *Acc. Chem. Res.*, 2016, **49**, 483–493.

6 P. N. Jiri Cejka, Russell E. Morris, *Zeolites in Catalysis*, Royal Society of Chemistry, Cambridge, **2017**.

7 P. Kumar, A. Das and B. Maji, *Org. Biomol. Chem.*, 2021, **19**, 4174–4192.

8 J. Liang, Z. Liang, R. Zou and Y. Zhao, *Adv. Mater.*, 2017, **29**, 1701139.

9 N. E. R. Zimmermann and M. Haranczyk, *Cryst. Growth Des.*, 2016, **16**, 3043–3048.

10 V. Gold, Ed., *IUPAC. Compendium of Chemical Terminology, 2nd ed. (the 'Gold Book'). Compiled by A. D. McNaught and A. Wilkinson. Blackwell Scientific Publications, Oxford (1997). Online version (2019-) created by S. J. Chalk. ISBN 0-9678550-9-8. https://doi.org/10.1351*, International Union of Pure and Applied Chemistry (IUPAC), Research Triangle Park, NC, 2nd ed.

11 H. Hofmann, K. A., Arnoldi, *Chem. Ber.*, 1906, **39**, 339.

12 D. E. Palin and H. M. Powell, *J. Chem. Soc.*, 1947, 208.

13 H. M. POWELL and J. H. RAYNER, *Nature*, 1949, **163**, 566–567.

14 Y. Shibata, *J. Coll. Sci. Imp. Univ. Tokyo*, 1916, **37**, 1–17.

15 William M. Jolly, J. C. Bailar Jr., in *Preparative inorganic reactions. Volume 1*, Interseience Publishers, 1964, vol. 1, pp. 1–27.

16 M. Fujita, Y. J. Kwon, S. Washizu and K. Ogura, *J. Am. Chem. Soc.*, 1994, **116**, 1151–1152.

17 M. Kondo, T. Yoshitomi, H. Matsuzaka, S. Kitagawa and K. Seki, *Angew. Chemie Int. Ed. English*, 1997, **36**, 1725–1727.

18 S. Kitagawa and M. Kondo, *Bull. Chem. Soc. Jpn.*, 1998, **71**, 1739–1753.

19 K. Barthelet, J. Marrot, D. Riou and G. Férey, *Angew. Chem. Int. Ed.*, 2002, **41**, 281–284.

20 S. S.-Y. Chui, S. M.-F. Lo, J. P. H. Charmant, A. G. Orpen and I. D. Williams, *Science*, 1999, **283**, 1148–1150.

21 H. Li, M. Eddaoudi, M. O'Keeffe and O. M. Yaghi, *Nature*, 1999, **402**, 276–279.

22 O. M. Yaghi, M. O'Keeffe, N. W. Ockwig, H. K. Chae, M. Eddaoudi and J. Kim, *Nature*, 2003, **423**, 705–714.

23 A. P. Côté, A. I. Benin, N. W. Ockwig, M. O'Keeffe, A. J. Matzger and O. M. Yaghi, *Science*, 2005, **310**, 1166–1170.

24 X.-C. Huang, Y.-Y. Lin, J.-P. Zhang and X.-M. Chen, *Angew. Chem. Int. Ed.*, 2006, **45**, 1557–1559.

25 V. A. Davankov and M. P. Tsyurupa, *React. Polym.*, 1990, **13**, 27–42.

26 R. Chinchilla and C. Nájera, *Chem. Rev.*, 2007, **107**, 874–922.

27 P. M. Budd, B. S. Ghanem, S. Makhseed, N. B. McKeown, K. J. Msayib and C. E. Tattershall, *Chem. Commun.*, 2004, 230.

28 M. Carta, K. J. Msayib and N. B. McKeown, *Tetrahedron Lett.*, 2009, **50**, 5954–5957.

29 D. J. O'Hearn, A. Bajpai and M. J. Zaworotko, *Small*, 2021, **17**, 2006351.

30 M. Thommes, K. Kaneko, A. V. Neimark, J. P. Olivier, F. Rodriguez-Reinoso, J. Rouquerol and K. S. W. Sing, *Pure Appl. Chem.*, 2015, **87**, 1051–1069.

31 H. Bildirir, V. G. Gregoriou, A. Avgeropoulos, U. Scherf and C. L. Chochos, *Mater. Horizons*, 2017, **4**, 546–556.

32 E. Van Der Voort, Pascal, Leus, Karen, De Canck, *Introduction to Porous Materials*, John Wiley & Sons Inc, 1st edn., 2019.

33 T. Blasco, A. Corma, M. T. Navarro and J. P. Pariente, *J. Catal.*, 1995, **156**, 65–74.

34 J. Iglesias, J. A. Melero and J. Sainz-Pardo, *J. Mol. Catal. A Chem.*, 2008, **291**, 75–84.

35 Z. Li, Z. Liu, H. Sun and C. Gao, *Chem. Rev.*, 2015, **115**, 7046–7117.

36 V. Georgakilas, J. A. Perman, J. Tucek and R. Zboril, *Chem. Rev.*, 2015, **115**, 4744–4822.

37 P. M. Ajayan, *Chem. Rev.*, 1999, **99**, 1787–1800.

38 J. Lee, O. K. Farha, J. Roberts, K. A. Scheidt, S. T. Nguyen and J. T. Hupp, *Chem. Soc. Rev.*, 2009, **38**, 1450.

39 S.-Y. Ding and W. Wang, *Chem. Soc. Rev.*, 2013, **42**, 548–568.

40 Y.-B. Zhang, J. Su, H. Furukawa, Y. Yun, F. Gándara, A. Duong, X. Zou and O. M. Yaghi, *J. Am. Chem. Soc.*, 2013, **135**, 16336–16339.

41 A. P. Côté, H. M. El-Kaderi, H. Furukawa, J. R. Hunt and O. M. Yaghi, *J. Am. Chem. Soc.*, 2007, **129**, 12914–12915.

42 F. J. Uribe-Romo, C. J. Doonan, H. Furukawa, K. Oisaki and O. M. Yaghi, *J. Am. Chem. Soc.*, 2011, **133**, 11478–11481.

43 K. T. Jackson, T. E. Reich and H. M. El-Kaderi, *Chem. Commun.*, 2012, **48**, 8823.

44 J. Guo, Y. Xu, S. Jin, L. Chen, T. Kaji, Y. Honsho, M. A. Addicoat, J. Kim, A. Saeki, H. Ihee, S. Seki, S. Irle, M. Hiramoto, J. Gao and D. Jiang, *Nat. Commun.*, 2013, **4**, 2736.

45 Q. Fang, Z. Zhuang, S. Gu, R. B. Kaspar, J. Zheng, J. Wang, S. Qiu and Y. Yan, *Nat. Commun.*, 2014, **5**, 4503.

46 P. Kuhn, M. Antonietti and A. Thomas, *Angew. Chem. Int. Ed.*, 2008, **47**, 3450–3453.

47 T. Ben, C. Pei, D. Zhang, J. Xu, F. Deng, X. Jing and S. Qiu, *Energy Environ. Sci.*, 2011, **4**, 3991.

48 I. M. Hönicke, I. Senkovska, V. Bon, I. A. Baburin, N. Bönisch, S. Raschke, J. D. Evans and S. Kaskel, *Angew. Chem. Int. Ed.*, 2018, **57**, 13780–13783.

49 O. K. Farha, I. Eryazici, N. C. Jeong, B. G. Hauser, C. E. Wilmer, A. A. Sarjeant, R. Q. Snurr, S. T. Nguyen, A. Ö. Yazaydın and J. T. Hupp, *J. Am. Chem. Soc.*, 2012, **134**, 15016–15021.

50 D. A. Reed, B. K. Keitz, J. Oktawiec, J. A. Mason, T. Runčevski, D. J. Xiao, L. E. Darago, V. Crocellà, S. Bordiga and J. R. Long, *Nature*, 2017, **550**, 96–100.

51 C. M. McGuirk, R. L. Siegelman, W. S. Drisdell, T. Runčevski, P. J. Milner, J. Oktawiec, L. F. Wan, G. M. Su, H. Z. H. Jiang, D. A. Reed, M. I. Gonzalez, D. Prendergast and J. R. Long, *Nat. Commun.*, 2018, **9**, 5133.

52 J.-R. Li, J. Sculley and H.-C. Zhou, *Chem. Rev.*, 2012, **112**, 869–932.

53 L.-L. Tan, H. Li, Y. Zhou, Y. Zhang, X. Feng, B. Wang and Y.-W. Yang, *Small*, 2015, **11**, 3807–3813.

54 K. Chen, D. Ray, M. E. Ziebel, C. A. Gaggioli, L. Gagliardi and S. C. Marinescu, *ACS Appl. Mater. Interfaces*, 2021, **13**, 34419–34427.

55 S. He, L. Wu, X. Li, H. Sun, T. Xiong, J. Liu, C. Huang, H. Xu, H. Sun, W. Chen, R. Gref and J. Zhang, *Acta Pharm. Sin. B*, 2021, **11**, 2362–2395.

56 S. Brunauer, P. H. Emmett and E. Teller, *J. Am. Chem. Soc.*, 1938, **60**, 309–319.

57 J.-S. Jung, S.-J. Ko, H.-B. Lee, S.-B. Lee, H.-J. Kim and J.-M. Oh, *Polymers (Basel).*, 2019, **11**, 155.

58 A. Tăbăcaru, C. Pettinari, M. Buşilă and R. M. Dinică, *Polymers (Basel).*, 2019, **11**, 1686.

59 J. Barberá, I. Lantero, S. Moyano, J. L. Serrano, A. Elduque and R. Giménez, *Chem. Eur. J.*, 2010, **16**, 14545–14553.

60 D. L. Reger, J. R. Gardinier and M. D. Smith, *Inorg. Chem.*, 2004, **43**, 3825–3832.

61 G. A. Santillan and C. J. Carrano, *Dalt. Trans.*, 2009, 6599.

62 A. Cingolani, Effendy, D. Martini, M. Pellei, C. Pettinari, B. W. Skelton and A. H. White, *Inorganica Chim. Acta*, 2002, **328**, 87–95.

63 D. L. Reger, R. F. Semeniuc and M. D. Smith, *Eur. J. Inorg. Chem.*, 2003, **2003**, 3480–2494.

64 D. L. Reger, R. F. Semeniuc, B. Captain and M. D. Smith, *Inorg. Chem.*, 2005, **44**, 2995–2997.

65 J. R. Gardinier, J. S. Hewage and S. V. Lindeman, *Inorg. Chem.*, 2014, **53**, 12108–12121.

66 C.-L. Chen, B.-S. Kang and C.-Y. Su, *Aust. J. Chem.*, 2006, **59**, 3.

67 M. Gennari, I. Bassanetti and L. Marchiò, *Polyhedron*, 2010, **29**, 361–371.

68 I. Bassanetti and L. Marchiò, *Inorg. Chem.*, 2011, **50**, 10786–10797.

69 I. Bassanetti, F. Mezzadri, A. Comotti, P. Sozzani, M. Gennari, G. Calestani and L. Marchiò, *J. Am. Chem. Soc.*, 2012, **134**, 9142–9145.

70 I. Bassanetti, A. Comotti, P. Sozzani, S. Bracco, G. Calestani, F. Mezzadri and L. Marchiò, *J. Am. Chem. Soc.*, 2014, **136**, 14883–14895.

71 I. Bassanetti, C. Atzeri, D. A. Tinonin and L. Marchiò, *Cryst. Growth Des.*, 2016, **16**, 3543–3552.

72 G. Bonfant, M. Melegari, D. Balestri, F. Mezzadri, V. Marzaroli, I. Bassanetti and L. Marchiò, *Inorg. Chem.*, 2020, **59**, 4140–4149.

73 G. R. Desiraju, J. J. Vittal and A. Ramanan, *Crystal Engineering - A Textbook*, Co-Published with Indian Institute of Science (IISc), Bangalore, India, 2011.

74 G. R. Desiraju, *J. Am. Chem. Soc.*, 2013, **135**, 9952–9967.

75 G. R. Desiraju, *Angew. Chemie Int. Ed. English*, 1995, **34**, 2311–2327.

76 H. Schmidbaur and A. Schier, *Angew. Chem. Int. Ed.*, 2015, **54**, 746–784.

77 G. Cavallo, P. Metrangolo, R. Milani, T. Pilati, A. Priimagi, G. Resnati and G. Terraneo, *Chem. Rev.*, 2016, **116**, 2478–2601.

78 IUPAC, *Chem. Int.*, 2010, **32**, 20–21.

79 C. W. Padgett, R. D. Walsh, G. W. Drake, T. W. Hanks and W. T. Pennington, *Cryst. Growth Des.*, 2005, **5**, 745–753.

80 P. Metrangolo, J. S. Murray, T. Pilati, P. Politzer, G. Resnati and G. Terraneo, *Cryst. Growth Des.*, 2011, **11**, 4238–4246.

81 C. Perkins, S. Libri, H. Adams and L. Brammer, *CrystEngComm*, 2012, **14**, 3033.

82 P. D. Rege, O. L. Malkina and N. S. Goroff, *J. Am. Chem. Soc.*, 2002, **124**, 370–371.

83 D. Cinčić, T. Friščić and W. Jones, *CrystEngComm*, 2011, **13**, 3224.

84 A. De Santis, A. Forni, R. Liantonio, P. Metrangolo, T. Pilati and G. Resnati, *Chem. Eur. J.*, 2003, **9**, 3974–3983.

85 F. C. Pigge, V. R. Vangala, P. P. Kapadia, D. C. Swenson and N. P. Rath, *Chem. Commun.*, 2008, 4726.

86 J. E. Hein, J. C. Tripp, L. B. Krasnova, K. B. Sharpless and V. V. Fokin, *Angew. Chem. Int. Ed.*, 2009, **48**, 8018–8021.

87 G. Alesso, V. Tabernero and T. Cuenca, *J. Organomet. Chem.*, 2012, **717**, 202–210.

88 SMART. Bruker AXS Inc., 2012.

89 TWINABS. Bruker AXS Inc., 2012.

90 L. Krause, R. Herbst-Irmer, G. M. Sheldrick and D. Stalke, *J. Appl. Crystallogr.*, 2015, **48**, 3–10.

91 G. M. Sheldrick, *Acta Crystallogr. Sect. A Found. Adv.*, 2015, **71**, 3–8.

92 G. M. Sheldrick, *Acta Crystallogr. Sect. C Struct. Chem.*, 2015, **71**, 3–8.

93 O. V. Dolomanov, L. J. Bourhis, R. J. Gildea, J. A. K. Howard and H. Puschmann, *J. Appl. Crystallogr.*, 2009, **42**, 339–341.

94 A. L. Spek, *Acta Crystallogr. Sect. C Struct. Chem.*, 2015, **71**, 9–18.

95 C. F. Macrae, I. J. Bruno, J. A. Chisholm, P. R. Edgington, P. McCabe, E. Pidcock, L. Rodriguez-Monge, R. Taylor, J. van de Streek and P. A. Wood, *J. Appl. Crystallogr.*, 2008, **41**, 466–470.

96 V. A. Blatov, A. P. Shevchenko and D. M. Proserpio, *Cryst. Growth Des.*, 2014, **14**, 3576–3586.

97 H. Pfeiffer, A. Rojas, J. Niesel and U. Schatzschneider, *Dalt. Trans.*, 2009, 4292.

98 J. Sun and S. A. Kozmin, *J. Am. Chem. Soc.*, 2005, **127**, 13512–13513.

99 P. Szuroczki, B. Boros and L. Kollár, *Tetrahedron*, 2018, **74**, 6129–6136.

100 M. Yao, J. Zhang, S. Yang, H. Xiong, L. Li, E. Liu and H. Shi, *RSC Adv.*, 2020, **10**, 3946–3950.

101 J. R. Gardinier, H. M. Tatlock, J. S. Hewage and S. V. Lindeman, *Cryst. Growth Des.*, 2013, **13**, 3864–3877.

102 D. Rosiak, A. Okuniewski and J. Chojnacki, *Polyhedron*, 2018, **146**, 35–41.

103 L. Yang, D. R. Powell and R. P. Houser, *Dalt. Trans.*, 2007, **0**, 955–964.

104 B. Li, S.-Q. Zang, L.-Y. Wang and T. C. W. Mak, *Coord. Chem. Rev.*, 2016, **308**, 1–21.

105 D. L. Reger, J. E. Collins, A. L. Rheingold, L. M. Liable-Sands and G. P. A. Yap, *Organometallics*, 1997, **16**, 349–353.

106 J.-S. M. Lee and A. I. Cooper, *Chem. Rev.*, 2020, **120**, 2171–2214.

107 J.-X. Jiang, F. Su, A. Trewin, C. D. Wood, N. L. Campbell, H. Niu, C. Dickinson, A. Y. Ganin, M. J. Rosseinsky, Y. Z. Khimyak and A. I. Cooper, *Angew. Chem. Int. Ed.*, 2008, **47**, 1167–1167.

108 Y. Tian and G. Zhu, *Chem. Rev.*, 2020, **120**, 8934–8986.

109 M. Rose, W. Böhlmann, M. Sabo and S. Kaskel, *Chem. Commun.*, 2008, 2462.

110 J. Fritsch, F. Drache, G. Nickerl, W. Böhlmann and S. Kaskel, *Microporous Mesoporous Mater.*, 2013, **172**, 167–173.

111 T. Ben, H. Ren, S. Ma, D. Cao, J. Lan, X. Jing, W. Wang, J. Xu, F. Deng, J. M. Simmons, S. Qiu and G. Zhu, *Angew. Chem. Int. Ed.*, 2009, **48**, 9457–9460.

112 J. Huang and S. R. Turner, *Polym. Rev.*, 2018, **58**, 1–41.

113 Q. Shilun and B. Teng, *Porous Polymers*, Royal Society of Chemistry, Cambridge, 2015.

114 A. Valverde-Gonzalez, M. Iglesias and E. M. Maya, *Chem. Mater.*, 2021, **33**, 6616–6639.

115 B. Li, R. Gong, W. Wang, X. Huang, W. Zhang, H. Li, C. Hu and B. Tan, *Macromolecules*, 2011, **44**, 2410–2414.

116 R. Dawson, T. Ratvijitvech, M. Corker, A. Laybourn, Y. Z. Khimyak, A. I. Cooper and D. J. Adams, *Polym. Chem.*, 2012, **3**, 2034.

117 Y. Luo, B. Li, W. Wang, K. Wu and B. Tan, *Adv. Mater.*, 2012, **24**, 5703–5707.

118 A. M. James, J. Reynolds, D. G. Reed, P. Styring and R. Dawson, *Materials (Basel).*, 2021, **14**, 1605.

119 N. B. McKeown, *Sci. China Chem.*, 2017, **60**, 1023–1032.

120 P. M. Budd, E. S. Elabas, B. S. Ghanem, S. Makhseed, N. B. McKeown, K. J. Msayib, C. E. Tattershall and D. Wang, *Adv. Mater.*, 2004, **16**, 456–459.

121 B. Singh, V. Sharma, R. P. Gaikwad, P. Fornasiero, R. Zboř il and M. B. Gawande, *Small*, 2021, **17**, 2006473.

122 H.S. Taylor, *Proc. R. Soc. London. Ser. A, Contain. Pap. a Math. Phys. Character*, 1925, **108**, 105–111.

123 L. Zhang, Y. Ren, W. Liu, A. Wang and T. Zhang, *Natl. Sci. Rev.*, 2018, **5**, 653–672.

124 P. Yin, T. Yao, Y. Wu, L. Zheng, Y. Lin, W. Liu, H. Ju, J. Zhu, X. Hong, Z. Deng, G. Zhou, S. Wei and Y. Li, *Angew. Chem. Int. Ed.*, 2016, **55**, 10800–10805.

125 Z. Liang, C. Qu, D. Xia, R. Zou and Q. Xu, *Angew. Chem. Int. Ed.*, 2018, **57**, 9604–9633.

126 Y. Shu, K. Miyake, J. Quílez-Bermejo, Y. Zhu, Y. Hirota, Y. Uchida, S. Tanaka, E. Morallón, D. Cazorla-Amorós, C. Y. Kong and N.

Nishiyama, *ChemNanoMat*, 2020, **6**, 218–222.

127 Z. Pu, I. S. Amiinu, R. Cheng, P. Wang, C. Zhang, S. Mu, W. Zhao, F. Su, G. Zhang, S. Liao and S. Sun, *Nano-Micro Lett.*, 2020, **12**, 21.

128 B. W. Zhang, Y. X. Wang, S. L. Chou, H. K. Liu and S. X. Dou, *Small Methods*, 2019, **3**, 1–25.

129 Q. Zhang and J. Guan, *Nano Res.*, 2022, **15**, 38–70.

130 C. Rivera-Cárcamo and P. Serp, *ChemCatChem*, 2018, **10**, 5058–5091.

131 N. Cheng, L. Zhang, K. Doyle-Davis and X. Sun, *Electrochem. Energy Rev.*, 2019, **2**, 539–573.

132 X. Wang, W. Chen, L. Zhang, T. Yao, W. Liu, Y. Lin, H. Ju, J. Dong, L. Zheng, W. Yan, X. Zheng, Z. Li, X. Wang, J. Yang, D. He, Y. Wang, Z. Deng, Y. Wu and Y. Li, *J. Am. Chem. Soc.*, 2017, **139**, 9419–9422.

133 J.-S. M. Lee, M. E. Briggs, T. Hasell and A. I. Cooper, *Adv. Mater.*, 2016, **28**, 9804–9810.

134 Y. Yang, Z. He, S. Wang, H. Wang and G. Zhu, *Energy & Fuels*, 2021, **35**, 19614–19623.

135 P. W. Miller, M. Nieuwenhuyzen, J. P. H. Charmant and S. L. James, *Inorg. Chem.*, , DOI:10.1021/ic800664f.

136 B. Li, Z. Guan, W. Wang, X. Yang, J. Hu, B. Tan and T. Li, *Adv. Mater.*, 2012, **24**, 3390–3395.

137 Y. Yang, T. Wang, X. Jing and G. Zhu, *J. Mater. Chem. A*, 2019, **7**, 10004–10009.

138 H. C. E. McFarlane and W. McFarlane, *Polyhedron*, 1988, **7**, 1875–1879.

139 M. Ferrer, L. Giménez, A. Gutiérrez, J. C. Lima, M. Martínez, L. Rodríguez, A. Martín, R. Puttreddy and K. Rissanen, *Dalt. Trans.*, 2017, **46**, 13920–13934.

140 G. Hogarth and T. Norman, *Inorganica Chim. Acta*, 1996, **248**, 167–174.

141 S. Bracco, D. Piga, I. Bassanetti, J. Perego, A. Comotti and P. Sozzani, *J. Mater. Chem. A*, 2017, **5**, 10328–10337.

142 J. Weber, M. Antonietti and A. Thomas, *Macromolecules*, 2008, **41**, 2880–2885.

143 T. Horibe, K. Nakagawa, T. Hazeyama, K. Takeda and K. Ishihara, *Chem. Commun.*, 2019, **55**, 13677–13680.

144 J. A. Vicente, A. Mlonka, H. Q. N. Gunaratne, M. Swadźba-Kwaśny and P. Nockemann, *Chem. Commun.*, 2012, **48**, 6115.

145 A. Bowden, P. N. Horton and A. W. G. Platt, *Inorg. Chem.*, 2011, **50**, 2553–2561.

146 A. W. G. Platt, *Coord. Chem. Rev.*, 2017, **340**, 62–78.

147 P. Kaur, J. T. Hupp and S. T. Nguyen, *ACS Catal.*, 2011, 1, 819–835.

148 S. Gopi, A. G. Ramu, S. Sakthivel, G. Maia, C.-H. Jang, D. Choi and K. Yun, *Chemosphere*, 2021, **265**, 129052.

149 Y. Roux, C. Duboc and M. Gennari, *ChemPhysChem*, 2017, **18**, 2606–2617.

150 X. Guo, X. Wan and J. Shui, *Cell Reports Phys. Sci.*, 2021, **2**, 100447.

151 J. F. Callejas, J. M. McEnaney, C. G. Read, J. C. Crompton, A. J. Biacchi, E. J. Popczun, T. R. Gordon, N. S. Lewis and R. E. Schaak, *ACS Nano*, 2014, **8**, 11101–11107.

152 S. Bhunia, S. K. Das, R. Jana, S. C. Peter, S. Bhattacharya, M. Addicoat, A. Bhaumik and A. Pradhan, *ACS Appl. Mater. Interfaces*, 2017, **9**, 23843–23851.

153 R. Nivetha, K. Gothandapani, V. Raghavan, G. Jacob, R. Sellappan, P. Bhardwaj, S. Pitchaimuthu, A. N. M. Kannan, S. K. Jeong and A. N. Grace, *ACS Omega*, 2020, **5**, 18941–18949.

154 X. Cui, S. Lei, A. C. Wang, L. Gao, Q. Zhang, Y. Yang and Z. Lin, *Nano Energy*, 2020, 70, 104525.

155 A. Wang, L. Cheng, W. Zhao, X. Shen and W. Zhu, *J. Colloid Interface Sci.*, 2020, **579**, 598–606.

156 H. Fang, J. Chen, M.-S. Balogun, Y.-X. Tong and J. Zhang, *ACS Appl. Nano Mater.*, 2018, **1**, 6477–6482.

157 Y. Zhang, S. Liu, Z.-S. Zhao, Z. Wang, R. Zhang, L. Liu and Z.-B. Han, *Inorg. Chem. Front.*, 2021, **8**, 590–619.

158 I.-A. Dascălu, E. A. Mikhalyova, S. Shova, B.-I. Bratanovici, R. Ardeleanu, N. Marangoci, V. Lozan and G. Roman, *Polyhedron*, 2021, **194**, 114929.

159 B. Rungtaweevoranit, C. S. Diercks, M. J. Kalmutzki and O. M. Yaghi, *Faraday Discuss.*, 2017, **201**, 9–45.

160 H. Li, M. Eddaoudi, T. L. Groy and O. M. Yaghi, *J. Am. Chem. Soc.*, 1998, **120**, 8571–8572.

161 G. Cai, P. Yan, L. Zhang, H.-C. Zhou and H.-L. Jiang, *Chem. Rev.*, 2021, **121**, 12278–12326.

162 M. Kandiah, M. H. Nilsen, S. Usseglio, S. Jakobsen, U. Olsbye, M. Tilset, C. Larabi, E. A. Quadrelli, F. Bonino and K. P. Lillerud, *Chem. Mater.*, 2010, **22**, 6632–6640.

163 J. H. Cavka, S. Jakobsen, U. Olsbye, N. Guillou, C. Lamberti, S. Bordiga and K. P. Lillerud, *J. Am. Chem. Soc.*, 2008, **130**, 13850–13851.

164 J. He, J. Huang, Y. He, P. Cao, M. Zeller, A. D. Hunter and Z. Xu, *Chem. Eur. J.*, 2016, **22**, 1597–1601.

165 X. Li, W. Ma, H. Li, Q. Zhang and H. Liu, *Coord. Chem. Rev.*, 2020, **408**, 213191.

166 B. Gui, K.-K. Yee, Y.-L. Wong, S.-M. Yiu, M. Zeller, C. Wang and Z. Xu, *Chem. Commun.*, 2015, **51**, 6917–6920.

167 X.-P. Zhou, Z. Xu, M. Zeller, A. D. Hunter, S. S.-Y. Chui and C.-M. Che, *Inorg. Chem.*, 2008, **47**, 7459–7461.

168 X.-P. Zhou, Z. Xu, J. He, M. Zeller, A. D. Hunter, R. Clérac, C. Mathonière, S. S.-Y. Chui and C.-M. Che, *Inorg. Chem.*, 2010, **49**, 10191–10198.

169 J. Seo, C. Bonneau, R. Matsuda, M. Takata and S. Kitagawa, *J. Am. Chem. Soc.*, 2011, **133**, 9005–9013.

170 J. Li, H. Fu, P. Hu, Z. Zhang, X. Li and Y. Cheng, *Chem. Eur. J.*, 2012, **18**, 13941–13944.

171 D. Drew, J. R. Doyle and A. G. Shaver, 2007, pp. 346–349.

172 D. Fraccarollo, R. Bertani, M. Mozzon, U. Belluco and R. A. Michelin, *Inorganica Chim. Acta*, 1992, **201**, 15–22.

173 R. J. Marshall, Y. Kalinovskyy, S. L. Griffin, C. Wilson, B. A. Blight and R. S. Forgan, *J. Am. Chem. Soc.*, 2017, **139**, 6253–6260.

174 C. Zeng, N. Wang, T. Peng and S. Wang, *Inorg. Chem.*, 2017, **56**, 1616–1625.

175 Y. Zhang, S.-C. Chien, K.-S. Chen, H.-L. Yip, Y. Sun, J. A. Davies, F.-C. Chen and A. K.-Y. Jen, *Chem. Commun.*, 2011, **47**, 11026.

176 F. Kniep, S. H. Jungbauer, Q. Zhang, S. M. Walter, S. Schindler, I. Schnapperelle, E. Herdtweck and S. M. Huber, *Angew. Chem. Int. Ed.*, 2013, **52**, 7028–7032.

177 S. Gao, L. Zhao, P. Zhao, Y. Huang and H. Zhao, *Inorganica Chim. Acta*, 2018, **480**, 173–176.

178 W. Morris, B. Volosskiy, S. Demir, F. Gándara, P. L. McGrier, H. Furukawa, D. Cascio, J. F. Stoddart and O. M. Yaghi, *Inorg. Chem.*, 2012, **51**, 6443–6445.

179 R. J. Marshall, S. L. Griffin, C. Wilson and R. S. Forgan, *J. Am. Chem. Soc.*, 2015, **137**, 9527–9530.

180 K. A. White, D. A. Chengelis, K. A. Gogick, J. Stehman, N. L. Rosi and S. Petoud, *J. Am. Chem. Soc.*, 2009, **131**, 18069–18071.

181 S. L. Griffin and N. R. Champness, *Coord. Chem. Rev.*, 2020, **414**, 213295.

182 J. M. Falkowski, T. Sawano, T. Zhang, G. Tsun, Y. Chen, J. V. Lockard and W. Lin, *J. Am. Chem. Soc.*, 2014, **136**, 5213–5216.

183 A. A. Bezrukov and P. D. C. Dietzel, *Inorg. Chem.*, 2017, **56**, 12830–12838.

184 T. Bunlaksananusorn and P. Knochel, *Tetrahedron Lett.*, 2002, **43**, 5817–5819.

185 H. Wang, Y. Li, Z. Tang, S. Wang, H. Zhang, H. Cong and A. Lei, *ACS Catal.*, 2018, **8**, 10599–10605.

186 A. M. Aguiar and T. G. Archibald, *Tetrahedron Lett.*, 1966, **7**, 5471–5475.

187 Q. Guan, B. Wang, X. Chai, J. Liu, J. Gu and P. Ning, *Fuel*, 2017, **205**, 130–141.

188 Q.-Y. Li, Y.-A. Li, Q. Guan, W.-Y. Li, X.-J. Dong and Y.-B. Dong, *Inorg. Chem.*, 2019, **58**, 9890–9896.

189 A. Schaate, P. Roy, A. Godt, J. Lippke, F. Waltz, M. Wiebcke and P. Behrens, *Chem. Eur. J.*, 2011, **17**, 6643–6651.

190 B. Lerma-Berlanga, C. R. Ganivet, N. Almora-Barrios, S. Tatay, Y. Peng, J. Albero, O. Fabelo, J. González-Platas, H. García, N. M. Padial and C. Martí-Gastaldo, *J. Am. Chem. Soc.*, 2021, **143**, 1798–1806.

191 Q. Yang, V. Guillerm, F. Ragon, A. D. Wiersum, P. L. Llewellyn, C. Zhong, T. Devic, C. Serre and G. Maurin, *Chem. Commun.*, 2012, **48**, 9831.

192 K. Manna, P. Ji, Z. Lin, F. X. Greene, A. Urban, N. C. Thacker and W. Lin, *Nat. Commun.*, 2016, **7**, 12610.

193 D. Saha, R. Zacharia, L. Lafi, D. Cossement and R. Chahine, *Int. J. Hydrogen Energy*, 2012, **37**, 5100–5107.

194 D. SAHA, Z. WEI and S. DENG, *Int. J. Hydrogen Energy*, 2008, **33**, 7479–7488.

195 D. Saha, Z. Wei and S. Deng, *Sep. Purif. Technol.*, 2009, **64**, 280–287.

196 X. Ye and D. Liu, *Cryst. Growth Des.*, 2021, **21**, 4780–4804.

197 K. Vasanth Kumar, G. Charalambopoulou, M. Kainourgiakis, A. Stubos and T. Steriotis, *Comput. Theor. Chem.*, 2015, **1061**, 36–45.

198 X. Wang, J.-Y. Luo, J.-W. Tian, D.-D. Huang, Y.-P. Wu, S. Li and D.-S. Li, *Inorg. Chem. Commun.*, 2018, **98**, 141–144.

199 D. Narváez-Celada and A. S. Varela, *J. Mater. Chem. A*, , DOI:10.1039/D1TA10440C.

200 H. D. Betts, O. M. Linder-Patton and C. J. Sumby, *Molecules*, , DOI:10.3390/molecules25194548.

201 J. P. M. Lommerse, A. J. Stone, R. Taylor and F. H. Allen, *J. Am. Chem.*

Soc., 1996, **118**, 3108–3116.

202 V. Thangavadivale, P. M. Aguiar, N. A. Jasim, S. J. Pike, D. A. Smith, A. C. Whitwood, L. Brammer and R. N. Perutz, *Chem. Sci.*, 2018, **9**, 3767–3781.

7. List of abbreviations

Ac	Acetone
BINAP	2,2'-bis(diphenylphosphaneyl)-1,1'-binaphthalene
CCDC	Cambridge Crystallographic Data Centre
COFs	Covalent Organic Frameworks
COSY	COrrelated SpectroscopY
DCE	Dichloroethane
DCM	Dichloromethane
Et_2O	Diethyl ether
EWG	Electron-withdrawing group
EDG	Electron-donating group
FC	Friedel Craft
HMBC	Heteronuclear Multiple Bond Correlation
HSQC	Heteronuclear Single Quantum Coherence
Hx	Hexane
AcOEt	Ethyl acetate
MeCN	Acetonitrile
MOFs	Metal Organic Frameworks
NMP	1-Methyl-2-pyrrolidinone
POFs	Porous Organic Frameworks
POPs	Porous Organic Polymers
KAPs	Knitted Aromatic Polymers
THF	Tetraydrofuran
TLC	Thin layer chromatography
r.t.	Room Temperature
FT-IR peak abbreviations	
w	Weak
m	Medium
s	Strong
br	Broad
NMR abbreviations	
s	singlet
d	doublet
t	triplet
q	quartet
m	multiplet
brs	broad singlet

8. Appendix I

Supplementary materials of Chapter 2

8.1 NMR spectra

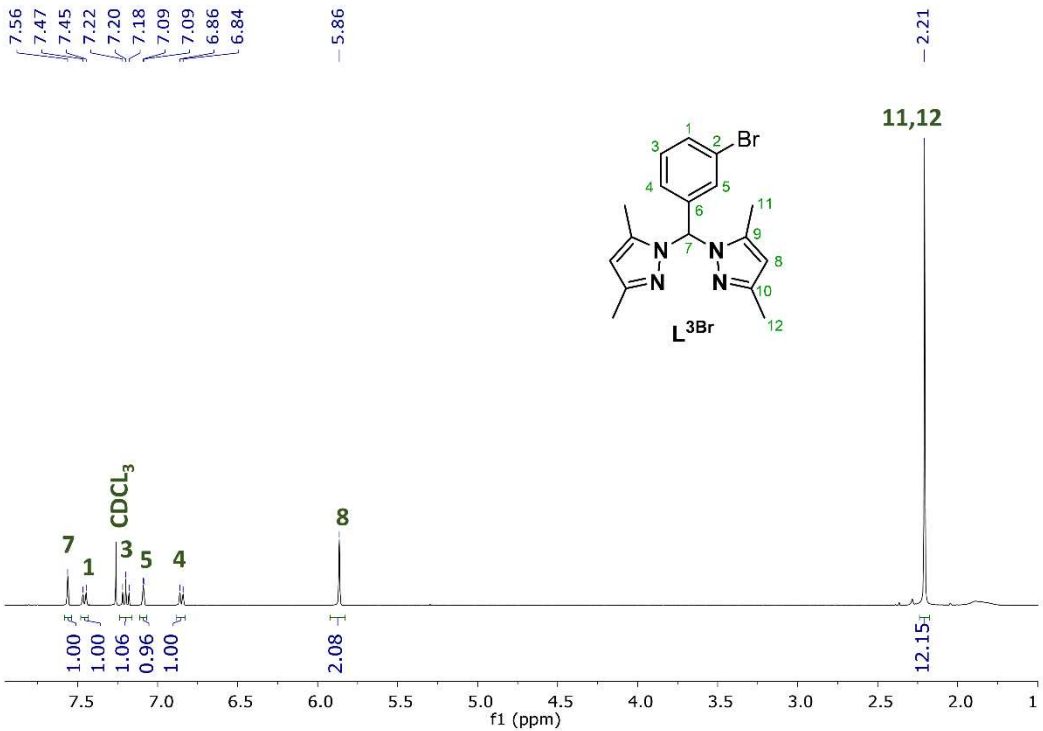

Figure A1. ^{1}H-NMR (400 MHz, $CDCl_3$) spectrum of L^{3Br}.

Appendix I

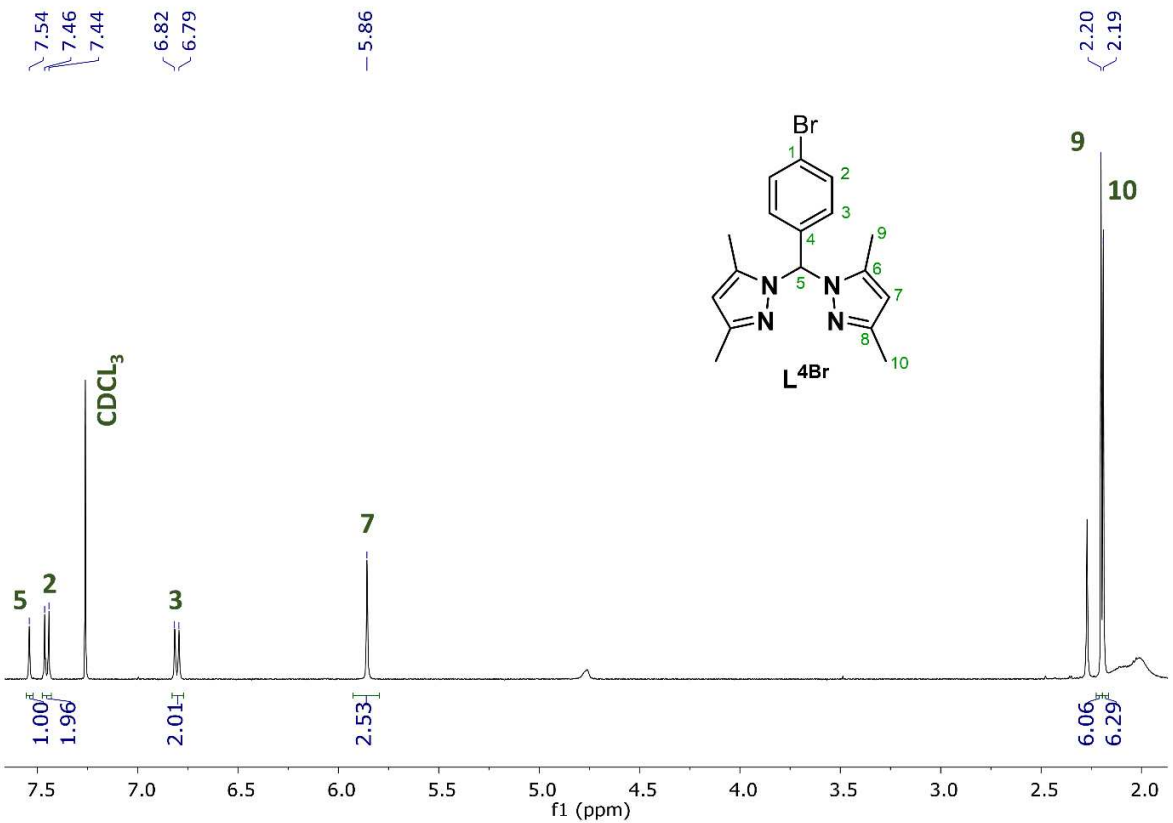

Figure A2. ^{1}H-NMR (400 MHz, $CDCl_3$) spectrum of L^{4Br}.

Appendix I

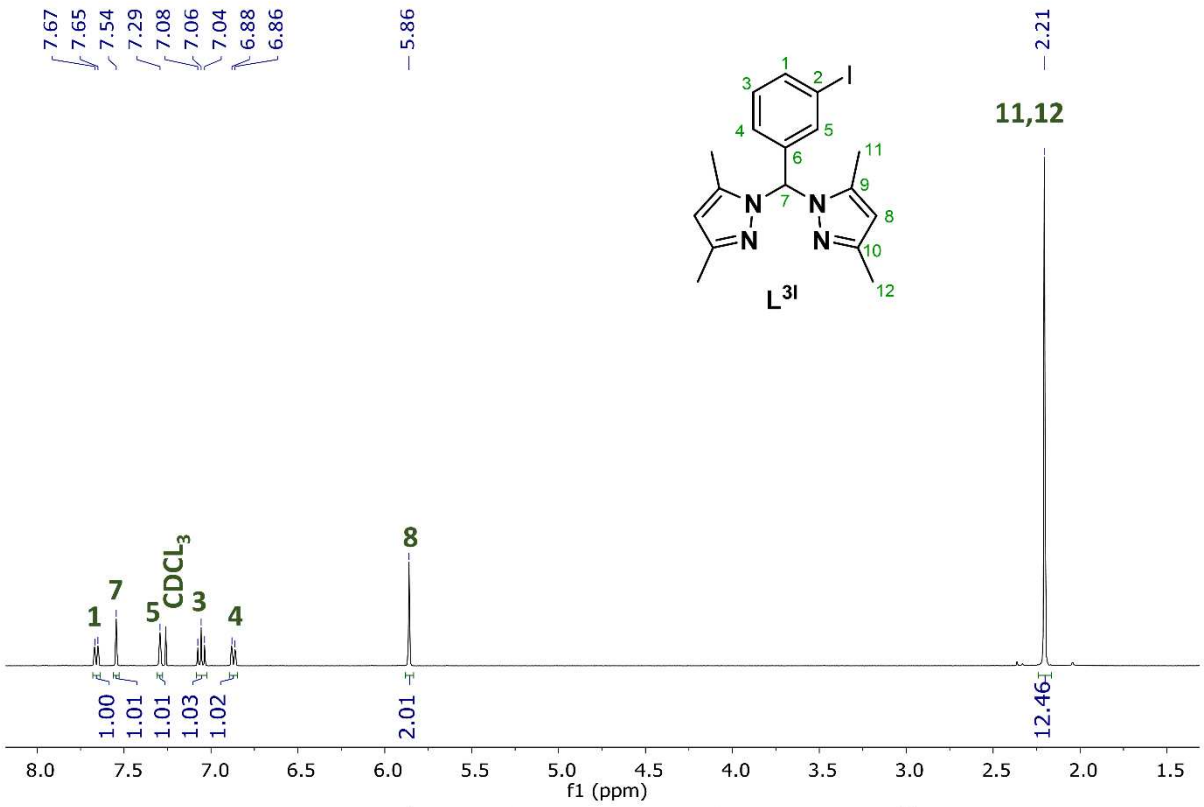

Figure A3. ^{1}H-NMR (400 MHz, $CDCl_3$) spectrum of L^{3I}.

Appendix I

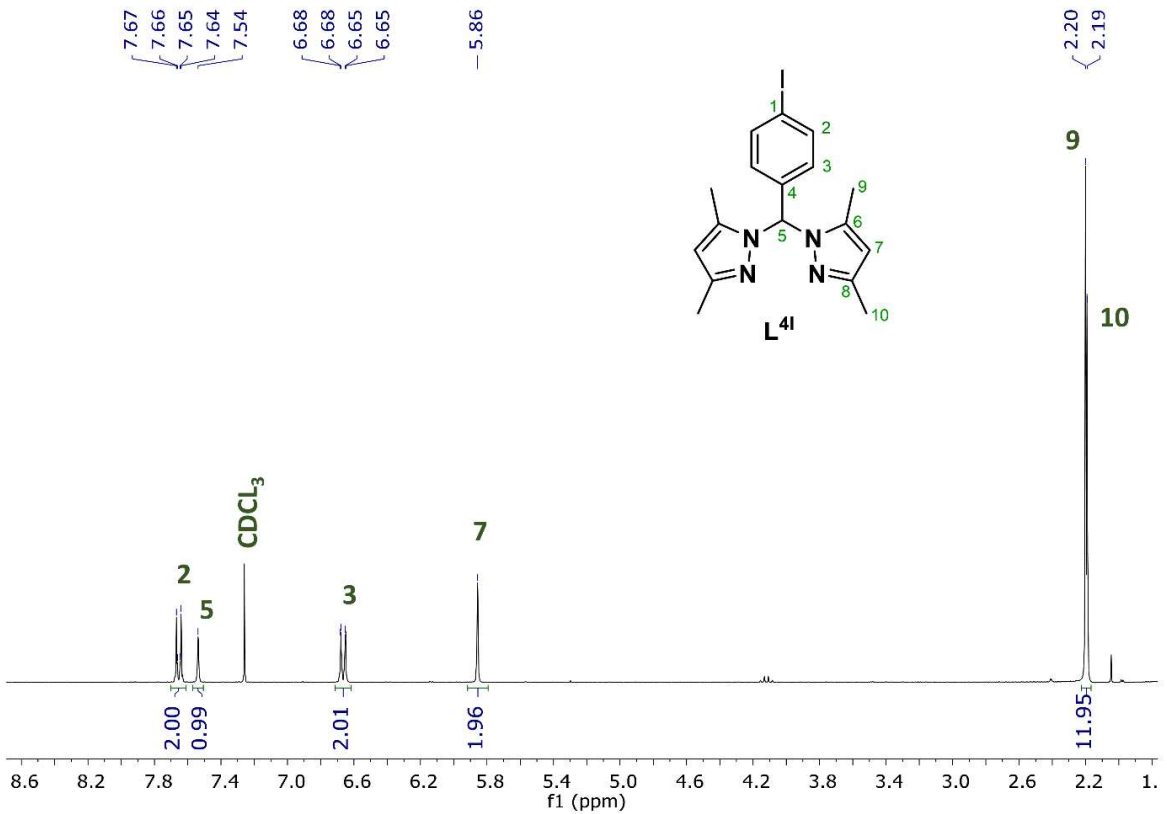

Figure A4. ^{1}H-NMR (300 MHz, $CDCl_3$) spectrum of L^{4I}.

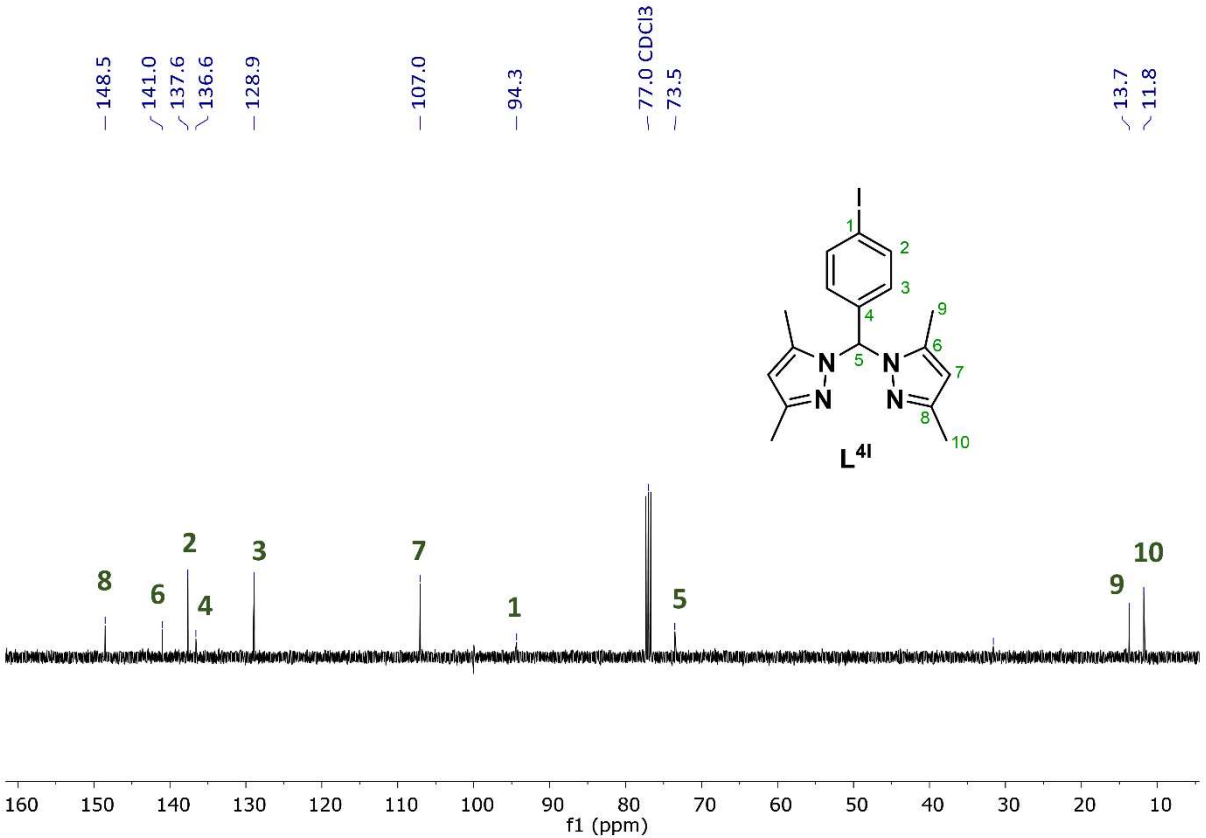

Figure A5. ^{13}C-NMR (100 MHz, $CDCl_3$) spectrum of L^{4I}.

Appendix I

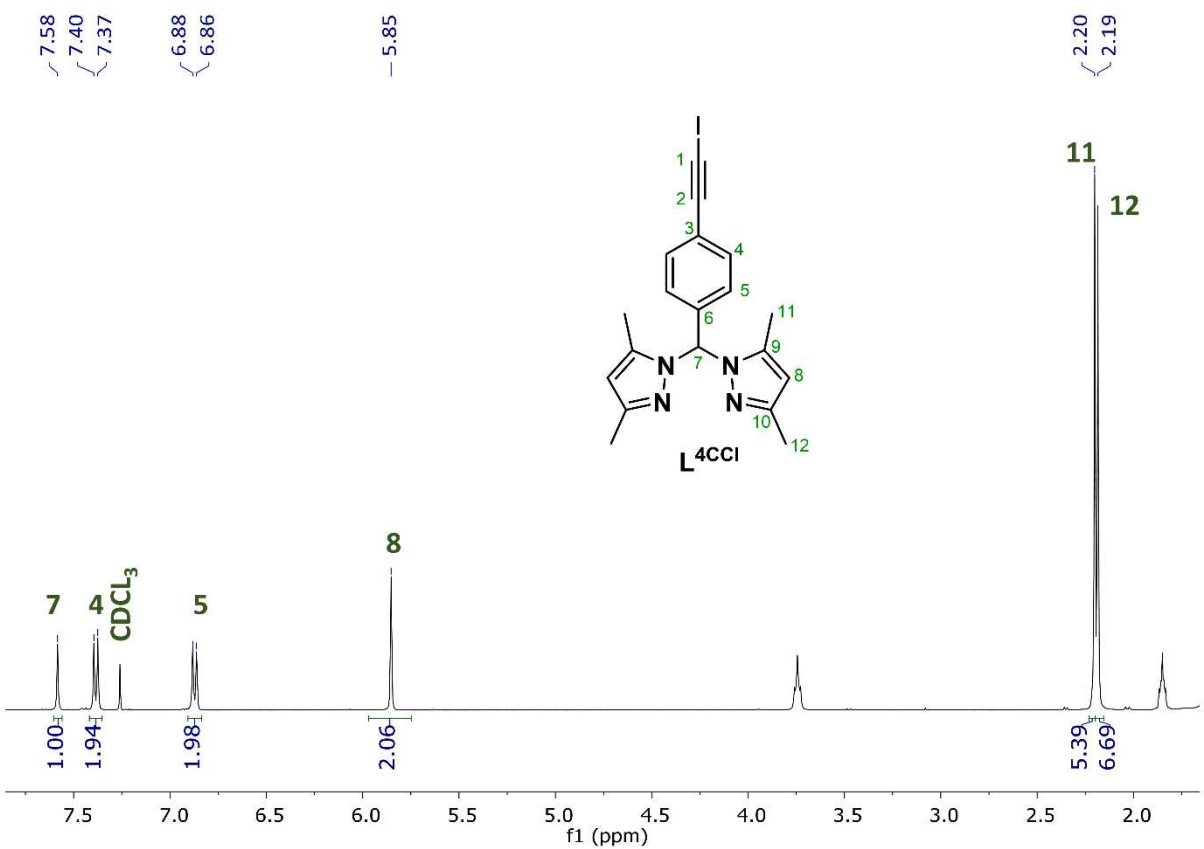

Figure A6. ^{1}H-NMR (400 MHz, $CDCl_3$) spectrum of L^{4CCl}.

Appendix I

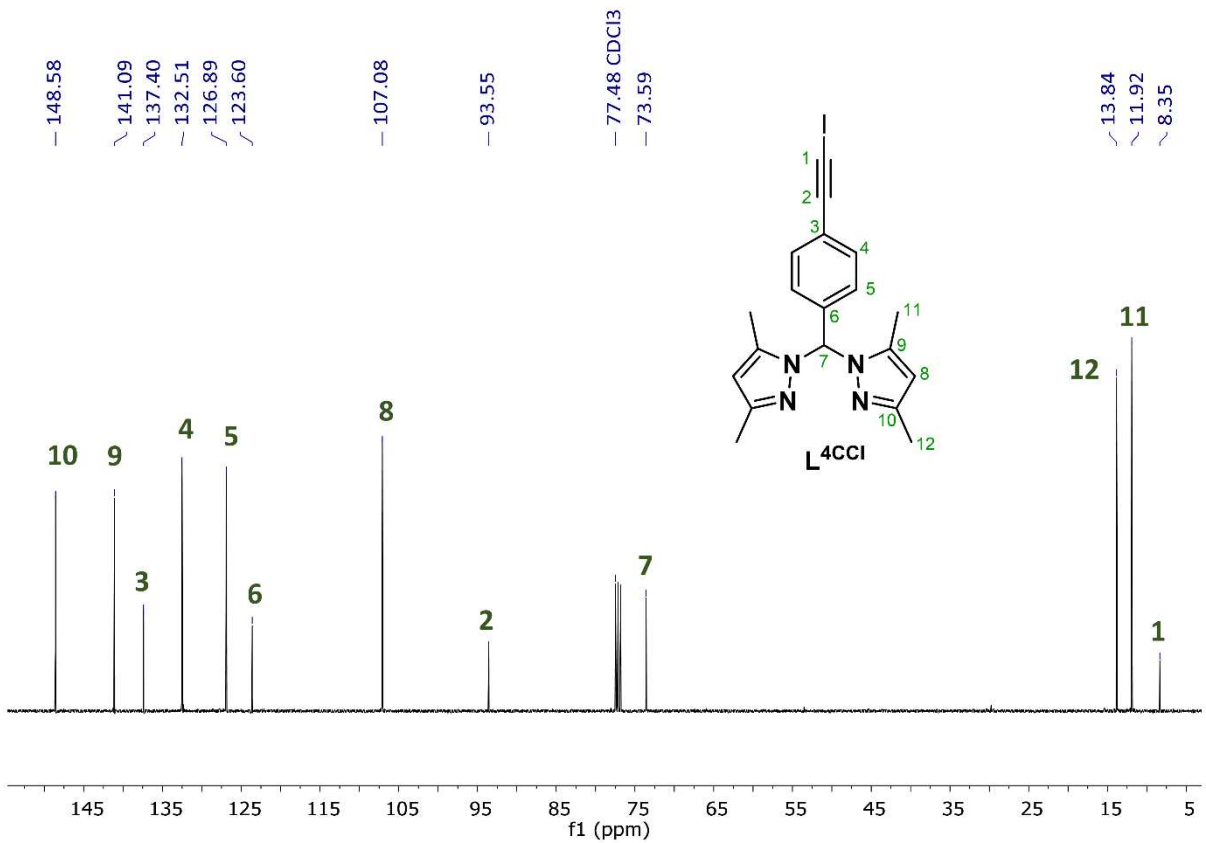

Figure A7. ^{13}C-NMR (100 MHz, $CDCl_3$) spectrum of L^{4CCl}.

Appendix I

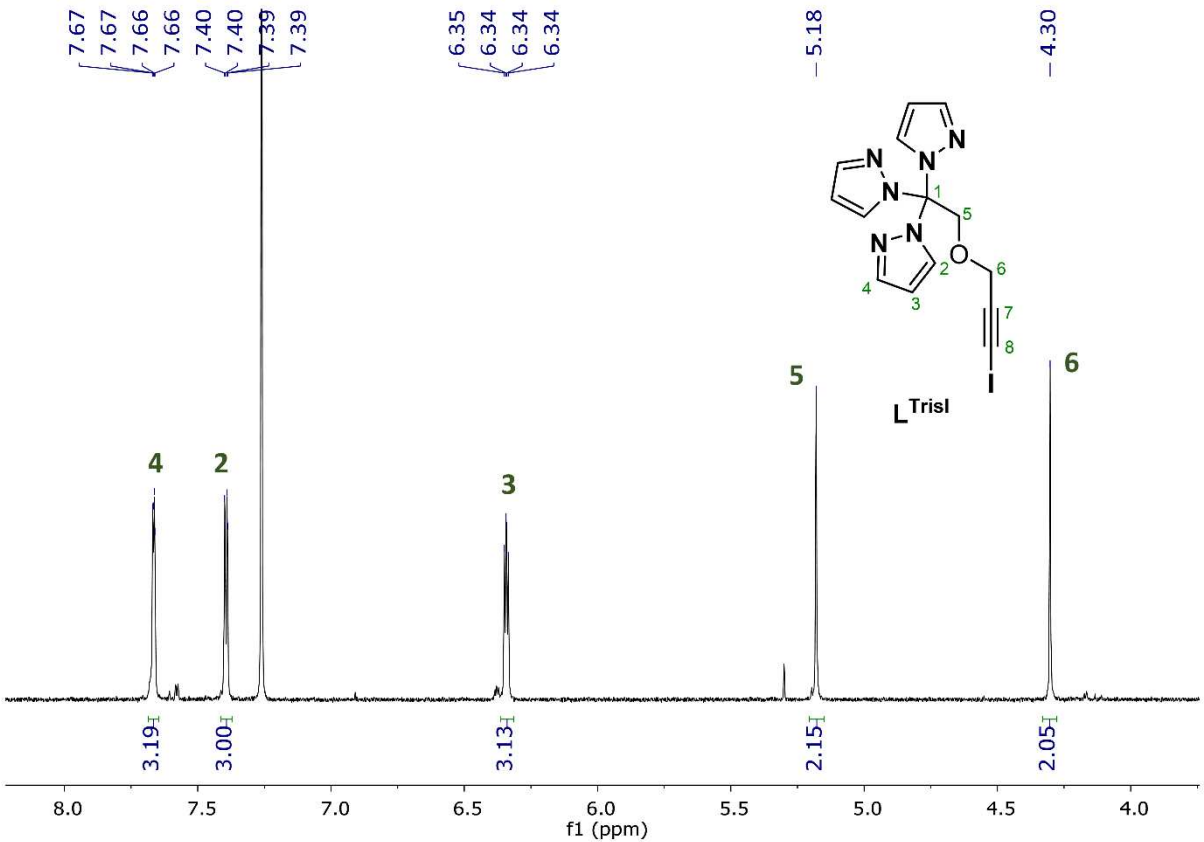

Figure A8. ^{1}H-NMR (300 MHz, $CDCl_3$) spectrum of L^{TrisI}.

Appendix I

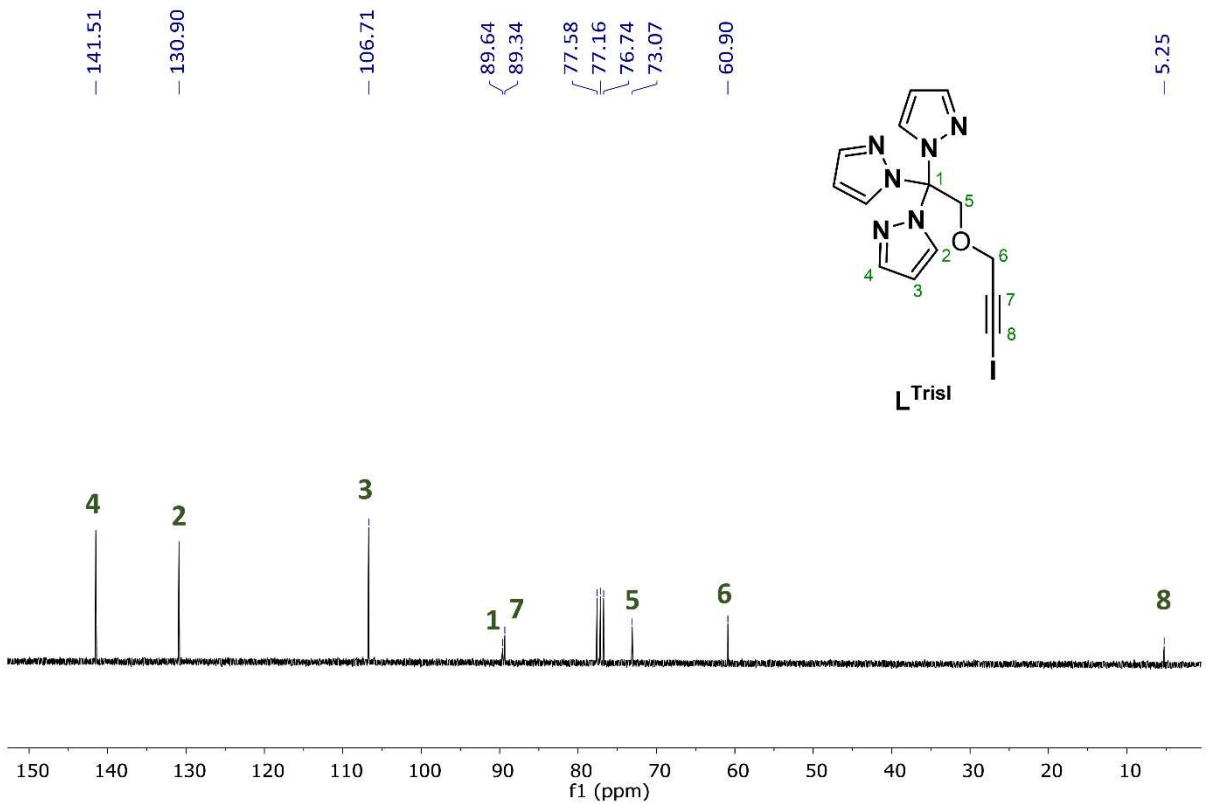

Figure A9. ^{13}C-NMR (75 MHz, $CDCl_3$) spectrum of L^{TrisI}.

Appendix I

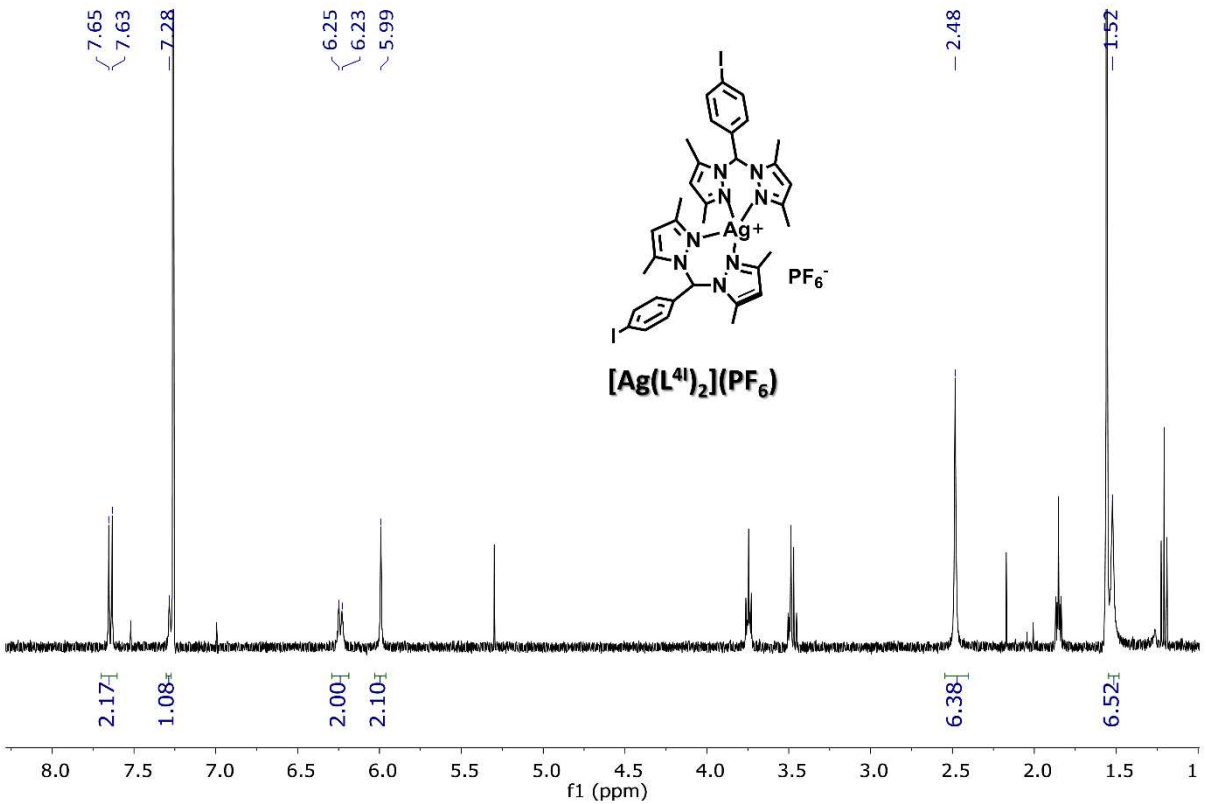

Figure A10. ^{1}H-NMR (400 MHz, $CDCl_3$) spectrum of complex $[Ag(L^{4I})_2]PF_6$.

Appendix I

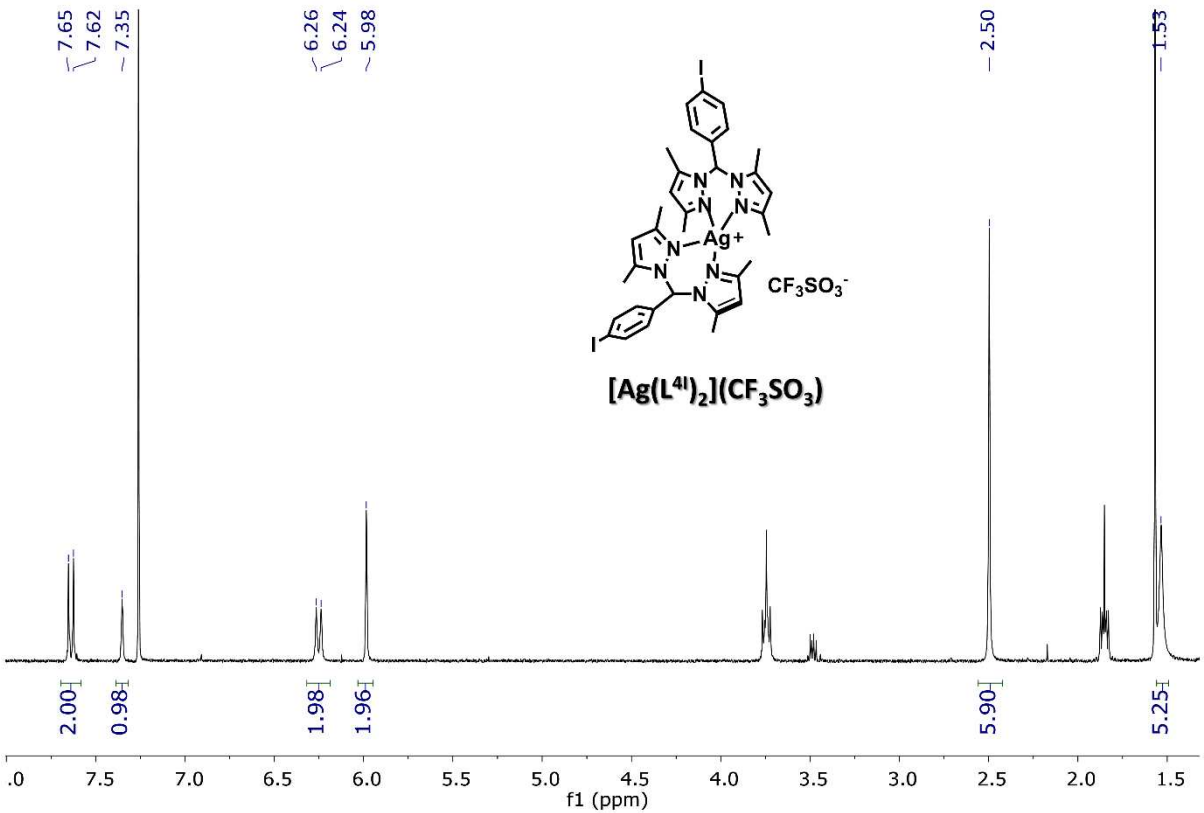

Figure A11. ^{1}H-NMR (300 MHz, $CDCl_3$) spectrum of complex $[Ag(L^{4I})_2]CF_3SO_3$.

Appendix I

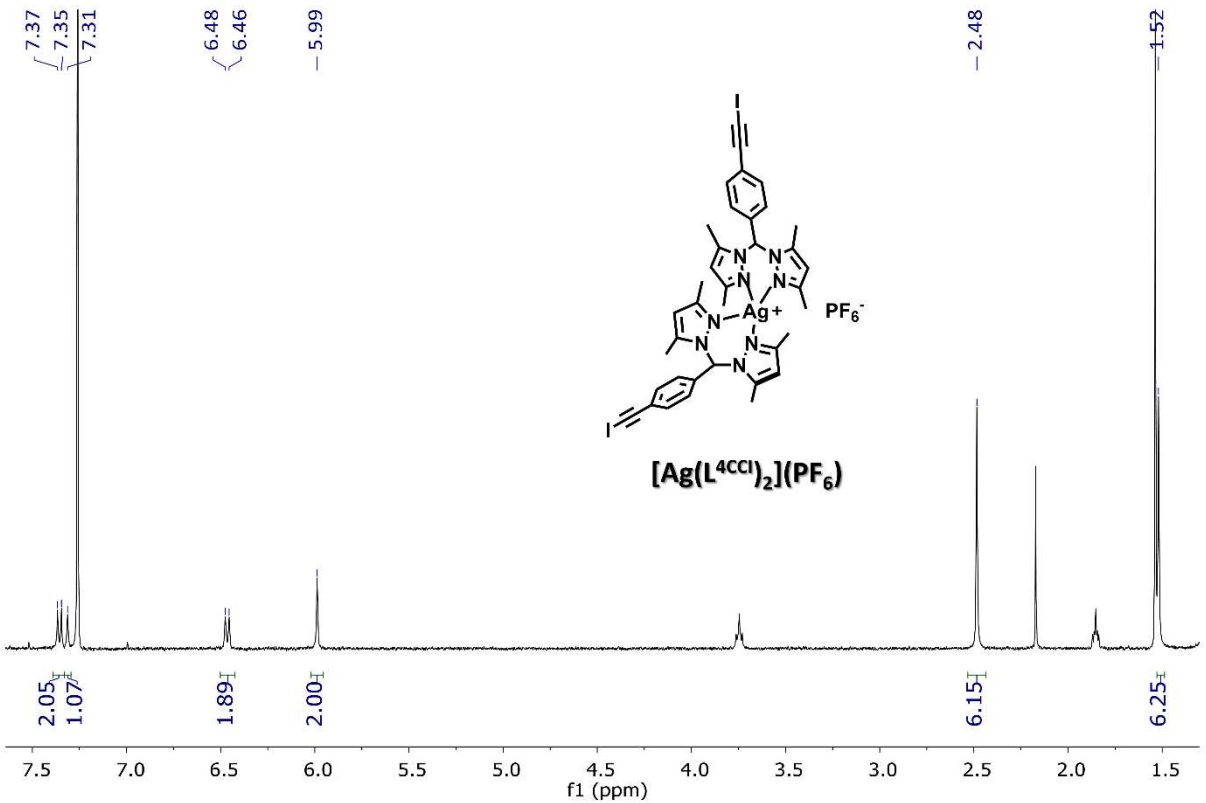

Figure A12. ^{1}H-NMR (400 MHz, $CDCl_3$) spectrum of complex $[Ag(L^{4CCl})_2]PF_6$.

Appendix I

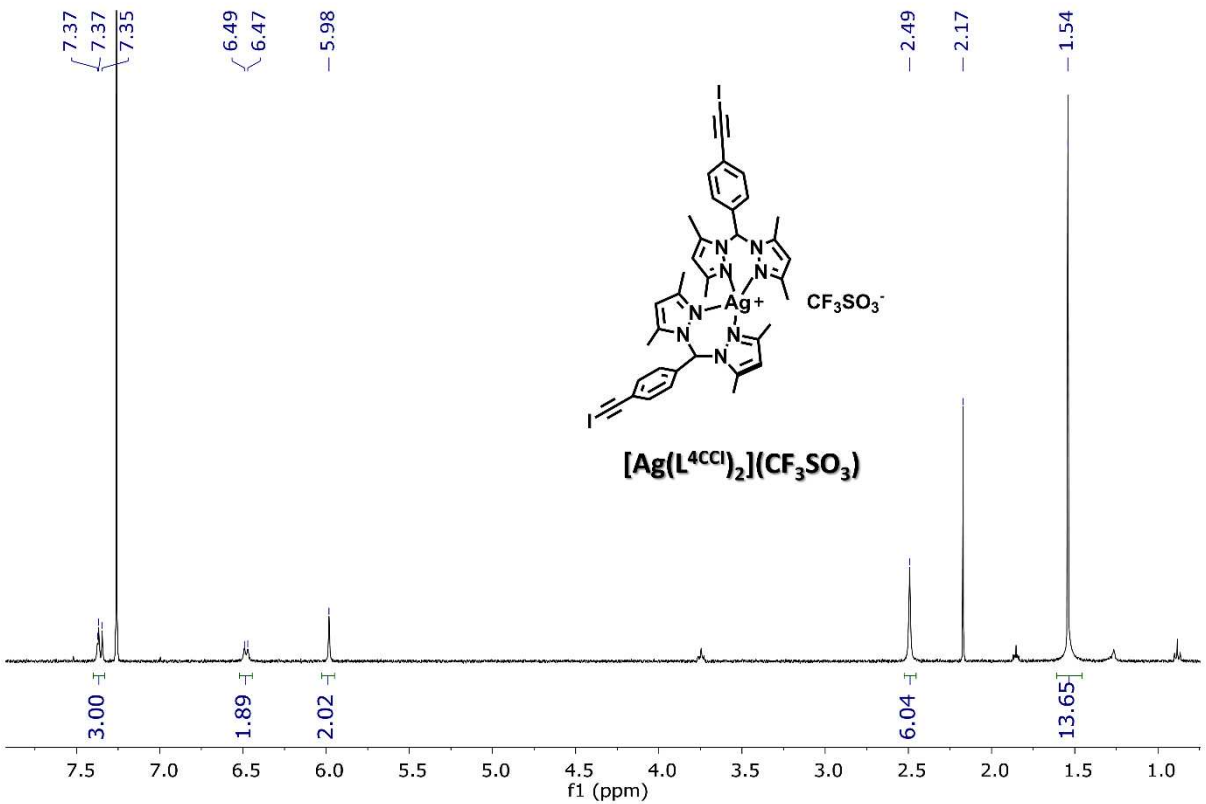

Figure A13. ^{1}H-NMR (400 MHz, $CDCl_3$) spectrum of complex $[Ag(L^{4CCl})_2]$ CF_3SO_3.

Appendix I

8.2 Crystal data and structural geometric parameters

Table A1. Summary of τ_4 and τ_4' indices for **1-12**, with coordination angles **β** and **α** (**β** > **α**).

Complex	β	α	τ_4	τ_4'
1	162.3	110.1	0.62	0.46
	160.2	113.1	0.61	0.47
2	160.7	110.6	0.63	0.47
3·DCM	151.5	116.3	0.65	0.54
	158.2	111.6	0.64	0.50
4	151.1	113.4	0.68	0.56
5·DCM	145.2	124.1	0.64	0.58
6	140.9	123.9	0.68	0.62
	162.0	111.4	0.61	0.46
7	156.0	110.6	0.66	0.52
	154.5	115.8	0.64	0.52
8	153.2	113.7	0.66	0.54
9·DCE	158.4	110.2	0.65	0.50
9-phase-1	156.2	114.0	0.64	0.51
10-phase-1	156.2	112.7	0.65	0.51
9-phase-2	142.0	119.9	0.70	0.63
	142.4	120.5	0.69	0.62
10-phase-2	143.1	119.5	0.69	0.62
	138.5	122.3	0.70	0.65
9-phase-3	152.2	117.1	0.64	0.53
10-phase-3	145.3	123.9	0.64	0.58
10·DCM	153.7	116.5	0.64	0.52
	156.2	114.4	0.63	0.50
11·THF	158.5	108.8	0.66	0.50
12	144.7	120.1	0.68	0.60

$$\tau_4 = \frac{360° - (\alpha + \beta)}{360° - 2\theta} \qquad \tau_4' = \frac{\beta - \alpha}{360° - \theta} + \frac{180° - \beta}{180° - \theta} \qquad \theta = 109.5°$$

Appendix I

Table A2. Selected geometric parameters (Å) for **1,2, 3**·DCM, **5**·DCM, **6.**

1		**2**	
Ag(1)-N(21)	**2.236(5)**	Ag-N(21)	**2.264(3)**
Ag(1)-N(24)	**2.250(4)**	Ag-N(24)	**2.270(3)**
Ag(1)-N(22)	2.467(5)	Ag-N(22)	2.386(3)
Ag(1)-N(25)	2.386(5)	Ag-N(25)	2.417(3)
Ag(2)-N(27)	**2.284(5)**		
Ag(2)-N(210)	**2.291(4)**		
Ag(2)-N(28)	2.398(5)		
Ag(2)-N(211)	2.415(5)		
3·DCM		**4**	
Ag(1)-N(21)	**2.219(4)**	Ag-N(21)	**2.248(2)**
Ag(1)-N(24)	**2.239(4)**	Ag-N(24)	**2.244(3)**
Ag(1)-N(22)	2.440(4)	Ag-N(22)	2.399(3)
Ag(1)-N(25)	2.373(4)	Ag-N(25)	2.385(3)
Ag(2)-N(27)	**2.226(4)**		
Ag(2)-N(210)	**2.251(4)**		
Ag(2)-N(28)	2.409(4)		
Ag(2)-N(211)	2.379(4)		
5·DCM		**6**	
Ag-N(21)	**2.226(6)**	Ag(1)-N(21)	**2.229(13)**
Ag-N(24)	**2.266(6)**	Ag(1)-N(24)	**2.299(13)**
Ag-N(22)	2.422(6)	Ag(1)-N(22)	2.409(13)
Ag-N(25)	2.343(6)	Ag(1)-N(25)	2.359(14)
		Ag(2)-N(27)	**2.230(13)**
		Ag(2)-N(210)	**2.282(13)**
		Ag(2)-N(28)	2.449(14)
		Ag(2)-N(211)	2.372(14)

Appendix I

Table A3. Selected geometric parameters (Å) for **7**, **8**, **9**-phase-1, **9**-phase-2, **9**-phase-3, **10**-phase-1, **10**-phase-2, **10**-phase-3**.**

7		**8**	
Ag(1)-N(21)	**2.245(4)**	Ag-N(21)	**2.260(4)**
Ag(1)-N(24)	**2.253(4)**	Ag-N(24)	**2.278(3)**
Ag(1)-N(22)	2.390(4)	Ag-N(22)	2.397(4)
Ag(1)-N(25)	2.375(4)	Ag-N(25)	2.381(4)
Ag(2)-N(27)	**2.277(4)**		
Ag(2)-N(210)	**2.256(4)**		
Ag(2)-N(28)	2.370(4)		
Ag(2)-N(211)	2.395(4)		
9-phase-1		**10**-phase-1	
Ag-N(21)	**2.213(8)**	Ag-N(21)	**2.232(7)**
Ag-N(24)	**2.226(8)**	Ag-N(24)	**2.229(6)**
Ag-N(22)	2.426(8)	Ag-N(22)	2.373(6)
Ag-N(25)	2.352(7)	Ag-N(25)	2.419(7)
9-phase-2		**10**-phase-2	
Ag(1)-N(21)	**2.30(2)**	Ag(1)-N(21)	**2.263(6)**
Ag(1)-N(24)	**2.31(2)**	Ag(1)-N(24)	**2.274(7)**
Ag(1)-N(22)	2.42(2)	Ag(1)-N(22)	2.422(6)
Ag(1)-N(25)	2.48(2)	Ag(1)-N(25)	2.419(7)
Ag(2)-N(27)	**2.26(2)**	Ag(2)-N(27)	**2.271(7)**
Ag(2)-N(210)	**2.24(2)**	Ag(2)-N(210)	**2.275(7)**
Ag(2)-N(28)	2.49(2)	Ag(2)-N(28)	2.424(7)
Ag(2)-N(211)	2.41(2)	Ag(2)-N(211)	2.431(7)
9-phase-3		**10**-phase-3	
Ag(1)-N(21)	**2.261(2)**	Ag(1)-N(21)	**2.18(3)**
Ag(1)-N(24)	**2.275(2)**	Ag(1)-N(24)	**2.23(3)**
Ag(1)-N(22)	2.371(2)	Ag(1)-N(22)	2.40(4)
Ag(1)-N(25)	2.377(2)	Ag(1)-N(25)	2.34(4)

Appendix I

Table A4. Selected geometric parameters (Å) for **9**·DCE, **10**·DCM, **11**·THF and **12.**

10·DCM		**9**·DCE	
Ag(1)-N(21)	**2.270(7)**	Ag(1)-N(21)	**2.205(3)**
Ag(1)-N(24)	**2.292(7)**	Ag(1)-N(24)	**2.210(3)**
Ag(1)-N(22)	2.391(7)	Ag(1)-N(25)	2.411(3)
Ag(1)-N(25)	2.338(8)	Ag(1)-N(22)	2.421(3)
Ag(2)-N(27)	**2.268(7)**		
Ag(2)-N(210)	**2.271(7)**		
Ag(2)-N(28)	2.377(7)		
Ag(2)-N(211)	2.384(7)		
11·THF		**12**	
Ag(1)- N(21)	**2.250(3)**	Ag(1)-N(21)	**2.270(5)**
Ag(1)- N(211)	**2.250(3)**	Ag(1)-N(24)	**2.280(6)**
Ag(1)- N(22)	2.405(4)	Ag(1)-N(22)	2.399(6)
Ag(1)-N(221)	2.405(4)	Ag(1)-N(25)	2.437(6)

Appendix I

Table A5. Geometric parameters for the XB interactions. The reported distances are expressed in (Å) and angles in (°). $\Delta = d(D\cdots A) - (r_D + r_A)$. $^{\#}R = d(D\cdots A)/(r_D + r_A)$ using the Bondi V.d.W radii.[201] $^{*}R = d(D\cdots A)/(r_D + r_A)$ using the Alvarez V.d.W radii.[201] See also Brammer et al. for an analogous description.[202]

D	A	D···A	C_{Ph}-D···A	D	R^{B}_{AD} #	R^{A}_{AD} *	Compound
X···C Interactions							
Br_6	C_{31}	3.416	167.6	-0.13	0.97	0.94	**3**·DCM
Br_3	C_{34}	3.410	173.1	-0.14	0.97	0.94	**4**
I_3	C_{512}	3.577	123.0	-0.10	0.97	0.94	**6**
I_6	C_{31}	3.519	165.0	-0.16	0.96	0.92	**6**
I_6	C_{21}	3.352	167.1	-0.15	0.91	0.88	**5**·DCM
X···X Interactions							
Br_9	Br_3	3.813	168.5	0.15	1.04	1.03	**3**·DCM
Br_6	Br_3	3.651	165.7	-0.05	1.00	0.98	**8**
Br_9	Br_6	3.626	163.6	-0.07	0.99	0.97	**7**
I_6	I_3	3.646	167.7	-0.31	0.92	0.89	**9**-phase-3
X···F Interactions							
Br_{12}	F_{414}	3.235	163.4	-0.09	0.98	0.97	**7**
I_{12}	F_{314}	3.376	157.4	-0.07	0.98	0.96	**10**-phase-2
Br_3	F_{37}	3.192	168.1	-0.13	0.97	0.96	**8**
I_{12}	F_{113}	3.340	155.4	-0.11	0.97	0.95	**10**·DCM
Br_6	F_{213}	3.137	175.3	-0.18	0.95	0.94	**7**
I_6	F_{113}	3.265	154.0	-0.19	0.95	0.93	**10**-phase-2
I_3	F_{17}	3.237	161.0	-0.21	0.94	0.92	**5**·DCM
I_3	F_{17}	3.221	167.1	-0.23	0.93	0.92	**9**-phase-3
I9	F_{614}	3.213	167.4	-0.24	0.93	0.92	**9**-phase-2
I_3	F_{314}	3.172	175.2	-0.28	0.92	0.91	**9**-phase-2
I_6	F_{2TB}	3.059	160.8	-0.39	0.89	0.87	**12**
I_3	F_{24A}	2.960	170.4	-0.49	0.86	0.85	**11**·THF
X···O Interactions							
I_6	O_{1S1}	3.296	170.1	-0.20	0.94	0.93	**10**-phase-1
I_3	O_{27}	3.130	177.9	-0.37	0.89	0.88	**10**-phase-3
I_9	O_{114}	3.091	177.1	-0.41	0.88	0.87	**10**·DCM
I_6	O_{113}	3.018	173.8	-0.48	0.86	0.85	**10**·DCM
I_3	O_{114}	2.987	173.4	-0.51	0.85	0.84	**10**-phase-2
I_9	O_{313}	2.965	174.9	-0.54	0.85	0.84	**10**-phase-2
I_3	O_{1T}	2.884	176.6	-0.66	0.82	0.81	**12**

$R1 = \Sigma||F_o|-|F_c||/\Sigma|F_o|$, $wR2 = [\Sigma[w(F_o^2-F_c^2)^2]/\Sigma[w(F_o^2)^2]]^{1/2}$, $w = 1/[\sigma^2(F_o^2) + (aP)^2 + bP]$, where $P = [\max(F_o^2,0) + 2F_c^2]/3$

Appendix I

Table A6. Summary of X-ray crystallographic data for **1**, **2**, **3**.

Identification code	**1**	**2**	**3**·DCM
Empirical formula	$C_{34}H_{40}AgF_6N_8P$	$C_{35}H_{40}AgF_3N_8O_3S$	$C_{70}H_{81}Ag_2Br_4Cl_4F_{12}N_{16}P_2$
Formula weight	813.58	817.68	2113.62
Temperature/K	296.15	296.15	200
Crystal system	Monoclinic	monoclinic	Monoclinic
Space group	$P2_1/n$	$P2_1/c$	$P2_1/c$
a/Å	19.306(10)	9.745(3)	9.8170(3)
b/Å	14.910(8)	25.803(7)	22.4885(7)
c/Å	26.556(10)	15.628(5)	40.4581(13)
α/°	90	90	90
β/°	93.928(9)	93.688(6)	90.8990(10)
γ/°	90	90	90
Volume/Å^3	7626(6)	3922(2)	8930.8(5)
Z	8	4	4
ρ_{calc}g/cm^3	1.417	1.385	1.572
μ/mm^{-1}	0.635	0.625	2.456
F(000)	3328.0	1680.0	4212.0
Crystal size/mm^3	0.21 × 0.18 × 0.15	0.27 × 0.21 × 0.15	0.21 × 0.19 × 0.15
Radiation	MoKα (λ = 0.71073)	MoKα (λ = 0.71073)	MoKα (λ = 0.71073)
2Θ range for data collection/°	2.528 to 51.362	3.052 to 51.362	4.528 to 51.414
Reflections collected	86623	28995	182457
Independent reflections	14494 [R_{int} = 0.1289, R_{sigma} = 0.0871]	7406 [R_{int} = 0.0598, R_{sigma} = 0.0618]	16943 [R_{int} = 0.0636, R_{sigma} = 0.0329]
Data/restraints/parameters	14494/186/1027	7406/0/467	16943/11/1049
Goodness-of-fit on F^2	1.013	1.027	1.047
Final R indexes [I>=2σ (I)]	R_1 = 0.0615, wR_2 = 0.1196	R_1 = 0.0432, wR_2 = 0.0962	R_1 = 0.0551, wR_2 = 0.1355
Final R indexes [all data]	R_1 = 0.1404, wR_2 = 0.1506	R_1 = 0.0799, wR_2 = 0.1098	R_1 = 0.0788, wR_2 = 0.1477
Largest diff. peak/hole / e Å^{-3}	0.53/-0.53	0.34/-0.48	1.22/-0.82

Appendix I

Table A7. Summary of X-ray crystallographic data for **4**, **5**·DCM, **6.**

Identification code	4	5·DCM	6
Empirical formula	$C_{35}H_{38}AgBr_2F_3N_8O_3S$	$C_{35}H_{40}AgCl_2F_6I_2N_8P$	$C_{74}H_{84}Ag_2F_6I_4N_{16}O_7S_2$
Formula weight	975.48	1150.29	2211.03
Temperature/K	200	200	200
Crystal system	monoclinic	monoclinic	monoclinic
Space group	$P2_1/c$	$P2_1/c$	$P2_1/c$
a/Å	9.9038(3)	9.4189(5)	9.6496(8)
b/Å	14.8885(5)	13.6612(8)	20.488(2)
c/Å	26.6950(10)	33.3236(19)	42.676(4)
α/°	90	90	90
β/°	97.062(2)	94.669(2)	93.483(3)
γ/°	90	90	90
Volume/Å^3	3906.4(2)	4273.6(4)	8421.7(13)
Z	4	4	4
ρ_{calc}g/cm^3	1.659	1.788	1.744
μ/mm^{-1}	2.675	2.141	2.055
F(000)	1952.0	2248.0	4352.0
Crystal size/mm^3	0.11 × 0.09 × 0.05	0.1 × 0.06 × 0.05	0.05 × 0.05 × 0.02
Radiation	MoKα (λ = 0.71073)	MoKα (λ = 0.71073)	MoKα (λ = 0.71073)
2Θ range for data collection/°	5.684 to 51.388	5.156 to 51.432	4.534 to 50.078
Reflections collected	56537	64709	34376
Independent reflections	7415 [R_{int} = 0.0555, R_{sigma} = 0.0296]	8103 [R_{int} = 0.1263, R_{sigma} = 0.0731]	14525 [R_{int} = 0.1999, R_{sigma} = 0.3534]
Data/restraints/parameters	7415/90/529	8103/10/523	14525/492/974
Goodness-of-fit on F^2	1.014	1.054	1.013
Final R indexes [I>=2σ (I)]	R_1 = 0.0358, wR_2 = 0.0814	R_1 = 0.0547, wR_2 = 0.1203	R_1 = 0.1020, wR_2 = 0.1485
Final R indexes [all data]	R_1 = 0.0496, wR_2 = 0.0887	R_1 = 0.1153, wR_2 = 0.1529	R_1 = 0.2752, wR_2 = 0.1975
Largest diff. peak/hole / e Å-3	1.20/-1.05	1.38/-1.31	0.92/-0.88

Appendix I

Table A8. Summary of X-ray crystallographic data for **7**, **8**, **9**·DCE, **10**·DCM.

Identification code	**7**	**8**	**9**·DCE	**10**·DCM
Empirical formula	$C_{34}H_{38}AgBr_2F_6N_8P$	$C_{35}H_{38}AgBr_2F_3N_8O_3S$	$C_{37}H_{44}AgCl_3F_6I_2N_8P$	$C_{73}H_{82}Ag_2Cl_6F_6I_4N_{16}O_6S_2$
Formula weight	971.38	975.48	1213.79	2393.70
Temperature/K	296.15	296.15	150	150
Crystal system	monoclinic	monoclinic	monoclinic	orthorhombic
Space group	$P2_1/n$	$P2_1/c$	$P2_1/n$	$Pca2_1$
a/Å	15.157(3)	9.743(5)	9.5602(2)	29.551(2)
b/Å	26.883(5)	26.387(11)	12.9737(4)	9.6583(7)
c/Å	19.711(4)	16.229(7)	37.2003(10)	31.178(2)
α/°	90	90	90	90
β/°	94.614(4)	93.090(12)	96.0100(10)	90
γ/°	90	90	90	90
Volume/Å^3	8005(3)	4166(3)	4588.6(2)	8898.7(11)
Z	8	4	4	4
ρ_{calc}g/cm^3	1.612	1.555	1.757	1.787
μ/mm^{-1}	2.603	2.508	2.056	2.125
F(000)	3872.0	1952.0	2380.0	4696.0
Crystal size/mm^3	0.2 × 0.2 × 0.15	0.27 × 0.23 × 0.15	0.19 × 0.09 × 0.07	0.25 × 0.08 × 0.05
Radiation	MoKα (λ = 0.71073)	MoKα (λ = 0.71073)	MoKα (λ = 0.71073)	MoKα (λ = 0.71073)
2Θ range for data collection/°	2.568 to 52.446	2.95 to 52.6	5.516 to 52.844	4.416 to 51.436
Reflections collected	95018	49787	73634	124372
Independent reflections	16022 [R_{int} = 0.1050, R_{sigma} = 0.0782]	8394 [R_{int} = 0.0960, R_{sigma} = 0.0684]	9386 [R_{int} = 0.0434, R_{sigma} = 0.0260]	16867 [R_{int} = 0.1358, R_{sigma} = 0.0983]
Data/restraints/parameters	16022/0/953	8394/0/486	9386/43/548	16867/13/1072
Goodness-of-fit on F^2	1.009	1.010	1.049	1.003
Final R indexes [I>=2σ (I)]	R_1 = 0.0538, wR_2 = 0.1185	R_1 = 0.0477, wR_2 = 0.0914	R_1 = 0.0364, wR_2 = 0.0855	R_1 = 0.0403, wR_2 = 0.0966

Appendix I

Final R indexes [all data]	R_1 = 0.1397, wR_2 = 0.1536	R_1 = 0.1145, wR_2 = 0.1143	R_1 = 0.0537, wR_2 = 0.0975	R_1 = 0.0533, wR_2 = 0.0999
Largest diff. peak/hole / e $Å^{-3}$	0.77/-0.67	0.65/-0.60	1.02/-1.62	2.31/-0.83

Appendix I

Table A9. Summary of X-ray crystallographic data for **9**-phase-1, **9**-phase-2, **10**-phase-1.

Identification code	**9**-phase-1	**9**-phase-3	**10**-phase-1
Empirical formula	$C_{70}H_{110}AgF_6I_2N_8O_9P$	$C_{34}H_{38}AgF_6I_2N_8P$	$C_{55}H_{78}AgF_3I_2N_8O_8S$
Formula weight	1714.29	1065.36	1429.98
Temperature/K	200.0	150	150.0
Crystal system	trigonal	monoclinic	trigonal
Space group	P-3	$P2_1/c$	P-3
a/Å	39.720(4)	9.9117(4)	39.897(2)
b/Å	39.720(4)	26.9021(12)	39.897
c/Å	9.5067(7)	15.1237(7)	9.5045(5)
α/°	90	90	90
β/°	90	94.878(2)	90
γ/°	120	90	120
Volume/Å^3	12989(3)	4018.1(3)	13102.3(15)
Z	6	4	6
ρ_{calc}g/cm^3	1.315	1.761	1.087
μ/mm^{-1}	1.028	2.141	1.008
F(000)	5280.0	2080.0	4344.0
Crystal size/mm^3	0.19 × 0.02 × 0.02	0.2 × 0.1 × 0.03	0.05 × 0.02 × 0.02
Radiation	MoKα (λ = 0.71073)	MoKα (λ = 0.71073)	MoKα (λ = 0.71073)
2Θ range for data collection/°	4.446 to 50.048	4.124 to 51.412	4.444 to 51.352
Reflections collected	88979	104920	320344
Independent reflections	15302 [R_{int} = 0.2320, R_{sigma} = 0.1842]	7623 [R_{int} = 0.0583, R_{sigma} = 0.0221]	16555 [R_{int} = 0.1008, R_{sigma} = 0.0396]
Data/restraints/parameters	15302/1/444	7623/0/477	16555/472/786
Goodness-of-fit on F^2	1.008	1.047	1.091
Final R indexes [I>=2σ (I)]	R_1 = 0.0990, wR_2 = 0.2189	R_1 = 0.0249, wR_2 = 0.0481	R_1 = 0.1132, wR_2 = 0.2851
Final R indexes [all data]	R_1 = 0.1855, wR_2 = 0.2543	R_1 = 0.0345, wR_2 = 0.0524	R_1 = 0.1306, wR_2 = 0.2970
Largest diff. peak/hole / e Å^{-3}	1.21/-1.07	0.71/-0.86	3.27/-2.27

Appendix I

Table A10. Summary of X-ray crystallographic data for $[Ag(L^{4CCl})_2](PF_6)\cdot THF$ (**11**·THF), and $[Ag(L^{4CCl})_2]$ (CF_3SO_3) (**12**).

Identification code	**10**-phase-2	**10**-phase-3	**11**·THF	**12**
Empirical formula	$C_{78}H_{92}Ag_2F_6I_4N_{16}O_8S_2$	$C_{35}H_{38}AgF_3I_2N_8O_3S$	$C_{42}H_{46}AgF_6I_2N_8OP$	$C_{39}H_{38}AgF_3I_2N_8O_3S$
Formula weight	2283.13	1069.46	1185.51	1117.50
Temperature/K	150	150.0	200.0	200.0
Crystal system	triclinic	orthorhombic	monoclinic	triclinic
Space group	P-1	$Pca2_1$	C2/c	P-1
a/Å	11.2548(7)	27.875(13)	15.7328(5)	11.0060(4)
b/Å	15.2294(10)	9.945(5)	20.8828(7)	14.0038(5)
c/Å	26.6509(18)	14.518(7)	17.8003(6)	15.7856(6)
α/°	99.860(3)	90	90	85.1660(10)
β/°	96.599(3)	90	117.8019(13)	78.1020(10)
γ/°	102.398(3)	90	90	69.3780(10)
Volume/Å^3	4340.7(5)	4025(3)	5173.1(3)	2227.97(14)
Z	2	4	4	2
ρ_{calc}g/cm^3	1.747	1.765	1.522	1.666
μ/mm^{-1}	1.997	2.145	1.673	1.942
F(000)	2256.0	2096.0	2336.0	1096.0
Crystal size/mm^3	0.09 × 0.07 × 0.02	0.04 × 0.03 × 0.01	0.18 × 0.12 × 0.06	0.12 × 0.07 × 0.02
Radiation	MoKα (λ = 0.71073)	MoKα (λ = 0.71073)	MoKα (λ = 0.71073)	MoKα (λ = 0.71073)
2Θ range for data collection/°	4.388 to 51.406	4.384 to 50.044	5.726 to 52.196	5.274 to 51.358
Reflections collected	33036	40628	66426	16854
Independent reflections	16530 [R_{int} = 0.0367, R_{sigma} = 0.0479]	7029 [R_{int} = 0.3732, R_{sigma} = 0.2746]	5096 [R_{int} = 0.0476, R_{sigma} = 0.0191]	8435 [R_{int} = 0.0779, R_{sigma} = 0.1065]
Data/restraints/parameters	16530/75/1061	7029/428/459	5096/123/359	8435/75/558
Goodness-of-fit on F^2	1.086	1.034	1.034	1.003
Final R indexes [I>=2σ (I)]	R_1 = 0.0684, wR_2 = 0.1690	R_1 = 0.1277, wR_2 = 0.2191	R_1 = 0.0475, wR_2 = 0.1278	R_1 = 0.0629, wR_2 = 0.1497

Appendix I

Final R indexes [all data]	R_1 = 0.0797, wR_2 = 0.1754	R_1 = 0.2694, wR_2 = 0.2842	R_1 = 0.0616, wR_2 = 0.1411	R_1 = 0.1056, wR_2 = 0.1696
Largest diff. peak/hole / e Å^{-3}	1.89/-1.19	1.63/-1.13	2.13/-1.50	0.82/-0.82

$$R1 = \Sigma||F_o|-|F_c||/\Sigma|F_o|,\ \ wR2 = [\Sigma[w(F_o^2-F_c^2)^2]/\Sigma[w(F_o^2)^2]]^{1/2},\ w = 1/[\sigma^2(F_o^2) + (aP)^2 + bP], \text{ where } \ P = [\max(F_o^2,0) + 2F_c^2]/3$$

8.3 Thermal Analysis

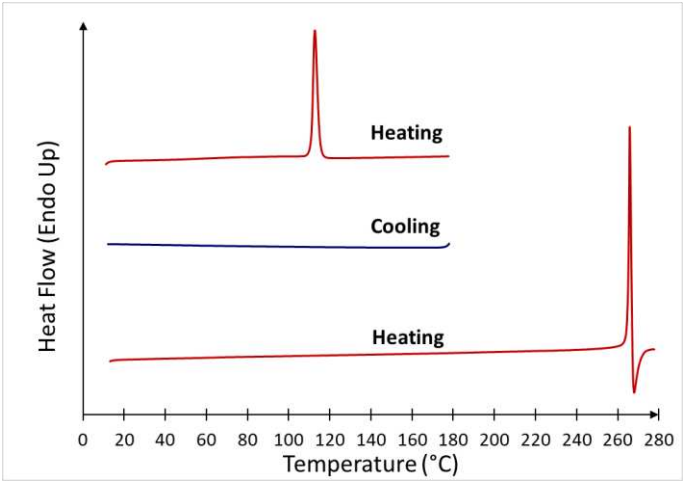

Figure A14. DSC traces of **9**-phase-2. Endothermic peak at 111°C and decomposition of the crystals at 264°C.

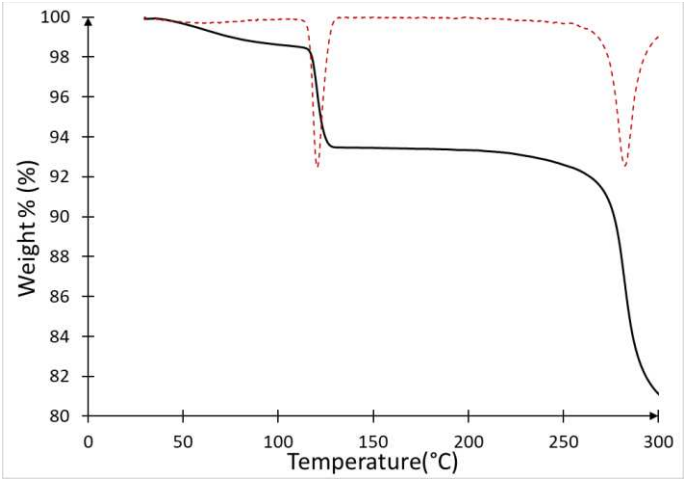

Figure A15. TGA trace of **9**-phase-2 (black line) and calculated derivate (red-dotted line). Weight loss (1.39 %) at 56°C, weight loss (5.10 %) at 120°C and weight loss (13.0 %) at 282°C due to the decomposition of the crystals.

Appendix I

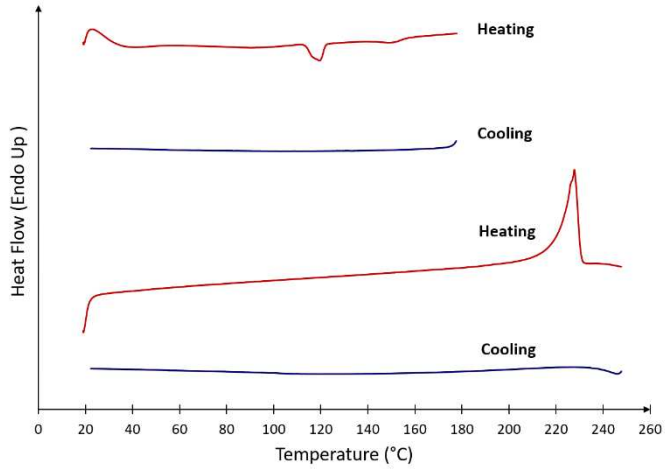

Figure A16. DSC traces of **10**-phase-2. Endothermic peak at 20°C and 113°C due to the exit of the solvent from crystals, exothermic peak at 113°C due to the phase transition from phase-2 to phase-3 and decomposition of the crystals at 221°C.

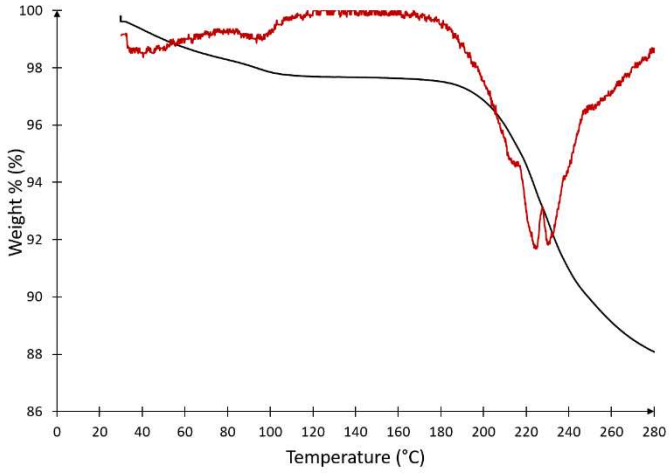

Figure A17. TGA trace of **10**-phase-2 (black line) and calculated derivate (red-dotted line). Weight loss (1.92 %) at 40°C and weight loss (10.3 %) at 225°C due to the decomposition of the crystals.

8.4 PXRD patterns

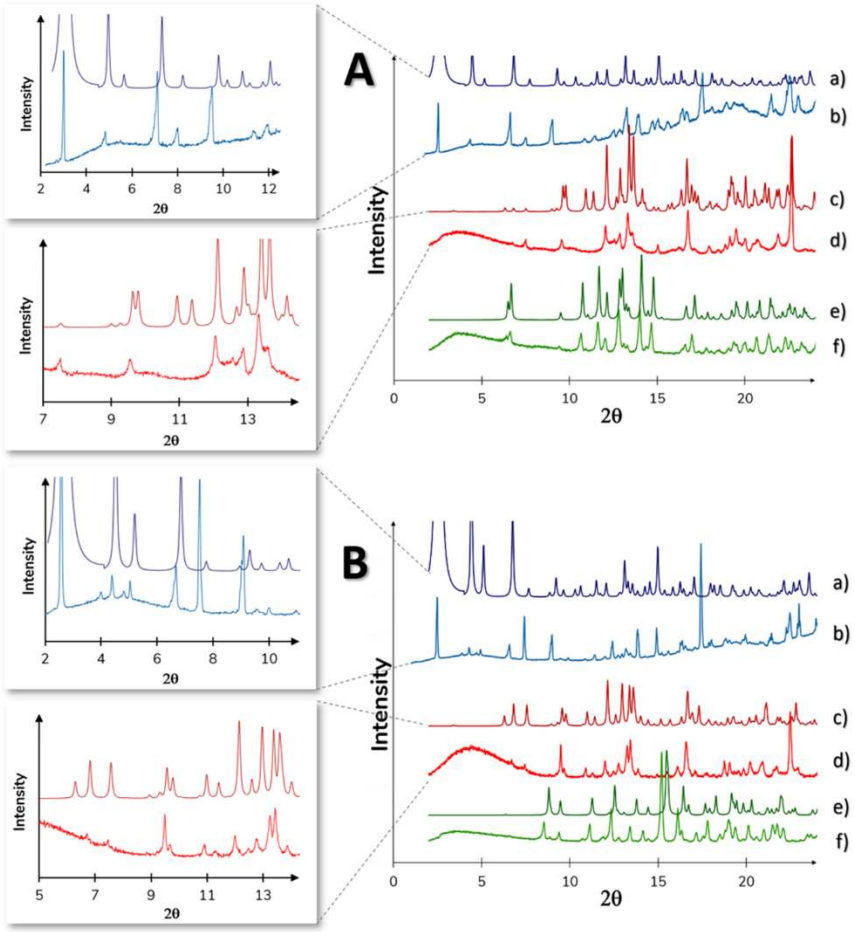

Figure A18. Overlap between the simulated and experimental XRD of the two systems: panel A: **9**-phase-1 (a,b), **9**-phase-2 (c,d), **9**-phase-3 (e,f) and panel B: **10**-phase-1 (a,b), **10**-phase-2 (c,d), **10**-phase-3 (e,f).

9. Appendix II

Supplementary Materials for Chapter 3

9.1 NMR spectra of synthetized monomers

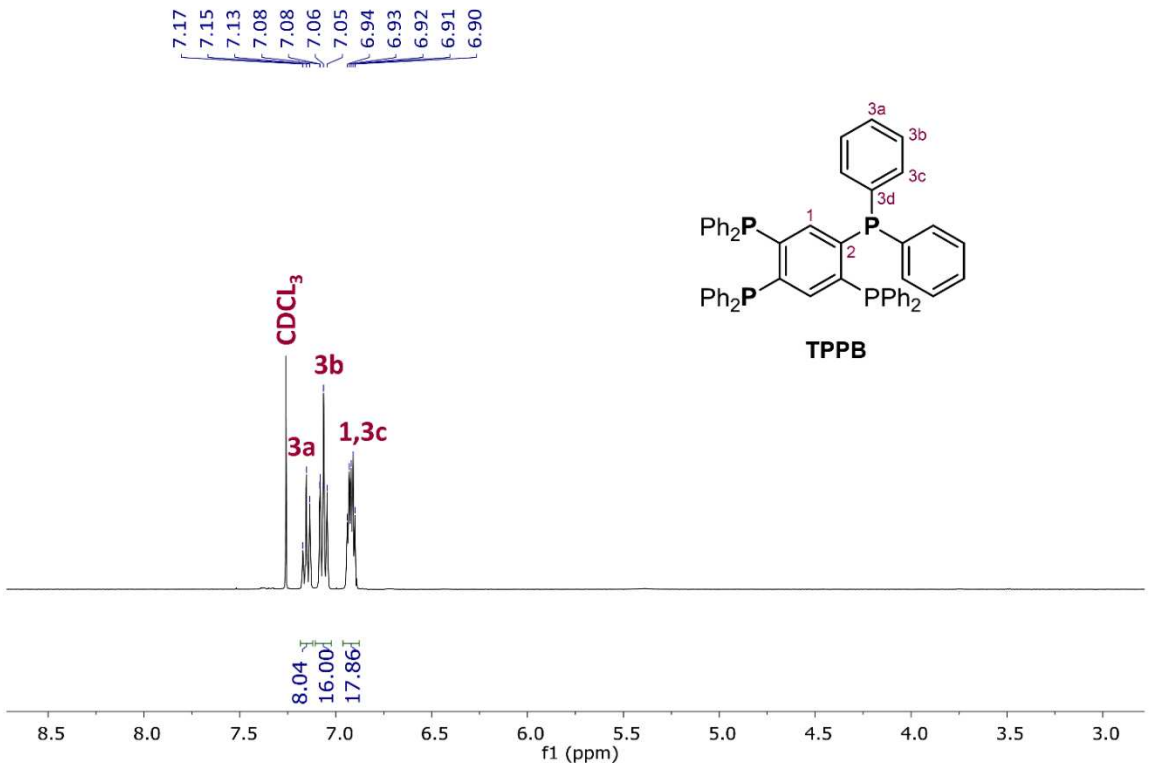

Figure B1. ^{1}H-NMR (400 MHz, $CDCl_3$) spectrum of TPPB.

Appendix II

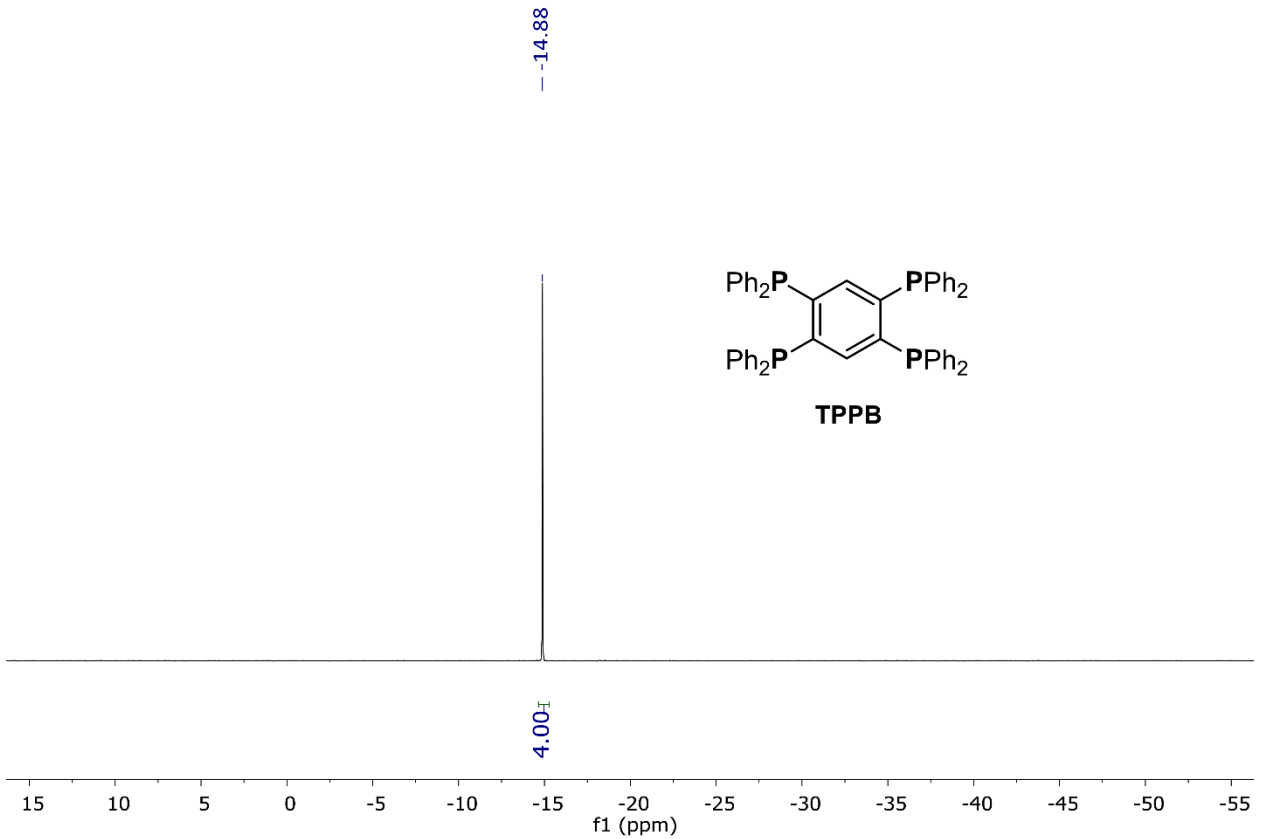

Figure B2. ^{31}P-NMR (162 MHz, $CDCl_3$) spectrum of TPPB.

Appendix II

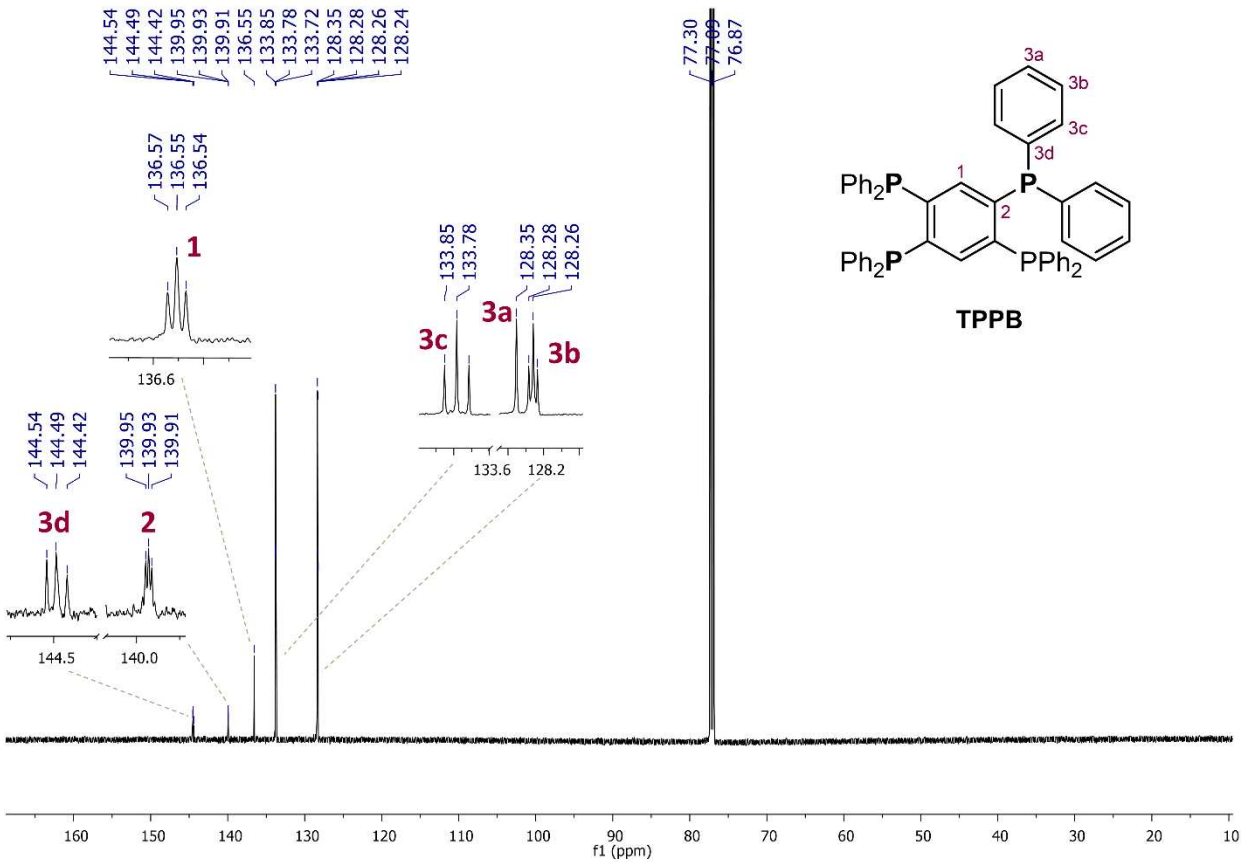

Figure B3. ^{13}C-NMR (151 MHz, $CDCl_3$) spectrum of TPPB.

Appendix II

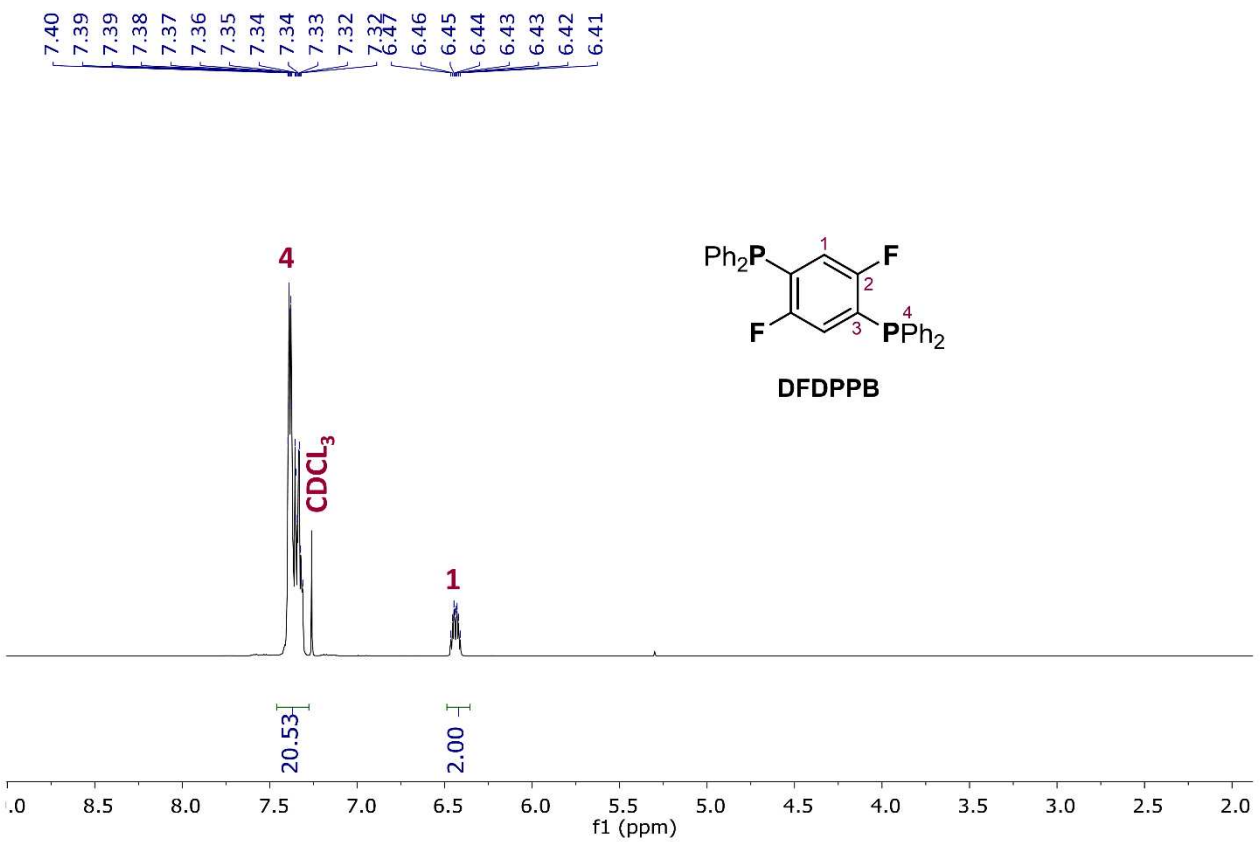

Figure B4. ^{1}H-NMR (400 MHz, $CDCl_3$) spectrum of DFDPPB.

Appendix II

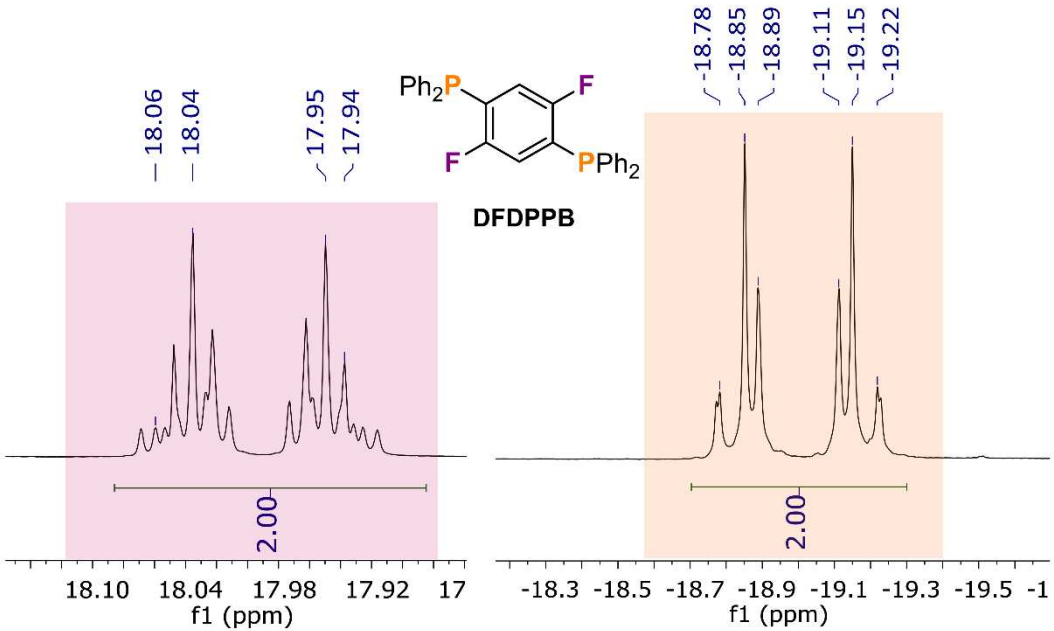

Figure B5. ^{19}F-NMR (565 MHz, $CDCl_3$) and ^{31}P-NMR (162 MHz, $CDCl_3$) spectrum of DFDPPB.

Appendix II

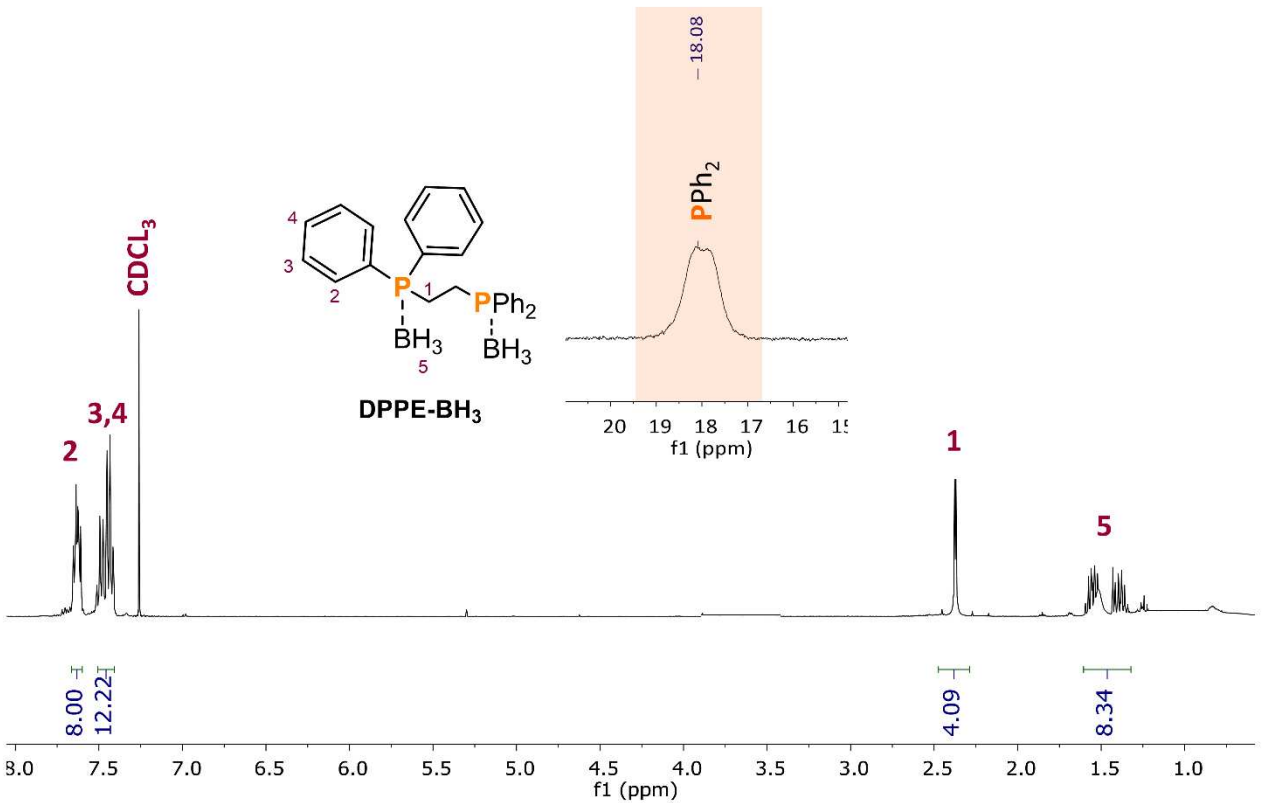

Figure B6. ^{1}H-NMR (400 MHz, $CDCl_3$) and ^{31}P-NMR (162 MHz, $CDCl_3$) spectrum of DPPE-BH_3.

9.2 Solid-state NMR spectra of POPs.

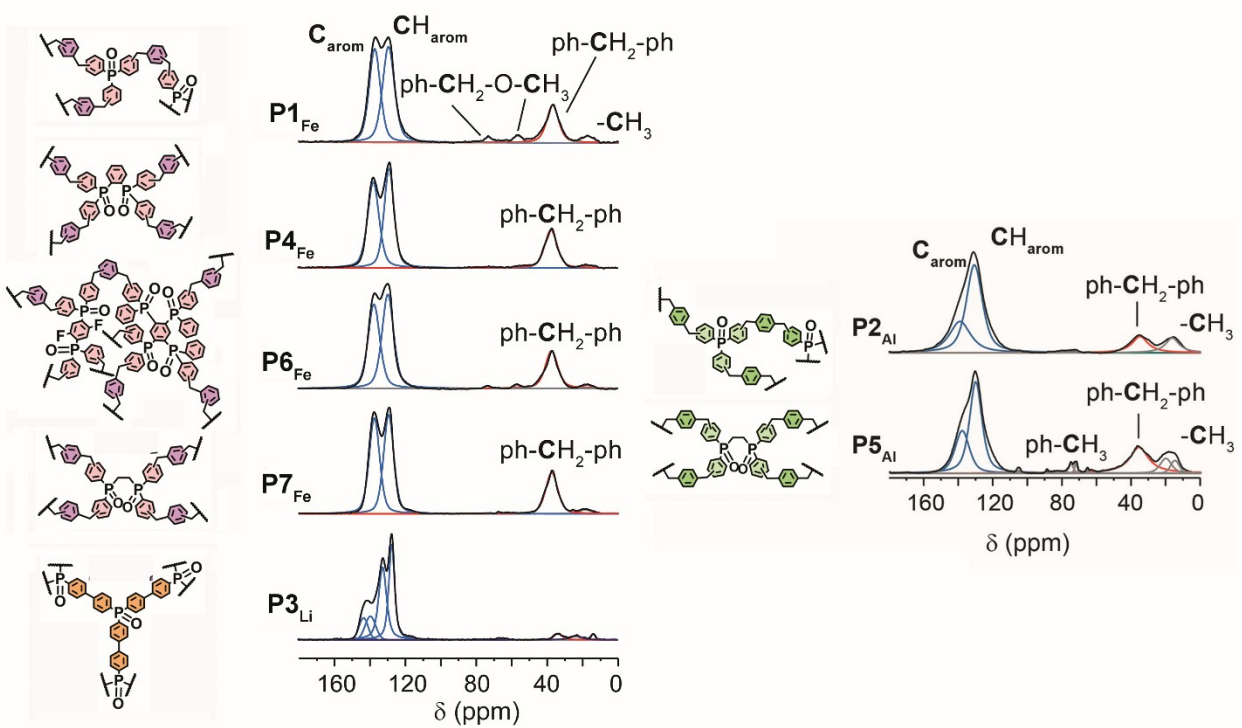

Figure B7. $^{13}C\{^{1}H\}$ CP MAS spectra of **P1-P7** materials performed at a spinning speed of 12.5 kHz and contact time of 2 ms.

Appendix II

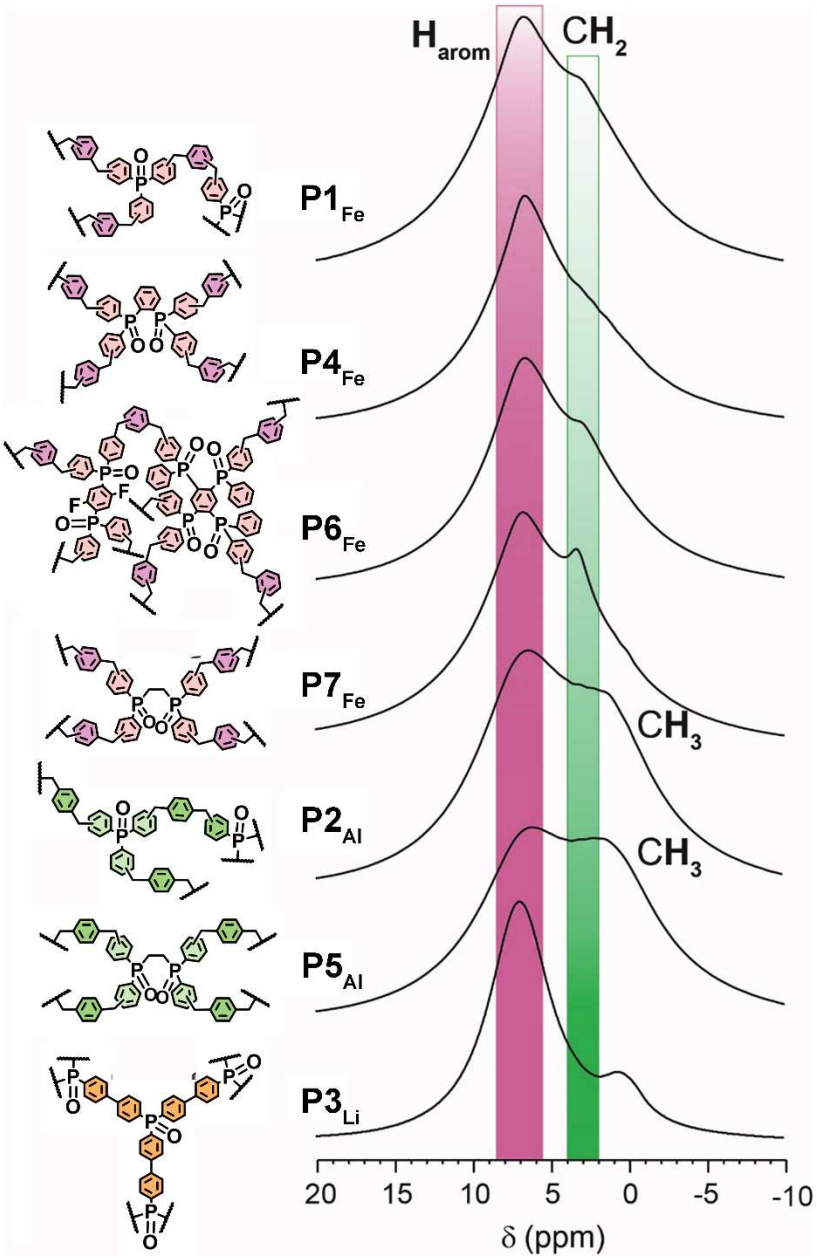

Figure B8. ^{1}H MAS spectra of **P1-P7** materials performed at a spinning speed of 12.5 kHz and recycle delay of 20 s.

Appendix II

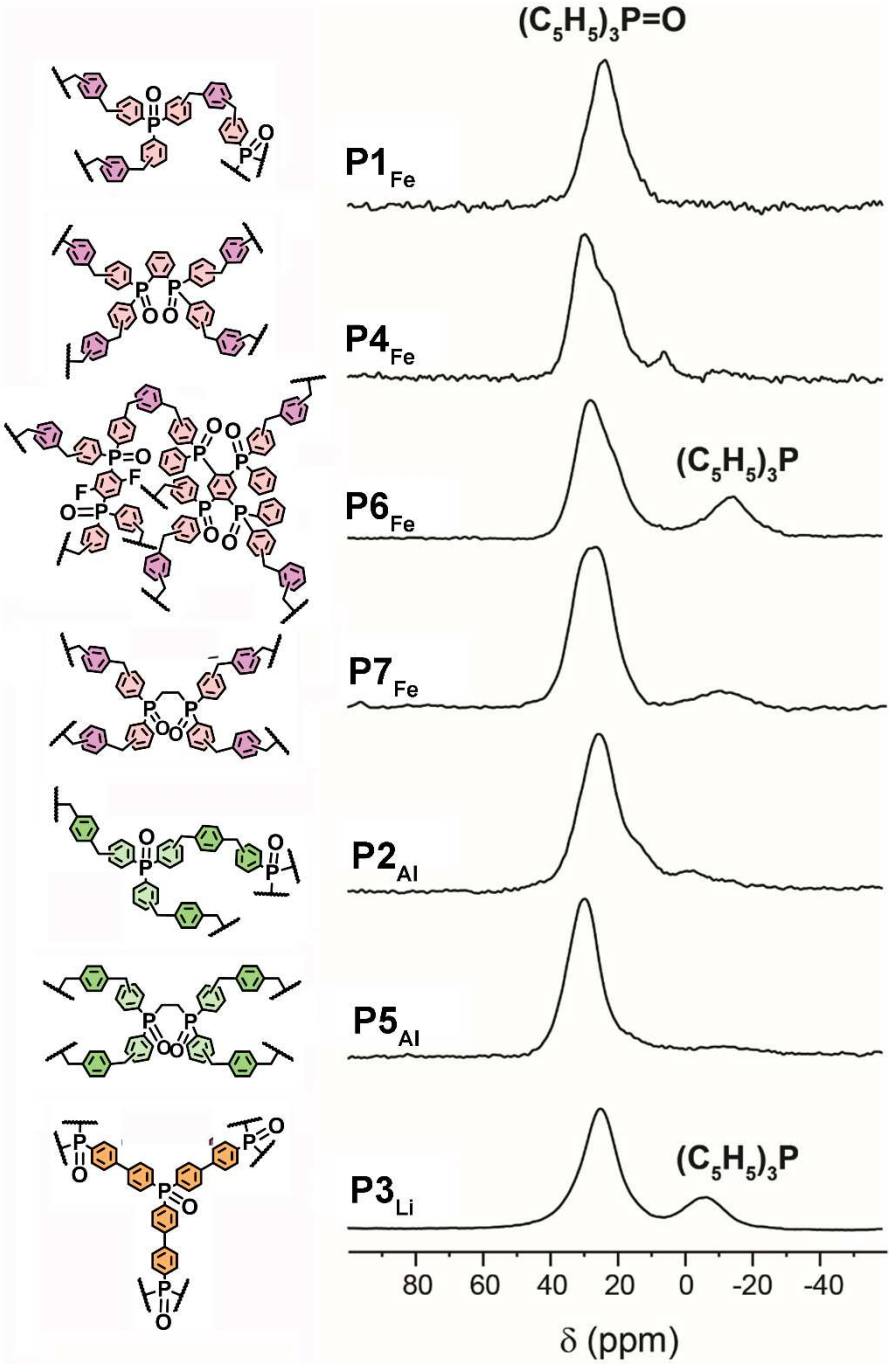

Figure B9. $^{31}P\{^{1}H\}$ CP MAS spectra of **P1-P7** materials performed at a spinning speed of 12.5 kHz and contact time of 8.5 ms.

Appendix II

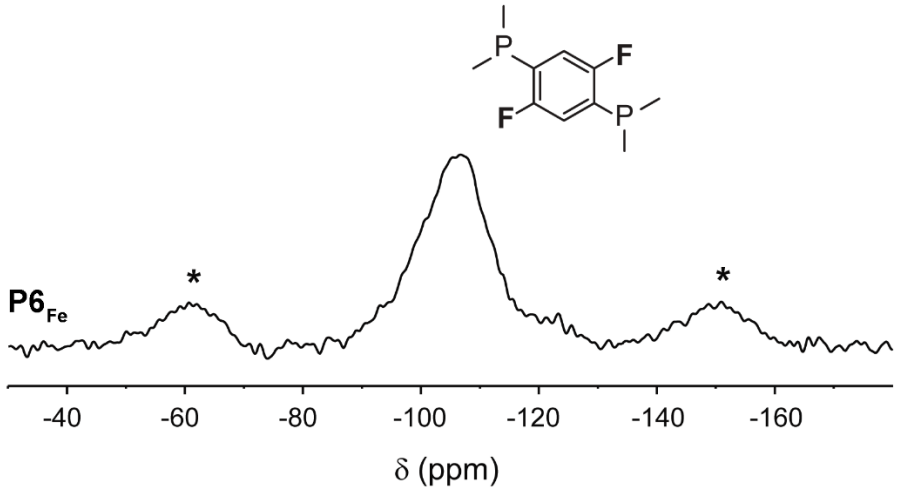

Figure B10. ^{19}F MAS spectrum of $\mathbf{P6_{Fe}}$ material performed at a spinning speed of 12.5 kHz and recycle delay of 20 s.

Appendix II

9.3 Crystal data of DFDPPB

Table B1. Crystal data and structure refinement for DFDPPB.

DFDPPB	
Empirical formula	$C_{30}H_{22}F_2P_2$
Formula weight	482.41
Temperature/K	200.0
Crystal system	triclinic
Space group	P-1
a/Å	5.7913(4)
b/Å	12.5845(7)
c/Å	17.0989(10)
α/°	78.690(3)
β/°	84.789(4)
γ/°	85.282(4)
Volume/Å^3	1214.28(13)
Z	2
ρ_{calc}g/cm^3	1.319
μ/mm^{-1}	1.889
F(000)	500.0
Crystal size/mm^3	0.25 × 0.05 × 0.02
Radiation	CuKα (λ = 1.54178)
2Θ range for data collection/°	7.178 to 140.12
Index ranges	-5 ≤ h ≤ 7, -15 ≤ k ≤ 15, -20 ≤ l ≤ 20
Reflections collected	7895
Independent reflections	4555 [R_{int}= 0.0664, R_{sigma}= 0.0785]
Data/restraints/parameters	4555/0/395
Goodness-of-fit on F^2	1.055
Final R indexes [I>=2σ (I)]	R_1= 0.0382, wR_2= 0.0869
Final R indexes [all data]	R_1= 0.0575, wR_2= 0.0934
Largest diff. peak/hole / e Å^{-3}	0.21/-0.27

$R1 = \Sigma||F_o|-|F_c||/\Sigma|F_o|$, $wR2 = [\Sigma[w(F_o^2-F_c^2)^2]/\Sigma[w(F_o^2)^2]]^{½}$, $w = 1/[\sigma^2(F_o^2) + (aP)^2 + bP]$, where $P = [\max(F_o^2,0) + 2F_c^2]/3$

9.4 IR-spectra

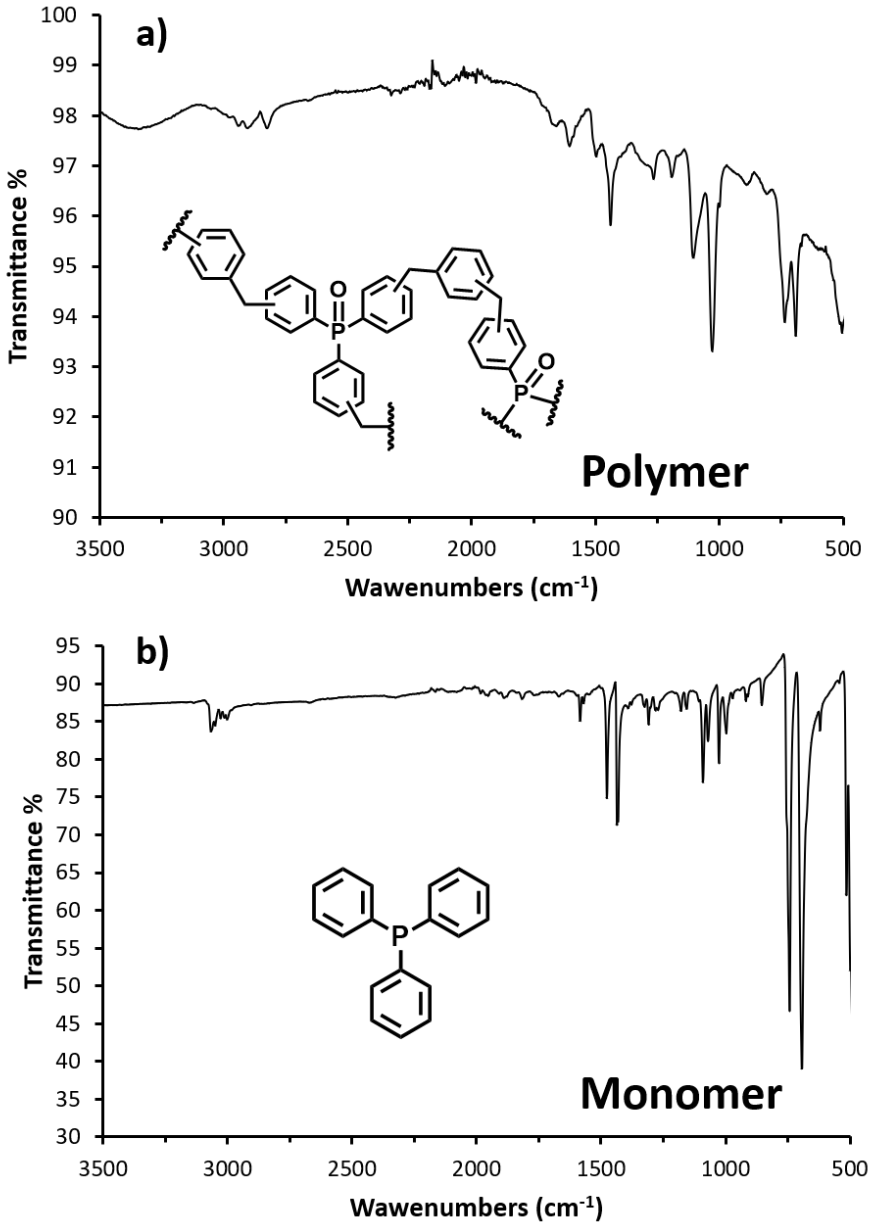

Figure B11. Comparison of the FT-IR spectra of the polymer $\mathbf{P1}_{Fe}$ (a) and of the corresponding triphenylphosphine monomer (b).

Appendix II

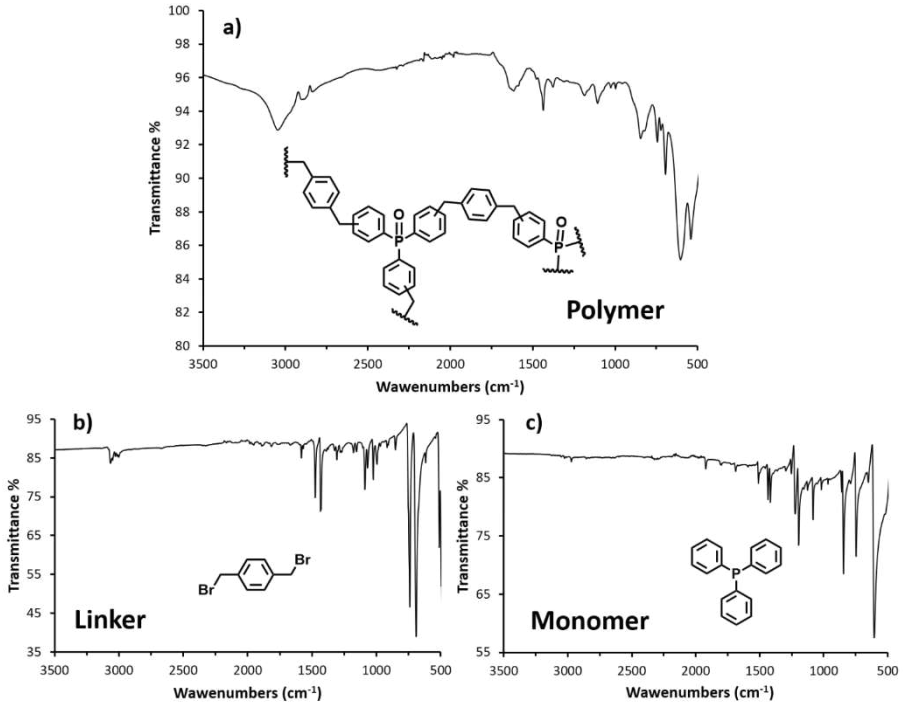

Figure B12. Comparison of the FT-IR spectra of the polymer $\mathbf{P2_{Al}}$ (a), 1,4-bis(bromomethyl)benzene linker (b) and of the corresponding triphenylphosphine monomer (c).

Appendix II

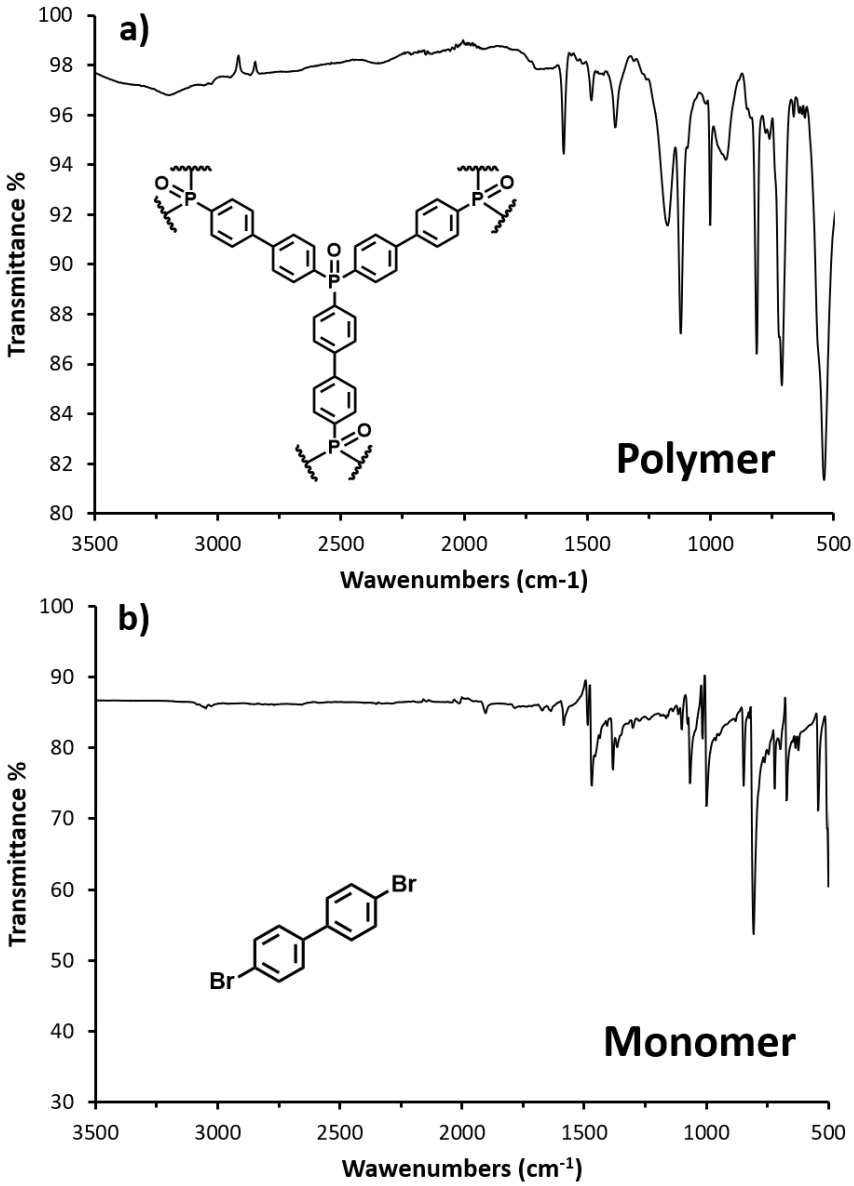

Figure B13. Comparison of the FT-IR spectra of the polymer $\mathbf{P3_{Li}}$ (a) and of the corresponding 4,4'-dibromo-1,1'-biphenyl monomer (b).

Appendix II

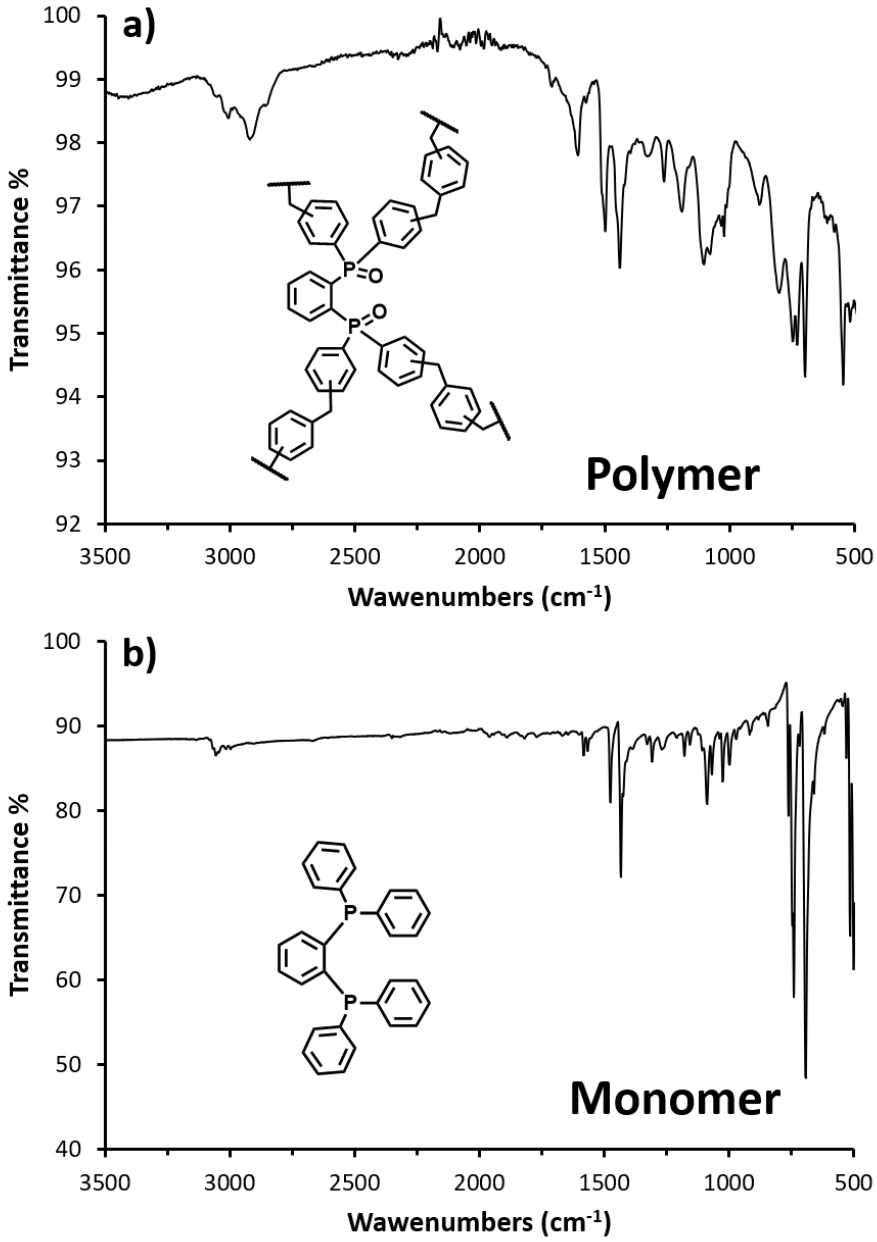

Figure B14. Comparison of the FT-IR spectra of the polymer $\mathbf{P4_{Fe}}$ (a) and of the corresponding 1,2-bis(diphenylphosphaneyl)benzene monomer (b).

Appendix II

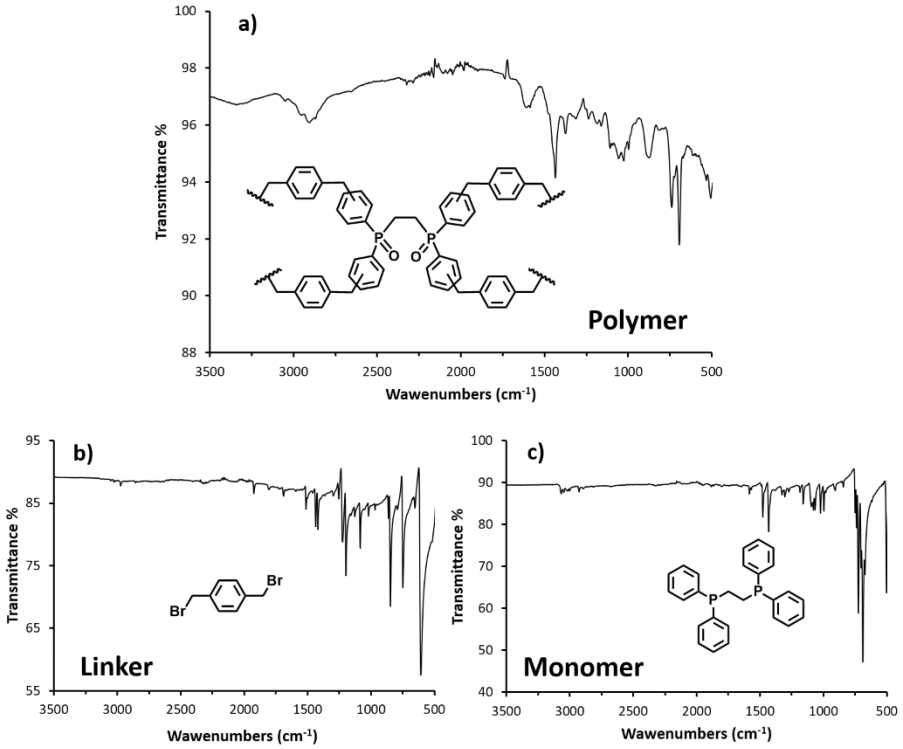

Figure B15. Comparison of the FT-IR spectra of the polymer $\mathbf{P5_{Al}}$ (a), 1,4-bis(bromomethyl)benzene linker (b) and of the corresponding 1,2-bis(diphenylphosphaneyl)ethane monomer (c).

Appendix II

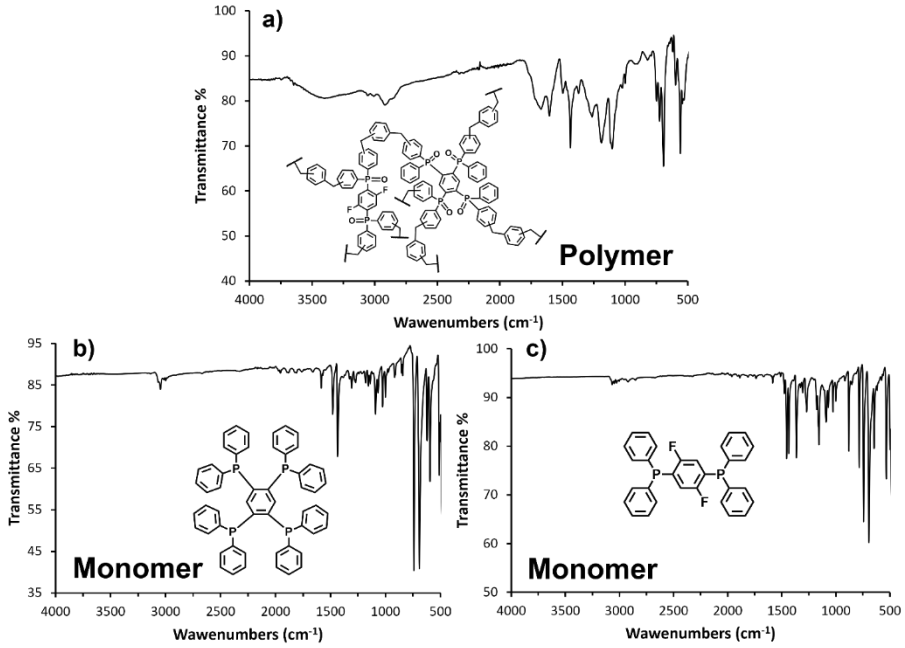

Figure B16. Comparison of the FT-IR spectra of the copolymer **P6** $_{Fe}$ (a) with of the corresponding monomers, 1,2,4,5-tetrakis(diphenylphosphaneyl)benzene (b) and (2,5-difluoro-1,4-phenylene)bis(diphenylphosphane) (c), respectively.

Appendix II

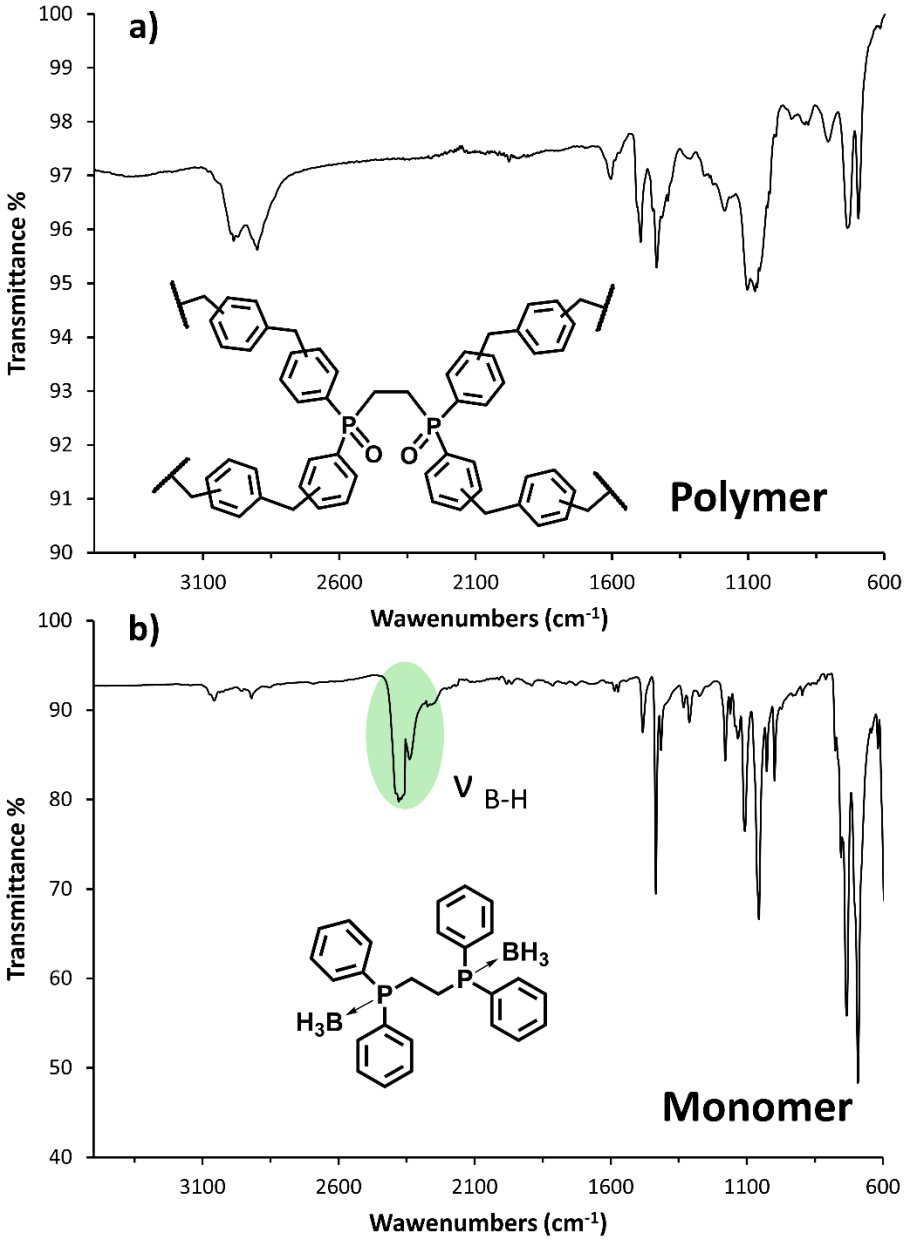

Figure B17. Comparison of the FT-IR spectra of the polymer $\mathbf{P7}_{Fe}$ (a) and of the corresponding protected 1,2-bis(diphenylphosphaneyl)ethane monomer (b).

9.5 Thermogravimetric Analysis of the polymers P1-P7

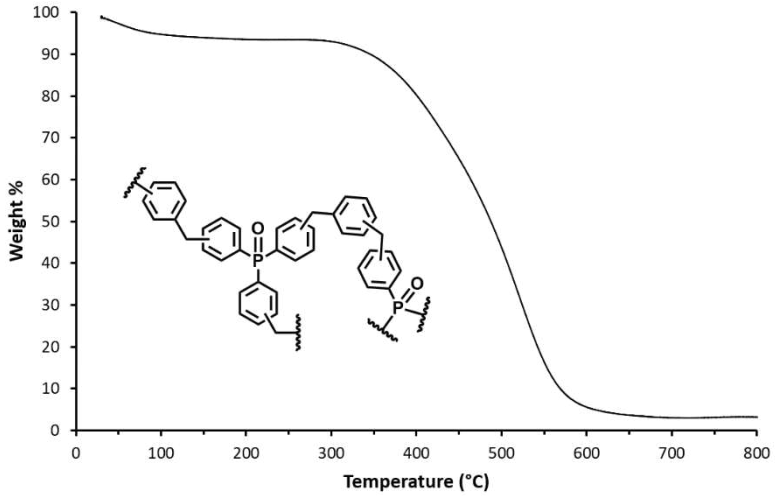

Figure B18. TGA trace of the polymer $\mathbf{P1}_{Fe}$. Solvent weight loss (5.6 %) at 49°C and weight loss (90.4 %) at 520°C due to the decomposition of the polymer.

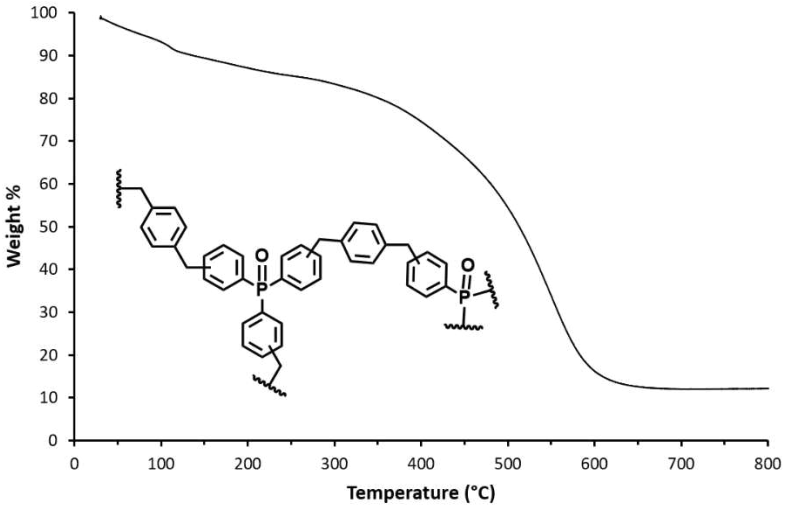

Figure B19. TGA trace of the polymer $\mathbf{P2}_{Al}$. Solvent weight loss (14.1 %) at 112°C and weight loss (73 %) at 549°C due to the decomposition of the polymer.

Appendix II

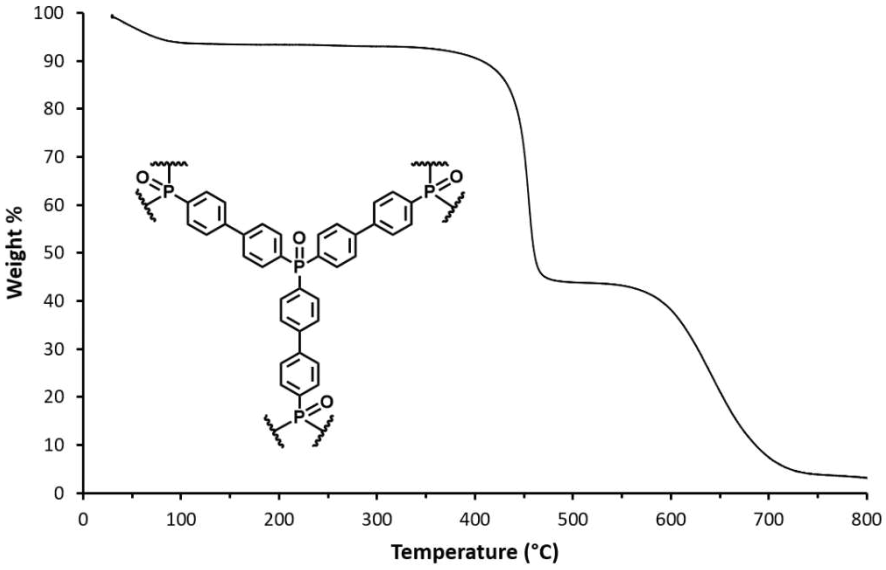

Figure B20. TGA trace of the polymer $\mathbf{P3}_{Li}$. Solvent weight loss (7.0 %) at 52°C, weight losses (49.1 %) at 455°C and (40.6 %) at 637°C due to the decomposition of the polymer.

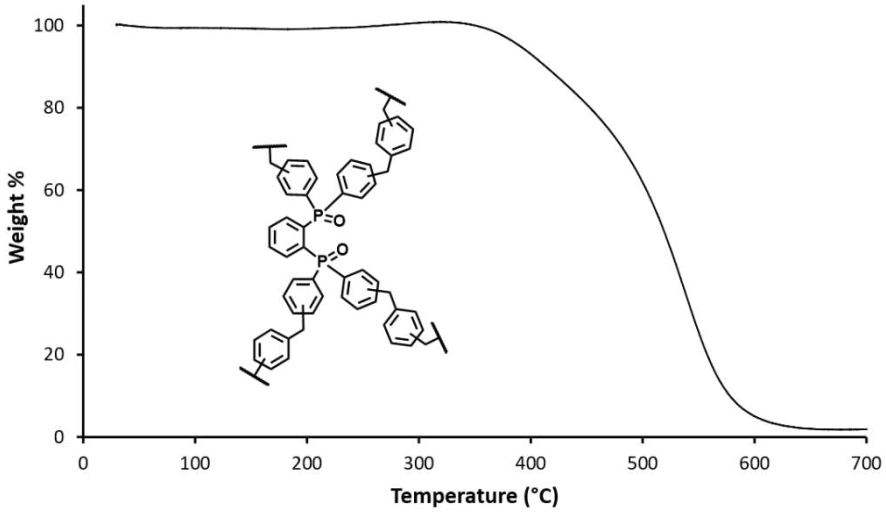

Figure B21. TGA trace of the polymer $\mathbf{P4}_{Fe}$. Weight loss (99.0 %) at 538°C due to the decomposition of the polymer.

Appendix II

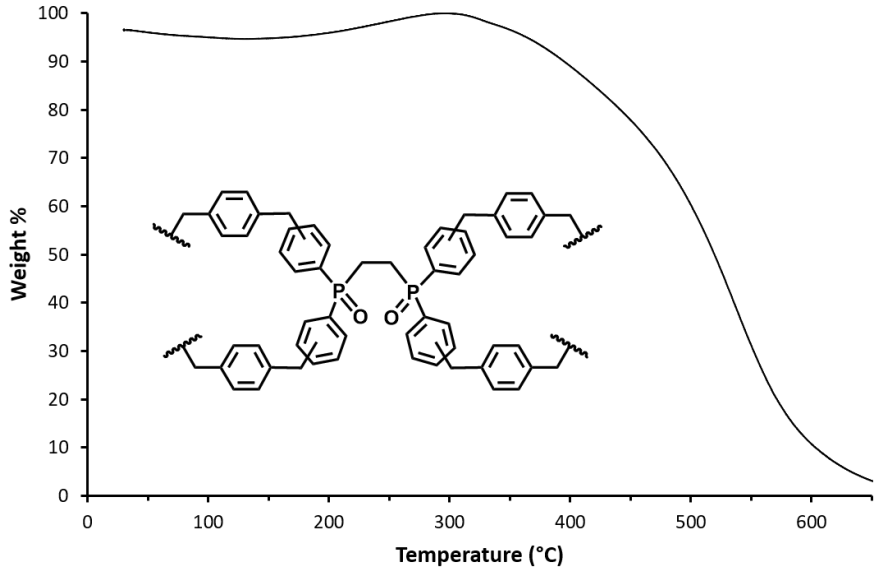

Figure B22. TGA trace of the polymer $\mathbf{P5}_{Fe}$. Solvent weight loss (3.4 %) at 44°C and weight loss (96.8 %) at 534°C due to the decomposition of the polymer.

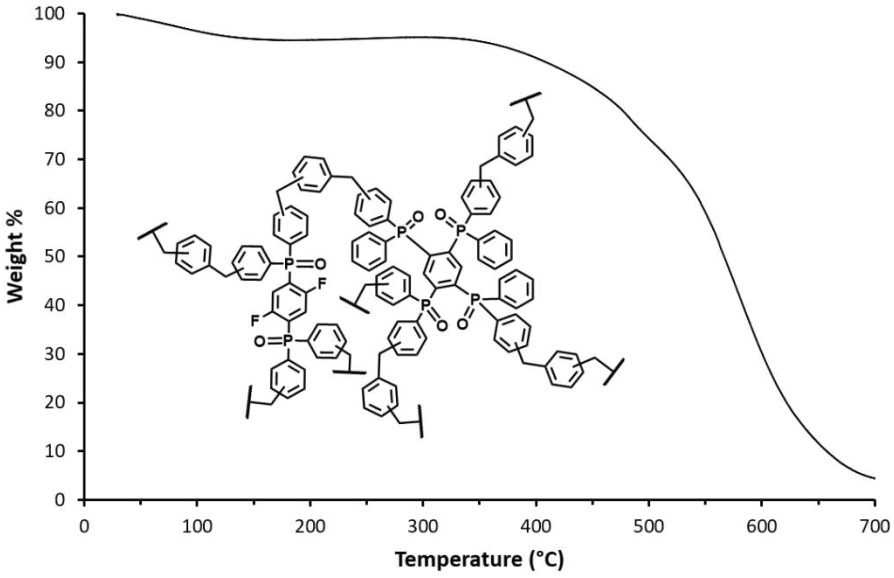

Figure B23. TGA trace of the polymer $\mathbf{P6}_{Fe}$. Solvent weight loss (4.9 %) at 92°C and weight loss (90.6 %) at 588°C due to the decomposition of the polymer.

Appendix II

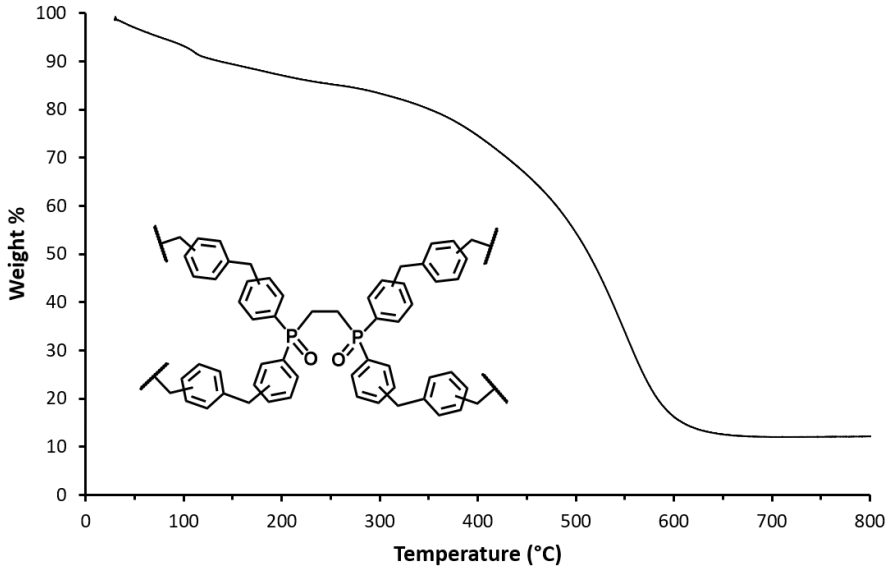

Figure B24. TGA trace of the polymer $\mathbf{P7}_{Fe}$. Solvent weight loss (1.4 %) at 140°C and weight loss (90.8 %) at 559°C due to the decomposition of the polymer.

Appendix II

9.6 Textural parameters of polymers

Table B2. Langmuir and BET surface area and total pore volume of polymer **P1-P7** and **Co@P3$_{Li}$**.

SAMPLE P_x	BET Surface Area (m^2/g)	Langmuir Surface Area (m^2/g)	Total pore volume (cm^3/g)
P1$_{Fe}$	640	727	0.377
P2$_{Al}$	208	235	0.128
P4$_{Fe}$	990	1125	0.920
P5$_{Al}$	224	254	0.147
P6$_{Fe}$	678	772	0.513
P7$_{Fe}$	331	374	0.214
P3$_{Li}$	275	306	0.293
Co@P3$_{Li}$	220	248	0.169

Appendix II

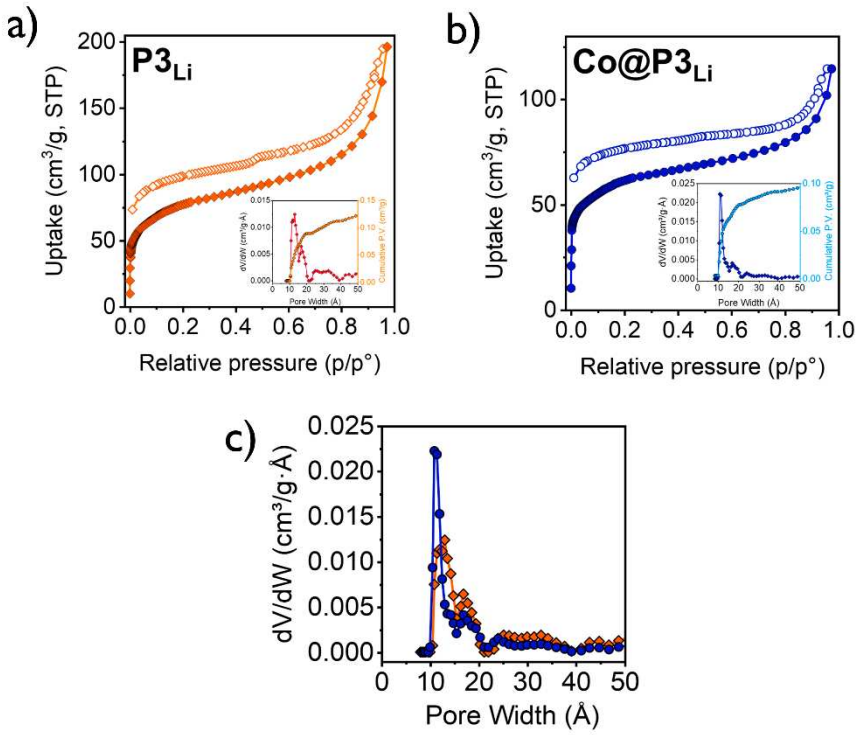

Figure B25. a) N_2 adsorption isotherms at 77 K (adsorption, ●; desorption, ○) for **P3$_{Li}$**. b) N_2 adsorption isotherms at 77 K (adsorption, ●; desorption, ○) for **Co@P3$_{Li}$**. Insets: differential pore size distribution (red, **P3$_{Li}$**, blue, **Co@P3$_{Li}$**) and cumulative pore size distribution (orange, **P3$_{Li}$**, light blue, **Co@P3$_{Li}$**) between 0 and 50 Å. c) Comparison between differential pore size distributions of **P3$_{Li}$** (orange) and **Co@P3$_{Li}$** (blue) between 0 and 50 Å.

9.7 ICP analysis of M@P_X

Table B3. ICP analysis of the polymers **Co@P1$_{Fe}$**, **Co@P2$_{Al}$**, **Co@P4$_{Fe}$**, **Co@P5$_{Al}$**, **Co@P6$_{Fe}$**.

SAMPLE P_X	% Co (w/w)	s.d.
Co@P1$_{Fe}$	4.22	0.04
Co@P2$_{Al}$	2.83	0.04
Co@P4$_{Fe}$	0.78	0.01
Co@P5$_{Al}$	1.94	0.05
Co@P6$_{Fe}$	1.95	0.05

Table B4. ICP analysis of the polymers **Co@P3$_{Li}$**, **Fe@P3$_{Li}$**, **Mo@P3$_{Li}$**, **Ni@P3$_{Li}$**.

SAMPLE P_X	% Co (w/w)	s.d.	% Fe (w/w)	s.d.	% Mo (w/w)	s.d.	% Ni (w/w)	s.d.
Co@P3$_{Li}$	4.51	0.06	-	-	-	-	-	-
Fe@P3$_{Li}$	-	-	6.88	0.04	-	-	-	-
Mo@P3$_{Li}$	-	-	-	-	4.73	0.02	-	-
Ni@P3$_{Li}$	-	-	-	-	-	-	1.93	0.03

9.8 EDX analysis

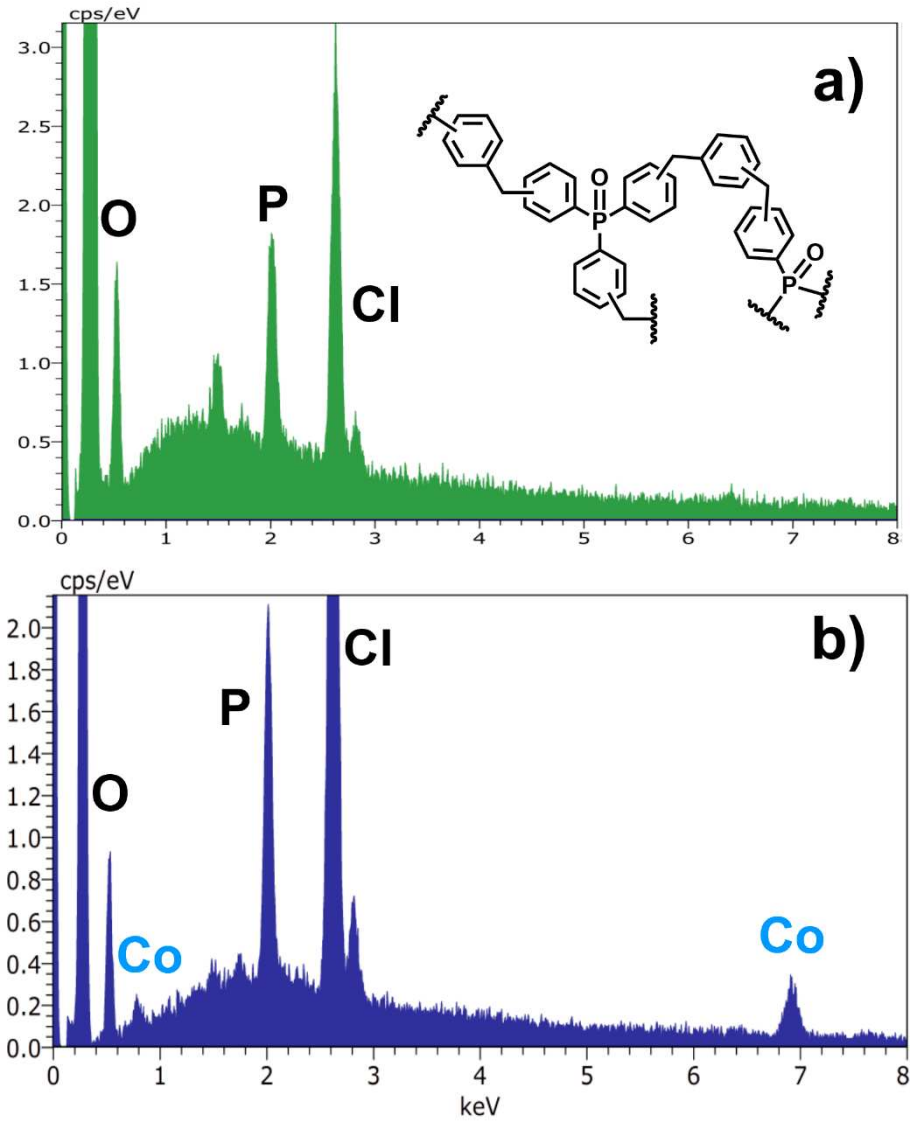

Figure B26. EDX analysis of $\mathbf{P1}_{Fe}$ (a) and $\mathbf{Co@P1}_{Fe}$ (b).

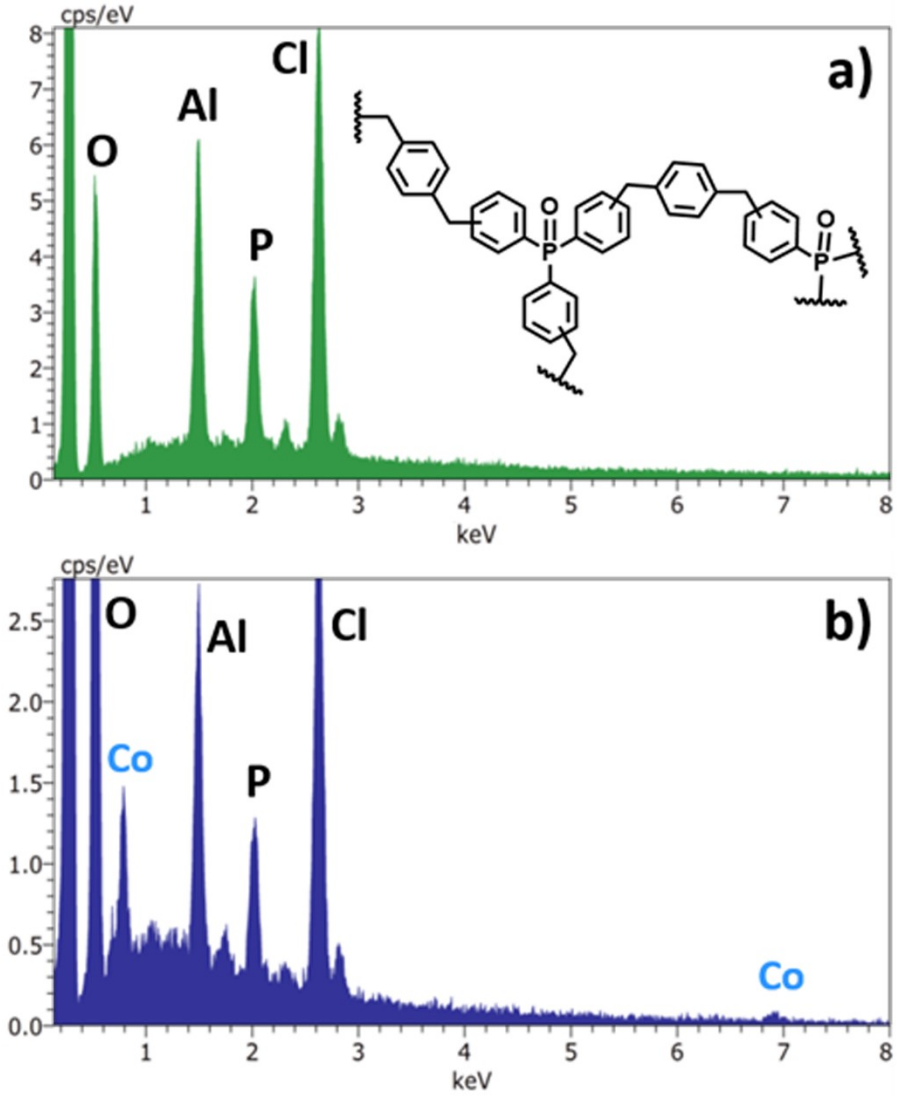

Figure B27. EDX analysis of $\mathbf{P2_{Al}}$ (a) and $\mathbf{Co@P2_{Al}}$ (b).

Appendix II

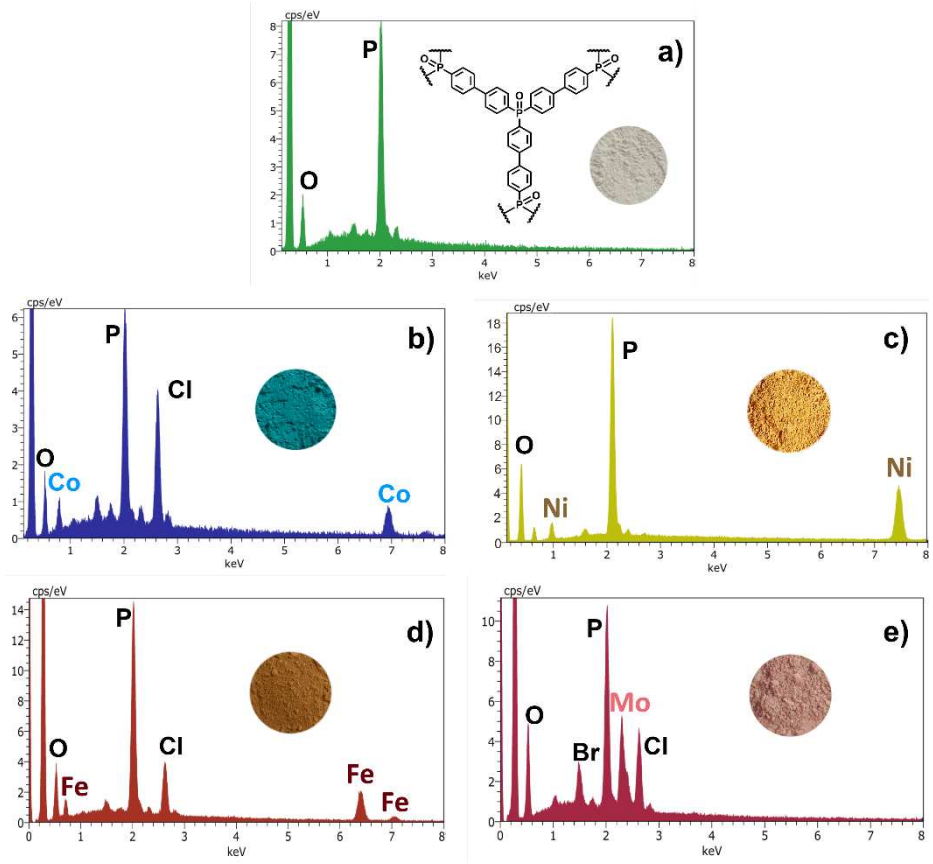

Figure B28. EDX analysis of $\mathbf{P3_{Li}}$ (a), $\mathbf{Co@P3_{Li}}$ (b), $\mathbf{Ni@P3_{Li}}$ (c), $\mathbf{Fe@P3_{Li}}$ (d), $\mathbf{Mo@P3_{Li}}$ (e).

Appendix II

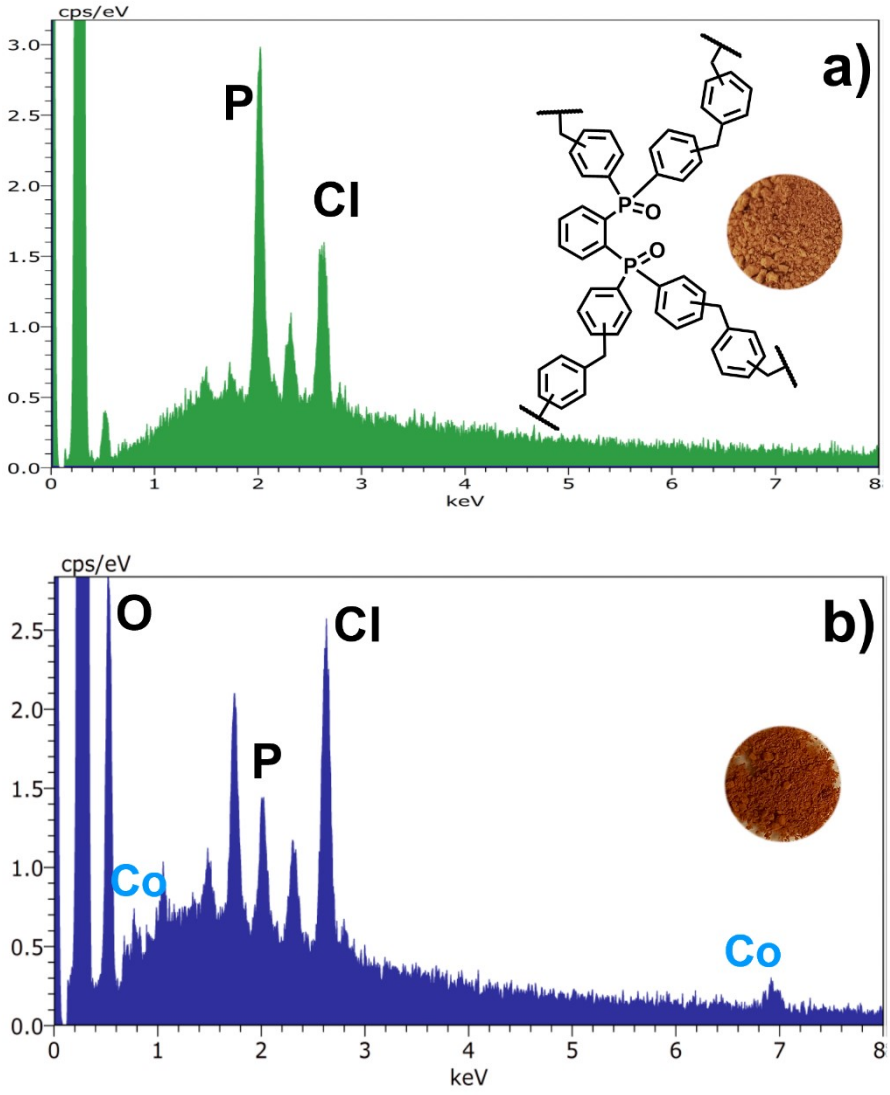

Figure B29. EDX analysis of $\mathbf{P4_{Fe}}$ (a) and $\mathbf{Co@P4_{Fe}}$ (b).

Appendix II

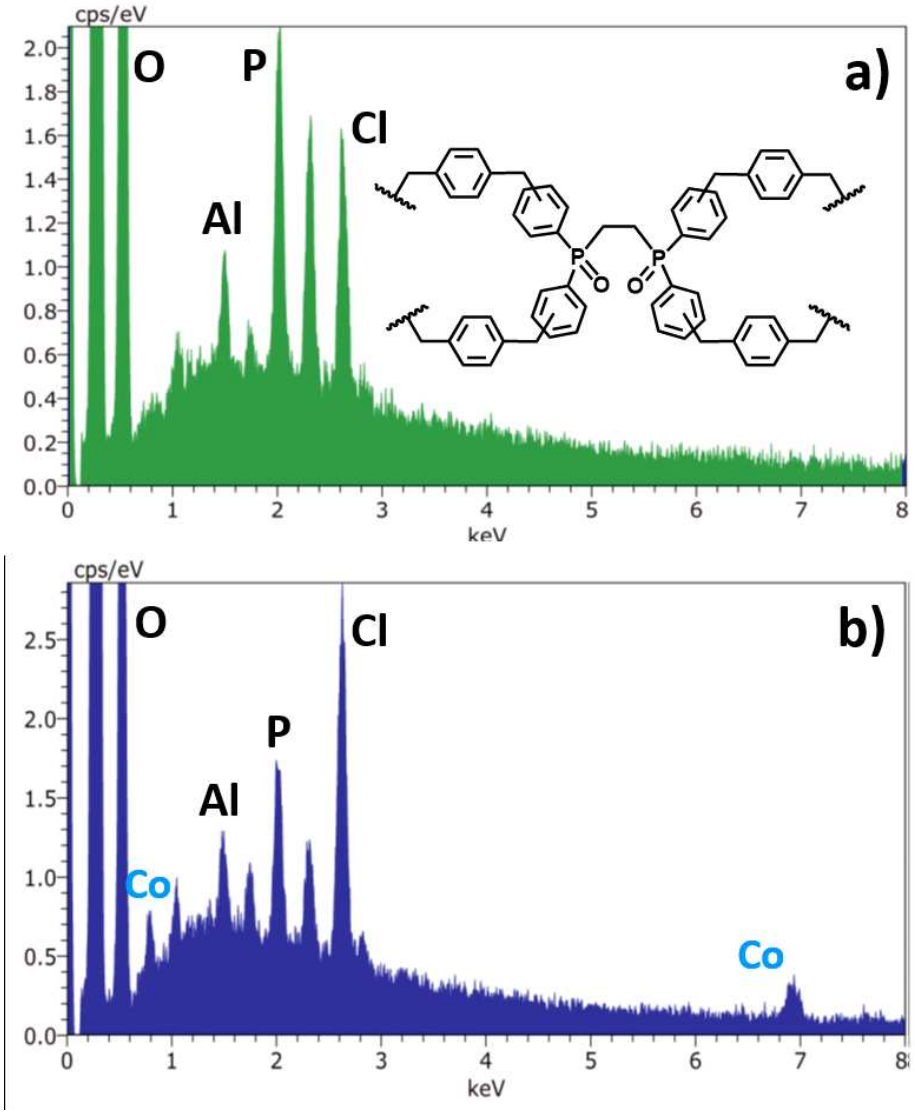

Figure B30. EDX analysis of $\mathbf{P5_{Al}}$ (a) and $\mathbf{Co@P5_{Al}}$ (b).

Appendix II

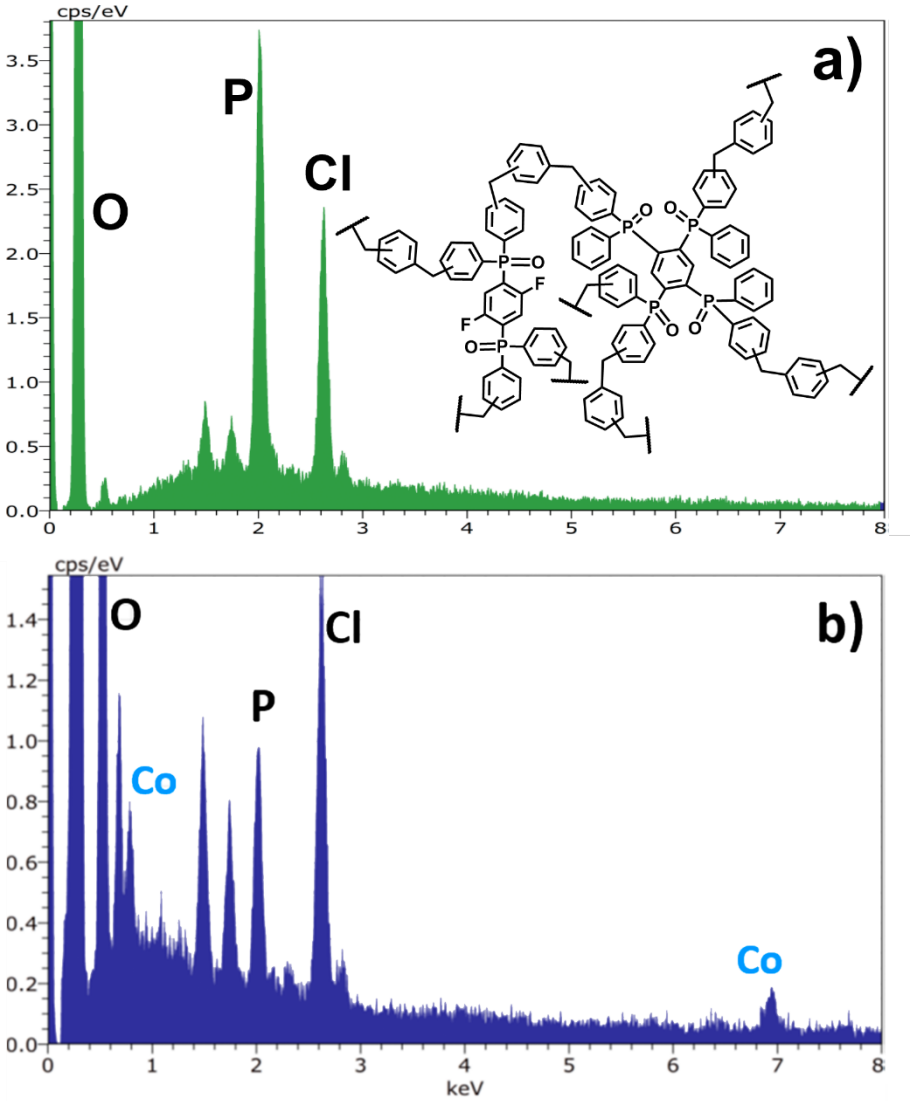

Figure B31. EDX analysis of **P6**$_{Fe}$ (a) and **Co@P6**$_{Fe}$ (b).

Appendix II

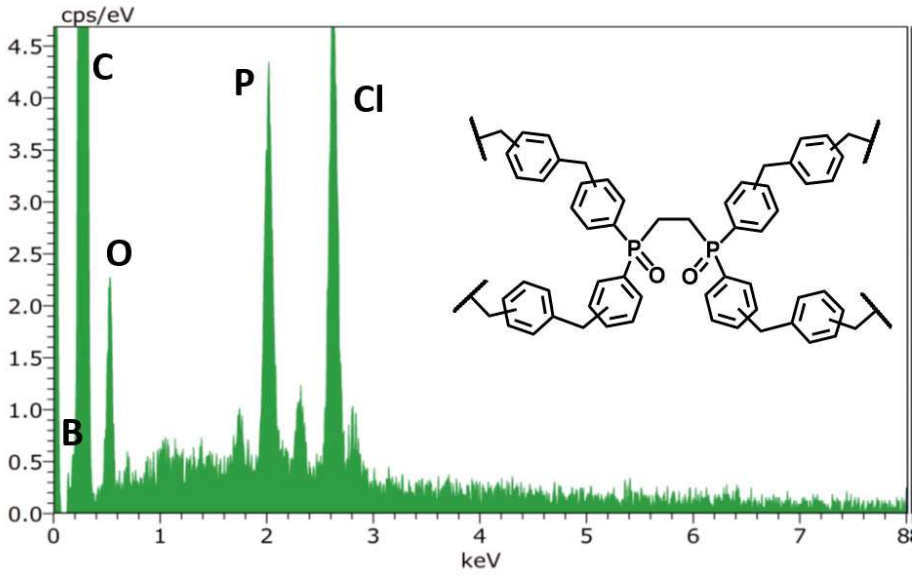

Figure B32. EDX analysis of $\mathbf{P7}_{Fe}$.

9.9 HER studies

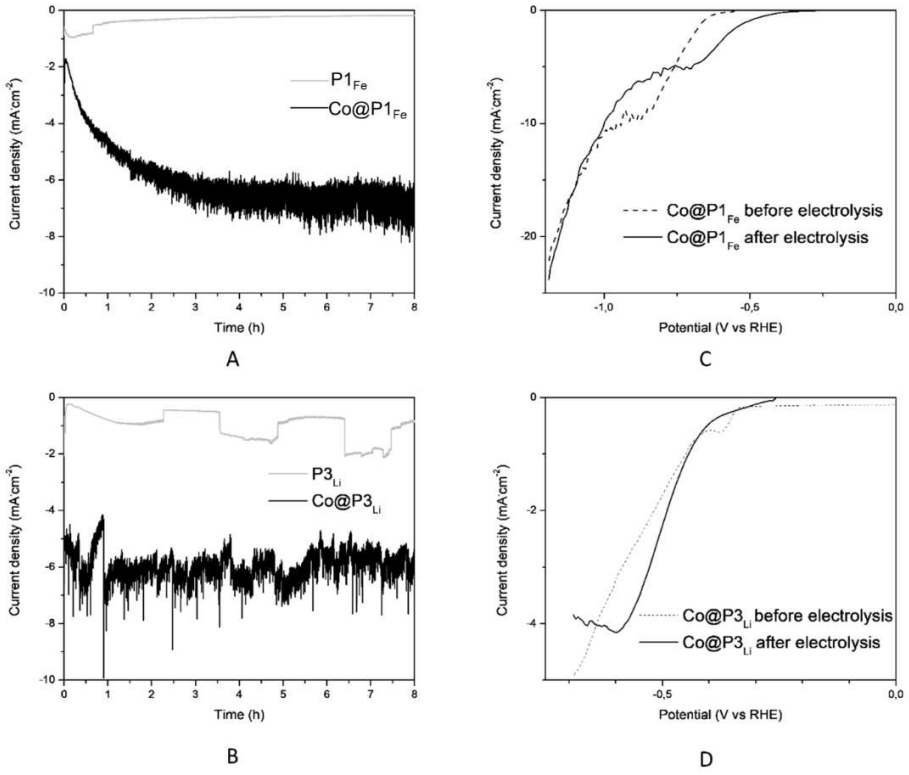

Figure B33. CPE experiments carried out at -0.68 V vs RHE for **Co@P1$_{Fe}$** (A) and **Co@P3$_{Li}$** (B) HER catalysts. LSVs curves recorded before and after electrolysis are shown in C for **Co@P1$_{Fe}$** and in D for **Co@P3$_{Li}$**.

Appendix II

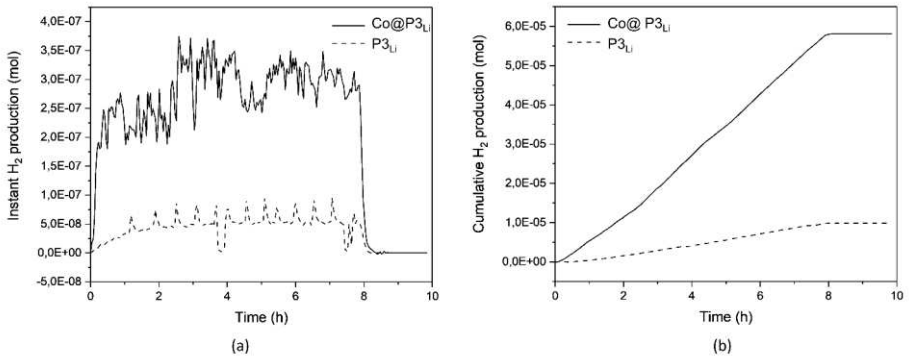

Figure B34. Instant (a) and cumulative (b) H_2 production during CPE experiments carried out at -0.68 V vs RHE for **Co@P3Li** vs **P3Li**.

3. Appendix III

Supplementary Materials for Chapter 4

3.1 NMR characterization of new molecules

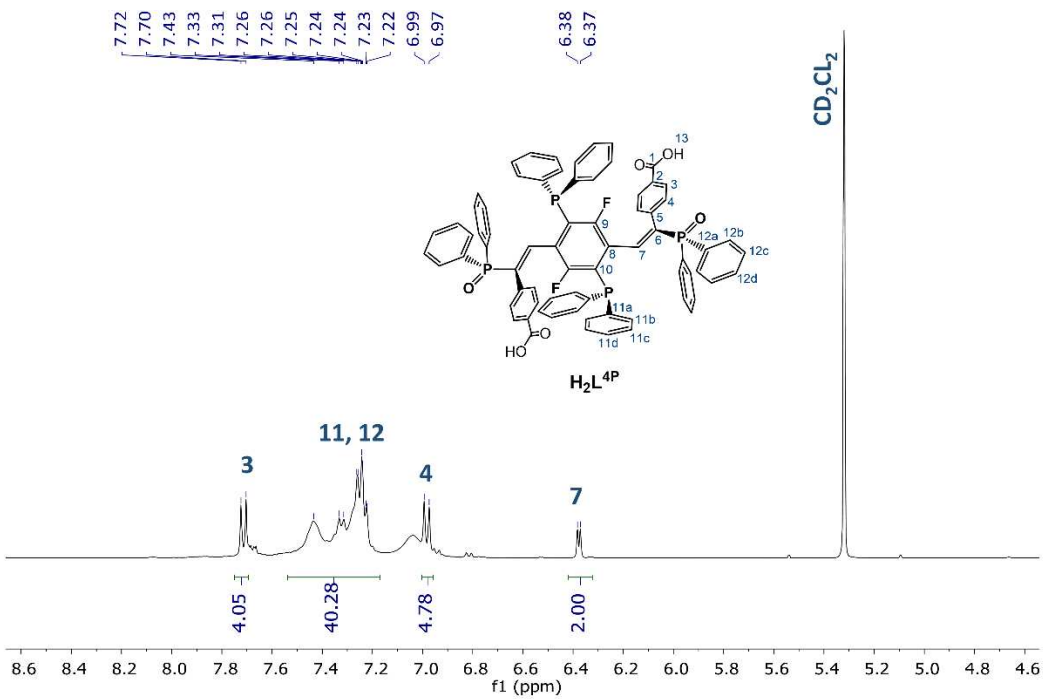

Figure C1. ^{1}H-NMR (400 MHz, CD_2Cl_2) spectrum of $\mathbf{H_2L^{4P}}$.

Appendix III

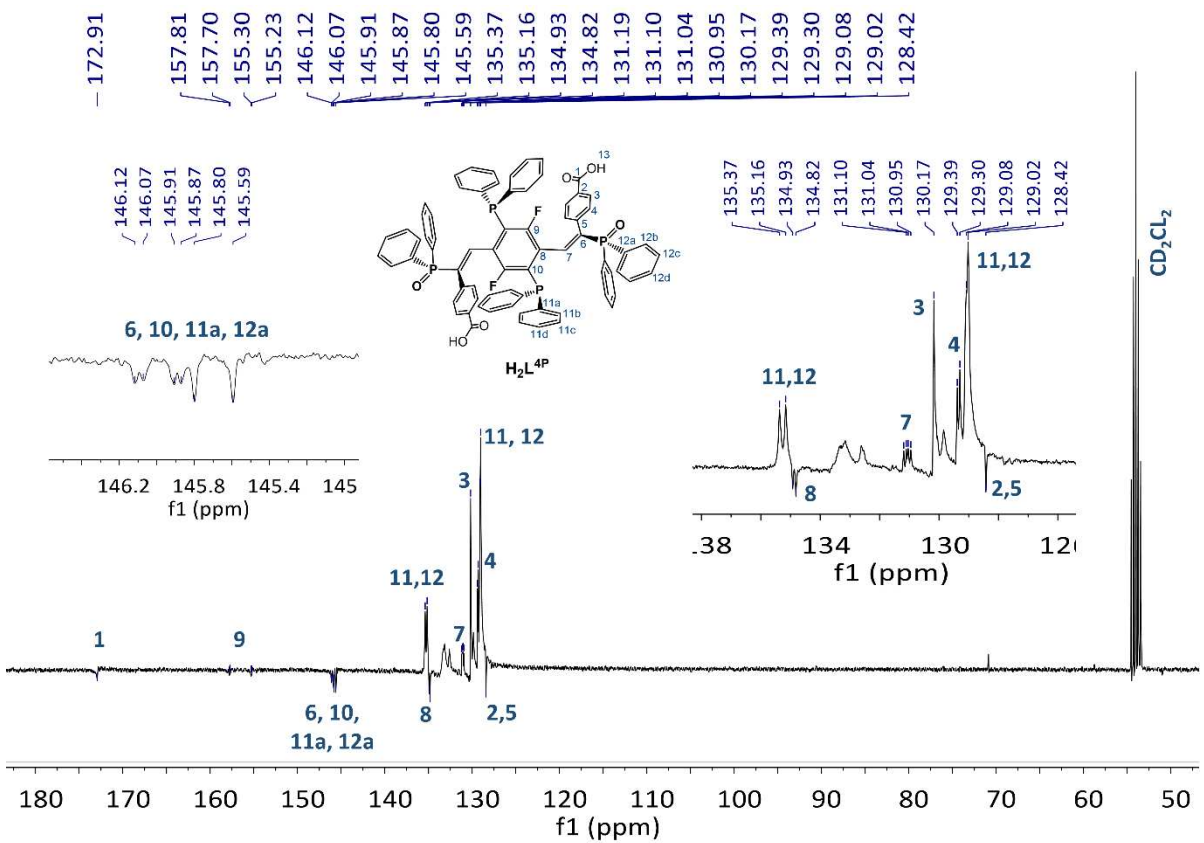

Figure C2. ^{13}C-deptq135 NMR (101 MHz, CD_2Cl_2) spectrum of $\mathbf{H_2L^{4P}}$.

Appendix III

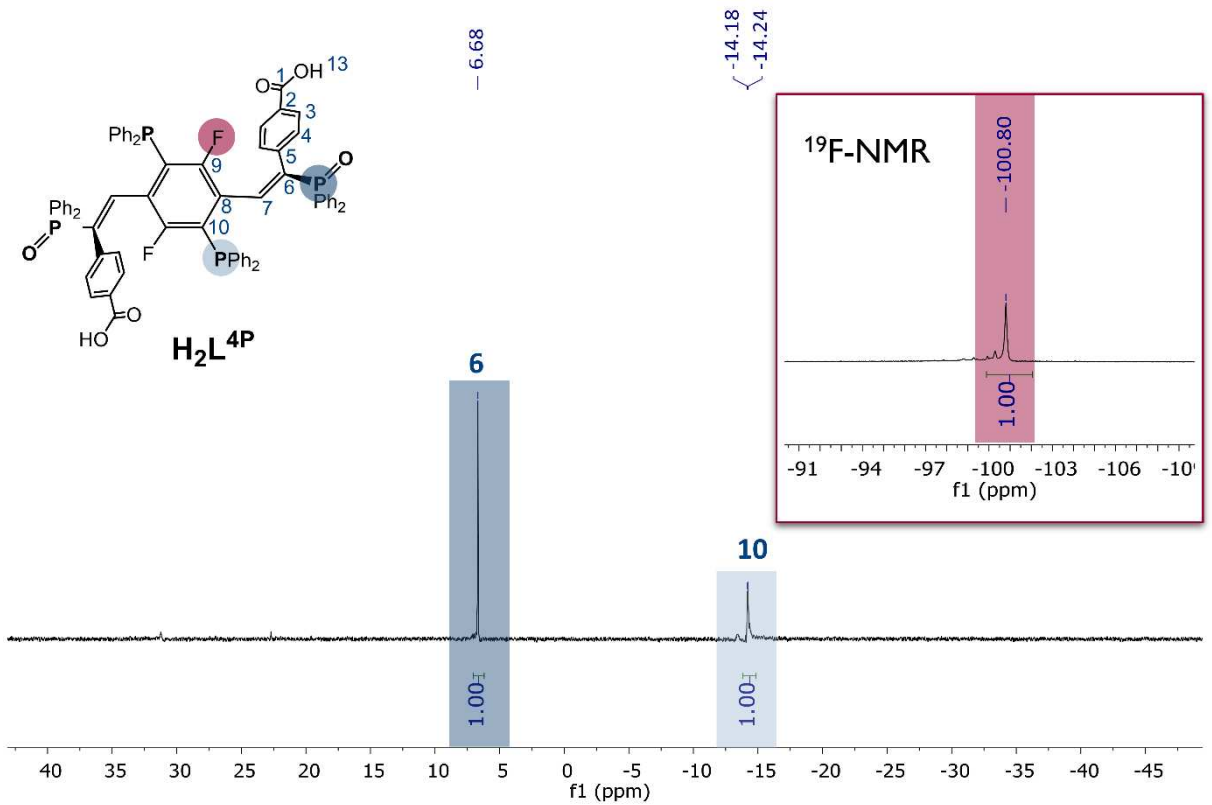

Figure C3. ^{31}P-NMR (162 MHz, CD_2Cl_2) and ^{19}F-NMR (565 MHz, CD_2Cl_2) spectrum of $\mathbf{H_2L^{4P}}$.

Appendix III

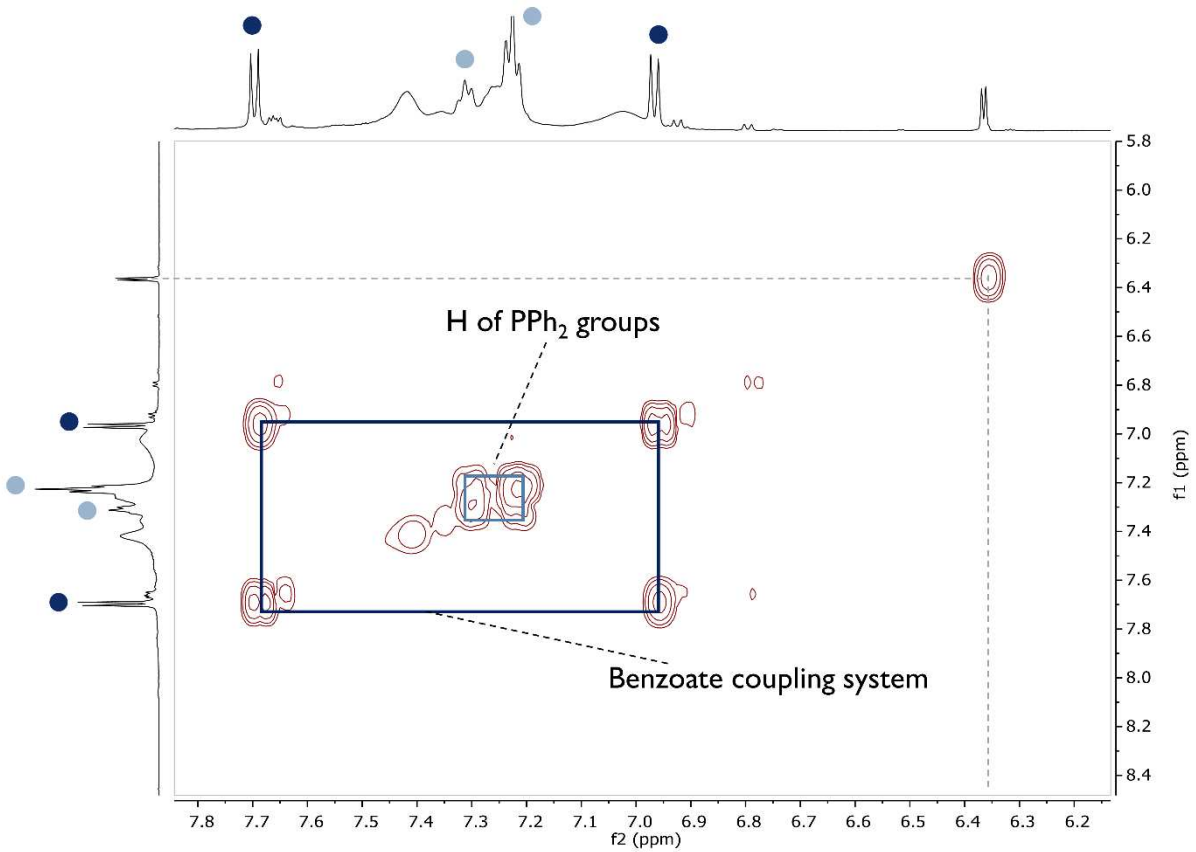

Figure C4. 2D ^{1}H-^{1}H COSY (600 MHz, CD_2Cl_2) spectrum of $\mathbf{H_2L^{4P}}$.

Appendix III

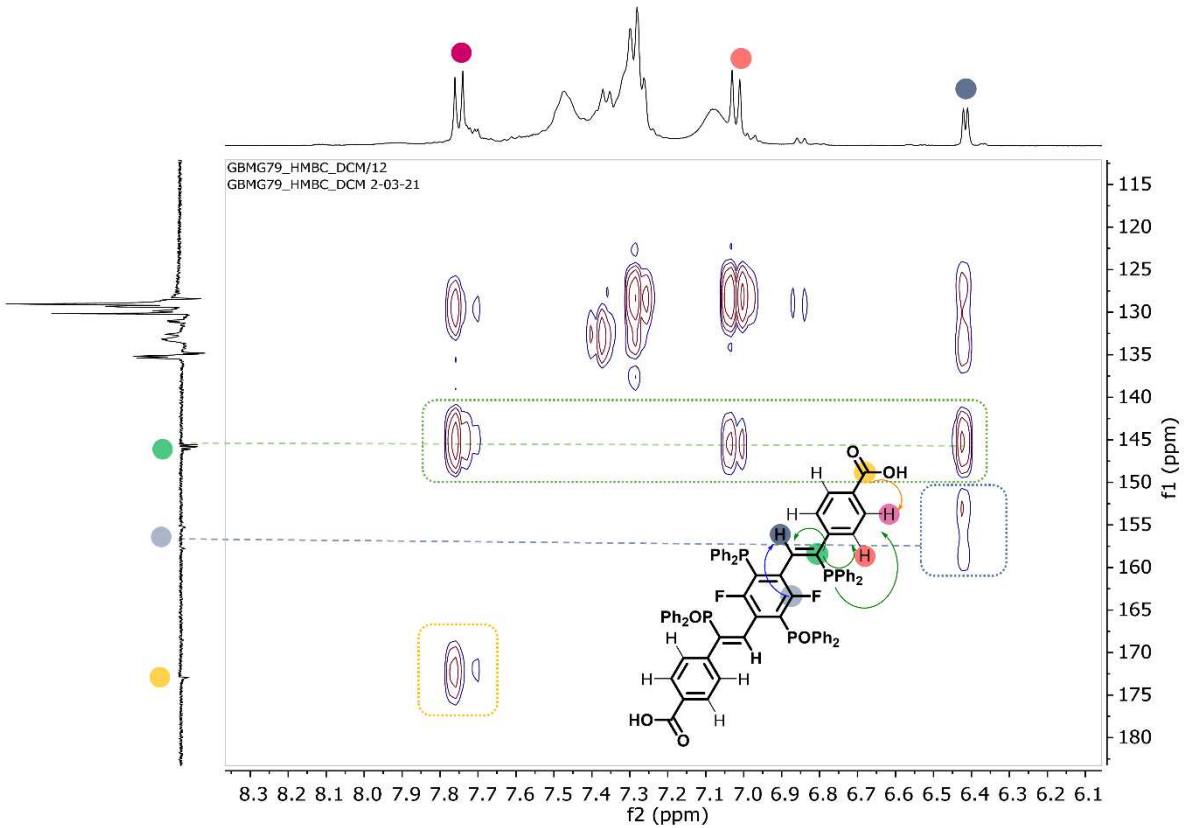

Figure C5. Expanded region (8.3 – 6.1 ppm) of 2D ^{1}H-^{13}C HMBC (400 MHz, CD_2Cl_2) of spectrum of $\mathbf{H_2L^{4P}}$.

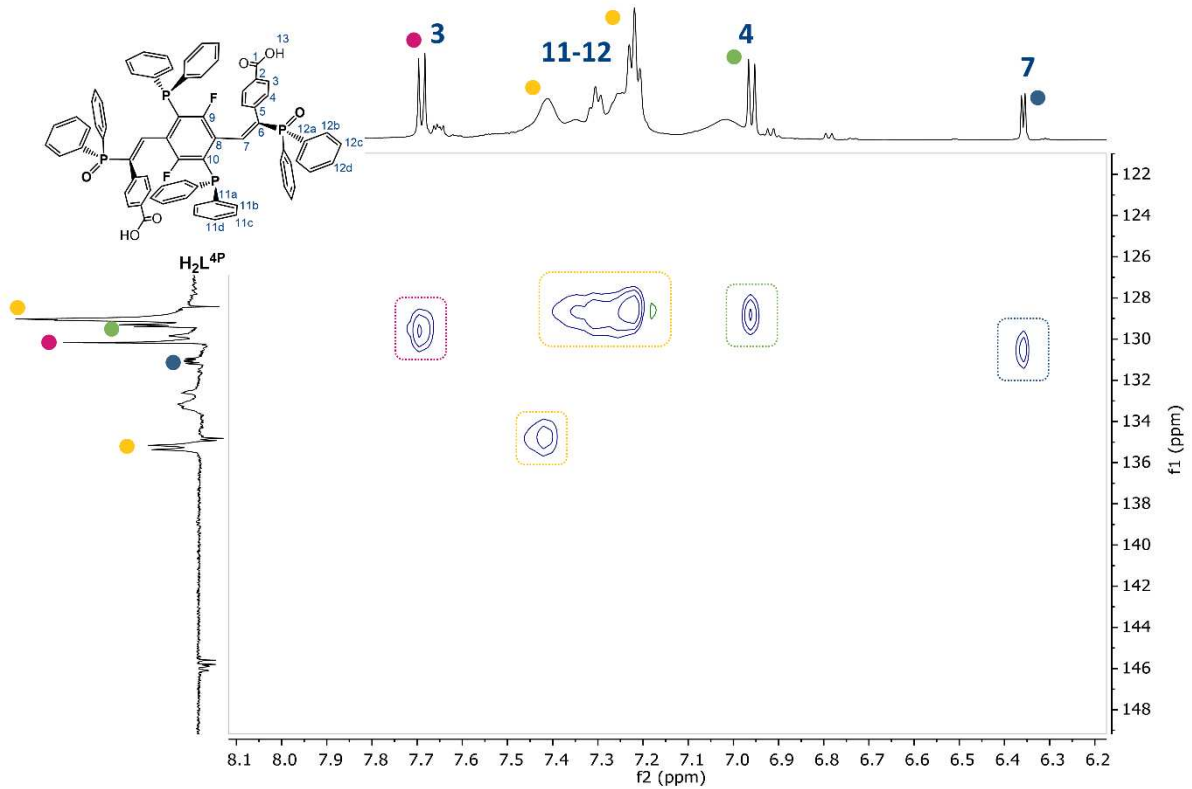

Figure C6. Expanded region of 2D ^{1}H-^{13}C HSQC spectrum (600 MHz, CD_2Cl_2) of $\mathbf{H_2L^{4P}}$.

Appendix III

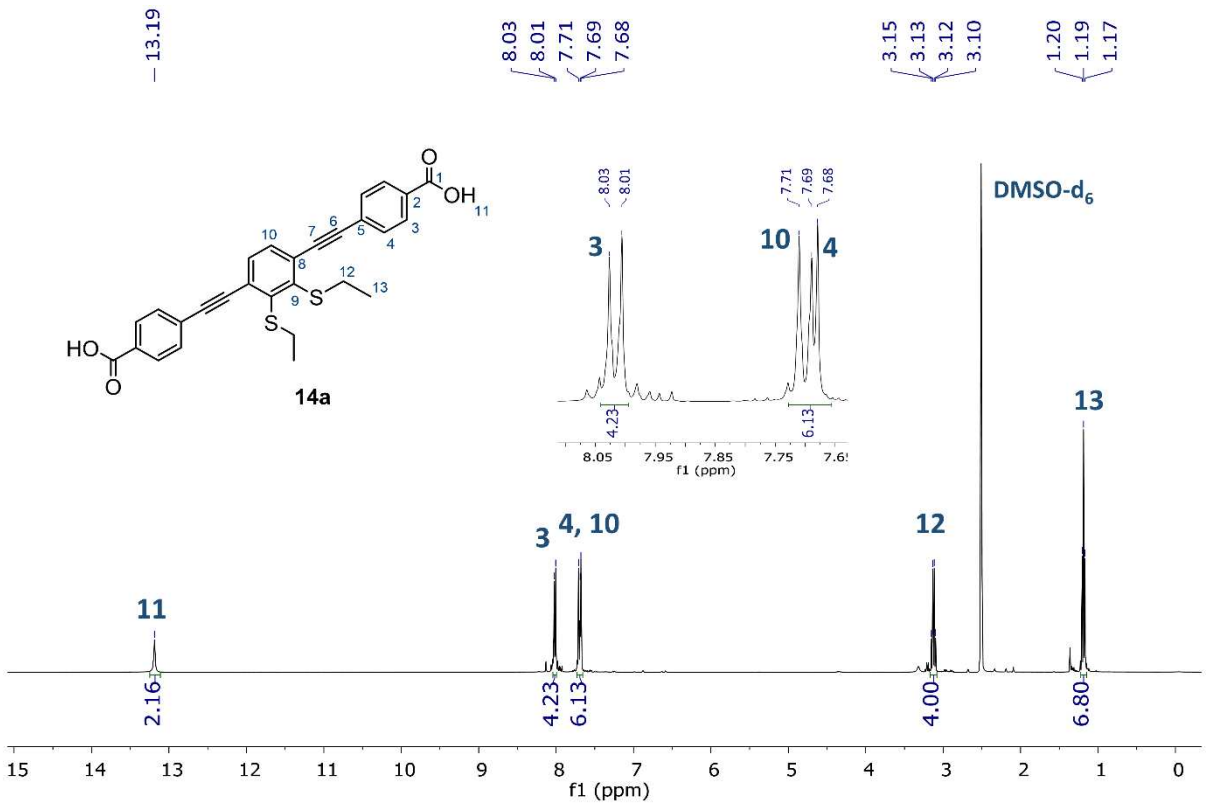

Figure C7. ^{1}H-NMR (400 MHz, DMSO-d_6) spectrum of **14a.**

Appendix III

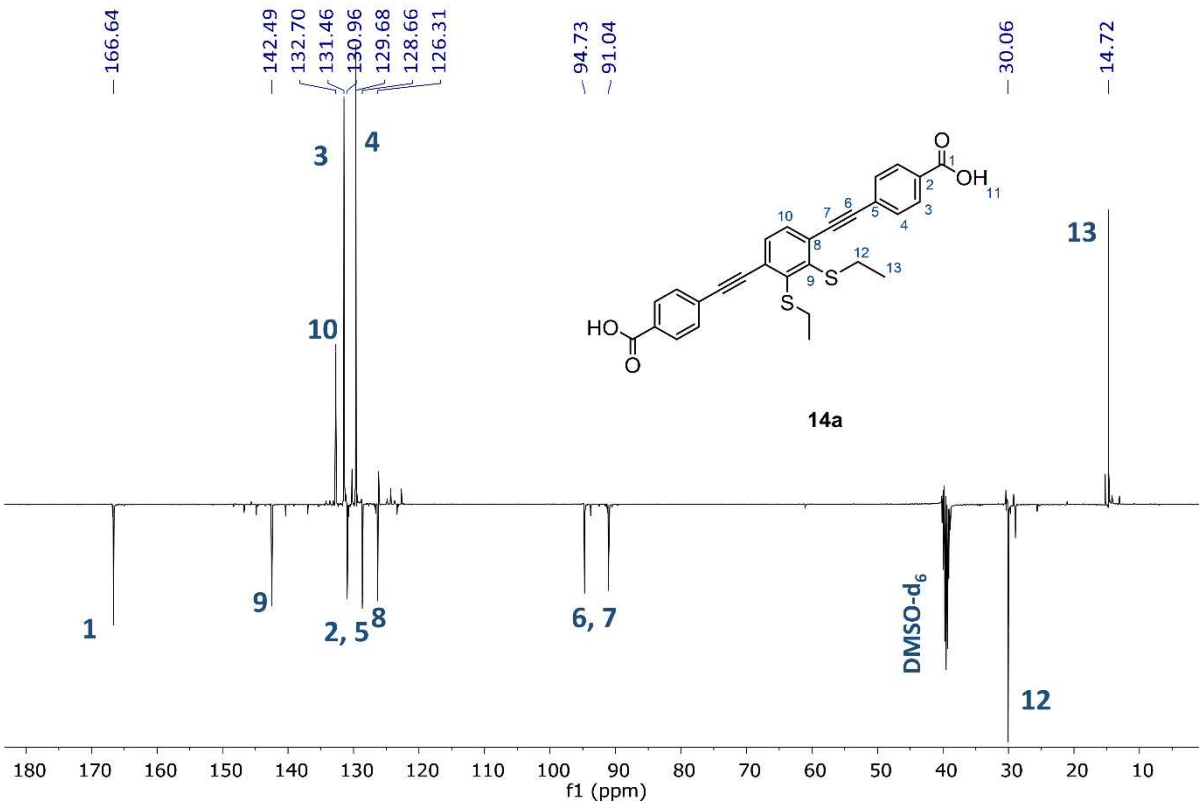

Figure C8. ^{13}C-deptq135 NMR (101 MHz, DMSO-d_6) spectrum of **14a**.

Appendix III

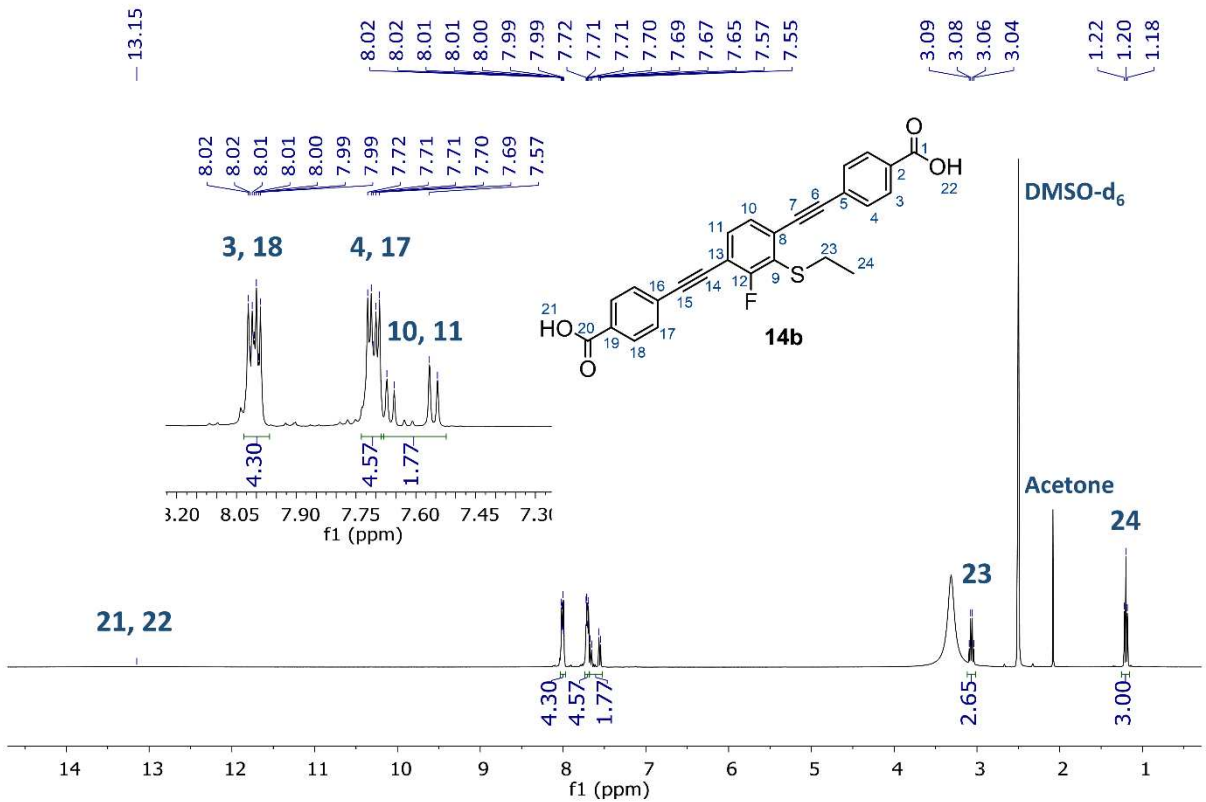

Figure C9. ^{1}H-NMR (400 MHz, DMSO-d_6) spectrum of **14b.**

Appendix III

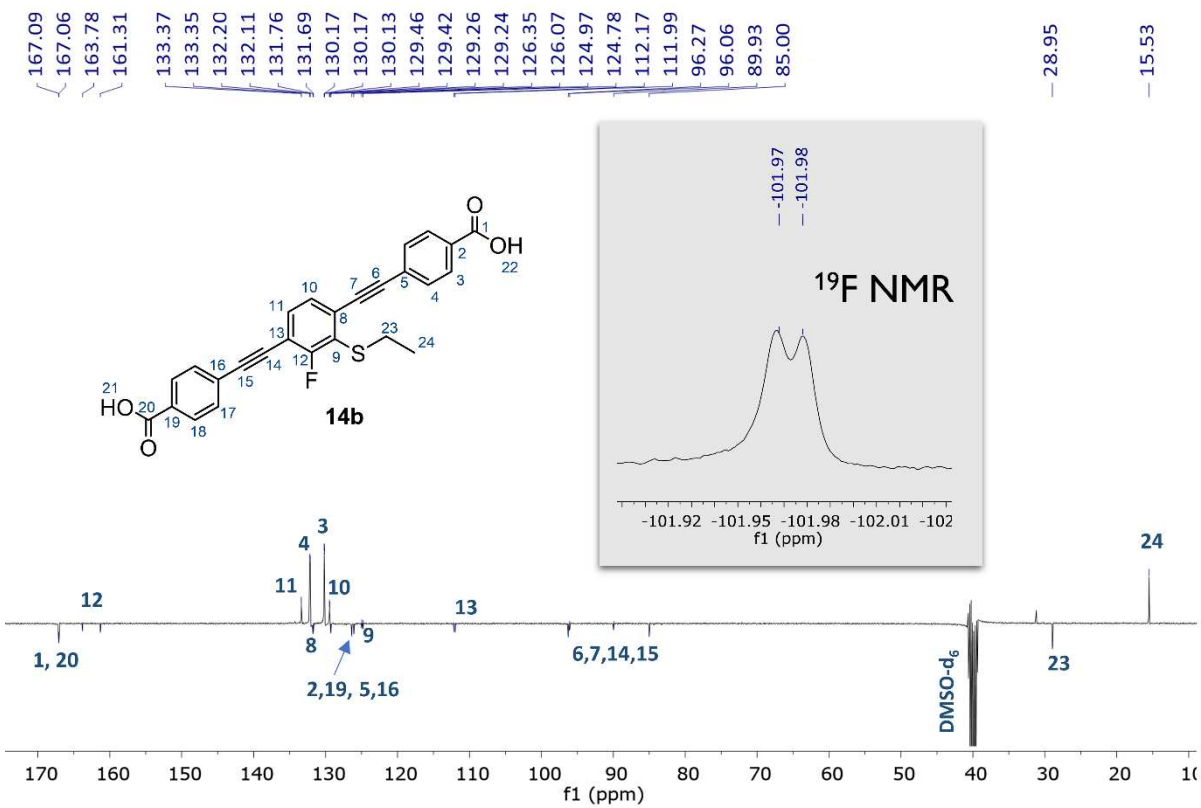

Figure C10. ^{13}C-deptq135 NMR (101 MHz, DMSO-d_6) and ^{19}F NMR (565 MHz, DMSO-d_6) (inset) spectrum of **14b**.

Appendix III

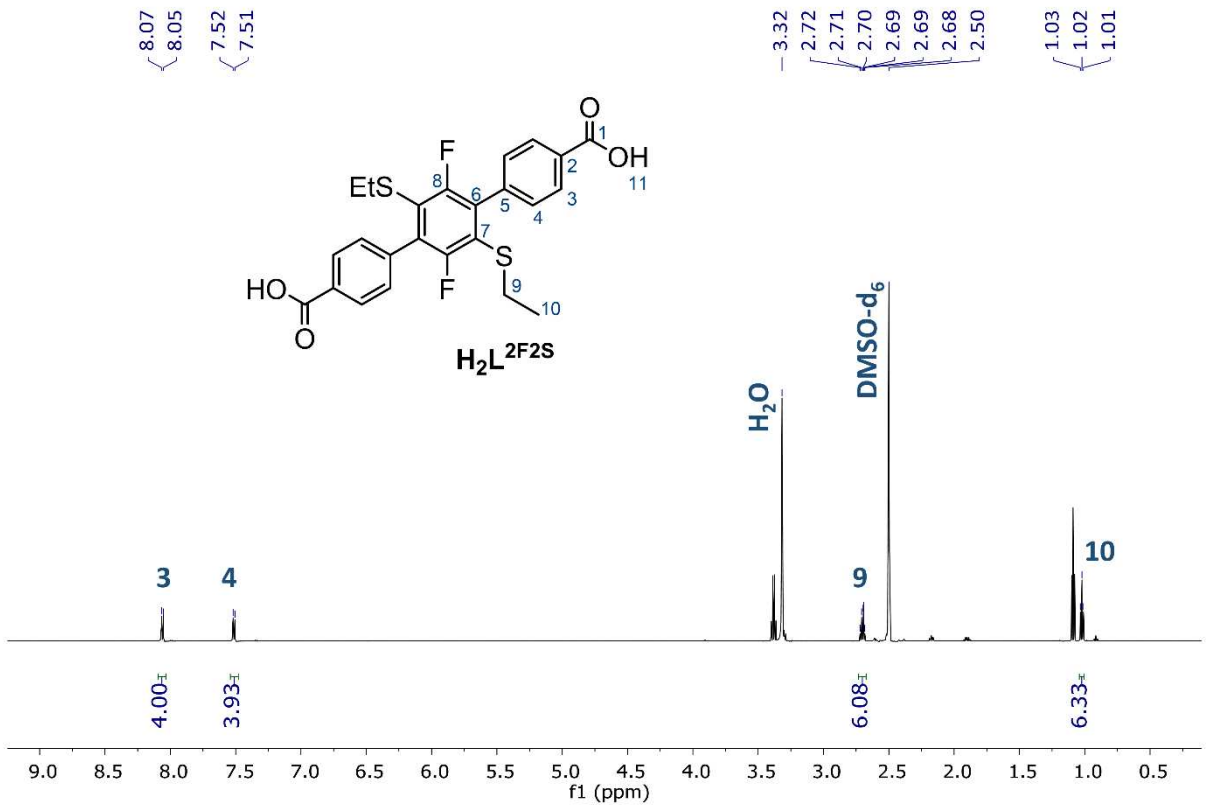

Figure C11. ^{1}H-NMR (400 MHz, DMSO-d_6) spectrum of $\mathbf{H_2L^{2F2S}}$.

Appendix III

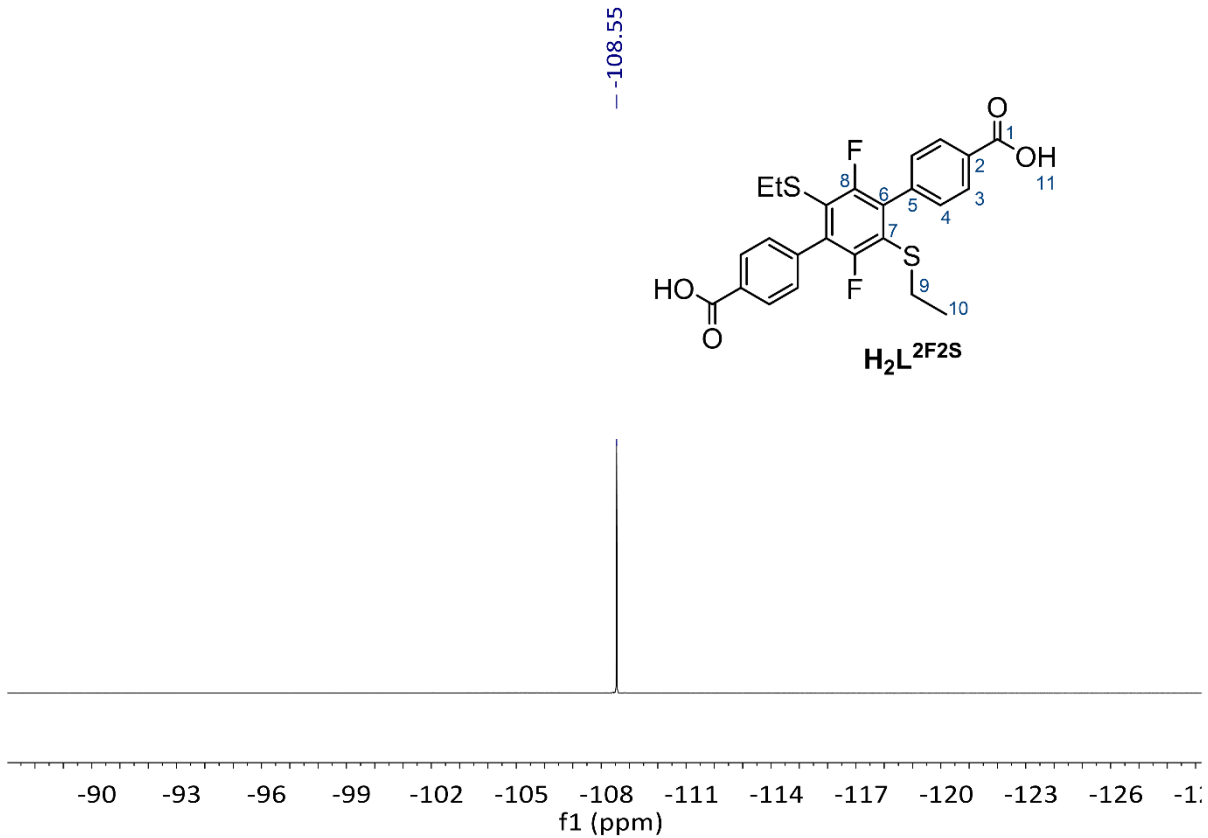

Figure C12. ^{19}F NMR (565 MHz, DMSO-d_6) spectrum of $\mathbf{H_2L^{2F2S}}$.

Appendix III

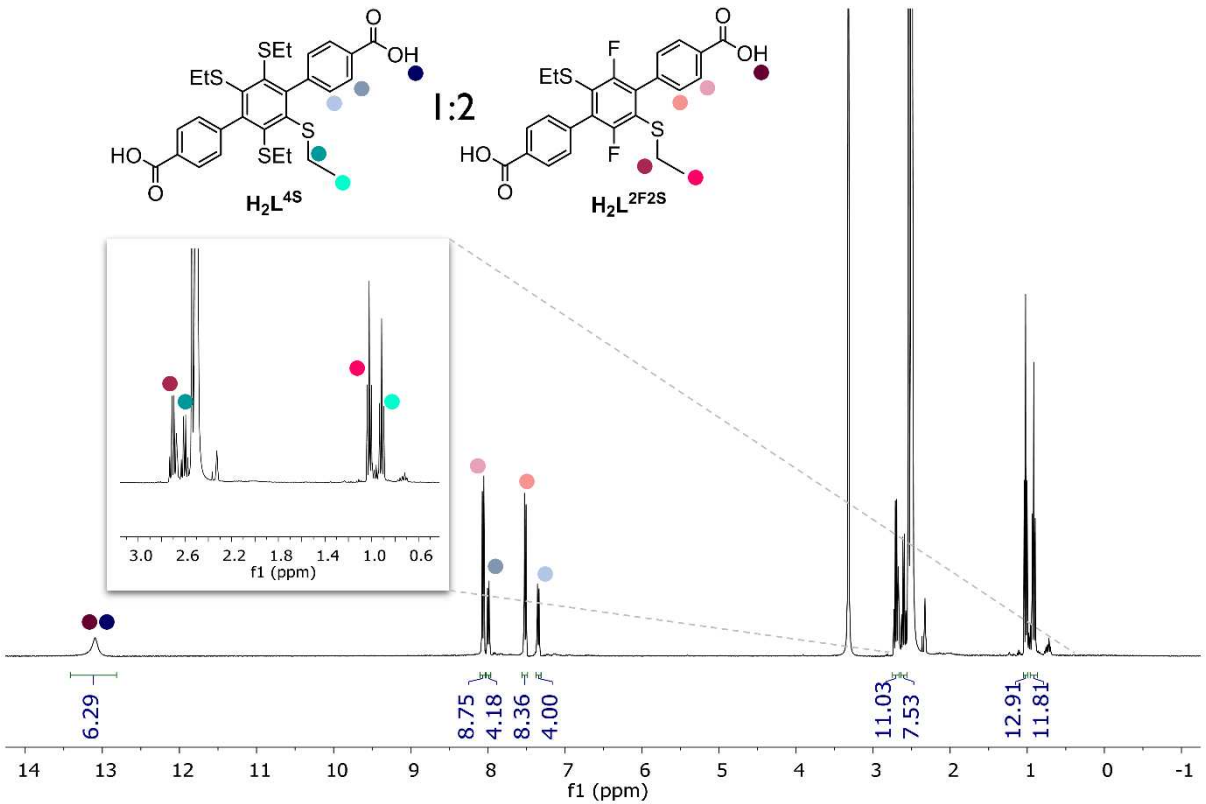

Figure C13. ^{1}H-NMR (400 MHz, DMSO-d_6) spectrum of **mixure of H_2L^{2F2S}** and **H_2L^{4S}.**

Appendix III

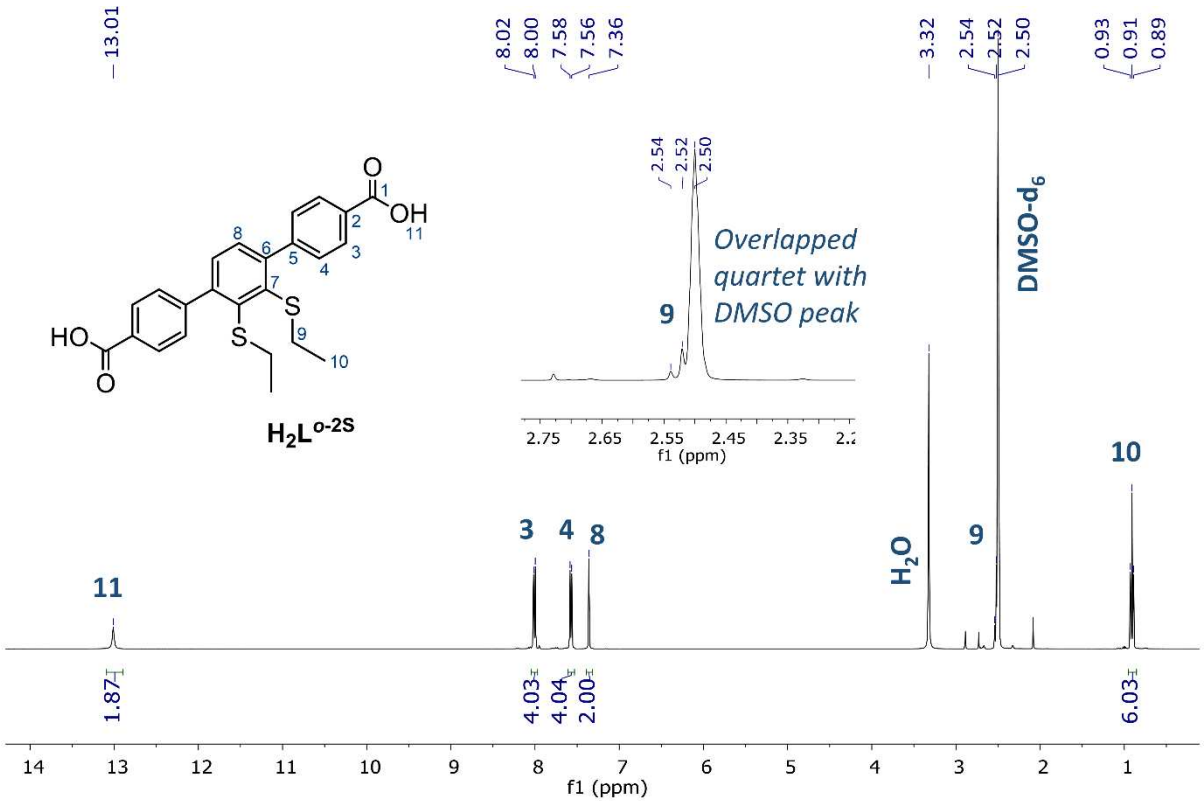

Figure C14. ^{1}H-NMR (400 MHz, DMSO-d_6) spectrum of $\mathbf{H_2L^{o\text{-}2S}}$.

Appendix III

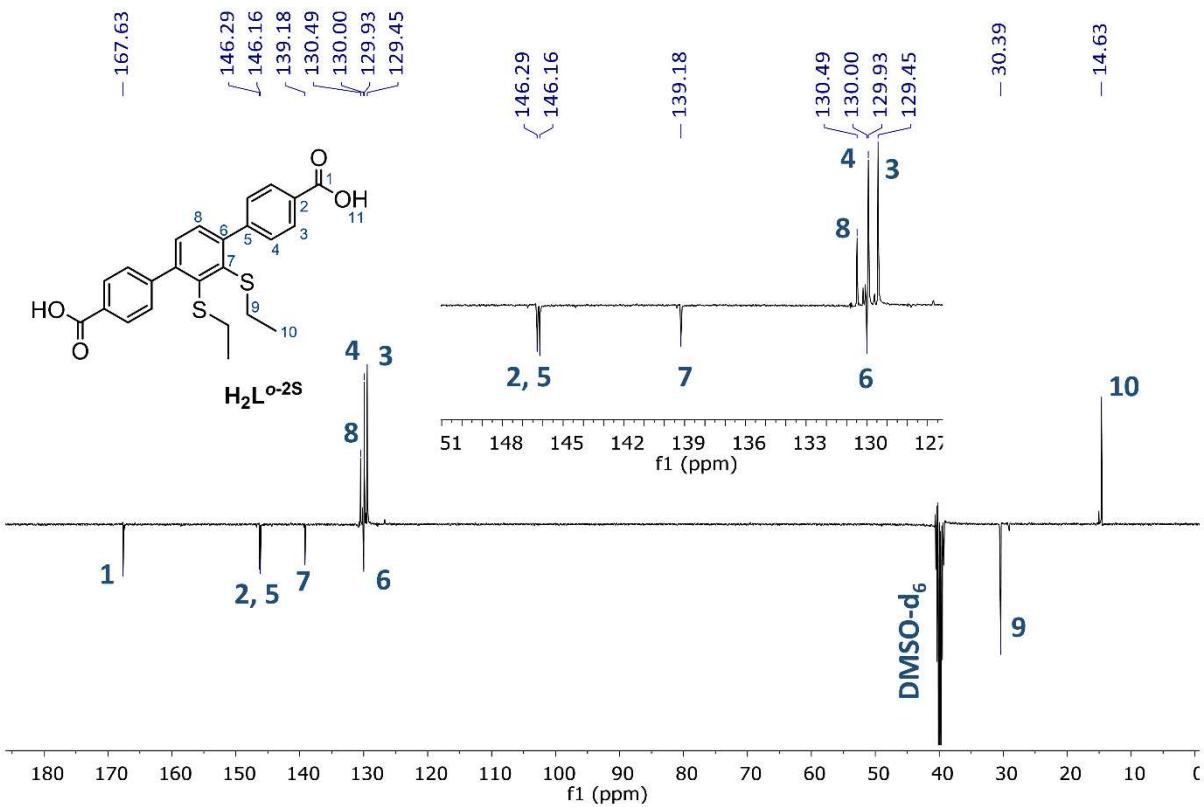

Figure C15. ^{13}C-deptq135 NMR (101 MHz, DMSO-d_6) spectrum of $\mathbf{H_2L^{o\text{-}2S}}$.

Appendix III

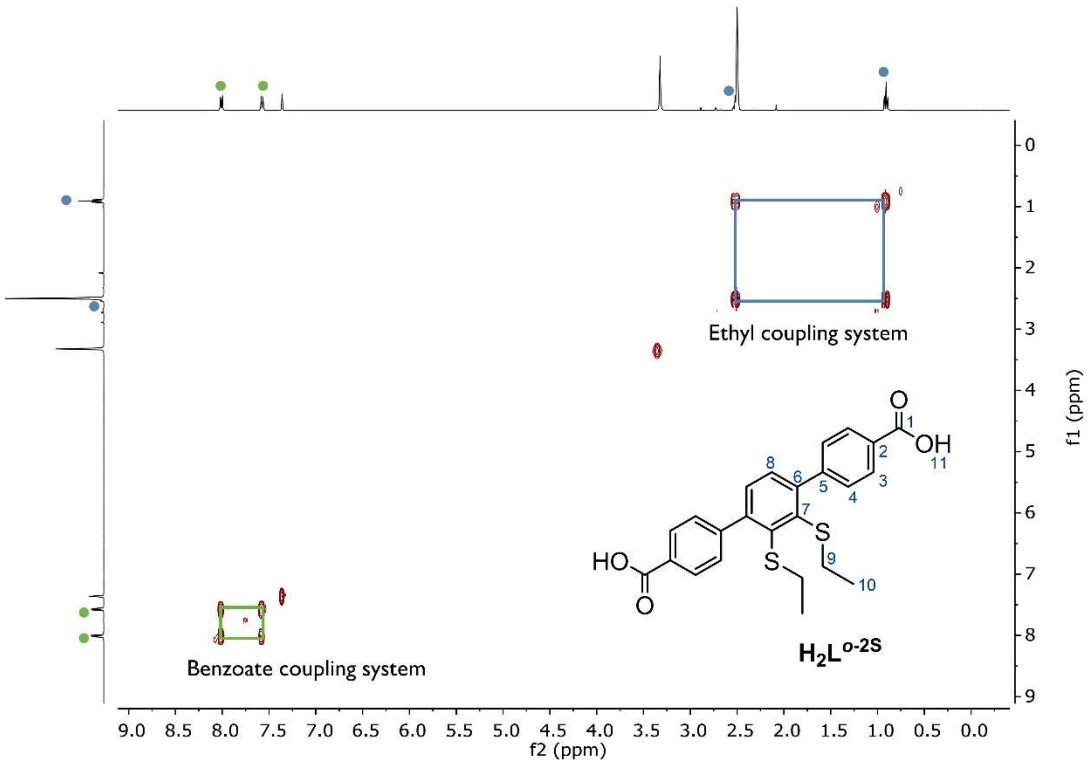

Figure C16. 2D ^{1}H-^{1}H COSY (400 MHz, DMSO-d_6) spectrum of $\mathbf{H_2L^{o\text{-}2S}}$.

Appendix III

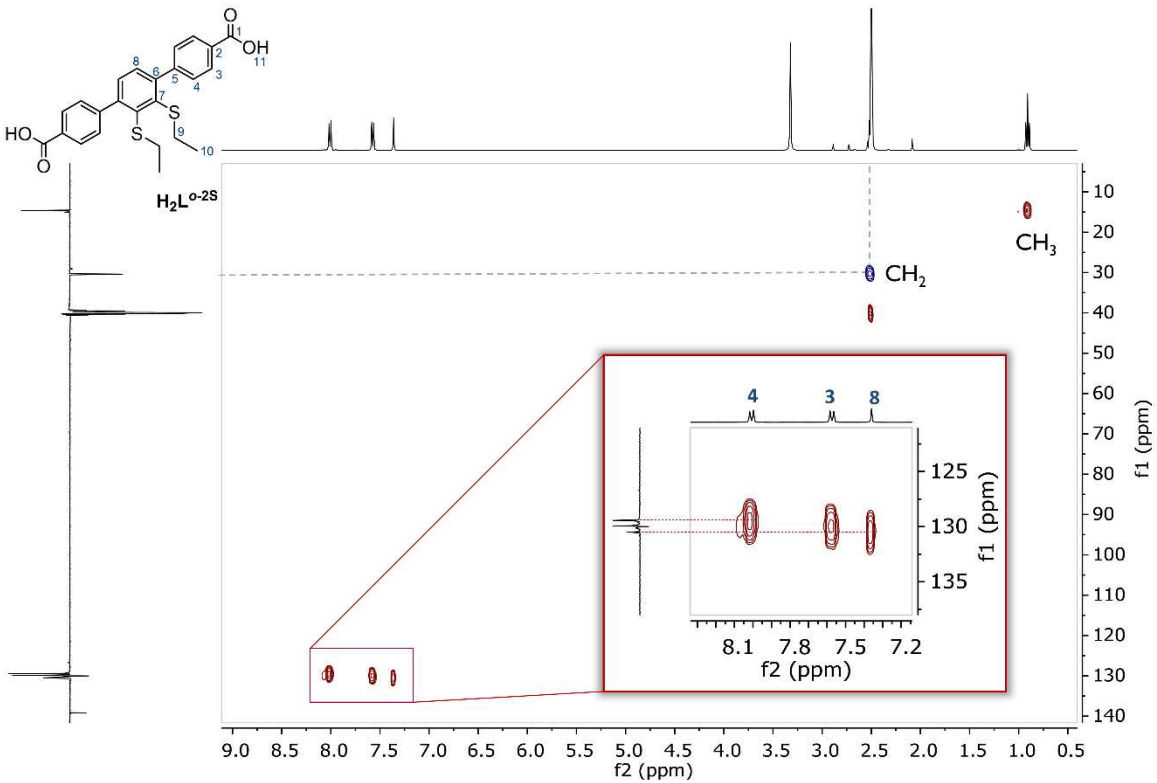

Figure C17. Expanded region (9.0 - 0.5 ppm) of 2D ^{1}H-^{13}C HSQC spectrum (400 MHz, DMSO-d_6) spectrum of $\mathbf{H_2L^{o\text{-}2S}}$.

Appendix III

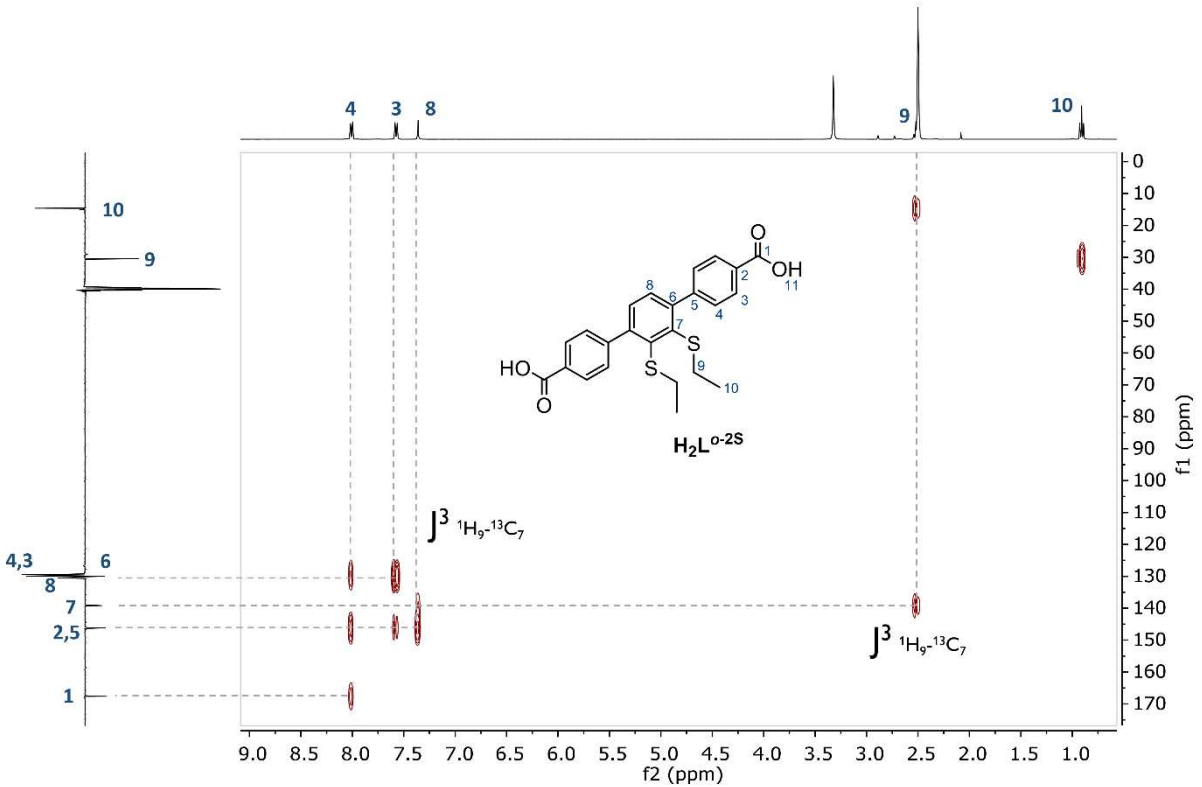

Figure C18. Expanded region (9.0 - 0.5 ppm) of 2D ^{1}H-^{13}C HMBC spectrum (400 MHz, DMSO-d_6) spectrum of $\mathbf{H_2L^{o\text{-}2S}}$.

Appendix III

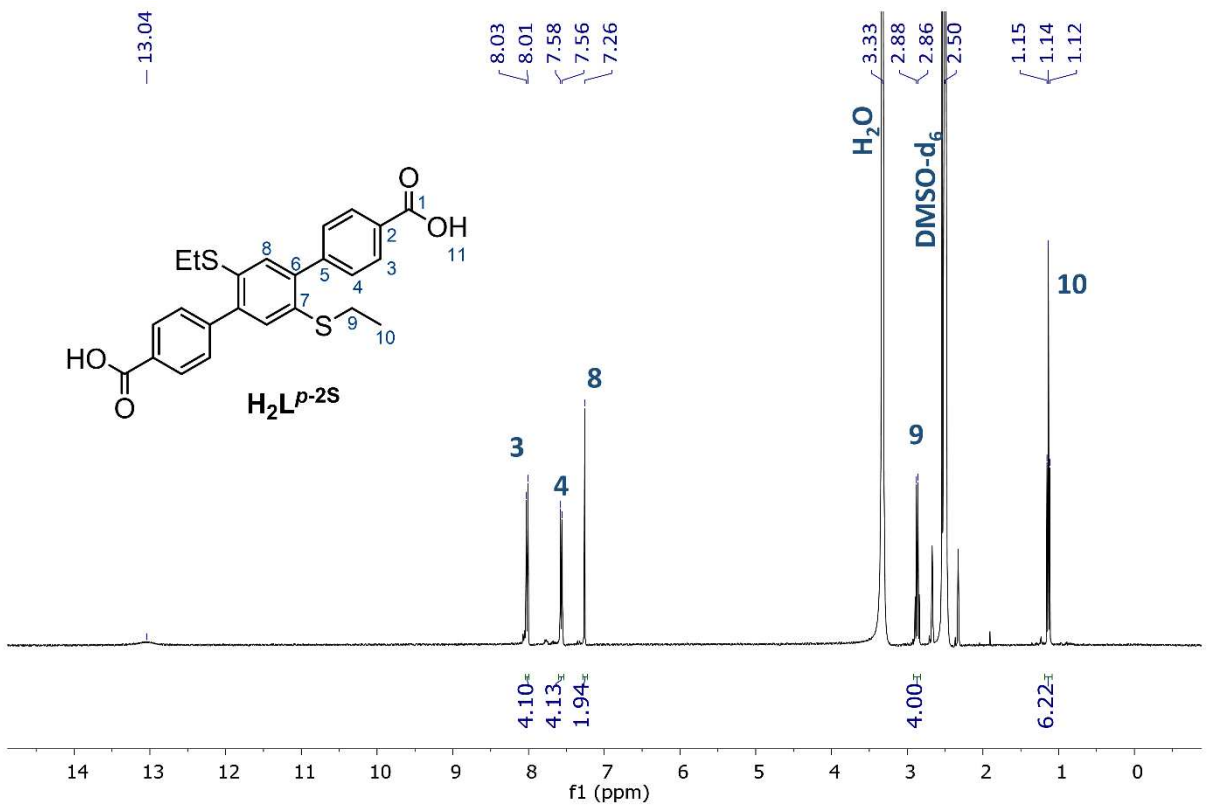

Figure C19. ^{1}H-NMR (400 MHz, DMSO-d_6) spectrum of $\mathbf{H_2L^{p\text{-}2S}}$.

Appendix III

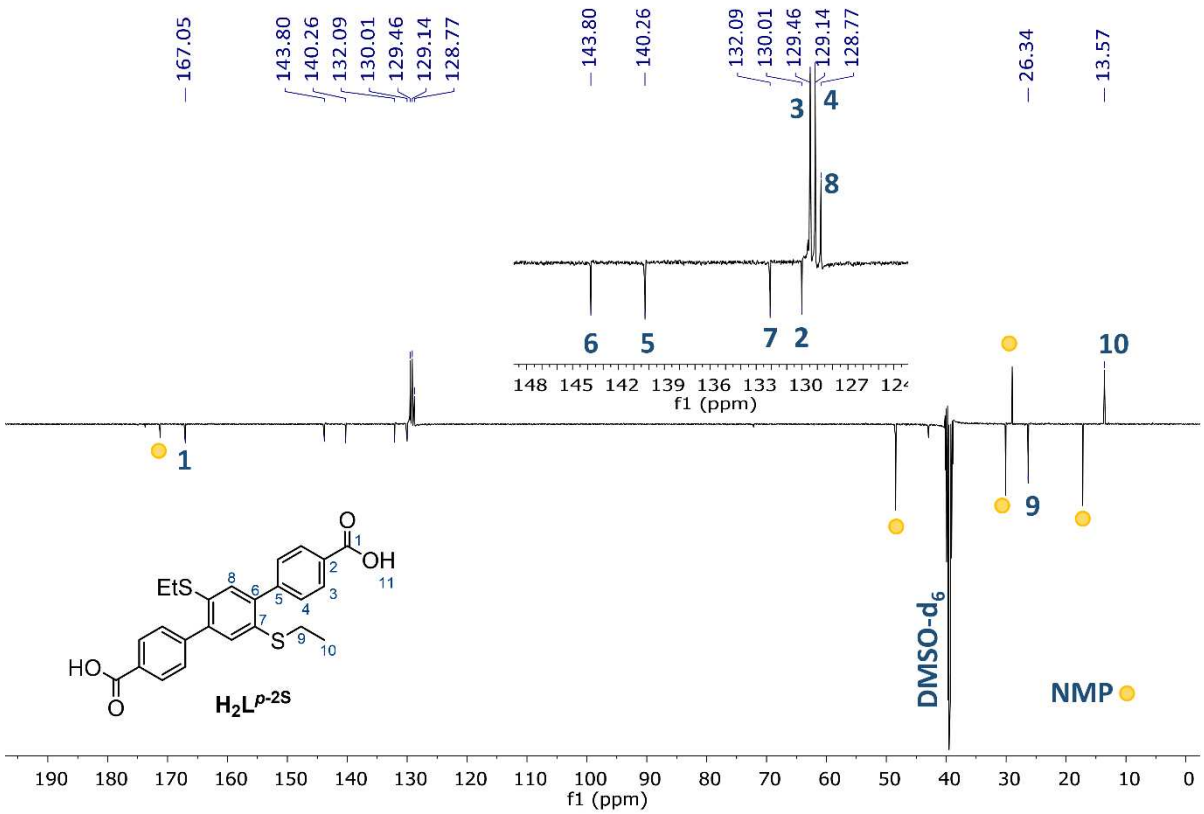

Figure C20. ^{13}C-deptq135 NMR (101 MHz, DMSO-d_6) spectrum of $\mathbf{H_2L^{p\text{-}2S}}$.

Appendix III

3.2 Crystal data

Table C1. Crystal data and structure refinement for $H_2L^{4Pox}\cdot DMSO$.

	H_2L^{4Pox}
Empirical formula	$C_{76}H_{64}F_2O_{8.4}P_4S_2$
Formula weight	1337.67
Temperature/K	150.0
Crystal system	triclinic
Space group	P-1
a/Å	8.8163(2)
b/Å	13.0270(4)
c/Å	15.7145(5)
α/°	68.342(3)
β/°	76.374(3)
γ/°	89.470(2)
Volume/Å^3	1624.14(9)
Z	1
ρ_{calc}g/cm^3	1.368
μ/mm^{-1}	2.209
F(000)	697.0
Crystal size/mm^3	0.075 × 0.05 × 0.035
Radiation	CuKα (λ = 1.54178)
2Θ range for data collection/°	6.25 to 140.126
Index ranges	-10 ≤ h ≤ 10, -14 ≤ k ≤ 15, -19 ≤ l ≤ 19
Reflections collected	23471
Independent reflections	6133 [R_{int} = 0.0369, R_{sigma} = 0.0301]
Data/restraints/parameters	6133/395/549
Goodness-of-fit on F^2	1.048
Final R indexes [I>=2σ (I)]	R_1 = 0.0603, wR_2 = 0.1738
Final R indexes [all data]	R_1 = 0.0702, wR_2 = 0.1869
Largest diff. peak/hole / e Å^{-3}	0.96/-0.89

$R1 = \Sigma||F_o|-|F_c||/\Sigma|F_o|$, $wR2 = [\Sigma[w(F_o^2-F_c^2)^2]/\Sigma[w(F_o^2)^2]]^{½}$, $w = 1/[\sigma^2(F_o^2) + (aP)^2 + bP]$, where $P = [\max(F_o^2,0) + 2F_c^2]/3$

Appendix III

Table C2. Crystal data and structure refinement for **13a** and **[$Ag_2L^{p\text{-}2F}$]**.

	13a	[$Ag_2L^{p\text{-}2F}$]
Empirical formula	$C_{30}H_{26}O_4S_2$	$C_{10}H_5AgFO_2$
Formula weight	514.63	284.01
Temperature/K	200.0	100
Crystal system	monoclinic	monoclinic
Space group	$P2_1/n$	$P2_1/c$
a/Å	6.9208(5)	13.417(14)
b/Å	32.763(3)	9.138(9)
c/Å	11.7334(9)	6.448(7)
α/°	90	90
β/°	105.276(3)	97.566(12)
γ/°	90	90
Volume/Å^3	2566.5(3)	783.6(14)
Z	4	4
ρ_{calc}g/cm^3	1.332	2.407
μ/mm^{-1}	0.242	3.401
F(000)	1080.0	548.0
Crystal size/mm^3	0.18 × 0.14 × 0.12	0.01 × 0.01 × 0.005
Radiation	MoKα (λ = 0.71073)	synchrotron (λ = 0.4134)
2Θ range for data collection/°	3.808 to 51.498	1.78 to 29.188
Index ranges	-8 ≤ h ≤ 8, -39 ≤ k ≤ 40, -14 ≤ l ≤ 14	-16 ≤ h ≤ 16, -11 ≤ k ≤ 11, -7 ≤ l ≤ 7
Reflections collected	30223	14530
Independent reflections	4907 [R_{int} = 0.0904, R_{sigma} = 0.0568]	1482 [R_{int} = 0.1237, R_{sigma} = 0.0764]
Data/restraints/parameters	4907/0/329	1482/12/138
Goodness-of-fit on F^2	1.018	1.027
Final R indexes [I>=2σ (I)]	R_1 = 0.0499, wR_2 = 0.1040	R_1 = 0.0358, wR_2 = 0.0848
Final R indexes [all data]	R_1 = 0.0821, wR_2 = 0.1170	R_1 = 0.0439, wR_2 = 0.0905
Largest diff. peak/hole / e Å^{-3}	0.22/-0.24	1.43/-0.61

$R1 = \Sigma||F_o|-|F_c||/\Sigma|F_o|$, $wR2 = [\Sigma[w(F_o^2-F_c^2)^2]/\Sigma[w(F_o^2)^2]]^{½}$, $w = 1/[\sigma^2(F_o^2) + (aP)^2 + bP]$, where $P = [\max(F_o^2,0) + 2F_c^2]/3$

Appendix III

Table C3. Crystal data and structure refinement for $H_2L^{p\text{-}2S}$ ·**DMSO** and $H_2L^{o\text{-}2S}$ ·**DMF**.

	$H_2L^{p\text{-}2S}$ ·DMSO	$H_2L^{o\text{-}2S}$ ·DMF
Empirical formula	$C_{28}H_{34}O_6S_4$	$C_{30}H_{36}N_2O_6S_2$
Formula weight	594.79	584.73
Temperature/K	200.0	200.0
Crystal system	triclinic	monoclinic
Space group	P-1	$P2_1/c$
a/Å	6.2914(7)	32.0159(6)
b/Å	9.4954(10)	7.76780(10)
c/Å	12.5601(11)	12.1912(2)
α/°	103.867(3)	90
β/°	93.158(4)	98.0430(10)
γ/°	95.704(4)	90
Volume/Å^3	722.43(13)	3002.04(8)
Z	1	4
ρ_{calc}g/cm^3	1.367	1.294
μ/mm^{-1}	0.369	0.222
F(000)	314.0	1240.0
Crystal size/mm^3	0.16 × 0.14 × 0.12	0.23 × 0.21 × 0.21
Radiation	MoKα (λ = 0.71073)	MoKα (λ = 0.71073)
2Θ range for data collection/°	4.448 to 51.732	3.854 to 52.074
Index ranges	-7 ≤ h ≤ 7, -11 ≤ k ≤ 11, -15 ≤ l ≤ 14	-39 ≤ h ≤ 39, -9 ≤ k ≤ 9, -15 ≤ l ≤ 15
Reflections collected	13126	24628
Independent reflections	2790 [R_{int} = 0.0520, R_{sigma} = 0.0392]	5917 [R_{int} = 0.0291, R_{sigma} = 0.0270]
Data/restraints/parameters	2790/0/179	5917/0/369
Goodness-of-fit on F^2	1.024	1.062
Final R indexes [I>=2σ (I)]	R_1 = 0.0440, wR_2 = 0.1015	R_1 = 0.0537, wR_2 = 0.1449
Final R indexes [all data]	R_1 = 0.0601, wR_2 = 0.1108	R_1 = 0.0579, wR_2 = 0.1484
Largest diff. peak/hole / e Å^{-3}	0.31/-0.40	1.39/-0.51

$R1 = \Sigma||F_o|-|F_c||/\Sigma|F_o|$, $wR2 = [\Sigma[w(F_o^2-F_c^2)^2]/\Sigma[w(F_o^2)^2]]^{½}$, $w = 1/[\sigma^2(F_o^2) + (aP)^2 + bP]$, where $P = [\max(F_o^2,0) + 2F_c^2]/3$

Appendix III

Table C4. Crystal data and structure refinement for H_2L^{2F2S}·**DMSO** and H_2L^{4S} ·**DMSO**.

	H_2L^{2F2S} ·DMSO	H_2L^{4S} ·DMSO
Empirical formula	$C_{28}H_{32}F_2O_6S_4$	$C_{32}H_{42}O_6S_6$
Formula weight	630.77	656.85
Temperature/K	200.0	200.0
Crystal system	triclinic	monoclinic
Space group	P-1	$P2_1/c$
a/Å	5.9962(2)	13.6089(8)
b/Å	8.8616(3)	27.8377(18)
c/Å	15.0061(5)	10.4520(6)
α/°	90.5810(10)	90
β/°	100.0830(10)	112.349(3)
γ/°	104.9920(10)	90
Volume/Å^3	757.04(4)	3662.2(4)
Z	1	4
ρ_{calc}g/cm^3	1.384	1.191
μ/mm^{-1}	0.366	3.218
F(000)	330.0	1368.0
Crystal size/mm^3	0.25 × 0.15 × 0.1	0.23 × 0.13 × 0.12
Radiation	MoKα (λ = 0.71073)	CuKα (λ = 1.54178)
2Θ range for data collection/°	4.766 to 51.66	6.35 to 141.97
Index ranges	-6 ≤ h ≤ 7, -10 ≤ k ≤ 10, -18 ≤ l ≤ 18	-16 ≤ h ≤ 16, -33 ≤ k ≤ 33, -11 ≤ l ≤ 12
Reflections collected	28468	49316
Independent reflections	2912 [R_{int} = 0.0343, R_{sigma} = 0.0151]	6996 [R_{int} = 0.1099, R_{sigma} = 0.0709]
Data/restraints/parameters	2912/2/246	6996/41/436
Goodness-of-fit on F^2	1.077	1.049
Final R indexes [I>=2σ (I)]	R_1 = 0.0307, wR_2 = 0.0825	R_1 = 0.0824, wR_2 = 0.2367
Final R indexes [all data]	R_1 = 0.0337, wR_2 = 0.0841	R_1 = 0.1227, wR_2 = 0.2807
Largest diff. peak/hole / e Å^{-3}	0.36/-0.31	0.77/-0.65

$R1 = \Sigma||F_o|-|F_c||/\Sigma|F_o|$, $wR2 = [\Sigma[w(F_o^2-F_c^2)^2]/\Sigma[w(F_o^2)^2]]^{½}$, $w = 1/[\sigma^2(F_o^2) + (aP)^2 + bP]$, where $P = [\max(F_o^2,0) + 2F_c^2]/3$

3.3 IR-spectra of new molecules

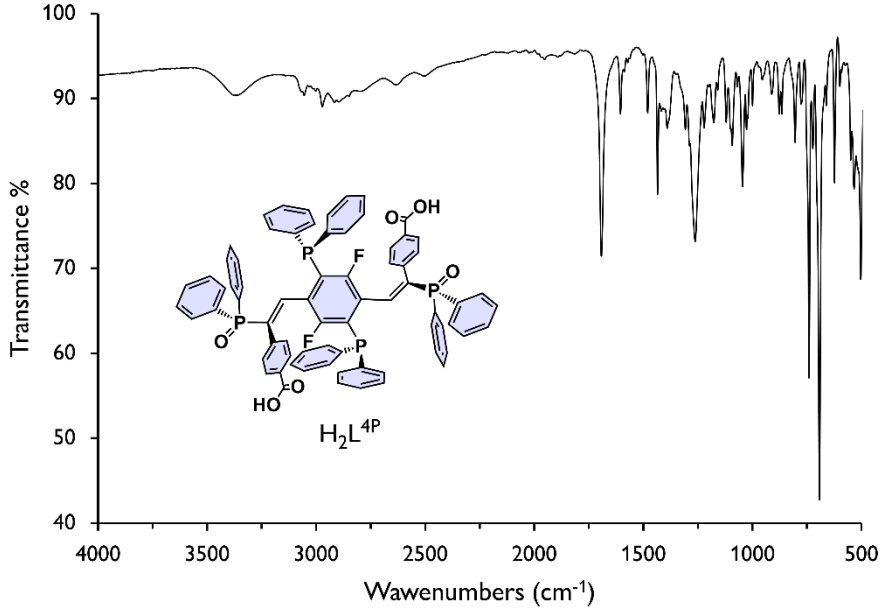

Figure C21. FT-IR spectrum (500-4000 cm^{-1}) of the ligand $\mathbf{H_2L^{4P}}$.

Appendix III

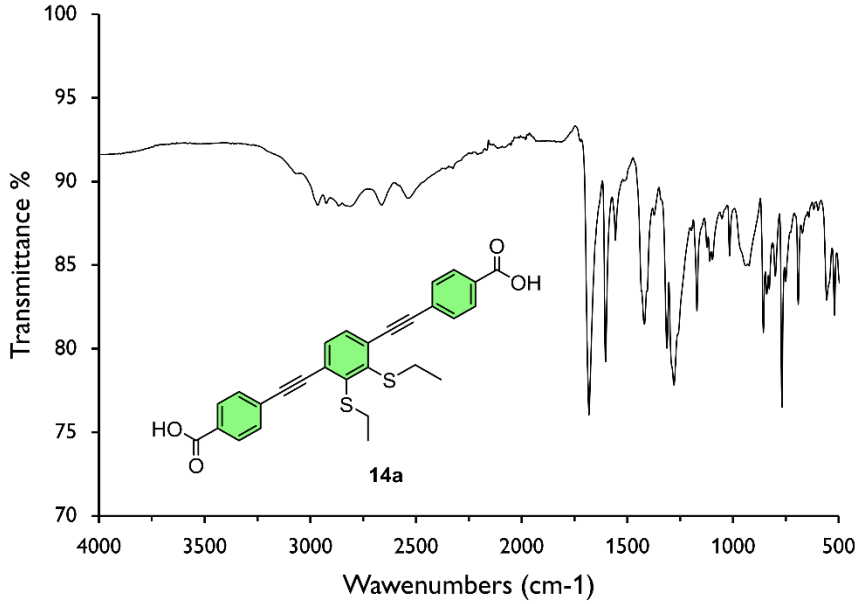

Figure C22. FT-IR spectrum (500-4000 cm^{-1}) of **14a**.

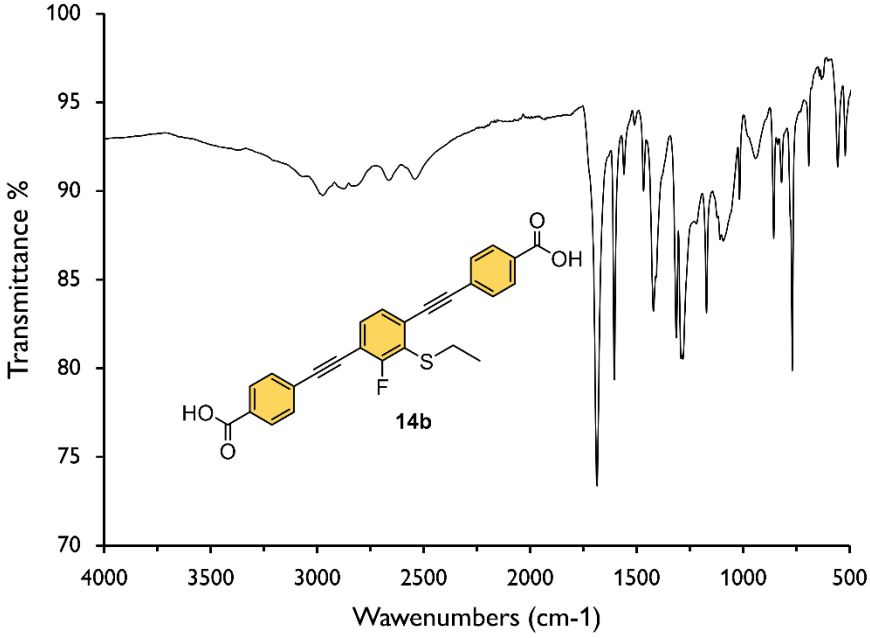

Figure C23. FT-IR spectrum (500-4000 cm^{-1}) of **14b**.

Appendix III

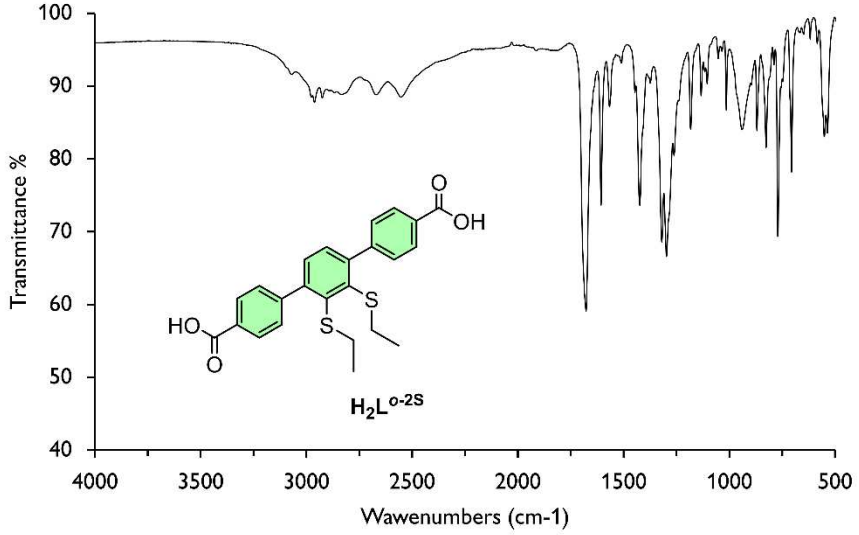

Figure C24. FT-IR spectrum (500-4000 cm^{-1}) of $\mathbf{H_2L^{o\text{-}2S}}$.

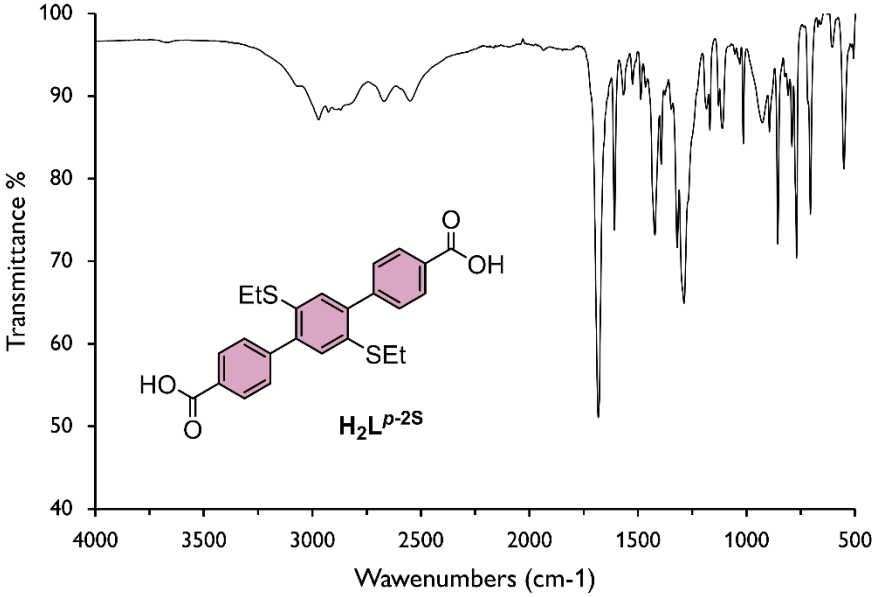

Figure C25. FT-IR spectrum (500-4000 cm^{-1}) of $\mathbf{H_2L^{p\text{-}2S}}$.

3.4 Zn complex with H_2L^{4P}

The preliminary investigation on the synthesis of zinc complex with H_2L^{4P} ligand is shown in Figure C26 and Table C5. The table shows the results and the experimental conditions performed. The new material displays a stability up to 200°C with a temperature of maximum degradation at 402°C and a weight loss of 51%.

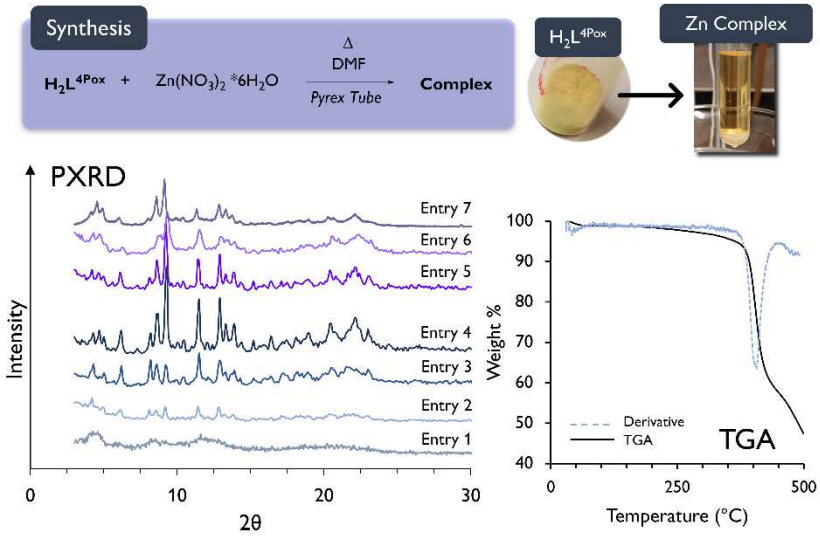

Figure C26. Synthesis of Zn complex with H_2L^{4Pox}, PXRD patterns of the resulting materials and TGA trace on the obtained zinc complex with H_2L^{4Pox}.

Table C5. Experimental conditions used to synthetize Zn complex with H_2L^{4Pox}.

	Conditions	Temp.	L:M Ratio	Time	Results
Entry 1	5 mL DMF in 20 mL tube	80°C	1:1	8 d	Amorphous
Entry 2	5 mL DMF in 20 mL tube	110°C	1:0.5	5 d	Crystalline
Entry 3	5 mL DMF in 20 mL tube	110°C	1:1	5 d	Crystalline
Entry 4	5 mL DMF in 20 mL tube	110°C	1:2	5 d	Crystalline
Entry 5	2 mL DMF in 10 mL tube	110°C	1:2.5	2 d	Crystalline
Entry 6	10 mL DMF in 20 mL tube	110°C	1:4	2 d	Amorphous
Entry 7	5 mL DMF in 20 mL tube	120°C	1:1	1 d	Amorphous

3.5 UiO-68-2F2S

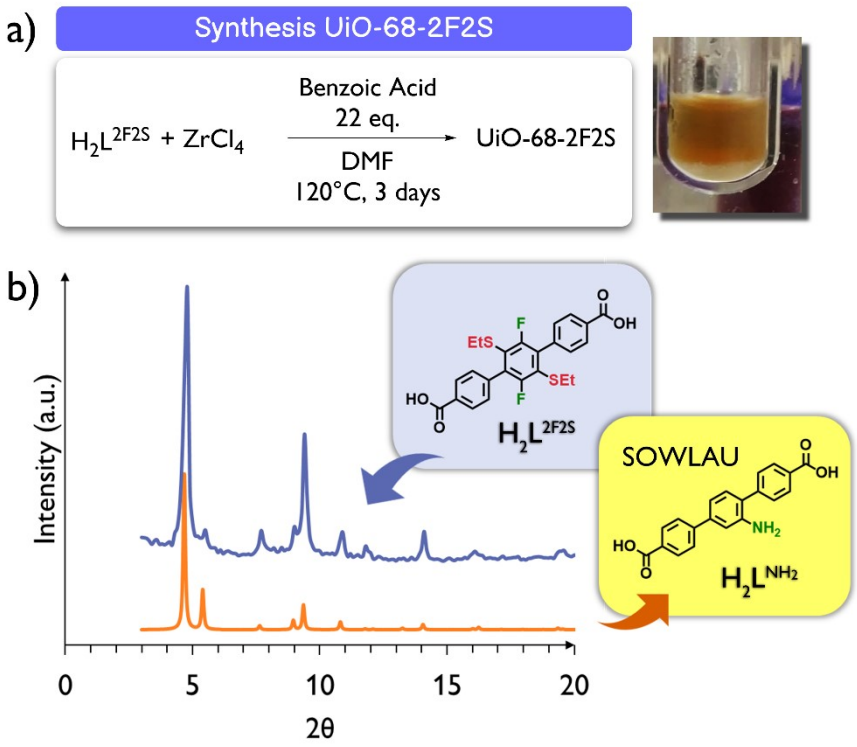

Figure C27. Synthetic conditions of UiO-68-2F2S, and PXRD comparison between the reported material and the data previously reported for the same family of MOFs (CCDC refcode SOWLAU).

3.6 Impregnation methods

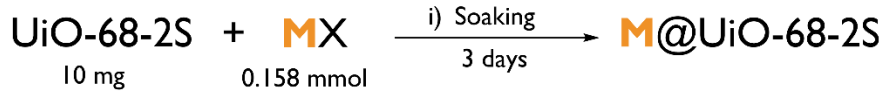

i)	Metal Precursor MX	Method	Solvent	Time (d)
Pd@UiO-68-2S	**Pd**$(OAc)_2$	Freeze and thaw	DMF	3
Pt@UiO-68-2S	*cis*-**Pt**$(MeCN)_2Cl_2$	Freeze and thaw	DMF	3
Co(NO$_3$)$_2$@UiO-68-2S	**Co**$(NO_3)_2$*$6H_2O$	Soaking at r.t.	THF	3
Co(OAc)$_2$@UiO-68-2S	**Co**$(OAc)_2$*$4H_2O$	Soaking at r.t.	EtOH	3
CoCl$_2$@UiO-68-2S	**Co**Cl_2*$6H_2O$	Soaking at r.t.	THF	3
Ni@UiO-68-2S	**Ni**$(NO_3)_2$*$6H_2O$	Soaking at r.t.	Acetone	3
Pd(COD)@UiO-68-2S	*cis*-**Pd**$(COD)Cl_2$	Freeze and thaw	DMF	3

Figure C28. Summary of the experimental conditions of the UiO-68-2S functionalization with palladium, platinum, cobalt and nichel.

3.7 ICP analysis

Table C6. ICP analysis of **UiO-68-2S** and **M@UiO-68-2S** materials.

	Sample	% **Zr** (w/w) s.d.	% **Pt** (w/w) s.d.	% **Pd** (w/w) s.d.	% **Co** (w/w) s.d.	% **Ni** (w/w) s.d.
1	UiO-68-2S	6.4 ± 0.1				
2	**Pt**@UiO-68-2S	5.27 ± 0.06	5.50 ± 0.03			
3	**Pd**@UiO-68-2S	4.71 ± 0.07		4.66 ± 0.04		
4	**Co**$(OAc)_2$@UiO-68-2S	1.57 ± 0.01			11.21 ± 0.04	
5	**Ni**@UiO-68-2S	5.72 ± 0.07				0.575 ± 0.008

3.8 EDX analysis

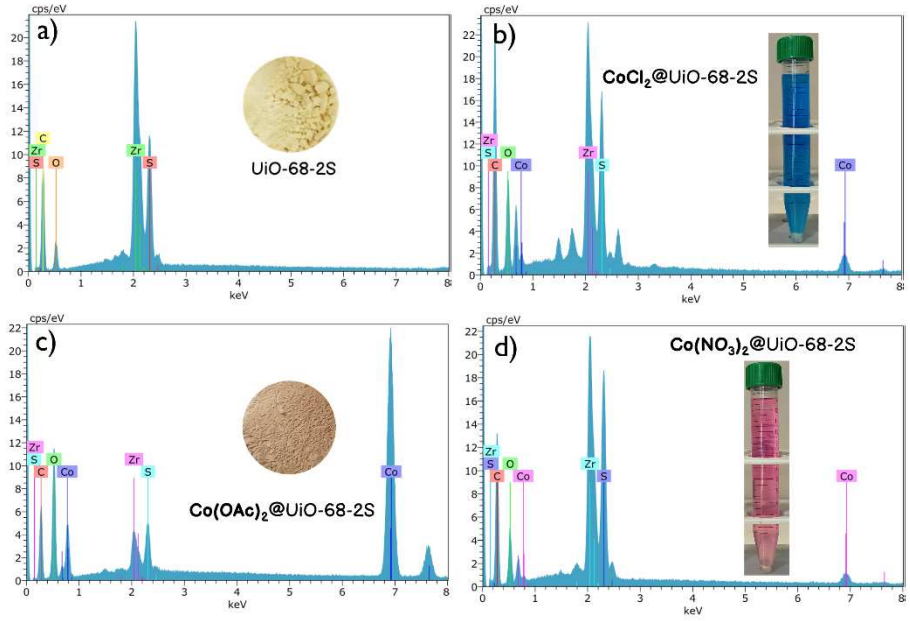

Figure C29. EDX analysis of **UiO-68-2S** (a), **Co**Cl_2@UiO-68-2S (b), **Co**$(OAc)_2$@UiO-68-2S (c) and **Co**$(NO_3)_2$@UiO-68-2S (d).

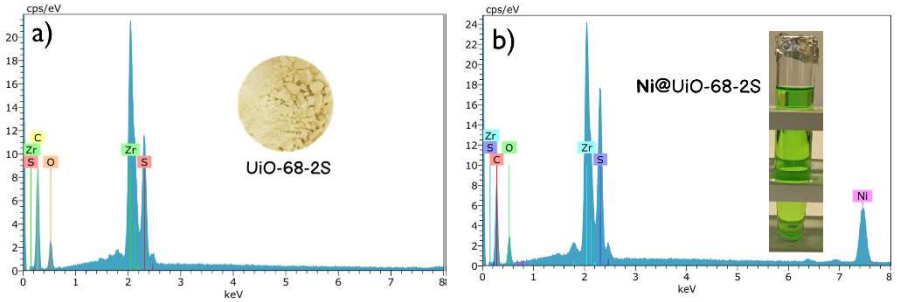

Figure C30. EDX analysis of **UiO-68-2S** (a) and **Ni**$(NO_3)_2$@UiO-68-2S (b).

Appendix III

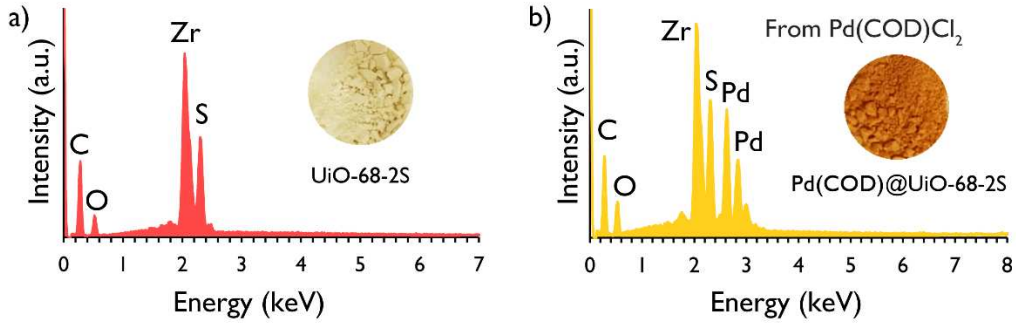

Figure C31. EDX analysis of **UiO-68-2S** (a) and **Pd**(COD)@UiO-68-2S (b).